The cold wire gas metal arc welding (CW-GMAW) process: Description and Applications

by

Rafael De Araujo Ribeiro

A thesis
presented to the University of Waterloo
in fulfilment of the
thesis requirement for the degree of
Doctor of Philosophy
in
Mechanical and Mechatronics Engineering

Waterloo, Ontario, Canada, 2020

Examining Committee Membership

The following served on the Examining Committee for this thesis. The decision of the Examining Committee is by majority vote.

Supervisor:	Adrian P. Gerlich Associate Professor, Dept. of Mech. and Mechatronics Engineering, University of Waterloo
Co-supervisor:	Kyle J. Daun Professor, Dept. of Mech. and Mechatronics Engineering, University of Waterloo
Internal Member:	Elliot Biro Assistant Professor, Dept. of Mech. and Mechatronics Engineering, University of Waterloo
Internal-External Member:	Mihaela Vlasea Assistant Professor, Dept. of Mech. and Mechatronics Engineering, University of Waterloo
Internal-External Member:	Scott Walbridge Associate Professor, Dept. of Civil and Env. Engineering, University of Waterloo
External Member:	Americo Scotti Professor, Division of Welding Technology, Högskolan Väst

AUTHOR'S DECLARATION

This thesis consists of material all of which I authored or co-authored: see Statement of Contributions included in the thesis. This is a true copy of the thesis, including any required final revisions, as accepted by my examiners.

I understand that my thesis may be made electronically available to the public.

STATEMENT OF CONTRIBUTIONS

This thesis includes ten chapters. Chapters 3 to 9, represent publications I authored or co-authored. It should be noted that the main work in the lab, including sample preparation, welding of the samples, mechanical testing, writing, and characterization, was done by my own. The following co-authors have contributed to the current work as outlined below:

Professor Adrian P. Gerlich supervised this PhD thesis.
Professor K.J. Daun co-supervised this thesis.

Mr. P.D.C. Assunção and Mr. E.B.F. Dos Santos helped me to prepare the welded samples and perform the welding process and collect the welding data.

Professor E.M. Braga helped with discussions.

The balance of this work is my own.

ABSTRACT

The demand for new and reliable welding processes comes from the need to improve productivity and quality in welding of new materials used in infrastructure projects. Among the areas where this development is crucial, is pipeline welding, which is performed in large infrastructure projects.

The development of new grades of high strength steels for line pipes has also driven the need for newer welding process which offer reduced heat input into the work piece, thus avoiding deterioration of the material properties. Since these steels are heat sensitive, the general goal is to increase deposition while maintaining similar nominal heat input into the steel. Cold wire gas metal arc welding (CW-GMAW) is a process that could offer such performance, however a comprehensive understanding of the process features is still lacking in the available literature.

To address this lack of understanding, the present work will present a comprehensive analysis of the CW-GMAW process while employing a constant voltage welding power source. First, this work reports a study on the metal transfer dynamics of the CW-GMAW process using high speed imaging synchronized with current and voltage. The droplet diameter and its frequency are estimated and correlated to different transfer mode regimes.

In addition, estimates of melting efficiency of the welds and geometry measurements of the beads are reported. Subsequently, a study on the application of CW-GMAW to fill 4 mm wide narrow gaps is reported, it was found that CW-GMAW provides better consistency during welding and avoids sidewall penetration which hamper the mechanical properties of the joints. An overview on current pulsation, on CW-GMAW, is also reported. It was found that cold wire feed rates affect welding with low peak to background current ratio causing differences on weld bead cooling rate, leading to differences in hardness. Globular to spray transition in CW-GMAW was also studied, and it was found that CW-GMAW transits faster to spray regime than standard GMAW.

In order to understand the effect of the cold wire feed rate on the energy transferred to the workpiece during welding, an uncertainty study on a water-flow calorimeter was performed, followed by calorimetry of CW-GMAW for the three natural transfer regimes (short-circuit, globular, and spray). Results show that the efficiency on CW-GMAW depends on cold wire feed rate and metal transfer. Lastly, the mechanical properties of welding joints are tested and the CW-GMAW provided better performance for the welding parameters tested.

In summary, the CW-GMAW process offers higher productivity than standard GMAW and can be employed successfully with or without pulsation control of current. The thermal efficiency of the process for the same metal transfer decreases with an increase in cold wire feed rate along with reduced dilution of the filler metal. This interesting process feature also qualifies the CW-GMAW for hardfacing applications.

Keywords: GMAW,CW-GMAW, metal transfer, arc dynamics, stability, droplet features and bead geometry measurements.

ACKNOWLEDGEMENTS

I would like to thank Dr. A.P. Gerlich and Dr. K.J. Daun for their advisorship through this doctorate. Moreover, I would like to acknowledge the help and promptitude of all my colleagues of the centre for advanced materials joining (CAMJ) of the University of Waterloo. And, lastly to Dr. Charles Kwan for the very interesting discussions.

Dedication

This work is dedicated to M.D.C.R.A. and R.N.P.R. for their support.
And, to my late father (*in memoriam*).

Table of Contents

List of Figures

List of Tables

List of Symbols

η_a Arc efficiency in % 16

θ Arc root angle in degrees 12

A_{base} Area in the weld bead due to the base metal in (mm^2) 19

A_{filler} Area in the weld bead due to the filler metal in (mm^2) 19

t_b Time during current background during pulsed gas metal arc welding. 69

$\frac{I_b}{I_p}$ Ratio between the background and the peak current 64

w Bead width in (mm) 20

Q_{CW} Cold wire absorbed power in (kJ/s) 36

$\dot{m}$ Cold wire mass feed rate in (kg/s) 36

λ_c Critical wavelength for droplet detachments according pinch instability theory, in (mm) 13

J Current density in arc electric (A/m^2) 12

ρ Density in (kg/m^3) 11

D Dilution in % 23

C_d Drag coefficient for welding droplet across the arc column 11

R_γ Effective radius of droplet in (mm) 13

$E_{arc+electrode}$ Energy transferred to the work-piece from the electric arc and the electrode in (kJ/s) 15

E_{bm} Energy transferred to the work-piece and employed to create the heat affected zone (HAZ) and diffused to through the base metal in (kJ/s) 15

E_{fz} Energy transferred to the work-piece and employed to create the fusion zone in (kJ/s) 15

E_{losses} Energy lost to the environment through different ways, e.g. radiation, convection, etc. in (kJ/s) 15

E Electric field across the arc in (V/m) 8

F_d Drag force in (N) 11

F_{em} Electromagnetic force in (N) 11

F_γ Surface tension force in (N) 11

F_g Gravitational force in (N) 11

v_f Fluid velocity (m/s) 11

q_{gross} Gross heat input in (J/mm) 18

q^* Net heat input per unit of length in (J/mm) 18

I_{sc} Welding power supply short-circuit current (A) 9

I Arc current in (A) 9

ν Kinematic viscosity in (mm^2/s) 20

L Latent heat of fusion (kJ/kg) 36

ϕ Angle between the electromagnetic force and the longitudinal axis of the arc, in degrees 12

B Magnetic field generated by the arc in (T) 12

μ_0 Magnetic permeability in vacuum in (N/A^2) 12, 13

η_m Melting efficiency in % 19

T_m Melting temperature in (K) 36

K_0 Modified Bessel function of second kind 17

Q_{net} Net heat input in (J/s) 16

Q Nominal heat input in (J/s) 16

P Non-dimensional melting power 20

A_p Projected area of the droplet on a perpendicular plane to fluid flow mm^2 11

r Radial distance from the heat source, where $r^2 = x^2 + y^2 + z^2$ in (m) 16

R Droplet radius in (mm) 11–13

T_0 Room temperature in (K) 16

k Thermal conductivity in (W/mK) 16

α Thermal diffusivity in (m^2/s) 16

V Welding travel speed (mm/s) 16

U_0 Welding power supply open circuit voltage in (V) 9

U Arc voltage in (V) 9

V_a Anode voltage fall in (V) 8

V_{column} Arc-column voltage fall in (V) 8

$V_{cathode}$ Cathode voltage fall in (V) 8

H_{base} Area in the weld bead due to the base metal in (J/mm^3) 19

H_{base} Area in the weld bead due to the base metal in (J/mm^3) 19

L Weld bead length in (mm) 18

t_{weld} Welding time in (s) 19

c_s Wire specific heat in (kJ/KgK) 36

γ Molten metal surface tension, in (N/m) 12

g Gravity acceleration equal to 9.81 (m/s^2) 11

l_a Arc length in (mm) 8

Chapter 1

Introduction

1.1 The Importance Of The Welding Industry

Welding is one of the most prominent manufacturing process in industry, since nearly every manufacturing route involves at least one welding operation during assembly. This scenario drives research with the aim of introducing newer welding processes that offer effective control of induced material properties through of process parameters.

A recent meeting of the American Welding Society (AWS) [12] noted that welding is strategic for the economic growth of a country. Specifically, it was suggested that, by 2020, welding needs to be completely integrated to other manufacturing process, and that the following goals are fundamental to this objective:

1. Increase of productivity through automation, cost reducing, and better process selection. It is expected that this actions will lead to reduction of 25% in the overall costs;

2. Enhance welding through correct process selection, aiming for higher integration to other manufacturing processes and higher versatility;

3. Better practices in education of welding personal, and higher rates of energy savings during manufacturing operation, in order to reduce heat input and post-welding operations (e.g straightening of distorted joints).

In summary, improvements to productivity, measured by deposition in (kg/h), and lower heat input are of fundamental importance to the next generation of welding processes. A prime example of heavy equipment welding (e.g. pipeline welding) involves the joining of high strength steels used to fabricate pipelines with higher productivity and reliability.

1.2 Pipeline Welding

In a recent report produced by the National Energy Board (NEB) of Canada [1], it was suggested that crude oil production will increase steeply until 2030, and then level off. This implies that there will be a need to increase the available infrastructure for transporting oil and its derivatives. Figure 1.1 shows the projected growing production of crude oil in Canada until 2040. Although there has been a steep rise in the rate of oil transport by rail in Canada due to keep up with this production, this presents a higher risk and impacts associated with derailment accidents involving oil tanker cars. [13].

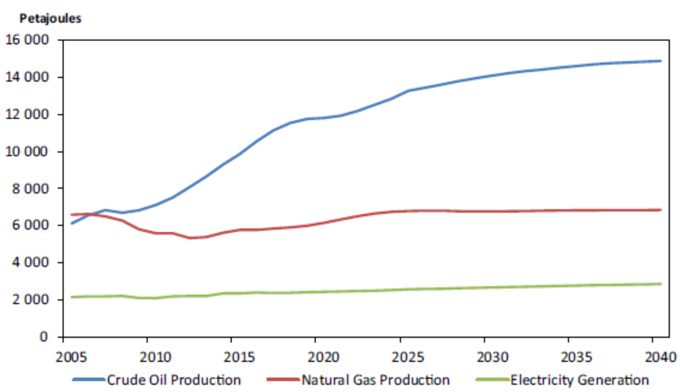

Figure 1.1: Energy production in Canada. [1].

Even in the case of natural gas transmission, there is a need for considerable growth to simply meet existing consumption demands. For example,TC Energy Inc recently announced the investment of $160 M for pipeline expansion [14] in order to transport extra 80 million cubic feet per day of natural gas needed for southern Ontario consumers. Additionally, the same company will invest $2 billion to expand the pipelines facilities of its Nova Gas Transmission Ltd.(NGTL) system, with ongoing investment until 2021 based on an existing contract. This project will consist of 273 km of pipelines and five compressing stations, representing a major infrastructure construction project in the near future. Figure 1.2 shows a sketch of the Nova project as well the existing NGTL pipelines. A consequence of these new investments in pipeline construction and/or expansion is the need to develop new welding process, since welding plays an important role as a joining method of the pipe sections.

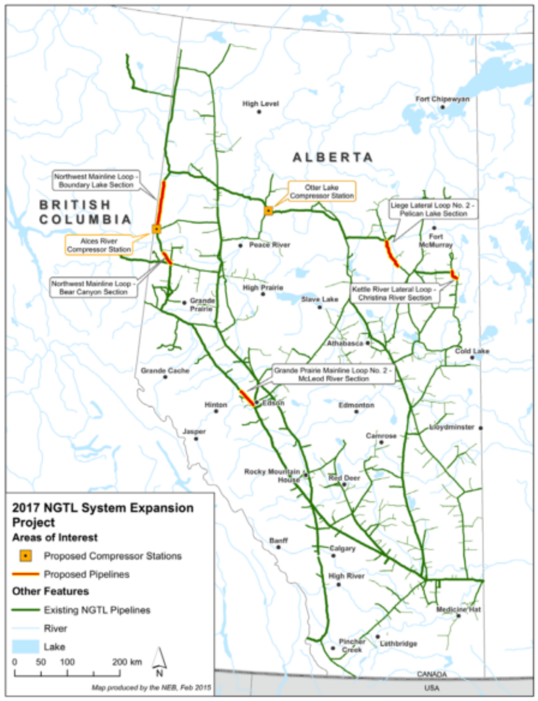

Figure 1.2: Map of the NGTL existing pipelines and projcted expansion. [2].

1.3 Welding Process: Productivity and Quality

Welding is the main method used for assembly of the pipe sections. A common paradigm for evaluating new welding process involves a compromise between productivity and quality, the latter impacting the reliability of joints produced. Various processes can be used for pipeline welding for instance, arc welding processes, laser welding, electron beam welding, and hybrid processes.

The main advantage of arc welding is its ability to efficiently fill the joint gaps. However, the high nominal heat input softens the heat affected zone (HAZ) of the welds, which can lead to embrittlement which is deleterious to the mechanical properties of the joints. Yapp and Blackman [15] provided a review on the latest developments related to pipeline applied welding process, highlighting the advantages of using two torches in the TANDEM GMAW process developed at Cranfield University.

The main advantage of laser welding derives from the highly focused laser energy which decreases the width of the HAZ compared to arc welding. However, this class of process is expensive, and is not widely used for pipelines. One of the earlier studies on the applications of laser welding to pipeline steels is attributed to Miranda et al.[16], which concluded that it was suitable for field applications, and that it produced welds having finer grain pattern when compared to gas tungsten arc welding (GTAW).

The use of electron beam welding (EBW) techniques is still emerging. Komizo [17] refers to its use in Japan in 1994; the main advantage considered is the low nominal heat input while welding and the ability to be applied in all positions. One of the drawbacks is the low productivity, due to complex equipment needed to the need to generate a local vacuum at the workpiece which can transfer the electron beam.

In order to couple productivity and quality, hybrid arc-laser welding processes were tested in pipelines. Recent research [18] examined the stability of the beam during root pass welding in the horizontal position, referring to energy and penetration as key parameters, and the results of these studies indicate sufficient stability. One of the main advantages of this class of processes is the coupling of high penetration with delivery of a filling metal which can theoretically permit the joining of thick plates without multiple passes.

1.4 Motivation

Motivated by the fact that new technologies are always required in pipeline welding in order to optimize productivity and reliability of pipe joints, this document reports research on the Cold Wire Gas Metal Arc Welding (CW-GMAW) process in terms of two areas:

a. A study on the feasibility to narrow groove welding; and

b. An evaluation of arc stability, metal transfer, bead geometry, dilution, thermal efficiency, and mechanical properties.

1.5 Objectives

1.5.1 General Objective

A general objective of this document relates to the study of CW-GMAW applied to narrow groove joint designs typical of pipeline welding, and also for V-groove joints. The key aspects/attributes involve: arc stability, the influence of the secondary wire on metal transfer mechanisms, and the implications of metal transfer mechanisms on bead geometry, on dilution, in addition to thermal efficiency measurements for CW-GMAW and standard GMAW and assessment of mechanical of weld joints.

1.5.2 Specific Objectives

In order address the research needs outlined in the previous subsection, this thesis is divided into the specific measurable goals related to the evaluation of the CW-GMAW process:

1. Test the feasibility of the process for narrow gap welding, and present specific features of metal transfer for narrow grooves;

2. Evaluate the role of cold wire feeding on the dynamics of the arc for constant voltage and pulsed regimes;

3. Determine the influence of cold wire on the globular to spray transfer;

4. Measure the thermal efficiency of the CW-GMAW process;

5. Assess the mechanical properties of CW-GMAW joints.

These aspects are investigated through experiments that focus on narrow gap welding feasibility, metal transfer dynamics, calorimetry of CW-GMAW, and on mechanical properties of weld joints fabricated using CW-GMAW.

1.5.3 Thesis Chapters Outline

This thesis consists of ten chapters outlined in the following list:

1. Chapter 1 provides an introduction including the motivation and research objectives;

2. Chapter 2 consists of a literature review that summarizes basic knowledge necessary for understanding the subsequent chapters in this thesis, and the general methodology and equipment used in this work. (Although each chapter has a methodology section reporting specific details of the experiments performed);
3. Chapter 3 discusses the metal transfer of CW-GMAW for the three natural transfer modes and estimates the melting efficiency of the CW-GMAW process;
4. Chapter 4 discusses the narrow gap welding application and the advantages of using CW-GMAW over standard GMAW;
5. Chapter 5 discusses the effect of cold wire feed on current control through pulsation, using a standard waveform, and its effect on microstructure and Vickers hardness;
6. Chapter 6 reports the effect of cold wire feed on the globular to spray transition which is investigated though high speed cinematography with synchronized electric signals acquisition;
7. Chapter 7 describes the effect of calorimeter parameters on the overall measurement uncertainty of thermal efficiency employing a traditional water-flow calorimeter;
8. Chapter 8 builds on the results discussed on Chapter 8 and reports the thermal efficiency of the CW-GMAW process;
9. Chapter 9 reports the tensile mechanical properties of CW-GMAW weld joints versus standard GMAW weld joints.
10. Finally, Chapter 10, reports the comprehensive conclusions, the suggestions for future work, and list of contributions originated from this thesis.

Chapter 2

Literature Review And General Methodology

2.1 Physics Of The Arc Welding Process

2.1.1 Principles Of The Electric Arc

An electric arc results from a discharge between two poles in a conductive medium such as an ionized gas. This discharge is then converted into light, sound, and heat. This physical phenomenon can be used as a controlled and directed heat source, as in the case arc welding and related techniques.

Thus, understanding the physical phenomena involving the electric arc and their interplay with heat transfer and the final properties of welds is of fundamental importance. In order to further study the electric arc, let us divide it into three regions: the anode, cathode, and arc column.

The anode is the the positive part of the arc which attracts electrons; the arc column comprises the region formed by the ionised plasma resulting from the shielding gas through which matter, electrons, and ions flow. The negative part of the arc is the cathode, which is the source of electrons. Figure 2.1 shows the contribution of the three zones of the electric arc to the overall voltage of the arc.

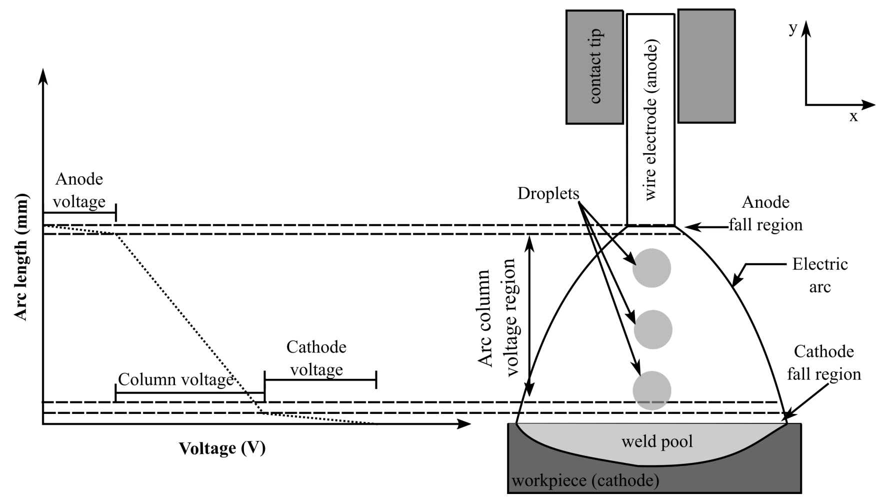

Figure 2.1: Voltage contribution of the arc zones.

The overall voltage can be expressed as the sum of the anodic fall voltage V_a, the column voltage V_{column}, and the cathodic fall voltage $V_{cathode}$.

$$V = V_a + V_{column} + V_c \tag{2.1}$$

where V_a represents the anodic fall, V_{column} the column voltage and $V_{cathode}$represents the cathodic fall voltage. In addition, one can further expand Equation 2.1 knowing that the voltage across the arc column is proportional to the arc length (l_a). Then, it is possible to write:

$$V = V_a + El_a + V_c \tag{2.2}$$

where E represents the electric field across the column. According to Marques [19] the value of E in a tungsten inert gas (TIG) arc for pure argon is around 1000 V/m. As $V_{column} \gg (V_a + V_c)$ the voltage across the arc is proportional to the arc length (l_a).

2.1.2 The Electric Arc Applied To Eelding

This section will introduce the some special features of the electric arc that are relevant to welding technology. The static characteristics of the arc welding power source, are so-named because they do not take into account dynamic variations in current(A) and voltage (V). The characteristic curve of the arc can be modelled by:

$$U = A + BI + \frac{C}{I} \tag{2.3}$$

where A, B and C are empirical constants, U is voltage and I is the current. Table 2.1 gives the values for A, B and C referring to Figure 2.2 which presents an example of static characteristics for gas tungsten arc welding (GTAW) arc for different arc lengths as well as the proportionality between voltage and arc length for selected currents. The GTAW arc is considered here for its relative simplicity and similarity with other consumable electrode arcs.

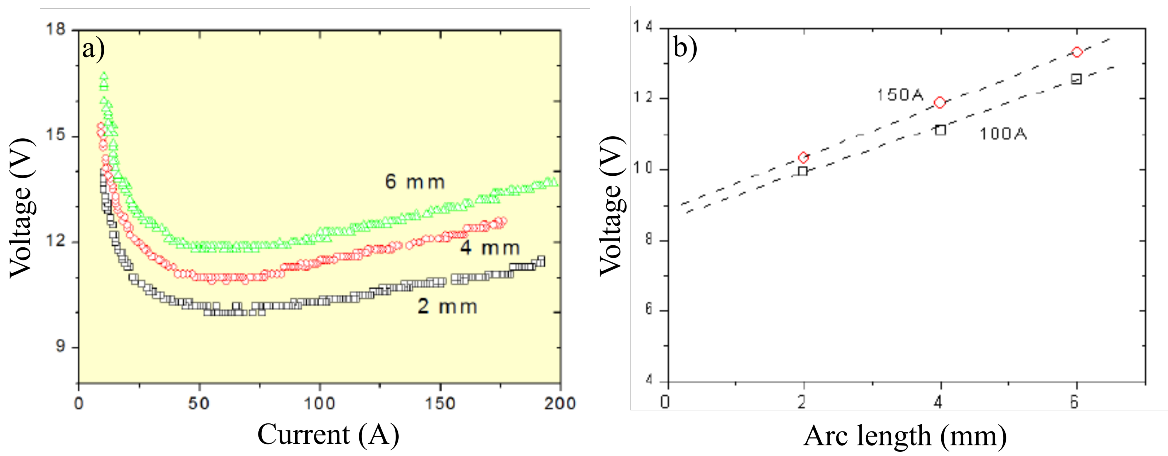

Figure 2.2: a) The arc static characteristics for different arc lengths (mm); b) The proportionality between voltage and arc length for two different current levels. Adapted from [3].

Another important feature is the characteristic power source curve. For the sake of simplicity just two types of power sources will be considered here: constant current (CC); and constant voltage (CV). Figure 2.3 shows schematics of the curves for these two sources: U_0 represents the voltage when there is no welding current and I_{sc} represent the short-circuit current.

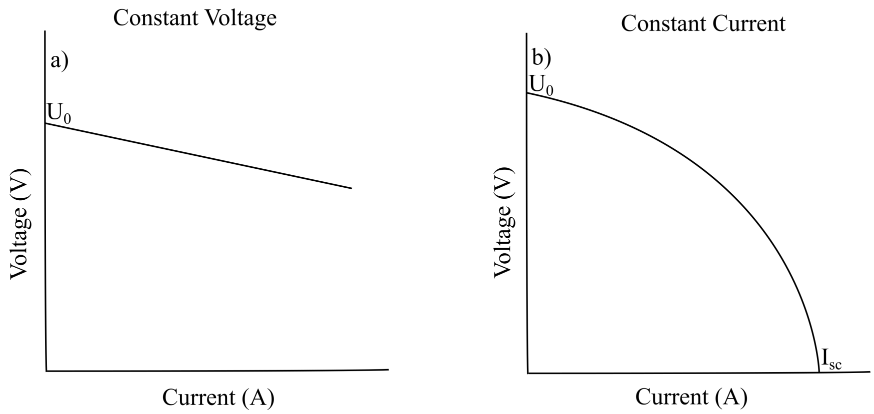

Figure 2.3: Two common types of welding power sources a) Constant voltage; b) Constant current.

Typically, the initial slope of the power source response curve is 0.02 V/A for constant voltage power sources, while for constant current sources the slope is on the order of 10 V/A. When operating the arc, the characteristic curve is superimposed on the source curve and their intersections correspond to the operation point for the parameters chosen [3].

Table 2.1: Values of the constants A, B and C for the characteristic curve of the welding power source [3].

$l_a(mm)$	A (V)	B(V/A)	C(V.A)
2	7.36	0.0163	75.3
4	8.89	0.0158	78.8
6	10.25	0.0179	61.4

2.1.3 Metal Transfer Modes In Arc Welding

Basically, according to Kim et al.[20] there are two main theories that account for the metal transfer in welding with consumable electrode:

a. The static force balance theory (SFBT) and;

b. The pinch instability theory (PIT)

The SFBT simply states that the droplet at the end of the electrode tip will detach when the equilibrium between the detaching forces and the attaching forces cannot be maintained.

The basic static forces that act on the droplet are:

1. Gravitational force (F_g) due to the weight of the droplet;
2. Drag force (F_d) due to due shielding gas and plasma flow;
3. The electromagnetic (F_{em}) force due to the self-induced magnetic field and;
4. The surface tension (F_γ) force between the liquid droplet and the molten metal column.

Then, generally, a droplet will detach when force balance is exceeded according to:

$$F_g + F_d + F_{em} = F_\gamma \tag{2.4}$$

The gravitational force can be written as the product of the the droplet mass and the gravity acceleration vector, assuming that the droplet is spherical,

$$F_g = \frac{4}{3}\pi R^2 \rho g \tag{2.5}$$

where R is the droplet radius, ρ is the density of the droplet and g is acceleration of gravity. The drag force existence was first suggested by Needham et al. [21] in 1960. The drag force is estimated

$$F_d = C_d A_p \left(\frac{\rho_f v_f^2}{2}\right) \tag{2.6}$$

where C_d is the drag coefficient, A_p is the projected area on the plane perpendicular to the fluid flow, ρ_f is the fluid density andv_f is the fluid velocity.

Equations for the electromagnetic force were derived by two different researchers, independently. Greene [4] assumed that the droplet is spherical and the arc root (i.e. the area of the droplet in which the arc is rooted and current is transferred) is a semi-angle of the centre of the spherical droplet. The same result was obtained by Amson in 1965 [22] when integrating the Maxwell stresses over the surface of the the droplet and extended the results for other forms than spherical. The electromagnetic force can be written as:

$$F_{em} = \int_V (J \times B)\, sin\phi dV \tag{2.7}$$

where B is the magnetic field, J is the current density, and ϕ is the angle between the force and the longitudinal axis of the of the droplet. Integrating Equation 2.7, one obtains:

$$F_{em} = \frac{\mu_0 I^2}{4\pi}\left[ln\frac{Rsin\theta}{b} - \left(\frac{1}{4} + \frac{1}{1-cos\theta}\right) + \frac{2}{(1-cos\theta)^2}ln\frac{2}{1+cos\theta}\right] \tag{2.8}$$

where μ_0 is the magnetic permeability in vacuum, R is the radius of the droplet, b is the radius of the electrode and θ is the semi-angle of the arc root. Figure 2.4 shows a schematic of the droplet, and the relationship between ϕ and θ.

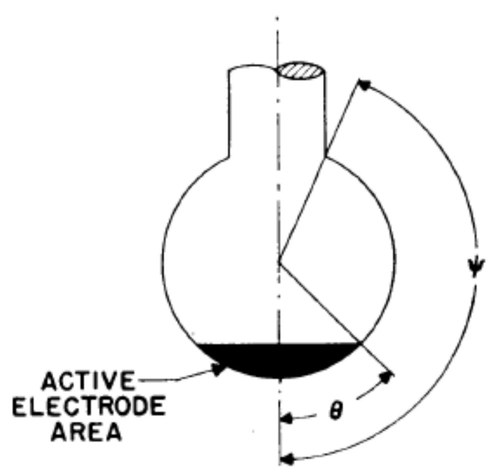

Figure 2.4: Schematics for the calculation of the electromagnetic force. Reproduced from [4].

The surface tension force according to [20] can be written as:

$$F_\gamma = 2\pi b\gamma \tag{2.9}$$

where γ is the surface tension of the liquid droplet and b is the radius of the electrode. More detailed analysis of the SFBT theory, specifically on the time variation of the axial magnetic force, can also be found in Jones et al.[23].

The PIT states that the droplet will detach when the liquid metal column is subjected to a perturbation whose wavelength is critical, forcing the column to break into a series of spherical droplets, according to Rayleigh instability theory.

This theory is based on the fact that spheres have a lower free energy per volume than a column of a droplet. Consequently, a disturbance with a critical wavelength will break the liquid column into droplets. Normally the perturbation is assumed to be sinusoidal for the sake of simplicity, and the metal droplet is assumed to be inviscid. The critical wavelength(λ_c) to break the liquid column into droplets is:

$$\lambda_c = \frac{2\pi R}{\left[1 + \frac{\mu_0 I^2}{2\pi^2 R_\gamma}\right]^2} \tag{2.10}$$

where R is the initial radius of the droplet column (cylinder), μ_0 is the magnetic vacuum permeability, and R_γ is the effective radius of the column, taking into account the bulged and pinched regions. One drawback of this theory is that is does not explain the repelling metal transfer when one uses a shielding gas rich in CO_2. One has to bear in mind that, in contrast to Rayleigh theory where the driving force for pinch was gravitational force, the driving force for pinch detachment is the self-induced electromagnetic force.

Since 1976 the International Institute of Welding (IIW) categorized the metal transfer in welding according to main mechanisms for natural metal transfer, as summarized in Table 2.2.

Table 2.2: IIW original Metal transfer classification (1976). Adapted from [10]

TRANSFER TYPE	EXAMPLE PROCESSES
1.0 Free flight transfer	
1.1 Globular	
1.1.1 Drop	Low current GMAW
1.1.2 Repelled	CO_2 shielded GMAW
1.2 Spray	
1.2.2 Streaming	Medium current GMAW
1.2.3 Rotating	High current GMAW
1.3 Explosive	SMAW (Coated electrodes)
2.0 Bridging transfer	
2.1 Short-circuit	Short-arc GMAW
2.2 Bridging without interruption	Welding w/ filler wire
3.0 Slag protected transfer	
3.1 Flux wall guided	SAW
3.2 Other modes	SMAW, FCAW

The original IIW classification considered only natural transfer modes, but the advent of electronic power sources made new transfer modes possible which correspond to the so-called controlled transfer modes. Norrish's review [24] incorporates the controlled transfer modes, such as synergic transfer, and dip transfer known as cold metal transfer (CMT).

Norrish highlights that the original IIW classification must be changed to account for new developments in power sources as well as in welding techniques. Similarly, Iordachescu (2008) [25] indicated that streaming and rotating metal transfers become independent main categories (and not types of spray), and a broad category called fundamental transfer modes is created to encompass both the natural and controlled transfer modes.

Scotti [26] proposed an updated classification dividing it broadly in contact transfer modes which encompasses, for example, short-circuit and surface tension transfer (STT), and free flight transfer modes which encompasses, for example, repelled globular and rotating spray.

In summary, many new developments in metal transfer driven by new power source technologies involve some unexplored phenomena, and this, ultimately points to the need of a revised IIW classification of metal transfer.

2.1.4 Heat Flow In Arc Welding

The thermal signature of the process is also important, especially when welding heat sensitive materials. Thus, it is vital to understand and control the effective heat input for a certain welding process, since it is fundamental to obtaining sound welds.

An earlier model (1995) for energy transfer from the arc and electrode ($E_{arc+electrode}$) to the work piece was proposed by DuPont & Marder [5], shown in Figure 2.5a. This simple model does not distinguish the different types of energy losses (E_{losses}) that occur during welding, and only accounts for the energy actually given to the fusion zone (E_{fz}) and to the base material (E_{bm}).

A more sophisticated model proposed by Scotti (2012) [27, 6], is shown in Figure 2.5b. It summarizes different types of energy losses, such as radiation and convection, in the arc and in the weld pool, as well in the work piece. Moreover, it considers different plate thicknesses. These models provide a different understanding of thermal signatures for welding processes. In Dupont's work [5] the heat input question for different welding processes was considered to be solved, and their work was merely an update review. Since then, the advent of new welding-applied calorimetric techniques reopened the heat input question. Also, the impact of the intrinsic errors of measurement techniques were considered along with their influence on the measured of heat input values.

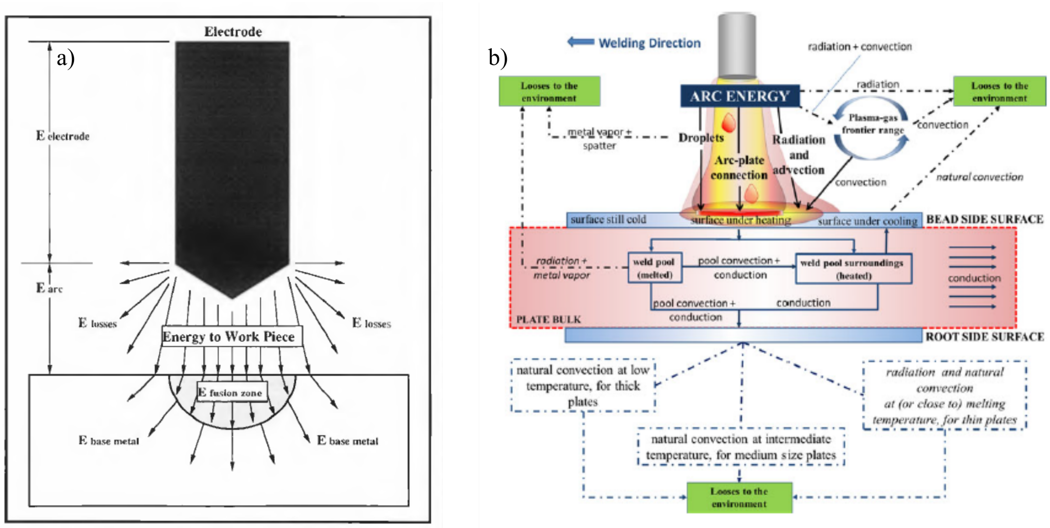

Figure 2.5: Schematics of energy balance of energy for an arc welding process: a) Dupont's Model [5], b) Scotti's model [6].

One of the first attempts to determine the temperature profiles in welds was by Rosenthal in 1941 [28]. To develop his equation, Rosenthal proposed the following hypotheses:

1. The heat flow is considered steady-state;
2. A point heat source was considered;
3. There is no phase change during the welding (no latent heat effects);
4. The solid is isotropic and thermal properties are constant;
5. There is no heat loss over the substrate surface;
6. There is no convection in the weld pool.

Figure 2.6 shows a schematic summary of the coordinates used to derive Rosenthal's equation. Rosenthal's equation for three dimension (3D) can be written as:

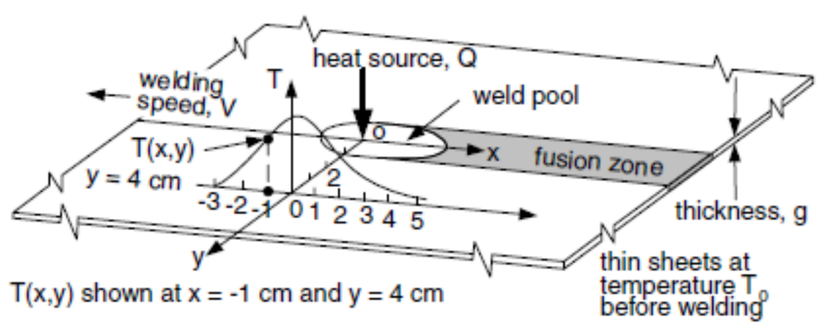

Figure 2.6: Schematics for the coordinates used to derive Rosenthal's equation. From [7].

$$\frac{2\pi\left(T-T_0\right)kr}{Q_{net}} = exp\left[\frac{-V\left(r-x\right)}{2\alpha}\right] \tag{2.11}$$

where T_0 stands for the substrate temperature before welding in (K), k is substrate thermal conductivity in (W/m.K), r is the radial distance the heat source center in (m) given by $r^2 = x^2 + y^2 + z^2$, Q_{net} is the net heat input which is written as $Q_{net} = Q\eta_a$ being η_a the arc efficiency, Q is the nominal heat input, V is the travel speed (m/s), and α is the thermal diffusivity in (m^2/s). The same equation can be written for 2D which yields,

$$\frac{2\pi\left(T-T_0\right)kt}{Q_{net}} = exp\left(\frac{Vx}{2\alpha}\right)K_0\left(\frac{Vr}{2\alpha}\right) \tag{2.12}$$

where K_0 stands for the modified Bessel function of second kind and zero order. Figure 2.1.4 shows the values of K_0 for different values of $\left(\frac{Vr}{2\alpha}\right)$.

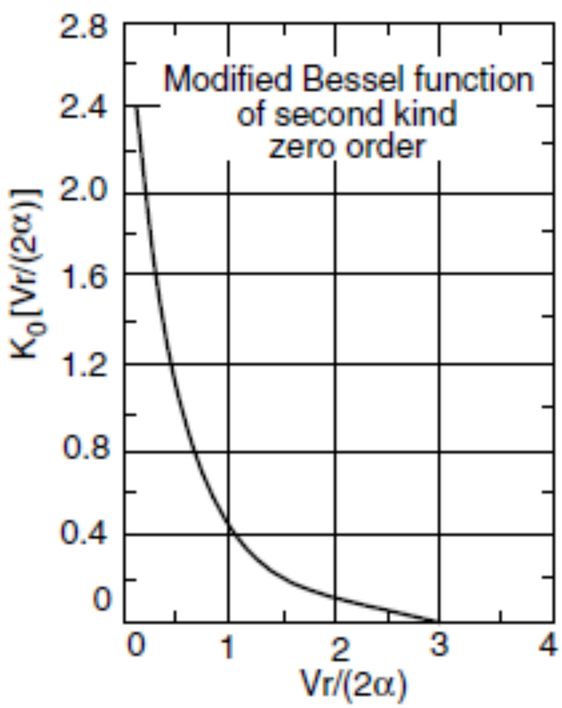

Figure 2.7: Variation of the Bessel function with $\left(\frac{VR}{2\alpha}\right)$. From [7].

The Rosenthal equation provides a segue to an important variable in welding research; arc efficiency, defined as the ratio between the net arc power over the power delivered to the workpiece by the welding power source [8].

$$\eta_a = \frac{Q_{net}}{Q} \tag{2.13}$$

Calorimetry is most often used to measure the thermal efficiency of the arc welding processes. Calorimetry involves measuring the heat delivered to the substrate using the temperature variation of a thermo-absorbent fluid which is inside the calorimeter. Meanwhile, inverse heat conduction analysis relies on the measurement of temperatures on the work piece using the heat equation to determine the heat source parameter. Table 2.3 gives the reported values of thermal efficiency of different fusion welding process according to Fuerschbach [11]. These values should not be generalized to all welding conditions, given that, there is no consensus in the literature regarding arc welding efficiency values.

Table 2.3: Reported thermal efficiencies of different fusion welding processes. Adapted from [11]

Welding process	Reported Therm. Efficiency(%)
GMAW	85
GTAW	67-80
SAW	90
SMAW	75

These reported values do not take into account different parameters that might affect thermal efficiency, such as shielding gas, arc length, substrate material, welding speed, and current/voltage waveforms. Recent works by Lyskevich et al. [6, 29] defined a quantity called the *gross heat input* which is a theoretical parameter that accounts for the heat that a process would be able to transfer to a weld bead of null length. For thin plates:

$$q^* = q_{gross}e^{-kL} \tag{2.14}$$

where q^* represents the absorbed heat per unit of weld length in (J/mm), q_{gross} is the gross heat input which represents the theoritical heat input for a bead of null length, in (J/mm) and L is weld length in (mm). One can see that with decreasing length, the absorbed heat per length trends to be equal approaches the gross heat input. Moreover, Liskevych et al. [6] were the first researchers to actually discuss the intrinsic error in a calorimetric measurement system (based on a liquid nitrogen calorimeter) and the effect on the measured values of thermal efficiency.

Haelsig et al.[30] used a new type of water calorimeter with variable water level and measured thermal efficiency of GMAW and GTAW accounting for the influence of voltage level (arc length), shielding gas flow rate and CO_2 content in the shielding gas, current waveform, and contact-tip-to-workpiece distance (mm), reporting a range of 66-82 % for GMAW and of 68-80 % for GTAW. Employing different materials, aluminium and steel, while using the same calorimeter, Haelsig [31], reported values of 69-85 % (steel) and 76-87 % (aluminium) for GMAW, which implies that far from being common, the subject of thermal efficiency for conventional welding of steel is still an unsolved subject in the literature.

Recently, Hurtig et al. [32] critically analysed a water-flow stationary calorimeter to evaluate the concept of calorimeter performance as a function of current, work-piece material and flow rate for the first time, with reported measurement error due to variations in parameters being $\pm 9\%$.

Another important factor to characterize a welding process is the melting efficiency (η_m) which is defined as the portion of heat transferred to the substrate that is actually used to melt the work-piece and filler metal. This value is defined as the ratio of melting enthalpy of the welding volume over the net heat input [5].

$$\eta_m = \frac{(A_{base} V t_{weld})\, H_{base} + (A_{filler} V t_{weld})\, H_{filler}}{\eta_a U I t_{weld}} \tag{2.15}$$

where A_{base} and H_{base} are the area formed by the base metal in a weld bead and volume melting enthalpy of the base metal (J/mm^3) and A_{filler} and H_{base} are the area formed by the filler metal in a weld bead, and volume melting enthalpy of the filler metal also in (J/mm^3), respectively. t_{weld} is the welding time in seconds. Figure 2.8 refers to these quantities.

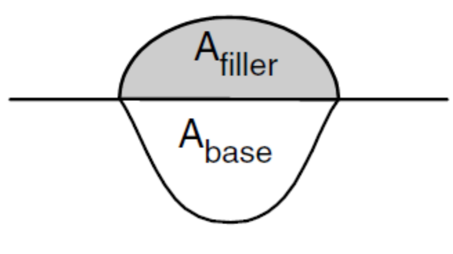

Figure 2.8: The areas due base and filler metals in a weld bead. Adapted from [7].

The literature also provides an alternative definition for melting efficiency, first given by Wells, for 2D heat transfer regime assuming Rosenthal's hypothesis, in 1952 [33].

$$\eta_m = \frac{1}{\dfrac{8\alpha}{5Vw} + 2} \tag{2.16}$$

where w is the bead weld width, V is the travel speed, and α is thermal diffusivity in m^2/s. Yet another relation describing melting efficiency is attributed to Okada (1977), for 3D heat transfer regime, also based on Rosenthal's theory[34, 35] as follows:

$$\eta_m = \frac{1}{1.35\left[1 + \left(1 + \frac{10.4\alpha^2}{Vw}\right)^{1/2}\right]} \tag{2.17}$$

Equations 2.16 and 2.17 show that melting efficiency will increase with travel speed and asymptotically approaches 0.48 for 2D geometries and 0.37 for 3D geometries [36]. One also observes that with increasing thermal diffusivity, the melting efficiency will decrease. Fuerschbach and Knorovsky (1991) [8] noticed that for GTAW and PAW the melting efficiency converges to 0.5 when plotted against the quantity $(\eta_a UIV)\,/\,(H\alpha\nu)$. In this work the non-dimensional melting power P is defined, which represents the part of the energy of the arc that is actually responsible for melting the work-piece and filler metals, where $H = H_{Base} + H_{Filler}$ and ν is the kinematic viscosity at the melting point (mm^2/s).

Figure 2.9 shows the original data reported by Fuerschbach and Knorovsky and exemplifies the methodology they used to determine the maximum theoretical melting efficiency. According to Fuerschanch's data, the theoretical melting efficiency for a 3D geometry is 0.346 and 0.407 for a 2D geometry. Dupont and Marder (1995) [5] compiled a process database for melting efficiency. Figure 2.1.4 shows the compiled data by Dupont and Marder [5].

Recently, there has been renewed interest in obtaining the melting efficiency for different joint configurations [37]. The values were reported to vary from 0.23 to 0.39.

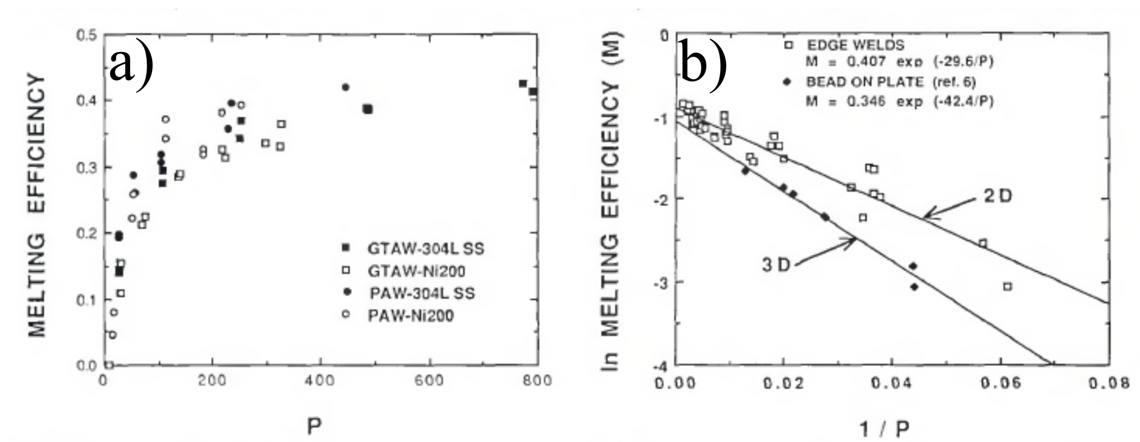

Figure 2.9: Melting efficiency data for GTAW and PAW for different materials: a) the original data as function of non-dimensional melting power; and b) semi-log plot of melting efficiency as function of inverse non-dimensional melting power (1/P). From [8].

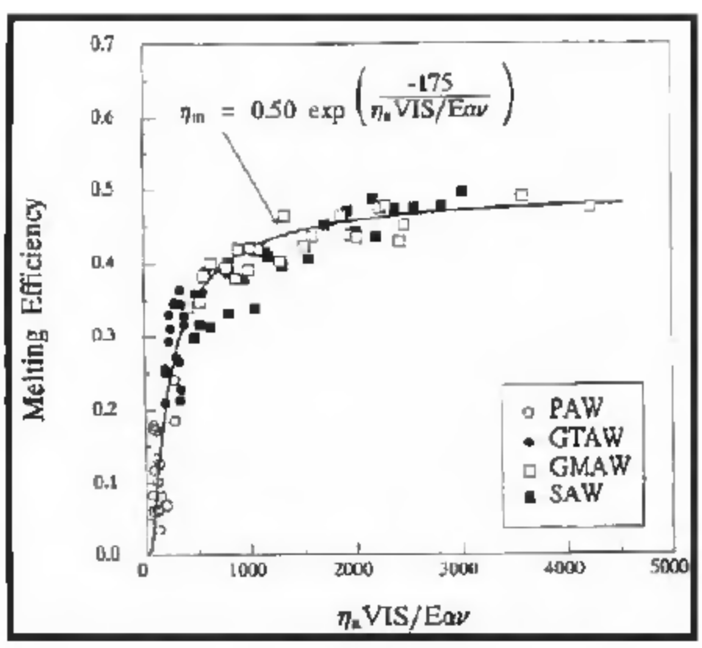

Figure 2.10: Compilled data for melting effciency for different arc welding processes. From [5].

2.1.5 Basic Arc Welding Metallurgy

This section will summarize the basics of welding metallurgy, focusing on the microstructural regions commonly found in welds, known as the weld metal (WM), the heat affected zone (HAZ), and the base metal. Figure 2.11 depicts these regions in a weld cross-section in comparison to the peak temperatures experienced, and phases predicted based on the iron-carbon phase diagram. The WM is the region of the weld where the temperature exceeds the melting temperature of the work-piece. The HAZ where the metal microstructure is affected by the heat during the welding process but experiences temperatures lower than the melting temperature of the substrate. Finally, the base metal is the region that is not affected by the heat during welding and preserves the same micro-structure of the substrate before welding.

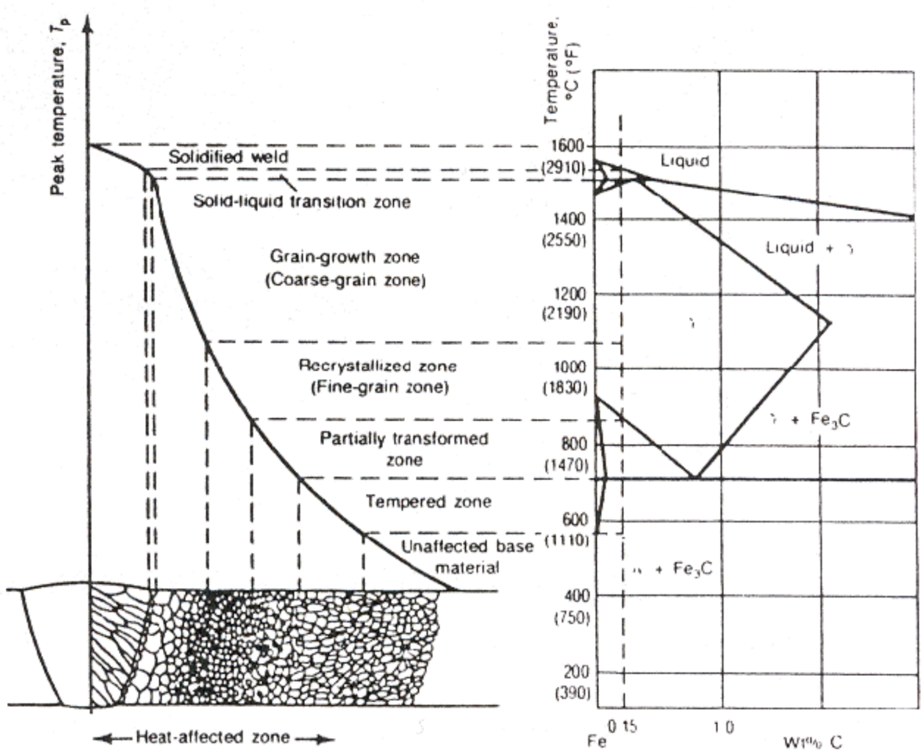

Figure 2.11: Macro-regions commonly found in a weld cross-section. Adapted from [9].

The HAZ in Figure 2.11 is further subdivided into 4 regions. The first zone is called the coarse-grained HAZ (CG-HAZ), which is immediately adjacent to the fusion line, the materials within this region is fully austenitized, and experiences a rapid growth of the austenite grains. The second region is the fine grained HAZ (FG-HAZ); this region is also heated to form austenite, but the maximum temperature achieved is lower than in the CG-HAZ such that particles do not dissolve, retarding the austenite grain growth. The inter-critical HAZ (IC-HAZ) is the region formed between the two critical temperatures A_{c1} and A_{c3}, so this region is not completely austenitized but has some some austenite. The last region is the sub-critical HAZ (SC-HAZ), which does not experience any metallurgical transformation except tempering.

Another important parameter is dilution, D. Referring back to Figure 2.8 the dilution can be defined using Equation 2.18:

$$D(\%) = \frac{A_{base}}{A_{base} + A_{filler}} \tag{2.18}$$

which indicates how much of the bead is formed by the base material. Dilution is also correlated by [36] to melting and arc efficiency. In general, higher dilution means a higher melting efficiency and vice-versa for standard arc welding processes.

2.2 Welding Processes For Narrow Gap Welding (NGW)

Pipelines are frequently welded using narrow gap (NG) joint geometries in order to reduce the quantity quantity of welding material consumed compared with wide gap (WG) grooves. This reduction in the deposited molten metal also helps to reduce weld distortion, since reducing the molten material volume will suppress solidification shrinkage. Figure 2.12 is a schematic showing the difference between wide grooves which have a typical groove angle around 30 degrees, compared to narrow grooves.

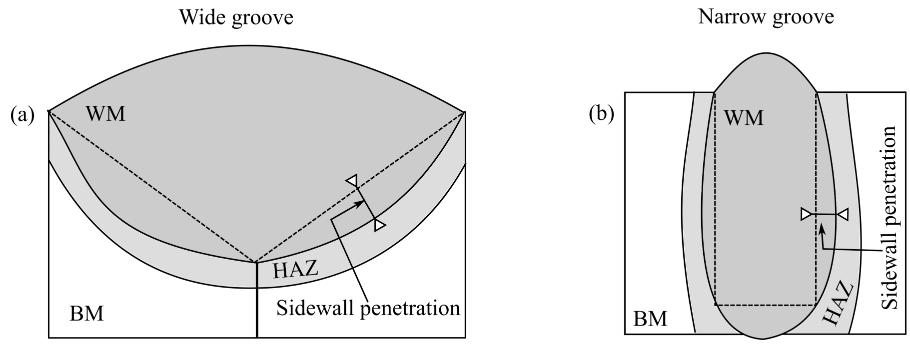

Figure 2.12: Schematic showing the difference between wide and narrow grooves.

Narrow gap welding (NGW) aims to reduce molten metal deposition volume and welding heat input by a reduction in groove width. Consequently, this technique decouples the relationship between welding time and plate thickness that is commonly found in standard welding techniques.

When the gas metal arc welding (GMAW) process is used for NGW, a low heat input condition is used in order to avoid groove sidewall erosion. To enhance groove sidewall fusion and wetting, a traditional approach is to oscillate the electric arc according to the procedure of Norrish and Nakamura [38] and [39], respectively, in order to distribute the heat over the joint.

There are many variations of the standard GMAW process used for narrow gap welding. Recently, Liu et al. [40] proposed a process modification which uses three wires, two of which are melted by the indirect arc. Phaonaim et al. [41] developed a hot wire hybrid laser process that can successfully weld a 3 mm gap narrow groove with adequate properties and consistent fusion of the sidewall. Nakamura et al. [39] proposed an oscillated arc GMAW process, which was shown to improve the arc pressure distribution over the melt pool and consequently increased the wetting of the groove side-walls by the melt pool.

Despite all these developments, preventing incomplete fusion resulting from the low heat input values used to avoid groove sidewall erosion still remains as a major challenge. This defect plays a role in crack initiation when the weldment is under service, and can be detrimental to its mechanical performance. There are additional drawbacks associated with this technique such as reliability of the equipment and costs associated with capital and maintenance [42].

The sensitivity of NG welds to arc disturbances, which also leads to defects, and the potential need to repair or re-work NG welds frequently requires time-consuming manual welding that can increase the overall cost of the fabrication procedure. This ultimately hampers the productivity of NGW methods, which would otherwise improve by decreasing the number of passes to weld intermediate and thick plates. As outlined one issue regarding NGW techniques is productivity, the next section will outline some possible solutions, such as new developed welding processes to overcome this issue.

2.3 Secondary Wire Assisted Arc welding: A Summary

This section gives an overview of the reported applications of secondary wire assisted welding as well as give an overview of the published information on the cold wire gas metal arc welding (CW-GMAW).

2.3.1 Three-electrode Welding Process

One of the earliest reported attempts to develop a welding process with an additional wire feeding is attributed to Arita [43], shown in Figure 2.13. They developed a direct-current electrode negative (DC-EN) twin GMAW system, and reported that this set-up configuration improved stability. The basic for stability improvement mechanism is based on the different polarity of the additional that balances the attraction of the two main twin wires in the main torch.

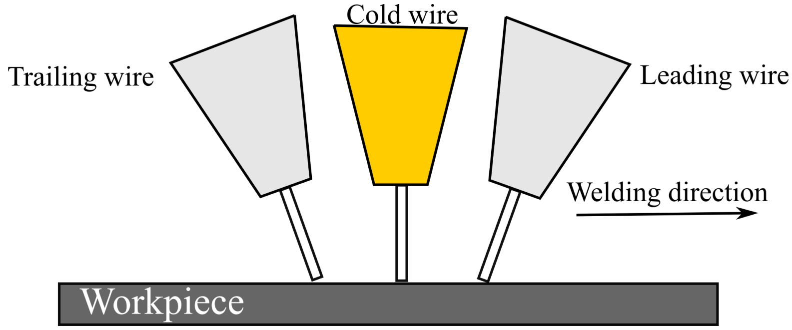

Figure 2.13: Schematic showing the 3-electrode welding.

One of the first works to utilize a cold wire (central filler wire) involves tandem GMAW applications [44],whose mechanism was similar to that of Arita [43], but with the electrode torches operating in direct current electrode positive (DCEP) mode. This study showed that introducing a cold wire would balance the interaction between the two arcs. Other characteristics reported in this work highlighted the reduction of welding instabilities while improving the weld metal deposition rate, measured in (kg/s).

2.3.2 The Double Electrode Gas Metal Arc Welding (DE-GMAW)

Double electrode gas metal arc welding (DE-GMAW) was developed by Li et al. [45], shown in Figure 2.14. This process includes a by-pass system in order to control the current, and consequently, control the heat input delivered to the substrate. Moreover, Li et al. [46, 47] demonstrated that this process is stable, and presents higher melting efficiency compared to the standard GMAW, although choosing appropriate by-pass parameters is key to controlling the process.

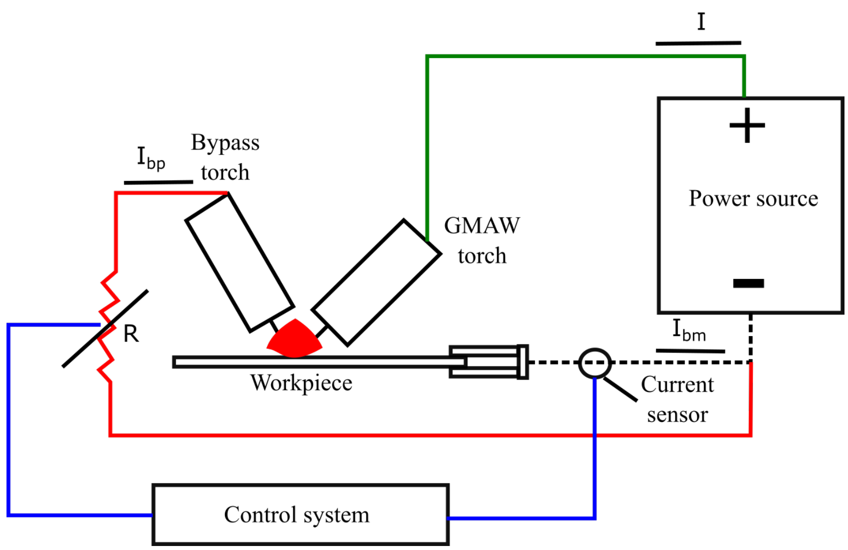

Figure 2.14: Schematic showing the DE-GMAW.

2.3.3 Twin-arc Gas Metal Arc Welding With Integrated Cold Wire

Xiang et al. [48] reported the same stabilizing effect of the cold wire for twin-arc GMAW, shown in Figure 2.15. One similarity of this work to the prior study by Hassler et al. [44]

is that the cold wire is fed straight into the melt pool forming an equilateral triangle with the two other wires. The mechanism proposed to explain the arc stabilization is that the cold wire promotes stabilization of the cathode, thereby avoiding arc length variations.

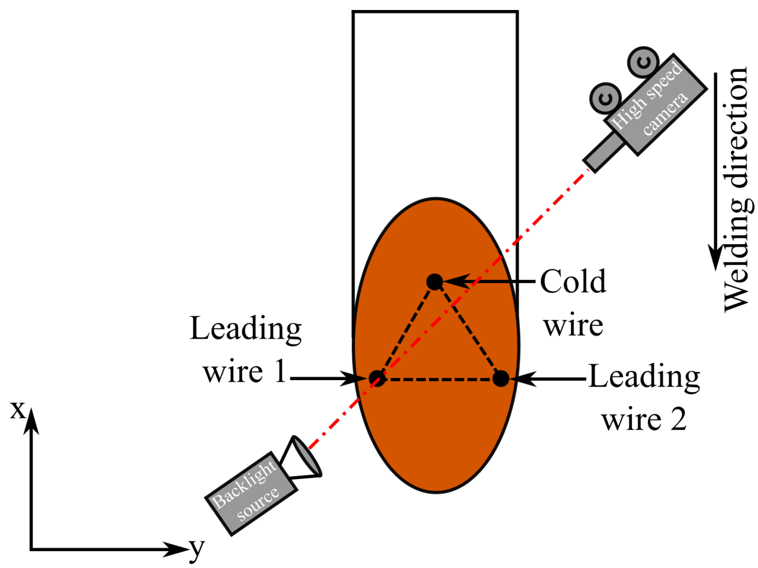

Figure 2.15: Schematic showing twin-arc GMAW with integrated cold wire.

2.3.4 Cold Wire Submerged Arc Welding (CW-SAW)

Regarding the influence of cold wire feeding in the observed joint metallurgy, Mohammadijoo et al. [49] reported that using cold wire in submerged arc welds (SAW), shown in Figure 2.16, reduced dilution and reduced the CG-HAZ area. Further analysis revealed that in the cold wire specimens the prior austenite grain size was reduced and there was a significant decrease of martensite-austenite (M-A) fractions in the HAZ which are considered to be detrimental to the mechanical strength of weld joints.

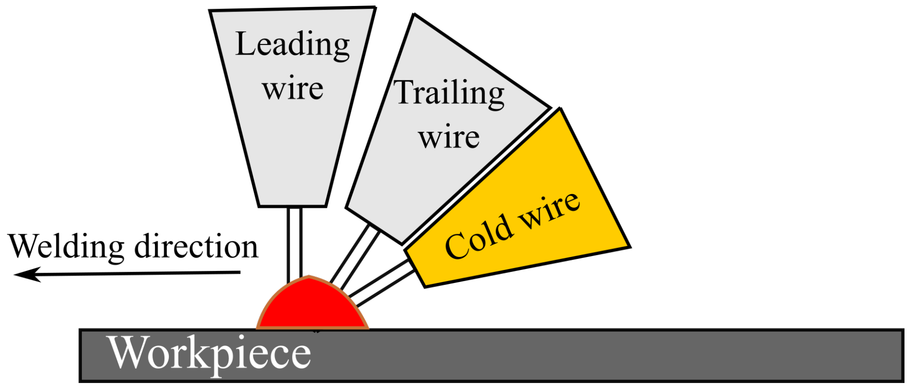

Figure 2.16: Schematic showing cold wire integrated submerged arc welding (SAW).

Further analysing the effect of cold wire on the Charpy impact results of SAW welds, Mohammadijoo et al. [50] noticed that the low temperature fracture toughness was improved by 38 % compared to the standard SAW, and the fraction of M-A phase was reduced by 7.5% vol. Overall, the decrease in HAZ area was accompanied by a 12 % increase in deposition.

2.3.5 Hot-wire Gas Metal Arc Welding (HW-GMAW)

Hot-wire gas metal arc welding (HW-GMAW) is another alternative that is frequently used for hardfacing of structures against wear, due to the controlled dilution which provides low carbide dissolution conferring high hardness to the weld bead [51]. Figure 2.17 shows the schematic of the HW-GMAW assuming the electrode wire positive as is customary.

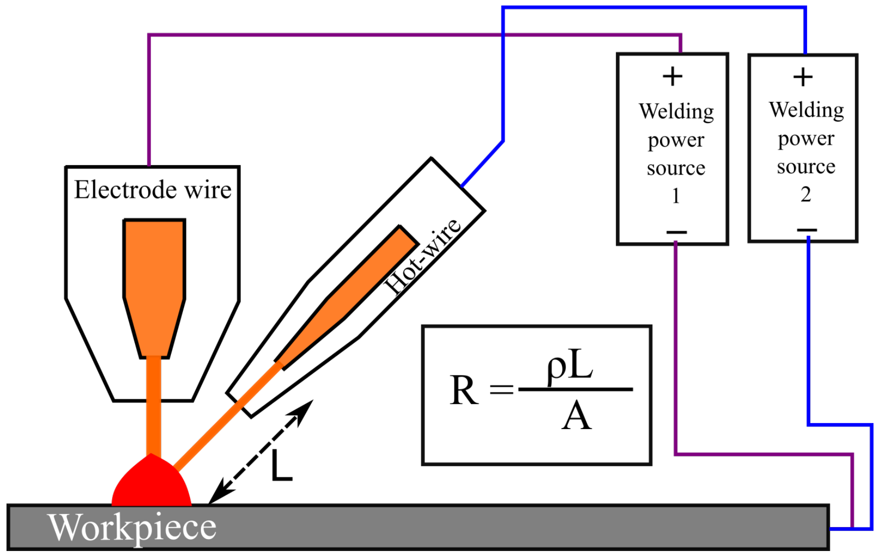

Figure 2.17: Detail showing the HW-GMAW process.

The HW-GMAW consists of a standard GMAW torch with an auxiliary wire resistively heated (hot-wire). This resistive heating of the hot-wire allows the reduction of the power of the arc, diminishing the total heat input in comparison to the standard GMAW. As the hot-wire is electrified, it can attract or repel the arc depending on its polarity. In general, assuming that electrode wire will be positive, negative polarity of the hot-wire will repel the arc. On the other hand, the positive hot-wire will attract the arc; as further discussed by Günther [52]. Another interesting feature of HW-GMAW is that the introduction of an auxiliary wire promotes a change in the melt flow of the weld pool accounting different cooling rates, as reported by Günther et al. in subsequent work [53].

2.3.6 Cold Wire Gas Metal Arc Welding (CW-GMAW)

The general paradigm in developing a secondary wire assisted welding process is to increase the deposition rate for similar heat inputs. To achieve similar benefits, the CW-GMAW was proposed; refer to Figure 2.18. Prior research provided evidence that introduction of cold wire leads to an increase in current, although, this increase in current does not lead to an increase in penetration [54].

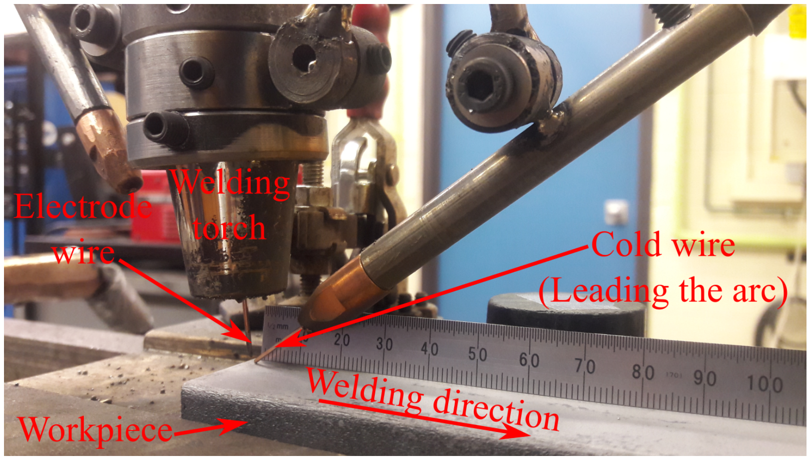

Figure 2.18: Detail showing the CW-GMAW process.

Further research [55] indicated that the CW-GMAW induced less residual stresses in welds leading to a superior fatigue life [56]. It was reported that the arc was pinned to the cold wire leading to a more consistent sidewall erosion than encountered through the standard GMAW, and moreover, the microstructures commonly found in the HAZ were improved by employing a cold wire [57]. Chapter 5 examines the feasibility of the CW-GMAW applied to NGW and describes the arc dynamics of the welds.

2.4 General Methodology

2.4.1 Overview

This chapter will deal only with the general methodology in this thesis. The specifics regarding each experiment will be reported in each chapter where the experiment and results are discussed.

2.4.2 Welding Equipment

The welds reported in this work were all performed using a Fanuc arcmate 120i six axis robotic arm operating in constant voltage, with the direct current electrode positive. The cold wire injecting system was manufactured specifically for this robotic arc and the cold wire was injected using a Lincoln R450 wire feed system, which was used to ensure a constant cold wire feed rate.

2.4.3 Welding Procedure

The general welding procedure consisted of welding bead on plate welds (flat position) to study the electric arc dynamics and metal transfer. The electric arc dynamics were studied using a LEM LT505-S current sensor and LEM LV100-100 voltage sensor. The voltage and current signals were modulated using a National Instruments^{TM}(DAQ) 6061 device, and read and stored using Labview. Generally, the electrical signals were acquired for two seconds at a frequency of 10 kHz.

The metal transfer during welding was studied using a FASTCAM UX50 160K-M-8GB high speed camera which was triggered by the voltage and current measurement software so that the images and electrical signals are synchronized. In order to investigate sidewall erosion in narrow gaps or mechanical properties the weld joint grooves were machined using end mills and the joint was assembled through tack welds.

2.4.4 Materials

This work focused on two types of steel: plain carbon steel was used for experiments dealing with the the physics of metal transfer, arc stability, and bead morphology. For experiments investigating sidewall erosion in narrow gap welding, X80 high strength low allowy steel was used, since this material is actually employed in pipeline welding. The V-groove welds reported in this work were manufactured using ASTM A131 Gr. A steel which is one the steels used in shipbuilding construction.

2.4.5 Hardness Map and Tensile Test

The hardness maps were performed using a Clemex Vickers hardness tester operating according to ASTM E384-17 [58]. The tensile tests were performed using a Tinius Olsen tensile tester with cross-head speed of 1 mm/min in conjunction with digital image correlation (DIC) software to analyse the material strain distribution during the tensile test. The DIC system consisted of a pair of 5 megapixel cameras connected to a computer with VIC-3D software by Correlated Solutions^{TM}.

Chapter 3

The CW-GMAW Process: Droplet Transfer and Geometry[1]

3.1 Overview

The metal transfer dynamics induced by adding the cold wire were examined during the three natural transfer modes in welding: short-circuit (low arc power), globular (intermediate arc power), spray (high arc power). For all three regimes their implications on weld bead geometry, dilution and melting efficiency are evaluated during cold wire gas metal arc welding (CW-GMAW). Bead-on-plate welds were conducted on 3/8 in (9.52 mm) thick AISI 1020 steel plates. Standard metallographic procedures were used to study dilution, which is used to infer the melting efficiency. The results provide evidence that increasing cold wire feeding rates will favour arc attachment to the cold wire rather than to the weld pool for all natural transfer modes. This influences dilution of the welds along with the melting efficiency. The findings are used to identify conditions where CW-GMAW offers higher melting efficiency than the standard GMAW process.

[1]This chapter is based on the following paper: Ribeiro, R. A.; Dos Santos, E. B. F.; Assunção, P. D. C.; Braga, E. M.; and Gerlich, .A. P. Cold wire gas metal arc welding: droplet transfer and geometry. Welding Journal 98, no. 5 (2019): 135S-149S. https://s3.amazonaws.com/WJ-www.aws.org/supplement/2019.98.011.pdf

3.2 Background

Welding melting rate is considered here as an indication of overall productivity in welding depends on other factors such as: welding speed, arc time and welding defect rate according to general manufacturing definitions [59]. Moreover, according to Suban and Tušek [60], melting rate is the most prominent factor to assess welding productivity; for this reason it is taken here as reference for assessing of welding productivity.

Several techniques can be employed to decouple productivity/melting rate from the heat input. These include, for example: double electrode (DE) – GMAW, cold wire submerged arc welding (CW-SAW), and cross-arc GMAW, which are outlined as follows.

A recently developed technique is double-electrode (DE)-GMAW, which uses a bypass electrode to limit the amount of current passing through the workpiece. The effect of the bypass current on arc stability and metal transfer was studied by Li and Zhang [46]. Using two GMAW power sources the bypass current was held constant, which improved metal transfer stability in spray transfer, and consequently nearly doubled the productivity over standard GMAW.

The consequences of these process modifications to increase productivity can also be noted in the reduction of the heat affected zone (HAZ), which leads to improved properties. For example, Mohammadijoo et al. [61] examined cold wire submerged arc welding (CW-SAW) and showed that the deposition rate was increased by 6% due to cold wire. In addition, the prior austenite grain size (PAGS) in the coarse grained heat affected zone (CGHAZ) was reduced, due to the decrease in heat input to the workpiece. Meanwhile, the heat affected zone fracture toughness [62] was increased due to the reduction of the fraction of martensite-austenite.

A further development in welding processes is the cross-arc GMAW, or (CA)-GMAW as proposed in a preliminary report by Chen et al.[63]. Generally, a cross-arc is established between a gas tungsten arc welding (GTAW) electrode and two carbon electrodes aiming to decouple deposition and heat input. The inter-wire current is related to the ionization degree of the arc, and the authors reported that this process is stable for different levels of GTAW currents. Moreover, weld stability increases with GTAW current; which allows deposition to be controlled independently of heat input.

Another approach to increasing the productivity of a welding process is by enhancing the melting efficiency, which represents the magnitude of the arc net power that is devoted to melting the base and filler metals. This improvement in melting efficiency is achieved when a larger fraction of the arc energy is used to create and sustain the melting pool.

Based on the work of DuPont and Marder [5], it is thought that the maximum value of melting efficiency for an arc shielded welding process is around 0.5 or 50% due to the intrinsic heat losses of the weld pool. Recently, Hackenhaar et al.[37] examined the melting efficiency of GMAW using a Box-Behnken designed experiment, and it was found that melting efficiency depends on the geometry of the welded part, which is consistent with differences in energy distribution and losses. Comparing the values of melting efficiency for T-joints and bead-on-plates the reported values asymptotically converged to 0.5, as expected. Moreover, T-joints had a lower melting efficiency, which one would expect with 3D heat flow regime.

Cold wire gas metal arc welding (CW-GMAW) was developed to provide an alternative to such costly specialized equipment in these welding processes. This was originally proposed to provide higher deposition in shipbuilding applications [64], where decreasing the heat induced distortion can be achieved by simply using an additional wire feeder to feed cold wire to the weld pool. Subsequently, Ribeiro et al. [54] showed that introducing the cold wire leads to a slight increase in current without consequent increase in penetration. Moreover, Costa Assunção et al. [57] successfully demonstrated that the use of CW-GMAW can facilitate narrow gap welding of joints with spacings as little as 5 mm. Importantly, CW-GMAW prevents detrimental sidewall erosion, and decreases the HAZ width in comparison to conventional GMAW welding. Further research on CW-GMAW by Costa [55] using an acoustic birefringence technique provided evidence that the use of cold wire reduces residual stress, and consequently there is evidence that CW-GMAW manufactured joints offer superior fatigue life, using standard fatigue tests and metallographic techniques, when compared to GMAW joints as proposed by Marques et al. [19].

This work evaluates the modifications to metal transfer induced by the cold wire feeding (non-energized) in CW-GMA welding for the three natural transfer modes, short-circuit, globular, and spray. The results show that, with the increase of cold wire feed rates, the arc attaches progressively more to the cold wire, leading to changes in dilution and melting efficiency. Moreover, estimates of melting efficiency were calculated assuming an average value of arc efficiency. A main focus is the potential to decouple welding deposition and nominal heat input during in CW-GMAW, which is a key feature of the new welding processes.

3.3 Experimental Methodology

Bead on plate welds were performed on AISI 1020 plates measuring 300 mm long, 150 mm wide and 9.52 mm thick. AWS ER70S-6 [65] was used as electrode(energized) and cold wire (non-energized) with nominal diameters of 1.2 mm and 0.9 mm, respectively. Table 3.1 presents the nominal compositions of the base metal and the wires used in this study.

Table 3.1: Nominal chemical composition of the base metal and welding wire.

Material	Nominal chemical composition (wt.%)						
	C	Si	Mn	P	S	Cr	Fe
AISI 1020	0.18	-	0.30	-	Max.0.005	-	Bal.
ER70S-6	0.15	1.15	1.85	0.025	0.035	0.05	Bal.

During the welding, high speed imaging was used to study the electric arc behaviour. The high-speed camera was operated at a frame rate of 5000 frames per second, with an aperture of f/22, and shutter speed of 25 μs. A narrow band pass filter of 900± 10 nm wavelength was used to limit the amount of arc radiation reaching the camera sensor. In parallel, the electric signals were acquired using a DAQ system with a frequency of 20 kHz for two seconds. Eight replicates were produced in order to assess the repeatability of the inferred dilution and melting efficiency values. Beads were subsequently cross-sectioned, prepared via standard metallographical procedures until final polishing with 1.0 μm alumina powder and etched with a 5 %Nital in order to show the macrostructure.

After that, the melting efficiency and dilution were calculated, following Equations 2.15 and 2.18, respectively. Generally, the GMAW and CW-GMAW thermal efficiencies were assumed to be the same. The shielding gas composition used was Ar-15% CO2 with a flow rate of 40 cfh (19 l/min). Table 3.2 gives the thermophysical properties used to calculate the melting efficiency.

Table 3.2: Parameters to calculate the melting efficiency for the bead welds.

η_a	H_{base} (J/mm^3)	H_{filler} (J/mm^3)
0.83	10.5	7.88

In Table 3.2 H_{base} is volumetric enthalpy of the base metal and, H_{filler} is the volumetric enthalpy of the filler metal. The physical quantities given in Table 3.3 were used in order to calculate the cold wire absorbed power, i.e how much of the arc power the cold wire is able to absorb. The absorbed heat by the cold wire, Q_{CW}, is the sum of the specific and latent heat of the additional wire excluding the vaporization of the liquid which requires the consideration of the increasing of temperature up to vaporization and change from the liquid state to gas.

$$\dot{Q}_{CW} = (\dot{m} c_s \Delta (T_m - T_0)) + (\dot{m} L) \tag{3.1}$$

where $\dot{m}$ represents the cold wire mass feed rate in (kg/s), c_s is the solid specific heat in (kJ/kg), T_m and T_0 are the wire melting temperature and the room temperature, respectively, in K; and L is the wire latent heat (in units of kJ/kg).

Table 3.3: Physical constants of the wire used ER70S-6 in the electrode and cold wire.

$D_{elec.}\,(mm)$	$D_{CW}\,(mm)$	$\rho\,(kg/m^3)$	$c_s\,(kJ/kgK)$	$L\,(kJ/kgK)$	$T_m\,(K)$	$T_0\,(K)$
1.2	0.9	7930	0.70	200	1723	293

Table 3.4 gives the parameters set in the welding source, for the three intended transfer modes, for the welds in this work.

Table 3.4: Welding parameters used for each transfer mode.

Mode	**WFS (in/min) [m/min]**	**Voltage (V)**	**Travel speed (in/min) [cm/min]**	**CTWD (mm)**
Short-circuit	250 [6.35]	20	25 [63.5]	22
Globular	250	25	25	22
Spray	350 [8.89]	30	25	22

3.4 Results and Discussion

3.4.1 Electrical Signals And Transfer Modes

Figure 3.1 presents oscillograms for the short-circuit conditions; one observes the presence of incipient short-circuits (by definition those with duration $\leq$ 2 ms). As the cold wire is in contact with the substrate, it can short-circuit the droplet being formed since the distance between the wire and the droplet is less than the distance from the wire to the workpiece, which explains the increase of short-circuits as the cold wire fraction is increased. This also leads to spatter formation. The cold wire also extends, in some conditions, the arcing period, which is the time between droplet formation and the short-circuit. This might be explained by the fact the arc now has to melt a higher mass to form the droplet, which takes more time considering the standard GMAW condition.

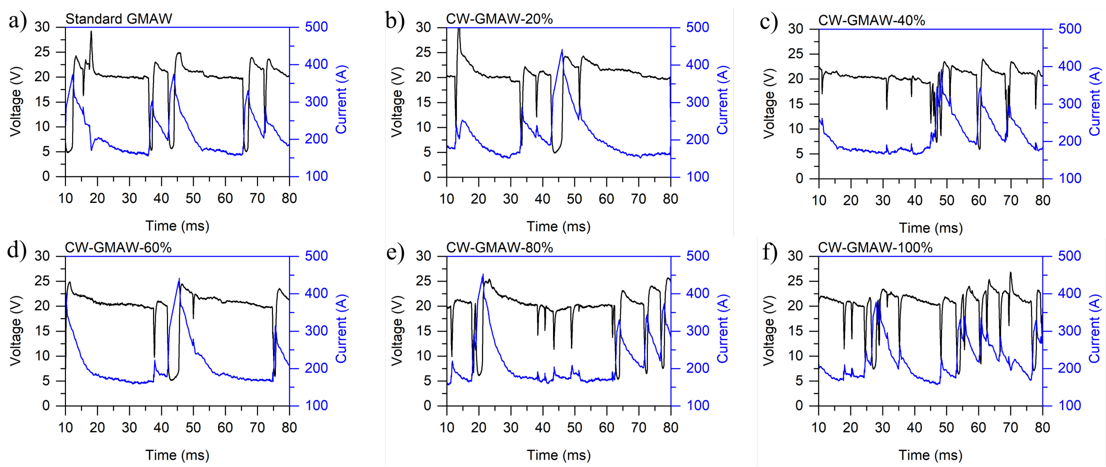

Figure 3.1: Oscillograms for short-circuit parameter. a)Standard GMAW; b)CW-GMAW-20%; c)CW-GMAW-40%; d)CW-GMAW-60%; e)CW-GMAW-80%; f) CW-GMAW-100%. Percentages represent a mass fraction of the quantity fed by the main wire.

Figure 3.2 shows the oscillograms for the globular condition[2]. In contrast to the short-circuit case, the cold wire is better melted here. This might be explained by the higher energy available in the system arc-weld pool. One can see some incipient short-circuit in the 120% and 140% conditions which indicates the occurrence of spatter.

[2]The parameters expected to achieve globular metal transfer were chosen, unfortunately, within the transition region to spray (the transition current is approximately 290 A [66]) which accounts for droplets being slightly higher than electrode diameter. This means that the metal transfer will be intermittently globular, since it is close to the transition current to spray. Moreover, as the average current will increase with the addition of cold wire feed, it is expected that the droplet diameters will further decrease for CW-GMA welding. In fact, it could be said that the globular parameter acts as a low power spray transfer regime.

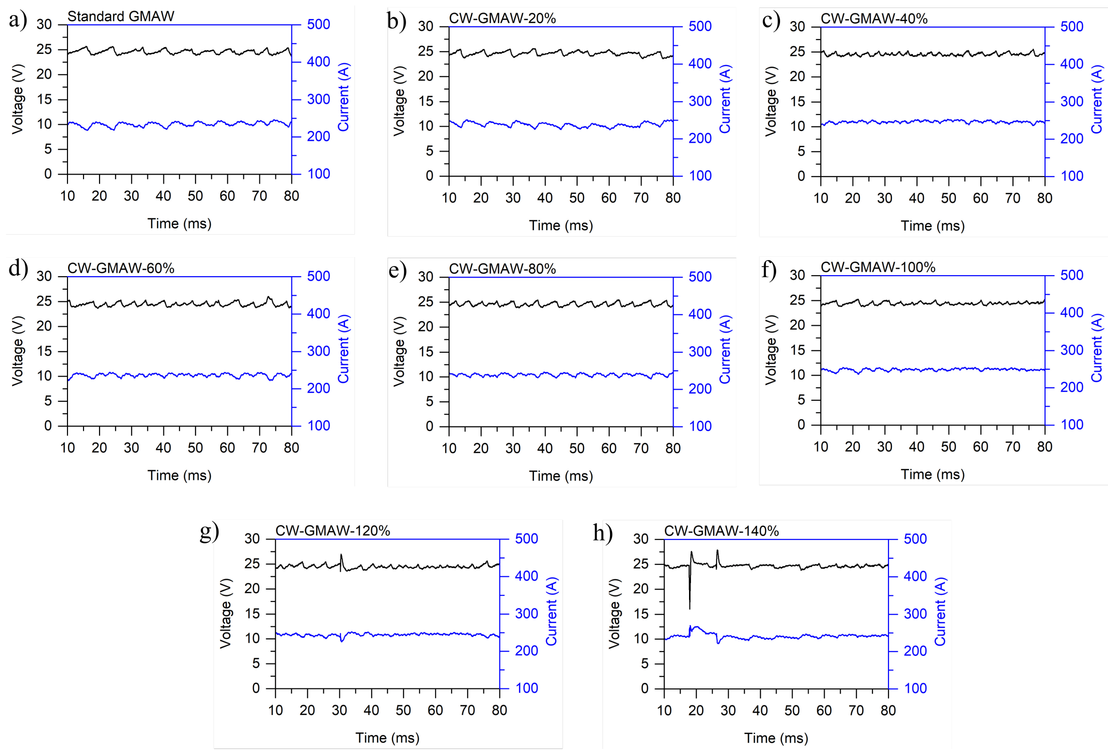

Figure 3.2: Oscillograms for globular parameter. a)Standard GMAW; b)CW-GMAW-20%; c)CW-GMAW-40%; d)CW-GMAW-60%; e)CW-GMAW-80%; f) CW-GMAW-100%; g)CW-GMAW-120%; h)CW-GMAW-140%. Percentages represent a mass fraction of the quantity fed by the main wire.

Figure 3.3 presents the electrical data for the spray condition. In this condition even higher energy is available in the system arc-melt pool, allowing higher amounts of cold wire to be fed compared to the short-circuit (low energy) condition. For these particular parameters it was possible only to reach 140 %; since further increasing the cold wire feed rate led to pronounced spatter.

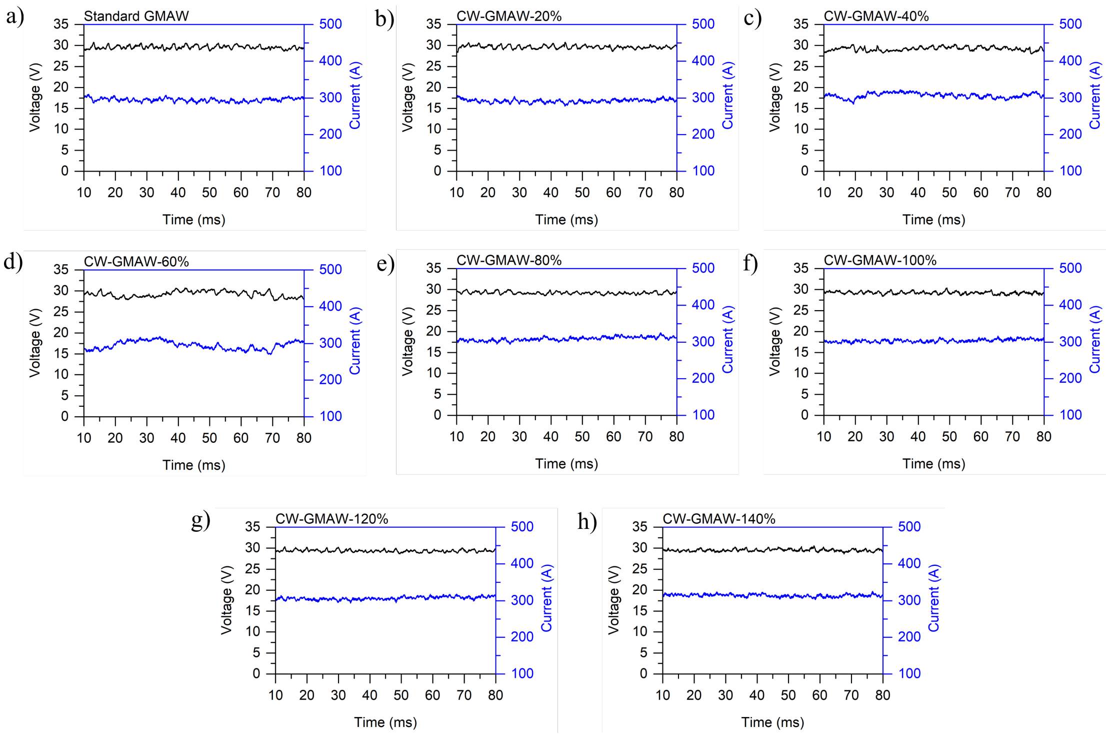

Figure 3.3: Oscillograms for the spray parameters. a)Standard GMAW; b)CW-GMAW-20%; c)CW-GMAW-40%; d)CW-GMAW-60%; e)CW-GMAW-80%; f) CW-GMAW-100%; g)CW-GMAW-120%; h)CW-GMAW-140%. Percentages represent a mass fraction of the quantity fed by the main wire.

During the welds, the arc may change position relative to the cold wire, independently of the welding transfer condition, as the cold wire is fed on. It was possible to distinguish three main arc positions:

a. *Electrode to pool melting*: In this condition the arc retains its straight position and the cold wire is melted inside the arc. Generally, this condition is observed for a cold wire feeding rate less than 60 %;

b. *Arc transition*: This condition shows a transition in the arc position. The arc starts to climb the cold wire but remains pinned to the work-piece. This condition generally happens for cold wire feeding rates between 60 % and 80 %;

c. *Wire to wire melting*: In this condition the arc is completely pinned to the cold wire, meaning that the weld pool was displaced to the cold wire. Generally, this condition happens for cold wire feeding ≥ 100 %.

Figure 3.4 shows the arc position in relation to the cold wire as function of different cold wire feeding rates.

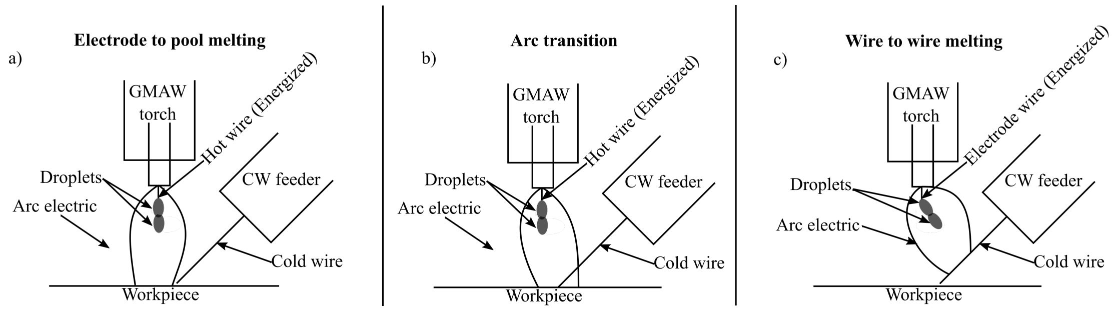

Figure 3.4: Arc positions in relation to the cold wire as observed for different cold wire feed rates. a)Arc melting; b)Arc transition; and c)Arc weld pool.

This change in the arc trajectory could be explained by two effects: the electron natural path; and the arc blow. The electrons' natural path effect implies that current will always flow in the path of lower resistance (shortest path). However, Reis et al. [67] showed that this effect for arc with equal contact-tip-to-workpiece distance is pronounced only at lower currents (lower arc stiffness).

In the case of CW-GMAW its was shown that the increase in cold wire feed rate leads to a slight increase in current, and according to [67] this leads to a weakening of the electrons' natural path (direction of lower current resistance) effect and an increasing in the jet plasma effect, proportional to an increase in current, which increases the arc stiffness to displacement. However, in spite of the phenomenon described by [67], the change in the arc trajectory is probably due to the arc finding the lowest current resistance path with the cathode spots likely moving to the cold wire.

Figure 3.5 shows the the arc deflection as function of the cold wire feeding for the short-circuit condition. Figure 3.6 shows the progressive deflection of the arc to the cold wire as the cold wire mass fraction is increased for the globular parameters. Figure 3.4.1 illustrates the progressive pinning of the arc to the cold wire as its mass fraction increases for the spray condition.

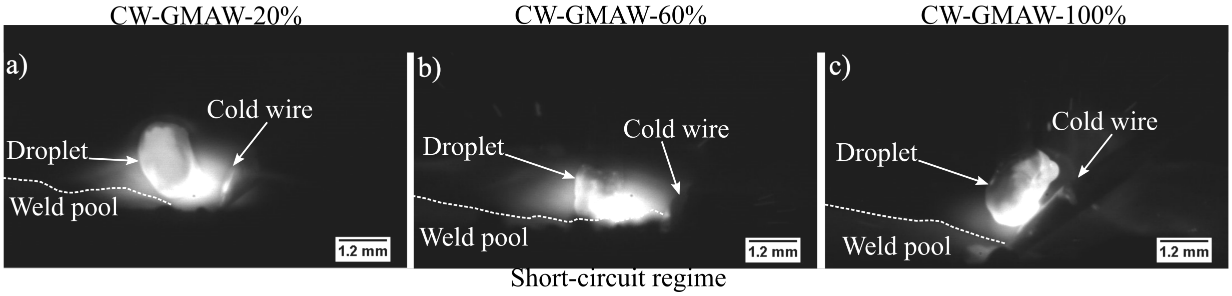

Figure 3.5: The climbing the arc in the cold wire for the short-circuit condition. a)20 % of cold wire, b)60 % of cold wire and c) 100 % of cold wire.

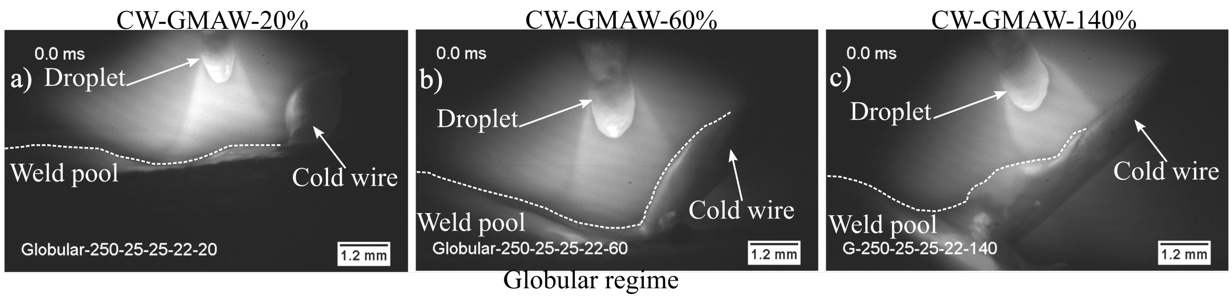

Figure 3.6: The deflection the arc in the cold wire for the globular condition. a)20 % of cold wire, b)60 % of cold wire and c) 140 % of cold wire.

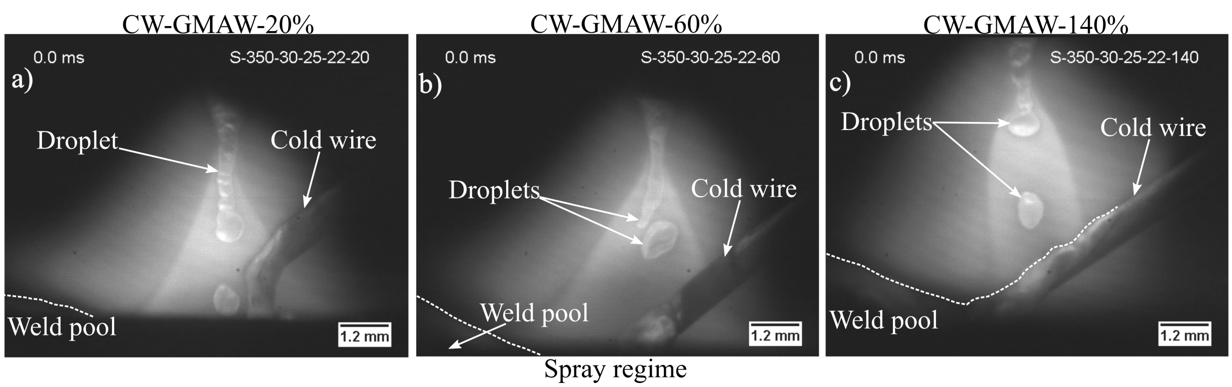

Figure 3.7: The deflection the arc in the cold wire for the spray condition. a)20 % of cold wire, b)60 % of cold wire and c) 140 % of cold wire.

As briefly described above, the increase of cold wire fraction has the same effect as increasing the wire feed speed (WFS), which causes an increase in current to balance the burn off rate in order to achieve stable mass transfer through the arc. For instance, the standard GMAW conditions had an average current of 299 A while the CW-GMAW at 140% feed rate involved approximately 321 A, an increase of 22 A in average (increase of 7.35 % on average).

The place where the cold wire is melted in the arc implies a difference in the cold wire absorbed power, which is the heat generated by the electric arc that is absorbed by the cold wire and re-drawn into the system arc-weld pool.

Figure 3.8a presents the instantaneous arc power versus the cold wire percentage for the three different sets of welding parameters taking into account the position of the arc in relation to the cold wire. One can observe, clearly, the transition in melting mode for different cold wire feed rates. Figure 3.8a a vertical line shows how much cold wire can be fed in order to keep a stable position of the arc to the cold wire. For instance, as the arc power increases, the electric arc and the weld pool move towards the cold wire.

Figure 3.8b shows the arc power versus the cold wire absorbed energy. The position of the arc related to the cold wire dictates how much power will be absorbed. The cold wire melting in the weld pool absorbs more power than any other cold wire position.

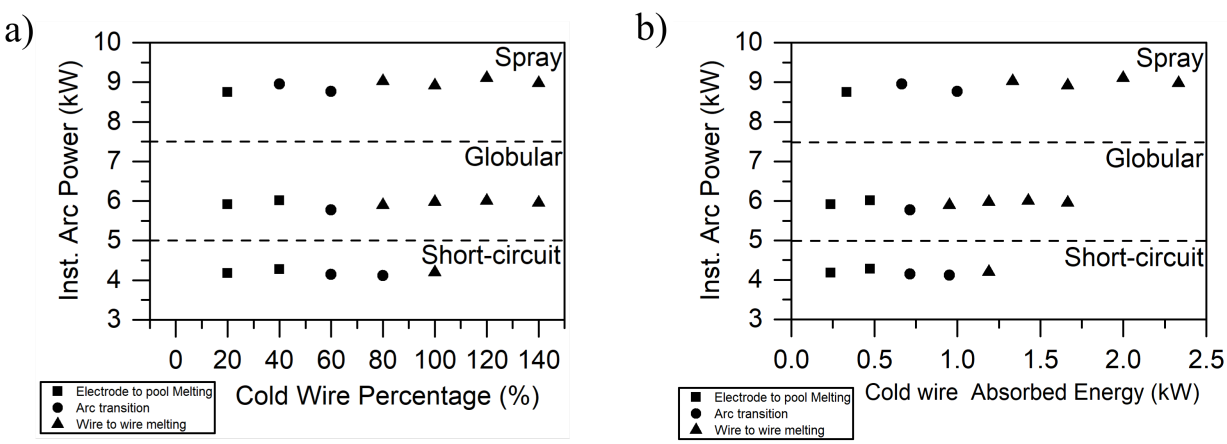

Figure 3.8: The influence of cold wire percentage feeding and absorbed energy in arc instantaneous power: a) arc power versus cold wire feed rate; b) arc power versus cold wire absorbed power.

3.4.2 Dilution And Melting Efficiency

The changes in metal transfer caused by cold wire feed, while increasing the deposition rates, caused a change in dilution and in melting efficiency since both are related to each other [36]. Figure 3.9 presents the dilution values for the three welding modes: short-circuit; globular; and spray. Each point presents the average in the middle, the standard deviation in the error bars, measured for each cold wire feed condition. The general trend is that the dilution decreases as the cold wire feeding rate increases, which is explained by the increase of mass deposited, which causes an increase in filler metal area at the expenses of base metal area of the bead.

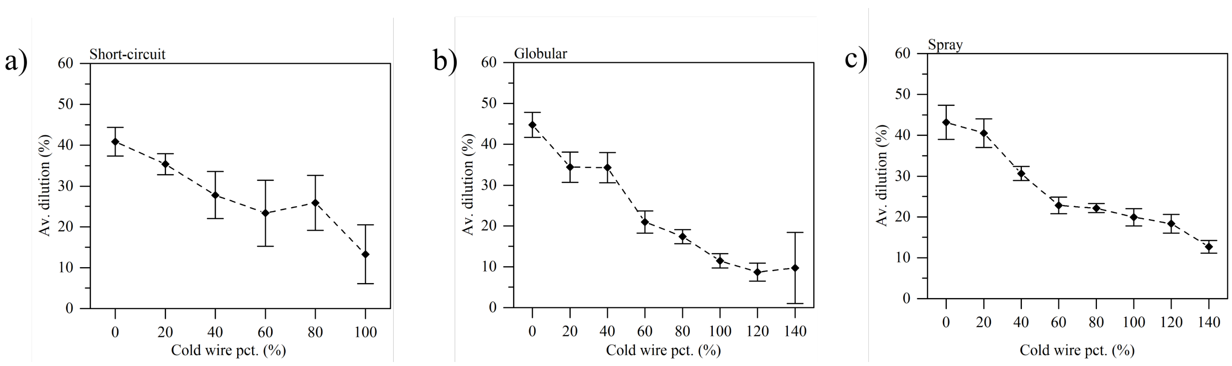

Figure 3.9: Dilution rates for the three welding conditions. a) short-circuit, b) globular, c) spray.

Figure 3.10 presents the melting efficiency for the three welding modes for all the cold wire feeding rates. The dashed line represents the theoretical melting efficiency of arc welding processes as defined by Fuerschbach [8]. These values of melting efficiency can be used to indicate for which cold wire feed, a higher fraction of heat will be specifically used to melt the substrate and filler metal. An increase in melting efficiency will mean, ultimately, a better use of the energy transferred to the workpiece, including the heat losses.

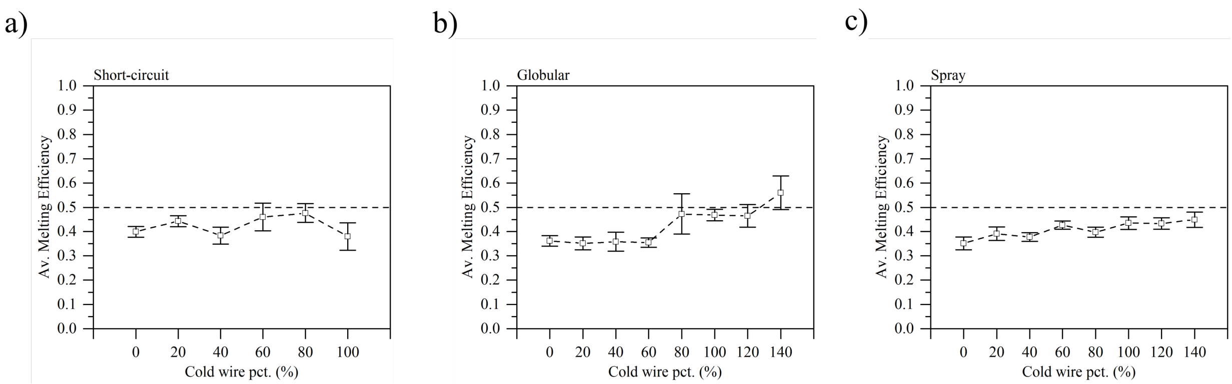

Figure 3.10: Melting efficiency for the three welding conditions. a)Short-circuit, b) Globular, c)Spray.

For globular and spray there is a clear trend, except for the short-circuit conditions, the increase in cold wire feeding rates determines an increase in the melting efficiency. This is due to increase in the filler metal area occasioned by the cold wire feeding which increases the numerator of Equation 2.15, and consequently, increasing melting efficiency. The effect of spatter might hinder the increase in melting efficiency for short-circuit conditions. For some situations the melting efficiency of the CW-GMAW welds exceed the theoretical limit proposed by Fuerschbach [8]. Also, this means that in the CW-GMAW process, a greater part of the energy delivered by the arc to the work-piece is actually used to melt the filler and base metals.

The observation that for globular transfer modes the maximum values measured of melting efficiency, for some cold wire feed rates, are superior to the theoretical value of melting efficiency might be explained by an energy balance. In the globular mode the arc power is intermediary, so the losses by radiation and convection in the spray mode are slight. Thus, the cold wire can absorb more energy to be re-introduced into the arc-pool system, consequently increasing melting efficiency.

As for the short-circuit case, the system itself has lower energy compared to other transfer modes, and it looses thermal energy transformed in spatter momentum during short-circuits. Accordingly, less energy is available to be absorbed by the cold wire. The opposite is true in the spray case, in which the system possess higher energy which is dissipated by radiation and convection, since the arc length is longer than the former conditions, impeding it from reaching of the theoretical melting efficiency limit.

Figure 3.9 and Figure 3.10 will help users to determine the amount of dilution for a particular quantity of cold wire feed and the approximate melting efficiency for that particular condition which will likely indicate the conditions are more efficient in terms of the energy used directly to make the weld pool.

3.5 Summary

Bead on plate welds were performed to investigate the metal transfer dynamics and its influence on dilution and melting efficiency for the three natural transfer modes: short-circuit; globular: and spray. Based on these experiments, one can draw the following conclusions:

1. The introduction of cold wire disturbs low energy arcs to a greater extent compared to intermediate and high energy ones;
2. The introduction of the cold wire changed the arc position in arc position relative to its longitudinal axis, which were called in this work: *arc melting*, *transition* and *weld pool*. This last position occurs for high cold wire feed rates, and in it the arc is completely pinned to the cold wire;
3. The variation in arc position leads to different cold wire rates of arc energy absorption;
4. The displacement of the arc relative to its longitudinal axis reduced the dilution of bead welds, as the cold wire feeding increases, and;
5. This reduction in dilution dictates an increase in the melting efficiency to approximately 55%, for globular transfer regime with 140% cold wire feed rate, which represents an increase in the energy used to melt base and filler metals, respectively, in relation to a constant net arc power.

Chapter 4

The CW-GMAW: Narrow Gap Welding Application [1]

4.1 Overview

Narrow gap welding (NGW) is a popular technique used to decrease the volume of molten metal and heat required to fill a joint. Consequently, deleterious effects such as distortion and residual stresses may be reduced. One of the fields where NGW is most employed is pipeline welding, where misalignment, productivity and mechanical properties are critical to a successful final assemblage of pipes. This work reports the feasibility of joining pipe sections with 4 mm-wide narrow gaps machined from API X80 linepipe using cold wire gas metal arc welding. Joints were manufactured using the standard GMAW and the CW-GMAW processes, where high speed imaging, voltage, and current monitoring were used to study the arc dynamic features. Standard metallographic procedures were used to study sidewall penetration, and the evolution of the heat affected zone during welding. It was found that cold wire injection stabilizes the arc wandering, thereby decreasing sidewall penetration while almost doubling deposition. However, this also decreases penetration, and incomplete penetration was found in the cold wire specimens as a drawback. However, adjusting the groove geometry or change in the welding parameters would resolve this problem.

[1] This chapter is based on the following paper: Ribeiro, Rafael A.; Assunção,Paulo D.C.; Dos Santos, Emanuel B.F.; Ademir Filho, A. C.; Braga, Eduardo M.; and Gerlich, Adrian P. Application of cold wire gas metal arc welding for narrow gap welding (NGW) of high strength low alloy steel. Materials 12, no. 3 (2019): 335-346. https://www.mdpi.com/1996-1944/12/3/335

4.2 Background

Narrow gap welding (NGW) is a technique used to weld thick joints with aim of reducing the molten metal deposited volume, ultimately decreasing distortion and residual stresses caused by thermal stresses developed during welding. One of the drawbacks associated with this technique is sidewall erosion caused by the arc wandering during welding. These eroded cavities can increase the probability to form a lack of fusion defect, if they are not refilled during the welding operation.

Various NGW variants were developed to overcome drawbacks such as: rotating arc, swing arc, and wave-shaped wire systems. Another reason to use these modified systems in narrow gap welding is to improve the wettability of the sidewall by the welding pool and to better distribute the heat across the weld to mitigate distortions. A common setback for these systems is their expense and the need for highly trained personnel in their operation, which considerably increases the costs of manufacturing.

Not only are arc-modified processes employed in NGW, but also increased deposition process are successfully used such as tandem gas metal arc welding (GMAW) [68] and twin GMAW [69]. However, these process rely on increased deposition, which increases, the amount of heat transferred to the substrate, leading to increased chance of distortion or residual stresses.

One alternative to these sophisticated welding processes is the cold wire gas metal arc welding (CW-GMAW), which consists of the standard GMAW with an extra cold wire (non-energized) fed into the arc-welding pool system. This process increases the deposition of the welds while mantaining the nominal heat input for the same welding parameters in standard GMAW. Ribeiro et al. [54] has shown that the feeding of cold wire causes a slight increase in current without a corresponding increase in penetration.

Costa Assunção et al. [57] recently studied the feasibility of this process to weld a 5 mm wide groove in ASTM A131 grade A steel, and revealed that, due to the pinning of the arc to the cold wire, the sidewall erosion was considerably reduced in comparison to welds manufactured with standard GMAW. Subsequent research by Costa et al. [55] studied the effect of the CW-GMAW on process-induced residual stresses, concluding that welds manufactured by CW-GMAW have lower levels of residual stresses. This decrease in residual stresses might explain the improvement in fatigue life reported by Marques et al. [56].

The present study further develops in the work by Costa Assunção et al. [57], and reports preliminary results regarding the application of CW-GMAW to weld high strength pipeline steels in narrow gap configuration. The feasibility of NGW employing CW-GMAW is assessed by comparing the severity of sidewall erosion in the welds and the presence of defects in the root pass. The results point to the general feasibility of NGW using CW-GMAW pipeline applications, and illuminate possible future research directions in order to avoid certain defects found during welding.

4.3 Experimental Methodology

Narrow joints were fabricated using both GMAW and cold wire gas metal arc welding (CW-GMAW). Figure 4.1 shows a schematic of the narrow groove geometry used in this work and the detail of cold wire positioning regarding the wire electrode and cold wire feeding angle. The grooves were welded using a Lincoln R500 welding power source linked to a Fanuc ArcMate 120i robotic arm. The size of the joints was 140 x 115 x 15 mm. In order to determine the reproducibility, three replicates were manufactured for each welding condition.

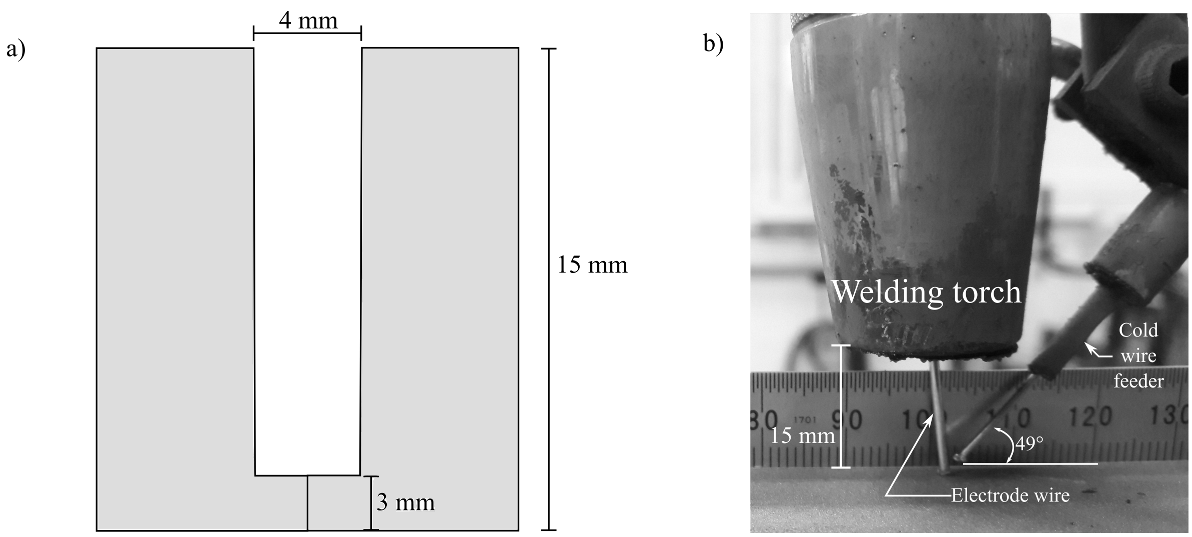

Figure 4.1: Schematics of the groove geometries used in this work: a) schematic narrow groove. b) detail of CW positioning and feeding angle.

In order to manufacture the welds a 1.2 mm diameter ER100S-G was used as an electrode, while the cold wire had a diameter of 1.0 mm. API X80 [57] was selected as the base metal. The nominal compositions of the electrodes and of the base metal are given in Table 4.1. Moreover, no weaving or preheating was used during welding.

Table 4.1: Nominal chemical composition of the welding wires and the base metal.

	C	**Mn**	**P**	**S**	**Ti**	**Mo**	**Ni**	**Cr**	**Fe**
ER100S-G	0.08	1.80	0.55	0.01	0.10	0.25-0.55	2.10	1.80	Bal.
API X80	0.22	1.85	0.025	0.015	0.06	-	-	-	Bal.

During welding the current and voltage signals were acquired at the sampling frequency of 20 kHz for two seconds with synchronized high speed imaging at 5000 fps with a shutter speed of 25 ms, an aperture of f/22, and a narrow band pass filter of $900 \pm 10nm$. The welding parameters used are reported in Table 4.2. For all welds, the shielding gas mixture used was Ar-15% CO_2 at a flow rate of 17 l/min, and the contact-tip-to-workpiece distance (CTWD) was maintained at 17 mm. The welding parameters were set to apply the same heat input using both processes.

Table 4.2: Welding parameters.

Welding process	**WFS (m/min)**	**Voltage (V)**	**Travel speed (m/min)**	**Cold wire feed ratio (%)**	**Deposition per pass (kg/h)**
GMAW	7.62	25	0.41	-	4.11
CW-GMAW	7.62	25	0.41	80	7.39

Once the experiments were completed, the specimens were subjected to standard metallographic procedure and etched in a 5% Nital solution to reveal the macrostructure. The hardness map was performed with 200 g of load and 10 s of dwell time using a Clemex microhardness testing system. The distance between indentations was 0.3 mm and the distance between lines was 0.3 mm.

4.4 Results

4.4.1 Electrical Data

Table 4.3 presents the actual electrical data for current, voltage and power probed for the welding conditions employed in this work. The heat input per pass was similar for both GMAW and CW-GMAW.

Table 4.3: Average electrical parameters sampled during welding and nominal resulting heat input as response of the welding power source.

Welding process	**Pass**	**Average inst. voltage (V)**	**Average inst. Current (A)**	**Average inst. power (W)**	**Nominal heat input (kJ/mm)**
GMAW	root	25.1	299.7	7520.1	1.1
	fill	25.1	270.6	6801.3	1.0
	cap	25.1	253.3	6427.1	0.9
CW-GMAW	root	25.1	292.2	7344.2	1.1
	fill/cap	25.2	277.9	6991.2	1.0

Oscillograms

Figure 4.2 shows the oscillograms for the standard GMAW condition. For the root pass one can notice a periodic repetition with period of approximately 3 Hz (Figure 4.3a). By correlating the electrical signals to the high speed images, it was observed that this repetition is a consequence of arc attachment to the groove sidewalls. Consequently, the power source applies an instantaneous increase in the arc current as shown in the detail, Figure 4.3b. It is possible that this is caused by the auto-regulation system of the power source which interprets the attachment of the arc to sidewalls as an increase in wire feed speed, and consequently, an increase in the current to keep the melting rate constant while the arc length is reduced due to the arc attachment to the groove walls [70].

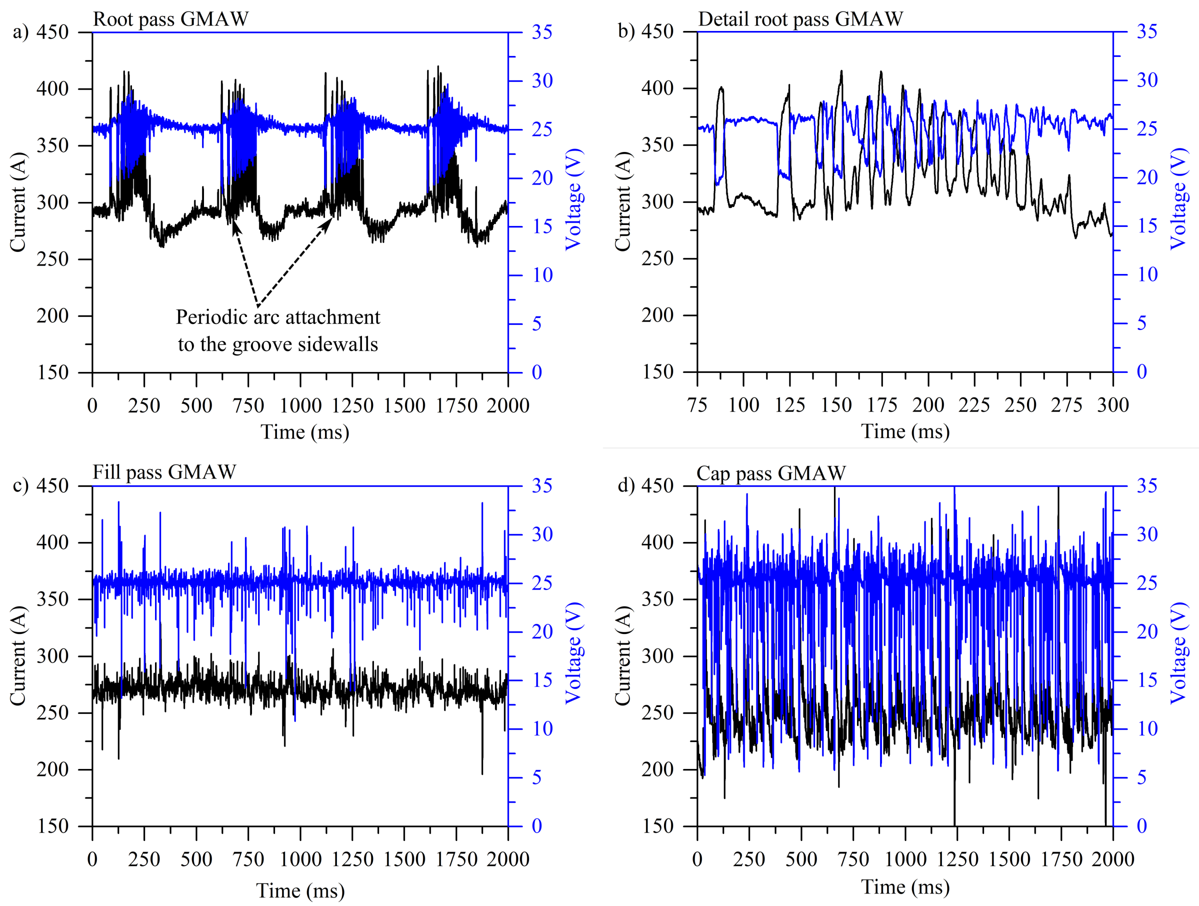

Figure 4.2: Typical oscillograms for the GMAW condition: a) root pass; b)detail of the root inside the period of repetition; c) fill pass; and d) cap pass.

On the other hand, this repetitive behaviour did not occur in the fill and cap passes (Figures 4.2c and 4.2d), likely to a reduced degree of arc constriction, and the shortest path to the electron conduction is the bottom of the groove and not the sidewalls. On the other hand, the severity of short-circuits in the cap pass are higher when compared to the filler pass. This suggests that the distance between the droplet (as shown in the videos) and the substrate is lower, favouring short-circuits.

Figure 4.3 shows the oscillograms for the CW-GMAW specimens. The periodic pattern observed in the oscillograms of GMAW for root pass was not observed for the entire sampling period in CW-GMAW of 2000 ms. This suggests the sidewall erosion was mitigated during CW-GMAW, since sidewall penetration causes the periodicity in the observed signal. Moreover, the short-circuit severity in the fill/cap pass is less prominent than that observed in the GMAW specimen.

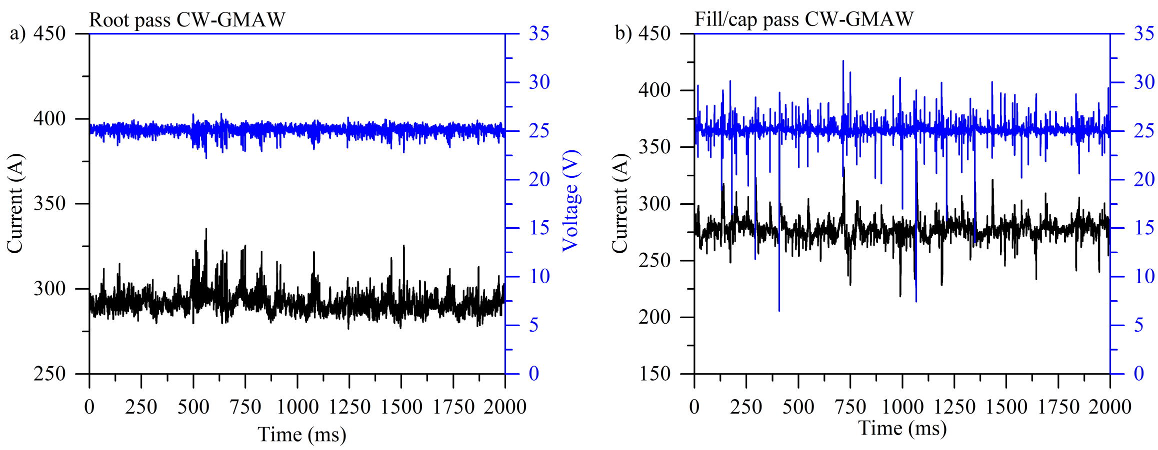

Figure 4.3: Typical oscillograms for the CW-GMAW condition: a) root pass. b) fill/Cap pass.

Cyclogrammes

Cyclogrammes are plots showing voltage versus current, and are used to study the events occurring in the electric arc . They are useful since they show the number of short-circuits and indicate the general arc stability of the process [71]. A more thorough discussion on cyclogrammes and its respective zones, is provided by Jorge et al. [72]. Figure 4.4 shows typical cyclogrammes for GMAW specimens, which shows that, during the root pass (Figure 4.4a), the number of short-circuits (region inside the dashed rectangle) is larger than the arc burning area (darker region, upper left-side of the dashed square). Ultimately, this cyclogramme points out to an unstable condition where the arc burning region is smaller compared to the perturbed region.

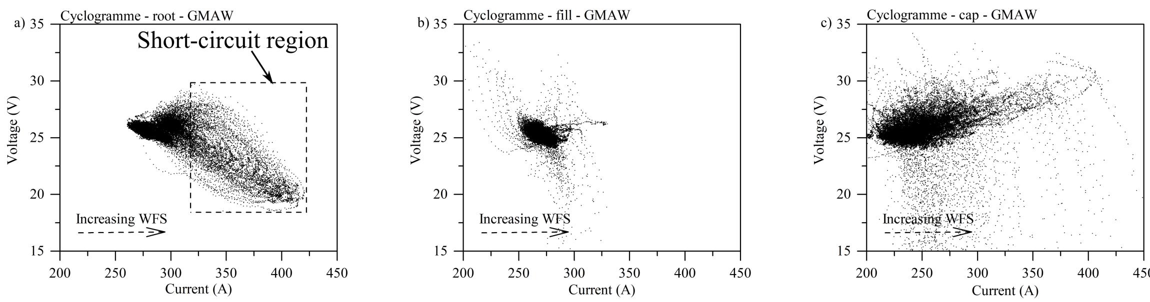

Figure 4.4: Cyclogrammes for the GMAW specimens: a) root pass; b) fill pass; and c) cap pass

As reflected by oscillograms, the fill pass was more stable, with some short-circuits and high voltage points, indicating large variations in arc length, shown in Figure 4.4b. In the cap pass (Figure 4.4c) one can notice a larger short-circuit region with slight variation in arc length. The results also suggest that there was a high variation in current, probably due to an increased quantity of metal to melt, interpreted by the power source as an increase in wire feed speed (higher melting speed).

Figure 4.5 shows the cyclogrammes for the CW-GMAW condition. From comparing the cyclogrammes for root pass between standard GMAW and CW-GMAW, the arc burning operation range for CW-GMAW is shorter, indicating that this was more stable than the root compared to GMAW. One observes the complete absence of short-circuits, shown in Figure 4.5a. This stabilization is attributed to the cold wire feed.

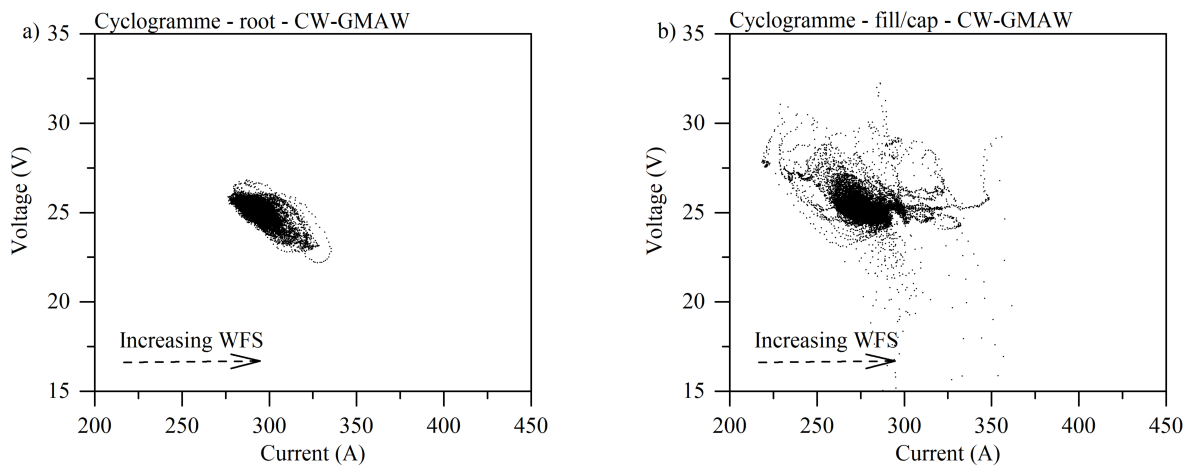

Figure 4.5: Cyclogrammes for the CW-GMAW specimens: a) root pass; and b) fill/cap pass.

Costa Assunção et al. [57] reported that inserting a cold wire causes the arc to become pinned to it, keeping the arc length almost constant while improving the melt-off rate, since the cold wire causes a slight increase in current, as reported by Ribeiro et al.[54]. Meanwhile, comparing the fill/cap condition (Figure 4.5b) between CW-GMAW and GMAW, one finds the existence of short-circuits and variation in arc length, suggested by high values of voltage for the same range of current.

4.4.2 High Speed Imaging

Figure 4.6 shows the high speed frames for the standard GMAW and CW-GMAW inside the grooves. As suggested by the electrical signals, it was possible to verify that the arc for the GMAW often attaches to the sidewalls, resulting in erosion. The arc attachment to sidealls can be ascribed to the arc seeking shortest electron path according to Zhang et al. [70]. The same author claims that arc attachment is avoided when welding in constant current mode, since the voltage continually varied in order to maintain a constant melting speed. Meanwhile, in CW-GMAW the arc attachment is to the cold wire, which prevents sidewall erosion. In Figure 4.6a one can discern that the arc is pinned to the rear (cold wire) and not to the sidewalls.

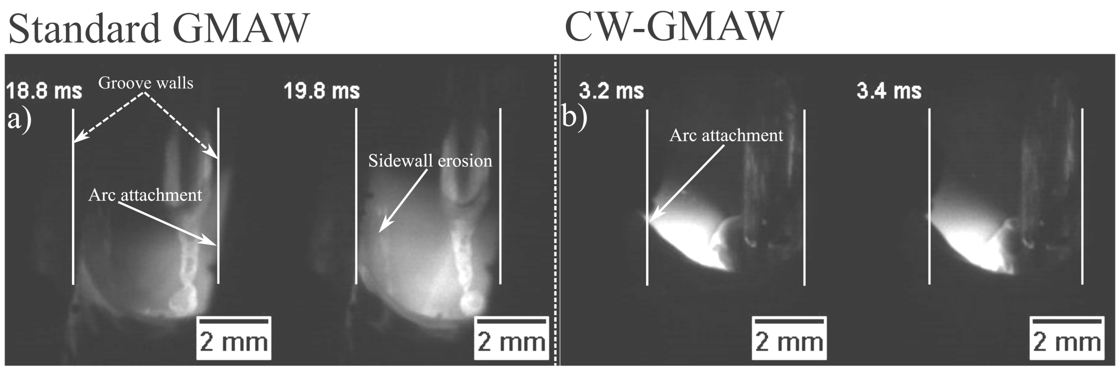

Figure 4.6: High speed frames, arc dynamic behaviour inside the groove: a) standard GMAW; and b) CW-GMAW.

4.4.3 Sidewall Erosion

The erosion in sidewall is triggered by the arc self regulation dynamics, which tries to establish the shortest path to electron flow, thereby increasing the melting rate. However, as the arc moves through the groove the attachment point is continually changing, melting multiple points across the groove walls. This multiple erosion points may have detrimental effects on the mechanical properties of the joint.

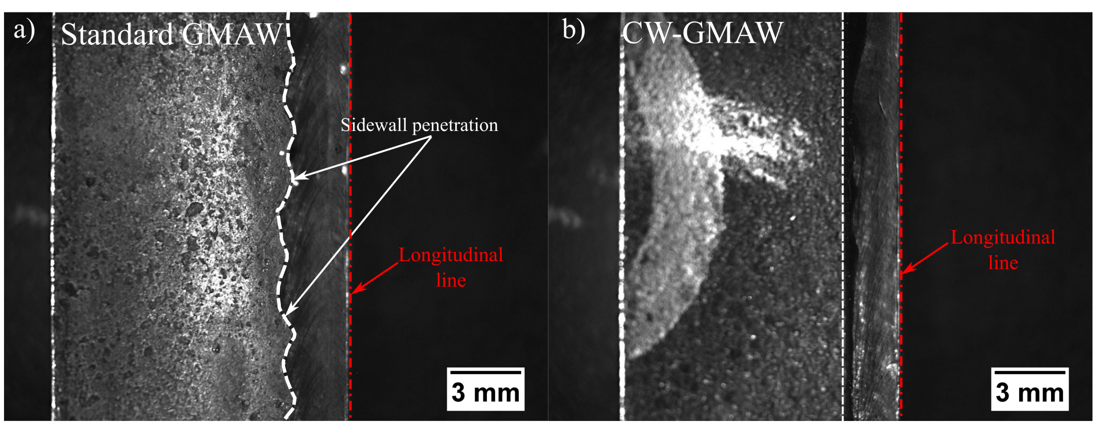

Figure 4.7: Top view of the sidewall penetration caused by the root pass. The specimens were cut along the longitudinal line (dashed red line): a) standard GMAW; and b) CW-GMAW.

Figure 4.7 shows the sidewall penetration caused by the root pass during welding. The standard GMAW erodes the sidewalls consistently as shown by oscillograms in Figure 4.2a. Every time the arc attaches to the sidewalls, intense and fast short-circuiting causes the current to increase abruptly in order to fuse the extra metal and restore the compatible voltage (arc length, in constant voltage) to the current pre-set before welding). Conversely, as in the CW-GMAW, when the arc is attached to the cold wire there is effectively no sidewall penetration, as can be seen in Figure 4.6a.

4.4.4 Influence Of CW-GMAW On The HAZ During The Root Pass

Figure 4.8 shows the evolution of the heat affected zone (HAZ) in the root pass for the standard GMAW welds for three bead locations: start, middle, and end. Arc wandering results in asymmetric welds. This is likely due to the inconsistency in penetration, which causes incomplete fusion. Moreover, the size of the root face also contributed to this issue. In addition, Figure 4.8 shows that as the weld progresses, the plate becomes hotter and consequently penetration is slightly increased towards the end of the weld.

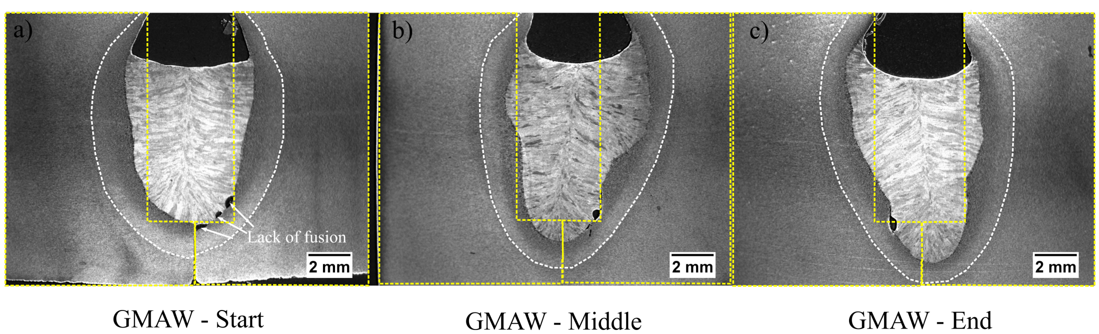

Figure 4.8: Root pass macrographs for the standard GMAW process: a) start of the joint; b) middle of the joint; and c) end of the joint.

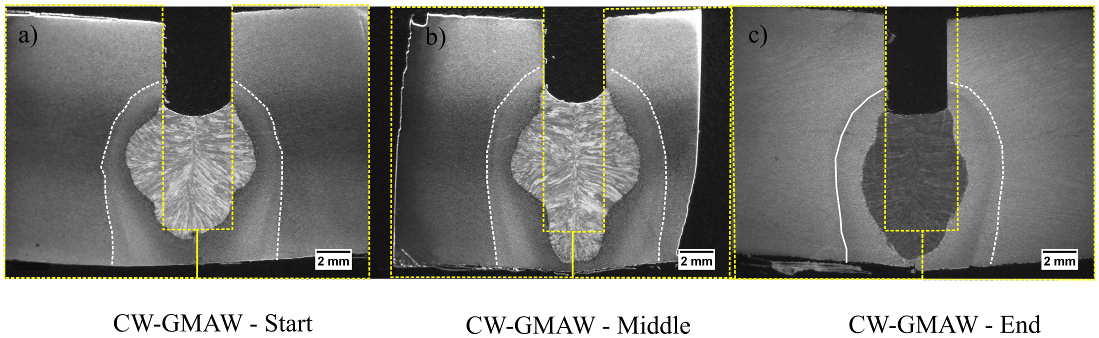

Figure 4.9: Root pass macrographs for the CW-GMAW process: a) start of the joint; b) middle of the joint; and c) end of the joint.

Figure 4.9 shows the root pass in three locations across the bead for CW-GMAW. No discontinuities (based on cross-sections inspection) are likely to occur in the root pass, and generally, the sidewall penetration in the root is much more symmetrical due to the arc pinning to the cold wire. Increasing the deposition has decreased the penetration of the weld, causing incomplete penetration.

4.4.5 Macrographs

Figure 4.10 shows the middle of bead cross-sections for both the standard GMAW and CW-GMAW. The middle cross-section of the standard GMAW has an acceptable morphology without discontinuities, while achieving suitable penetration in the root face. Conversely, incomplete penetration persists in CW-GMAW. The CW-GMAW welds also have inclusions, most likely, oxides, due to the increased level of titanium in the weld metal introduced by the cold wire feed, as the same type of wire is used as electrode and cold wire.

The presence of inclusions highlights the need of more careful grinding after the root to clean the silicates formed during welding pool solidification. Another features that differs between the cross-sections is the number of passes needed to fill them with weld material. Standard GMAW requires three passes while CW-GMAW only requires two. Ultimately, the overall heat input in CW-GMAW is lower due to the fewer passes needed to fill the gap.

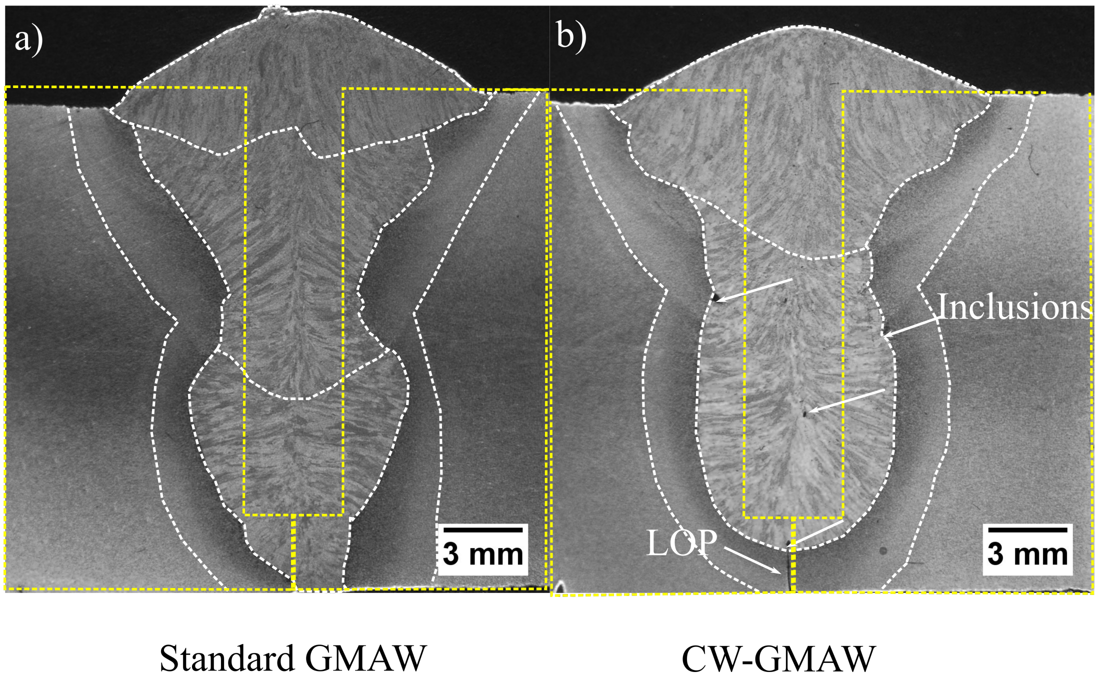

Figure 4.10: Middle of the bead cross-section showing the final weld morphology: a) conventional GMAW; and b) CW-GMAW. The arrows indicate discontinuities such as inclusions and incomplete fusion.

There are two ways to mitigate incomplete fusion, increase the current by means of wire feed speed to increase penetration, or a decrease the root face height can facilitate higher penetration penetration. A change in the joint geometry can be made to include a reverse root pass, which is called ”mechanized GMAW” [38].

4.4.6 Micrographs

In this section the HAZ width of the standard GMAW and CW-GMAW specimens will be compared. Costa Assunção [57] reported, in previous work, that the intercritical heat affected zone (ICHAZ), which is formed as the material cools from 800 and 500 degrees Celsius, is narrower in CW-GMAW welds compared to GMAW.

Weld interface - Root pass

Figure 4.11a shows the HAZ from the weld interface to base metal in the conventional GMAW specimen, Figure 4.11b shows the HAZ from the interface but for the CW-GMAW. In both specimens the images were taken at the root pass, in a one pass weld, refer back, to Figures 4.8b and 4.9b, respectively.

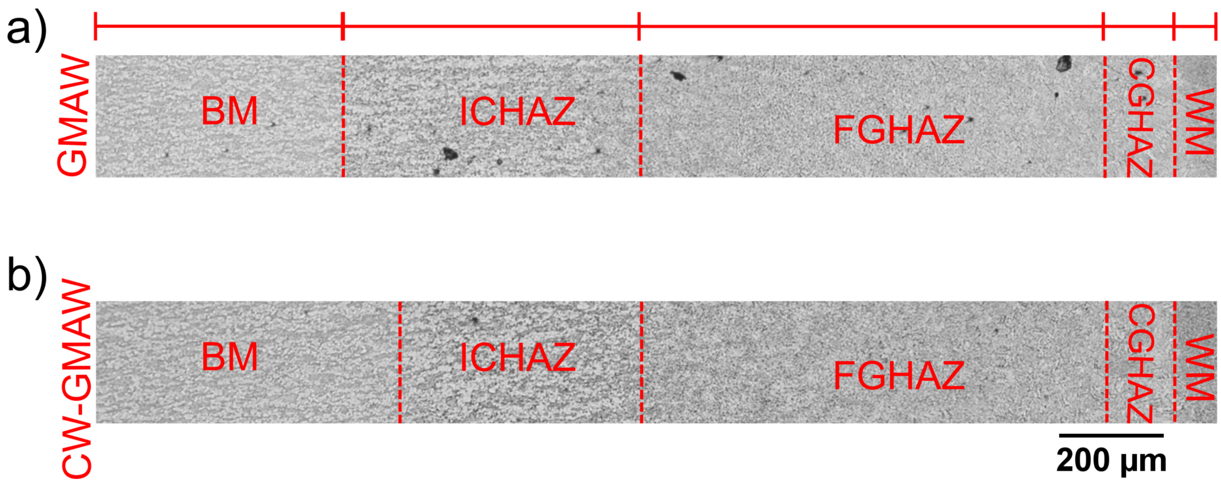

Figure 4.11: HAZ width in the GMAW specimen showing the WM, CGHAZ, FGHAZ, and, ICHAZ: a)standard GMAW; and b)CW-GMAW

The ICHAZ is slightly narrower in CW-GMAW than in the standard GMAW. This is consistent with previous research, and suggests that CW-GMAW specimens have a faster cooling time between 800 and 500 °C compared to the conventional GMAW specimens. This seems to indicate that less heat is actually applied across the weld joint during CW-GMAW.

4.4.7 Vickers Hardness

The strength of the joints are characterized by Vickers hardness mapsof the cross-sections. Figure 4.12 shows the hardness map of the completed joint for standard GMAW and CW-GMAW specimens.

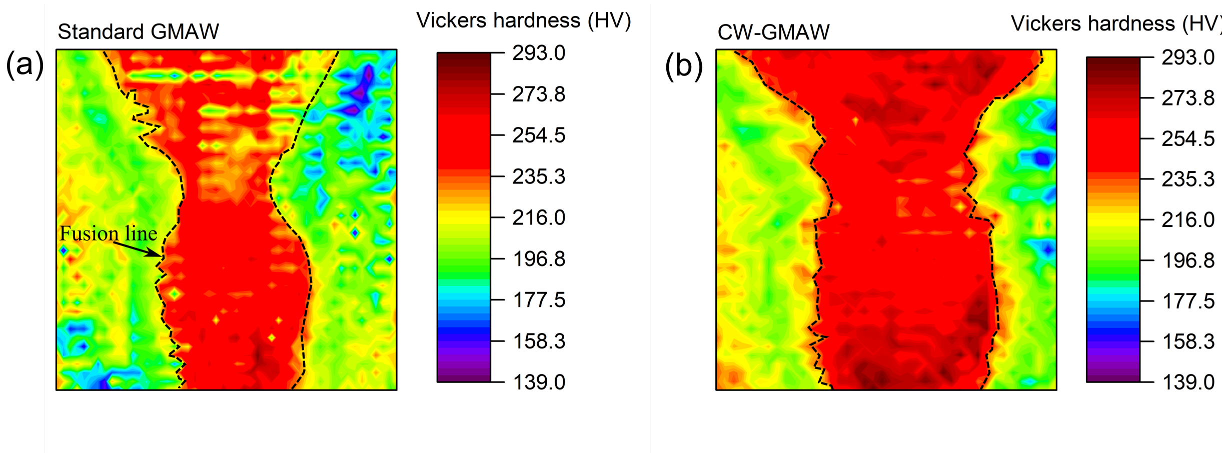

Figure 4.12: Hardness map of the cross-sections: a) standard GMAW; and b) CW-GMAW, with weld interface marked by dashed lines.

The Vickers hardness of the CW-GMAW weld is higher, which indicates that the cooling rate of the weld metal in CW-GMAW was faster than the standard GMAW. This results seems consistent with the prior research [73]. In Chapter 4 it was reported that for some conditions the melting efficiency of CW-GMAW is higher than in conventional GMAW. The melting efficiency is defined as the amount of heat actually transferred to the melting pool divided by the total welding power, and a difference of this value might explain slower cooling rates.

Figure 4.13 shows the hardness map of the root pass in cross-section extracted from the middle of the joint. The values are similar in standard GMAW and CW-GMAW. However, comparing Figures 4.12 and 4.13, shows that the bottom of the CW-GMA welds is harder than the botton of conventional GMAW. Since, the hardness patterns of the roots were similar, this results likely indicates that the cooling rate near the root is faster in CW-GMAW. However, the exact reason for this is unclear, but may be due to a faster heat transfer due to a larger contact area with the base metal and also a higher temperature between the weld and base metals in CW-GMA welds.

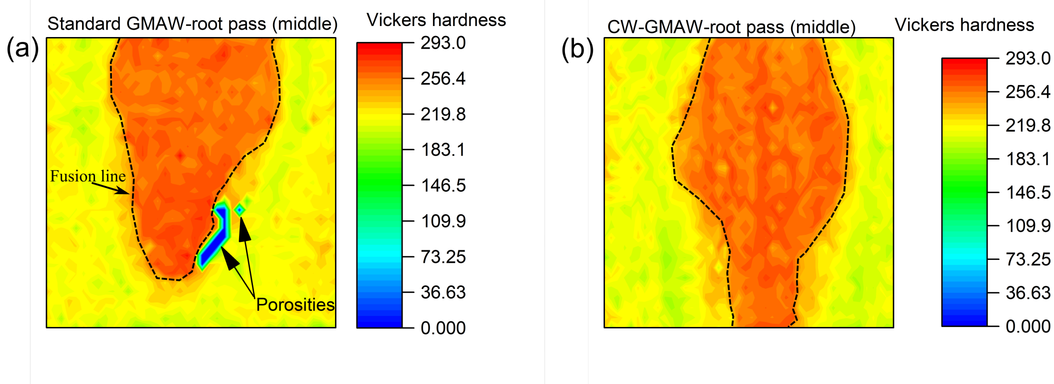

Figure 4.13: Hardness map of the root pass, middle cross-section: a) standard GMAW; and b) CW-GMAW, with weld interface marked by dashed lines.

4.5 Discussion

The electrical oscillograms in Figure 4.2 show that the standard GMAW experiences some sort of oscillating pattern, which may correspond to the arc attaching to and detaching from the sidewalls sidewalls, which may be a function of the power source internal regulation in constant voltage mode [70]. The arc attaches to sidewall so that the current flows in the shortest path in order to minimize the potential.

This phenomenon in constant voltage (CV) mode leads ultimately to the melting of the contact tip and interruption of the welding processes. However, it has been noted that in constant current (CC) mode this process does not occur since the reduction in arc length, induced by the arc attachment to the sidewall, causes a small reduction in arc length compared to the reduction in current, so that the power source reaches a new equilibrium point.

In contrast, in CW-GMA welding the current path is shortest to the cold wire, which causes the arc to attach to it instead of the sidewalls. Consequently avoiding sidewall erosion. Moreover, the arc is much more stable in CW-GMA welding (Figure 4.3) than in standard GMAW (Figure 4.2) as confirmed by the cyclogrammes for the the two cases. The root pass performed using CW-GMAW (Figure 4.5a) is more stable than in the conventional GMAW (Figure 4.4a) which has a tail corresponding to short-circuits caused by the sidewall erosion (dashed square).

Regarding the cap pass, in conventional GMAW the arc tends to climb towards the contact as indicated by the higher values of voltage (increase in arc length) and current in

Figure 4.4c. However, in CW-GMAW this phenomenon was less prevalent.

High speed images were used to investigate the arc dynamical behaviour. The images show that the arc attaches to the sidewalls in standard GMAW because of the internal regulation of the source in CV, as discussed earlier (Figure 4.6). In CW-GMAW, as expected from the electrical signals, no sidewall erosion was detected, as can be seen in Figures 4.6 and 4.7.

Figure 4.8 shows the macrographs of the joint manufactured using conventional GMAW. One can observe that there are some lack-of-fusion defects. These are caused by the arc climbing and over-melting in one direction, leaving gap and a lack-of-fusion. In contrast, in CW-GMAW one can notice that as the arc is pinned to the cold wire, leading to a more stable melting pattern and avoiding incomplete fusion across the joint (Figure 4.9).

The macrographs Figure 4.10, taken from the middle of joints, highlight the difference in productivity between the two methods. The standard GMAW joint is completely filled with three passes while the the CW-GMAW is filled in only two passes. However, one observes that in relation to the cold wire joint there is a lack of penetration due to the arc pinning to the cold wire which limits the penetration and dilution of the weld.

Figures 4.11 compares the HAZ for standard GMAW and CW-GMAW. The difference in their size can be attributed to differences in thermal signature. The difference in ICHAZ may indicate a higher thermal gradient in CW-GMAW than in conventional GMAW. This thermal gradient might result from a improved melting efficiency in CW-GMAW for some conditions.

Figures 4.12 and 4.13 show the hardness maps over the complete macro and the root pass for both conventional GMAW and CW-GMAW, respectively. The Vickers hardness values in CW-GMAW, Figure 4.12, point to a lower cooling time (higher cooling rate) which might be linked to the higher thermal gradient caused by the possibly higher melting efficiency in CW-GMAW. This may explain the higher hardness in CW-GMAW compared to the standard GMAW. Regarding the root pass, the difference in hardness is likely due to the larger gradient formed by the larger joined area in the CW-GMAW root. This leads to higher cooling rates in the reheated root of the weld metal, with higher hardness.

4.6 Summary

Narrow groove welds in API X80 were fabricated using the standard GMAW and the CW-GMAW in order to assess the process feasibility using CW-GMAW for a joint with a 4 mm gap. Taking into account the results discussed the following conclusions can be drawn:

1. The welds produced using the GMAW process featured serious sidewall penetration that might compromise their mechanical integrity;

2. The welds fabricated using CW-GMAW did not present sidewall erosion during the root pass; conversely the increase in deposition compromised the penetration in the root region;

3. The amount of inclusions found in the the cold wire welds might be linked to the grade of the welding wires used.

Chapter 5

The CW-GMAW: An Overview On Pulsed Current [1]

5.1 Overview

The demand to join newer and higher strength materials has motivated the development of controlled arc current waveforms in order to enhance weld metal deposition while controlling heat input. Controlled waveforms used in pulsed gas metal arc welding (P-GMAW) usually involve a square wave pulse which can result in reduced nominal heat input, distortion, and residual stresses. A method to mitigate these problems is by cold wire pulsed gas metal arc welding (CW-P-GMAW) to enhance P-GMAW by feeding a cold wire (non-energized) into the weld pool. In this chapter, the feasibility of the process is reported and the influence of cold wire feeding on pulse parameters for low and high background to peak current ratios, $\frac{I_b}{I_p}$, were investigated through high-speed cinematography with synchronized current and voltage sampling, as well as evaluation of cross-sections via metallography. These measurements show that the cold wire reduces the heat transferred across the heat-affected zone (HAZ) for low current ratios.

[1] This chapter is based on the following paper: Ribeiro, R.A.; Assunção, P. D. C.; Dos Santos, E. B. F. ; Braga, E. M.; and Gerlich, A. P. An overview on the cold wire pulsed gas metal arc welding. Welding in the World (2019): 1-18. https://link.springer.com/article/10.1007/s40194-019-00826-w

5.2 Background

Yudodibroto et al. [74] reported that convection within the welding pool is triggered by impinging droplets in P-GMAW and that is likely a result of differences in electrical field intensities at the peak vs. background values of current. However, the mechanism for changing the droplet behaviour was not hypothesized. Dos Santos et al. [75] that the two different current profiles entail differences in droplet detachment and droplet tapering due to differences in iron metal vapour quantity. Moreover, the droplet momentum was faster for profiles with lower background currents. Further research by Dos Santos et al. [76] has shown that spray streaming transfer can be achieved during high frequency current pulsation, leading to reduced heat input while maintaining deposition rates.

The quality of the weld is a function of the waveform shape, as reported by Pal and Pal [77], since pulsation increases penetration due to arc oscillation and refines the grains inside the weld metal. In addition, Gosh [78] showed that the weld temperature distribution can be controlled through pulsation, and used this strategy to decrease the level of residual stresses for narrow gap welding. The same author discussed the effect of pulsation on the deposition of austenitic stainless steel on a C-Mn steel substrate. It was found that increasing the pulse frequency leads to a refined overlay microstructure, thus improving the mechanical properties. Tong et al. [79] discussed the effect of AC and DC current on P-GMAW of aluminium; they found that AC mode induces less penetration than the DC mode. The same authors noticed that increasing the electrode negative ratio the distortion of the aluminium plates decreased.

The use of auxiliary cold wire feeding is not restricted to standard GMA welding. This technique has also been employed in submerged arc welding (SAW) and gas tungsten arc welding (GTAW). For instance, Mohammadijoo et al. [50] reported using a cold wire feed improved the toughness of the heat affected zone (HAZ) through refinement of the prior austenite grain size. Pai et al. [80] compared cold wire to hot-wire GTAW and found that both can be suitably applicable to weld pipes in the nuclear sector. Hassler [44] showed that in tandem GMAW, [2] the interaction is beneficial to arc stability. Recently, Xiang et al. [48] showed that the interaction between a cold wire and twin GMAW can improve weld stability through stabilization of the cathode spots.

Among the new processes to improve in welding productivity is cold wire pulsed gas metal arc welding (CW-P-GMAW), consisting of the standard GMAW coupled with a cold wire

[2] In Tandem GMAW two wire feed units and two welding power sources are used in conjunction so that the wires are continuously fed using a special welding torch to form a single weld pool. The main advantage of this process is its deposition which can be in the order of 24 kg/h.

(non-energized) feed in order to increase deposition without increasing nominal heat input. The CW-GMAW process was reported by Ribeiro et al. [54] as causing a slight increase in current without an increase in penetration. This process has provides lower levels of distortion [81] , consequently achieving lower residual stresses [55]. Recently, Costa Assunção [57] assessed the feasibility of this process to weld butt joints with a 5mm-wide narrow gap.

This chapter reports the feasibility of CW-P-GMAW and the influence of the cold wire on arc dynamics when an square wave pulse with an exponential decay is applied. The influence of the cold wire feed on bead appearance and cross-section geometry are assessed. To the best of the author's knowledge, this is the first time that this variation of P-GMAW has been attempted.

This technique is well-suited to narrow gap welding (NGW) of pipelines. In its present form, NGW of pipelines involves two major challenges: the sidewall erosion, which can impair the mechanical properties of the joint; and b) excessive heating, which leads to excessive residual stresses. CW-P-GMAW can overcome both issues due to the nature of pulsation, which reduces both the heat input and the tendency of the arc to pin to the cold wire, therefore suppresses sidewall erosion.

5.3 Experimental Methodology

5.3.1 Materials

Bead-on-plate welds were deposited on AISI 1020 [82] plain carbon steel flat bars measuring 2 in (51 mm) x 7 in (178 mm) x 3/8 in (9.53 mm). The wire used was AWS A5.18 ER 70S-6 [65]. The electrode wire had a 1.2 mm nominal diameter; while the cold wire had a 0.9 mm nominal diameter. Table 5.1 presents the nominal chemical composition for the substrate and the welding wire. The shielding gas used was a mixture of Ar-15%CO_2 at a flow of 19 l/min.

Table 5.1: Nominal chemical (% wt.) compositions of the welding wires and the substrate.

Material	**C**	**Si**	**Mn**	**P**	**S**	**Cr**	**Fe**
AISI 1020	0.17-0.23	-	0.30-0.60	<0.040	<0.0050	-	Bal.
ER70S-6	<0.15	0.80-1.25	1.40-1.85	<0.025	<0.035	<0.15	Bal.

5.3.2 Welding Procedure

A general set-up is shown in Figure 5.1: Figure 5.1a indicates the cold wire injector and the high speed camera used to study the arc dynamics, while Figure 5.1b shows the detail of cold wire feeder. High speed imaging was done at 5000 frames per second with a shutter speed of 25 microseconds, and a narrow pass band filter of 900 $\pm$ 10 nm was used to limit the light reaching the camera sensor. Current and voltage were sampled at 10 kHz using a data acquisition system (DAQ), where the electric data were acquired for two seconds.

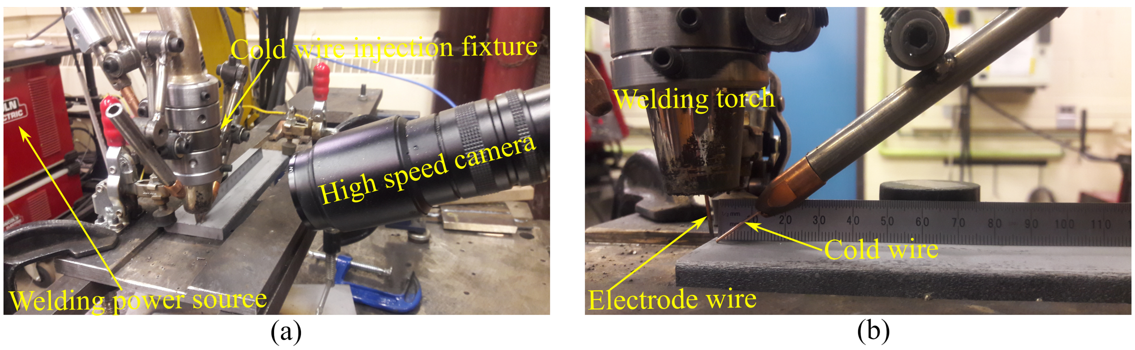

Figure 5.1: Experimental set-up cold wire: a) Cold wire feeder and high speed camera; b) Detail of cold wire feeding.

A Lincoln R500 welding power source was employed to perform the welds in cold wire pulsed gas metal arc welding (P-GMAW) using synergic control. Low background to peak (I_b/I_p), and high background to peak current ratios were evaluated. Figure 5.2 shows these two pulsed current profiles.

In order to create the two levels of current ratio employed in this work, the power source parameters were set using wire feed speed (in/min), travel speed (in/min), and trim regulation. One can obtain different current ratios by varying these three variables. The trim setting controls the arc length through indirect voltage control in order to have a more stable welding process. Low values of trim correspond to low arc lengths, while high values of trim promote a long arc.

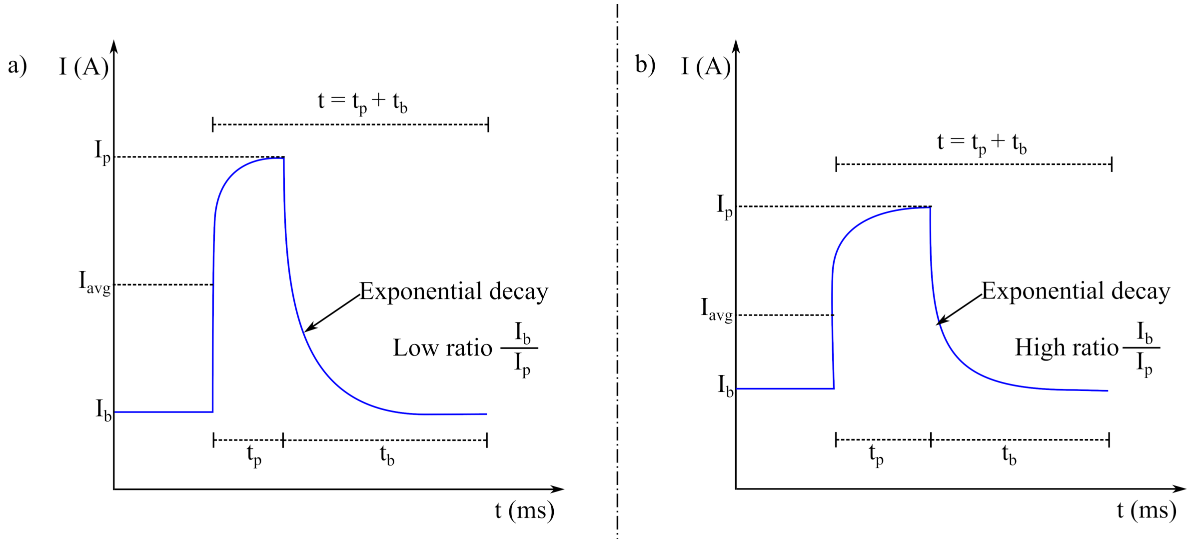

Figure 5.2: Current pulse profiles used in the welds. a) Lower current ratio, b) Higher current ratio.

The welding parameters for these two sets of welds are shown in Table 5.2. The cold wire (CW) mass rate was determined from the wire feed speed and is expressed as a percentage fraction of the mass feed rate through the electrode wire. Each condition was carried out twice to assess repeatability.

True power (TP) was calculated based on the instantaneous values of current and voltage according to [83] using:

$$TP = \frac{1}{n}\sum_{i=1}^{n}(U_i \times I_i) \tag{5.1}$$

where U_i (V) and I_i(A) represent the instantaneous values of voltage and current, respectively. This parameter was then used to calculate true heat input (THI) for a given travel speed (TS). This is not equivalent to the process specific heat input, which must also account for the process thermal energy efficiency, according to [84] and [85]:

$$THI = \frac{TP}{TS} \tag{5.2}$$

Table 5.2: Welding parameters set on the power source

<table>
<tr><th>Condition</th><th>Welding process</th><th>WFS (in/min) [m/min]</th><th>Trim</th><th>Travel speed (in/min) [cm/min]</th><th>Cold wire mass rate (%)</th></tr>
<tr><td>1</td><td>P-GMAW</td><td rowspan="4">250 [6.3]</td><td rowspan="4">1.5</td><td rowspan="8">16 [41]</td><td>0</td></tr>
<tr><td>2</td><td>CW-P-GMAW</td><td>20</td></tr>
<tr><td>3</td><td>CW-P-GMAW</td><td>60</td></tr>
<tr><td>4</td><td>CW-P-GMAW</td><td>100</td></tr>
<tr><td>5</td><td>P-GMAW</td><td rowspan="4">300 [7.6]</td><td rowspan="4">1.0</td><td>0</td></tr>
<tr><td>6</td><td>CW-P-GMAW</td><td>20</td></tr>
<tr><td>7</td><td>CW-P-GMAW</td><td>60</td></tr>
<tr><td>8</td><td>CW-P-GMAW</td><td>100</td></tr>
</table>

The resulting value of true heat input is reported in kJ/mm, taking the travel speed in (mm/s). Mean current (I_{avg}) was calculated according to [78]:

$$I_{avg} = \left[\frac{(I_b t_b + I_p t_p)}{(t_b + t_p)} \right] \tag{5.3}$$

where I_b the background current in (A), t_b is the background time in milliseconds, and I_p is the peak current in milliseconds. One can note that this is just a weighted average while the effective current (I_{eff}) was also calculated [78]:

$$I_{eff} = \sqrt{\left[k_p {I_p}^2 + (1 - k_p)\, {I_b}^2 \right]} \tag{5.4}$$

where k_p is the duty cycle of current waveform, which represents how much time the current is kept in the peak over the waveform period. This can be calculated according to [78]:

$$k_p = \frac{t_p}{(t_p + t_b)} \tag{5.5}$$

Lastly, the droplet diameter was estimated based a mass balance according to [86]:

$$d = \sqrt[3]{\left(\frac{{d_e}^2 \cdot WFS}{40 \cdot f_d} \right)} \tag{5.6}$$

where ${d_e}^2$ is the diameter of the wire electrode, WFS is the wire feed speed, and f_d is the droplet detachment frequency. Since the pulse control aims to achieve a one-droplet-per-pulse (ODPP) transfer mode, the droplet frequency equals the pulse frequency.

After welding, each of the specimens was cut into three cross-sections and subjected to standard metallographic procedures, including grinding and polishing with a final media of 1 micrometer alumina solution, and etched with a 2% Nital solution in order to reveal macro and microstructure. Bead penetration, width, height, dilution, and heat affected zone (HAZ) area were measured using imaging analysis software. Vickers hardness maps of the weld metal and HAZ were performed using 500 gf and 10 s as dwell time.

5.4 Results

5.4.1 Electrical Data

The electrical data, average and RMS voltage, average and RMS current, and average and RMS power sampled during welding are presented in Table 5.3. The values of true power and true heat input are indicated in Table 5.4. Average power and true power coincide since they were calculated using the instantaneous values of current and voltage.

Table 5.3: Average and RMS values of voltage, current, and power sampled during welding.

Condition	**Average voltage (V)**	**RMS voltage (V)**	**Average current (A)**	**RMS current (A)**	**Average power (kW)**	**RMS power (kW)**
1	31.5	31.7	205.0	275.8	7.6	9.7
2	31.5	31.8	206.0	275.9	7.6	9.9
3	31.5	31.8	208.5	276.4	7.7	9.9
4	31.4	31.7	212.2	282.0	7.8	10.0
5	21.4	22.1	164.3	252.7	4.8	6.8
6	21.4	22.1	171.5	256.7	4.9	7.0
7	21.4	22.2	178.9	264.0	5.1	7.1
8	21.4	22.1	188.5	270.4	5.2	7.1

The values of peak current and background current are shown in Figure 5.3. These are used to calculate the current ratio, presented in Table 5.4. There is little variation of ratio values with the introduction of cold wire, as could be expected, among conditions with the same current waveform.

Table 5.4: True power (kW) and true heat input (kJ/mm) for all the welding conditions

Condition	**Process**	**True Power (kW)**	**True heat input (kJ/mm)**	**Peak-to-background current ratio**	**Cold wire feed (%)**
1	P-GMAW	7.6	1.1	0.1	0
2	CW-P-GMAW	7.6	1.1	0.1	20
3	CW-P-GMAW	7.7	1.2	0.1	60
4	CW-P-GMAW	7.8	1.2	0.1	100
5	P-GMAW	4.8	0.7	0.08	0
6	CW-P-GMAW	4.9	0.7	0.09	20
7	CW-P-GMAW	5.1	0.8	0.08	60
8	CW-P-GMAW	5.2	0.8	0.08	100

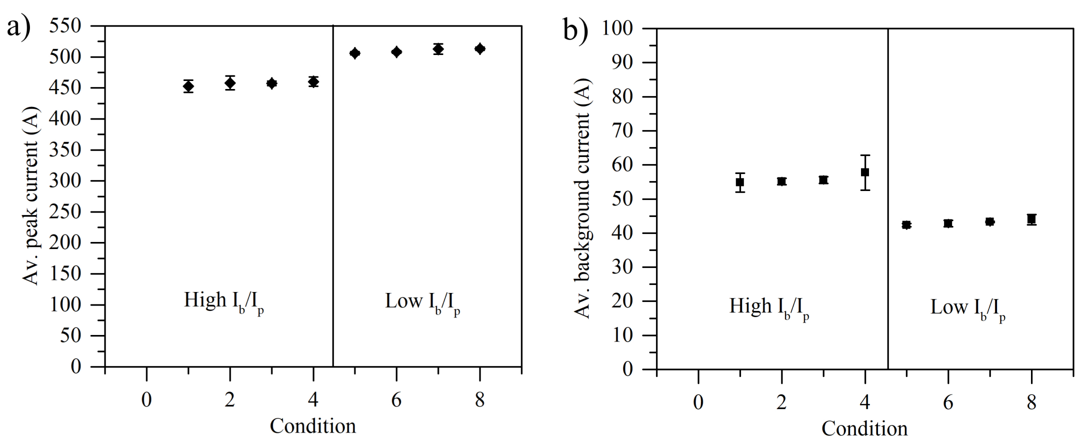

Figure 5.3: Values of current levels in pulsed current: a) peak current; and b) background current. The conditions can be seen at Table 5.2.

The average current peak and background times are presented in Figure 5.4, while the frequency and duty cycle are presented in Figure 5.5. As in the case of P-GMAW, the average and effective currents, plotted in Figure 5.8. In order to investigate the arc stabilitythe oscillograms for all the conditions were plotted in Figure 5.4 and Figure 5.5. It can be seen see that the cold wire does not seem to affect the current waveform for a high ratio, while it does for low ratios.

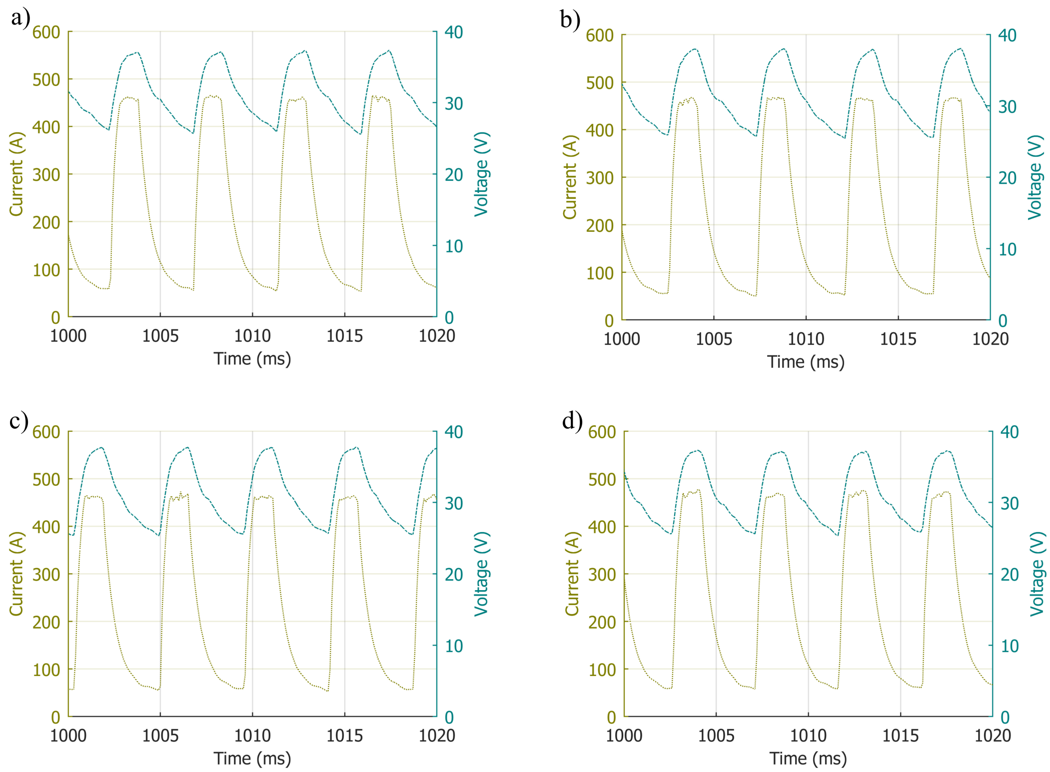

Figure 5.4: Oscillograms for conditions of high current ratio: a) P-GMAW; b) CW-P-GMAW-20%; c) CW-P-GMAW-60%; and d) CW-P-GMAW-100%.

The effect of the cold wire in the low current ratio conditions can be seen in Figure 5.5; the standard condition, the arc length is drastically reduced in comparison to the high current ratio condition due to the low trim setting of the power supply. This short arc length (low value of trim) allows the droplet to touch the weld pool, while it is still attached to the electrode. This causes a short-circuit, and the detachment of the droplet occurs in the transition from peak to background.

Introduction of the cold wire (20%) reduces the arc stability, since the droplet could short-circuit by contacting the cold wire. This situation is demonstrated by the extra peaks between the standard current peak, due to the power source reaction as the arc re-strikes (Figure 5.5b). However, a 60% cold wire mass ratio still exhibits short-circuits but without the sudden reaction of the power source (increase in current) although, apparently, there is no change in the point of droplet detachment.

The introduction of 100% of cold wire seems possible without impairing the local stability of signal (Figure 5.5d). This behaviour is possibly explained by the fact that the droplet detaches before touching the molten pool.

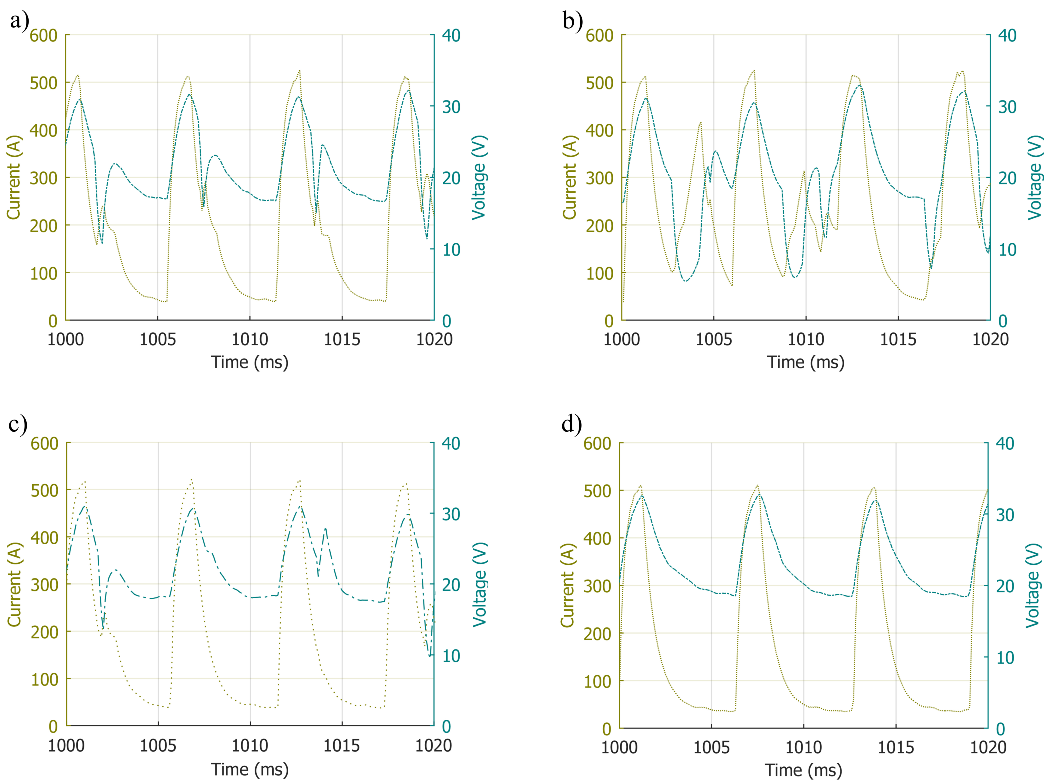

Figure 5.5: Oscillograms for conditions of low current ratio: a) P-GMAW; b) CW-P-GMAW-20%; c) CW-P-GMAW-60%; and d) CW-P-GMAW-100%.

Ribeiro et al. [54] reported that the introduction of cold wire causes the current to increase in order to melt the additional material the surplus of material to melt. For the conditions reported in Figure 5.6, the use of a high current ratio induces a change in the current peak time. However, for a low current ratio the peak time is increased in order to melt the extra cold wire material. The background time does not change significantly for both current ratios.

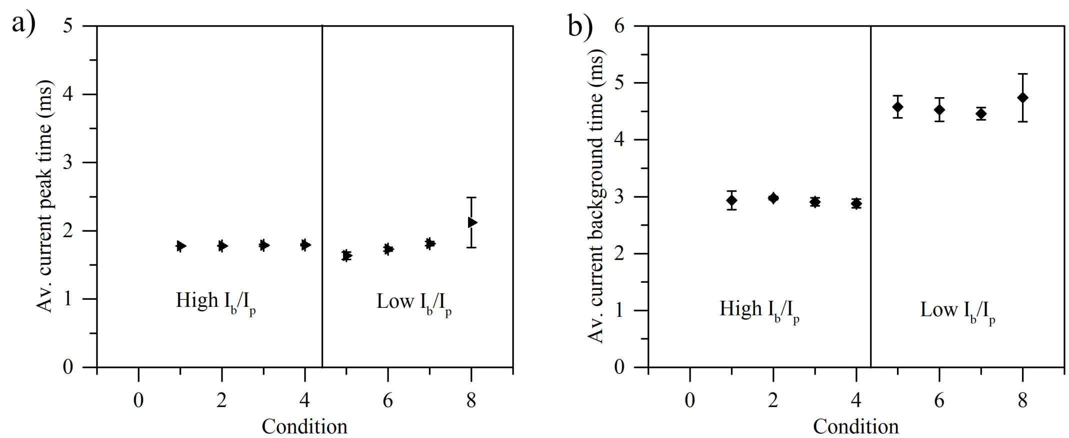

Figure 5.6: Average current peak and background times: a) peak time; and b) Background time. The conditions can be seen at Table 5.2.

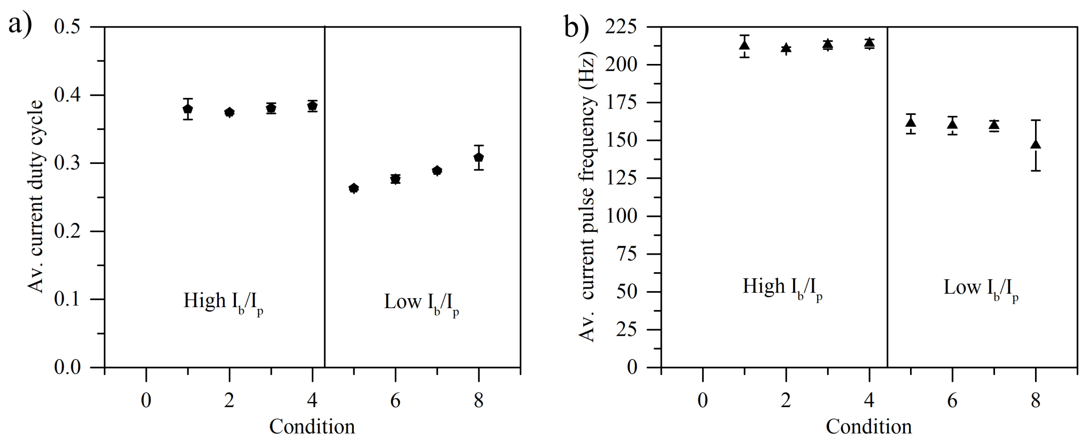

Figure 5.7: a) The influence of the welding conditions on: a) duty cycle; and b) current frequency. The conditions can be seen at Table 5.2.

As expected this difference in peak times for different current ratios entails a difference in duty cycle. One observes in Figure 5.7a that for low current ratio the duty cycle increases whereas for high current the duty cycle remains constant. One might surmise that the introduction of cold wire would affect the detachment frequency, which is set to achieve one-droplet- per-pulse (ODPP), on the contrary Figure 5.7b shows that the frequency is almost unchanged by the addition of cold wire.

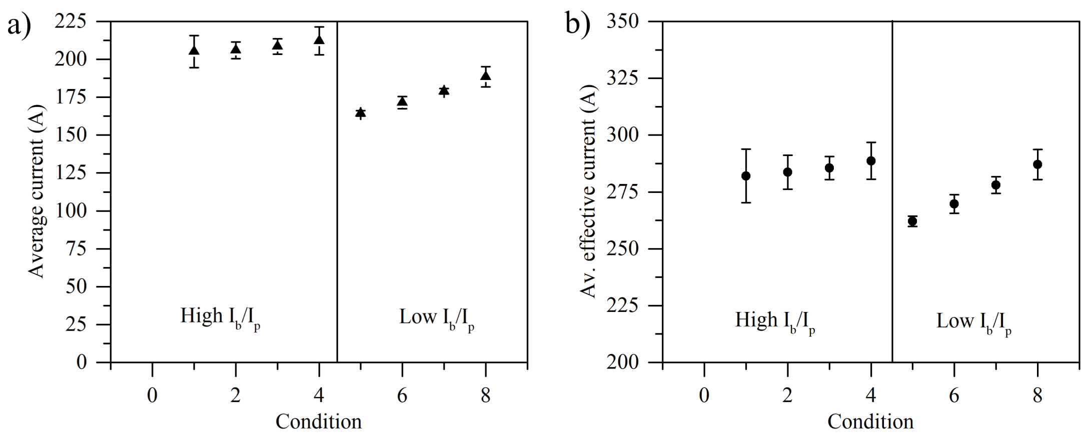

Figure 5.8: Values of a) Average (mean) current and b) Effective current for the welding conditions. The conditions can be seen at Table 5.2.

The effect of introducing the cold wire on duty cycle leads to changes in average current and effective current as shown in Figure 5.8. Since the average current is a weighted average, any change in peak or background times will cause this value to change. As effective current is a function of duty cycle, one observes that it increases for low current ratio, but not to high current ratio. The implications on how the power source internal regulation responds to the addition of cold wire for different duty cycles will be discussed in the Section 5.5.

5.4.2 Metal Transfer Mechanism

The metal transfer under standard conditions for the high current ratio's case are shown in Figure 5.9. The pressure of the arc and droplet momentum cause the formation of a depression (indicated by the arrow) in Figure 5.9c. Moreover, the droplet detached axially is deflected sideways as it falls (Figure 5.9d), which is apparently due to arc pressure.

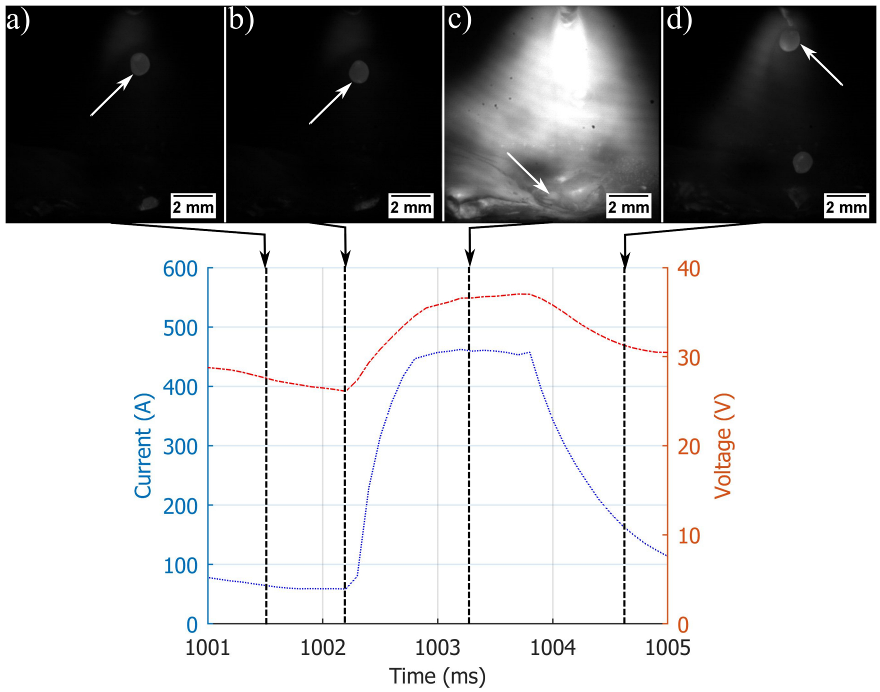

Figure 5.9: Metal transfer over one period for the standard P-GMAW with 250 ipm-1.5-16ipm.

Figure 5.10 shows the metal transfer when a feed rate of 20% cold wire is applied in the high current condition. Figure 5.10b shows that the cold wire is melted by the heat of the arc (indicated by the arrow), and there is no metal transfer from the cold wire until the droplet is sufficiently large to touch the melting pool. In this condition the cold wire metal transfer is dominated by surface tension.

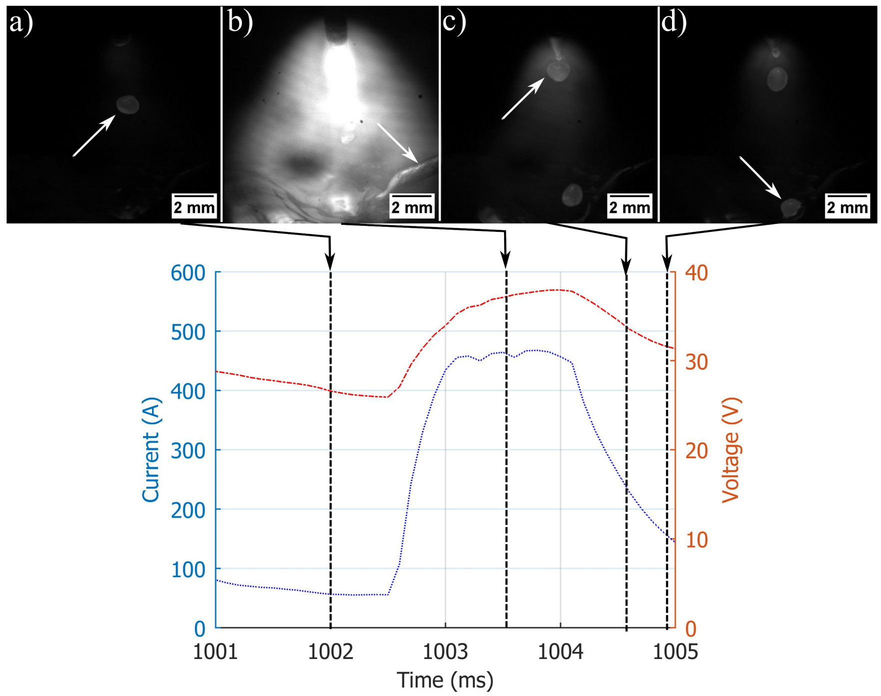

Figure 5.10: Metal transfer over one period for CW-P-GMAW-250ipm-1.5-16ipm-20%.

Figure 5.11 shows the case of 60% cold wire feed rate in which metal transfers directly into the welding pool, which drastically differs from the mechanism with a 20% feed rate. The depression formed by the arc pressure is reduced (Figure 5.11b). Droplet detachment is axial and the droplet tends to impinge the cold wire area (Figure 5.11d). This suppresses the transfer of droplet momentum to the molten pool, reducing the penetration of the weld bead.

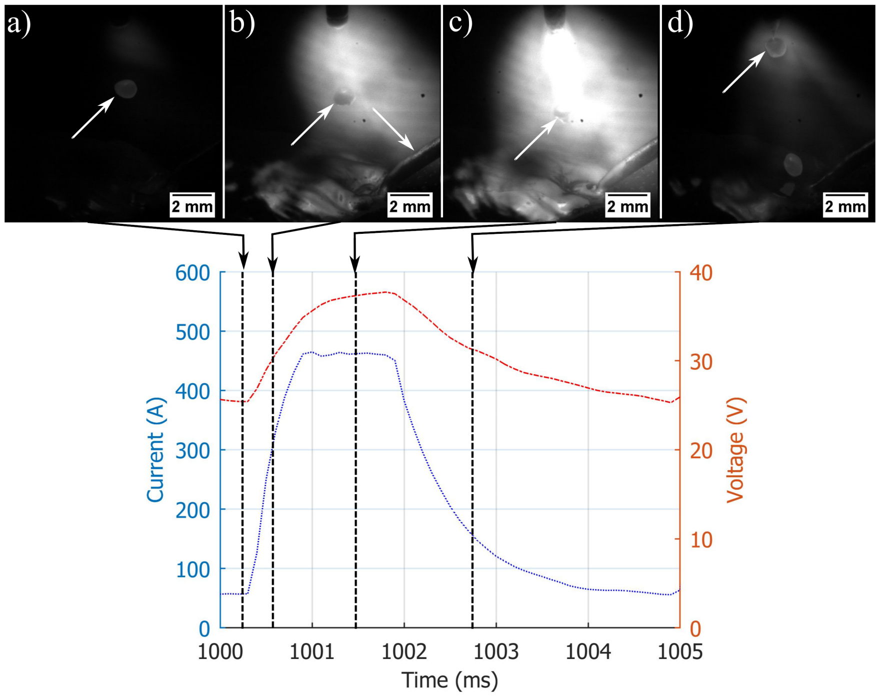

Figure 5.11: Metal transfer over one period for CW-P-GMAW-250ipm-1.5-16ipm-60%.

The metal transfer when a 100% cold wire feed is applied is shown in Figure 5.12. The cold wire is fed directly into the weld pool in this situation, and this leads to a slight deflection of the arc. Droplets now impinge onto the cold wire, which acts as shield for the welding pool (Figure 5.12d). This suppresses momentum transfer to the pool. In this condition the weld pool diameter reduces by approximately 1 mm. Ridges can be observed on the surface of the weld pool, which indicate the contact pressure exerted by the wire on the pool as noted in (igure 5.12c.

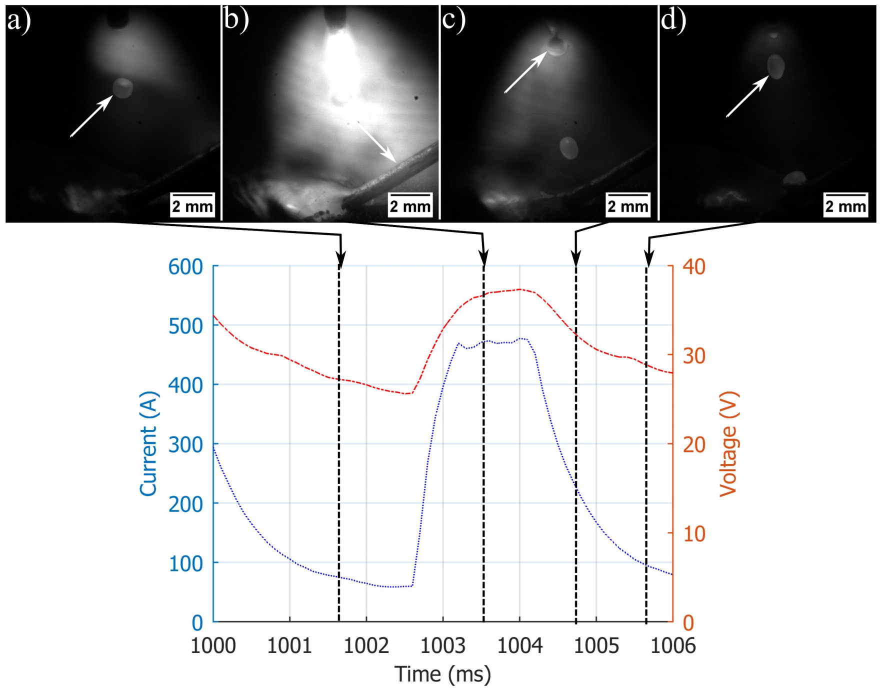

Figure 5.12: Metal transfer over one period for CW-P-GMAW-250ipm-1.5-16ipm-100%.

Figure 5.13 shows the metal transfer for standard pulsed GMAW with a low current ratio. The arc length is shorter compared to Figure 5.9. Consequently, the distance travelled by the droplet also decreases in this condition. In Figure 5.13d, one observes that the droplet short-circuits before detachment causing the detachment to be unstable, leading to spatter.

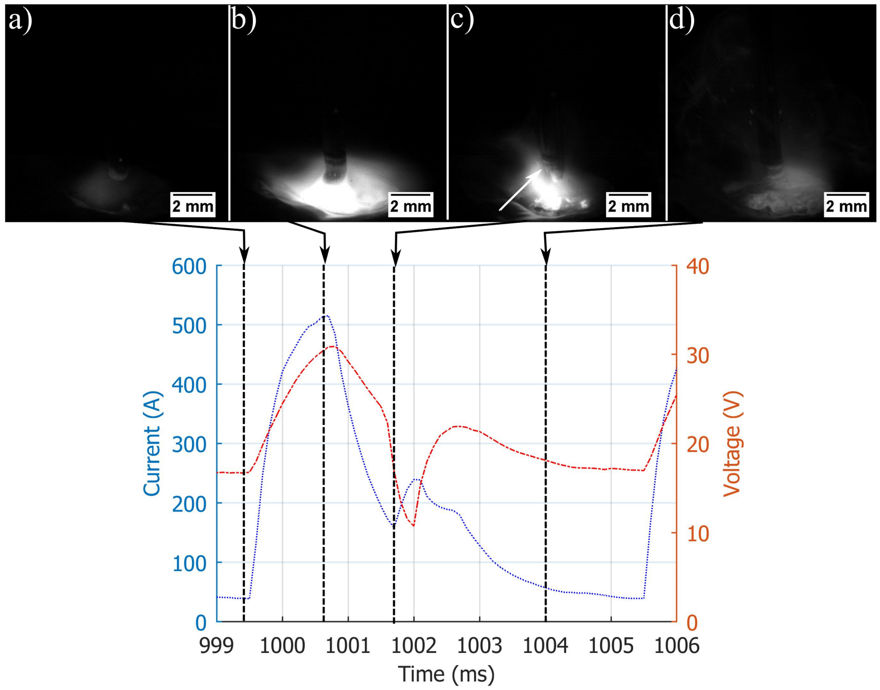

Figure 5.13: Metal transfer over one period for P-GMAW-300ipm-1.0-16ipm.

Figure 5.14 shows metal transfer for a low current ratio with a 20% cold wire is feed rate, similar to the high current condition, the cold wire metal transfer is driven by surface tension, when the droplet formed from the cold wire touches the welding pool. In this condition, again, the short-circuit of the droplet occurs due to the small arc length, which impairs arc stability.

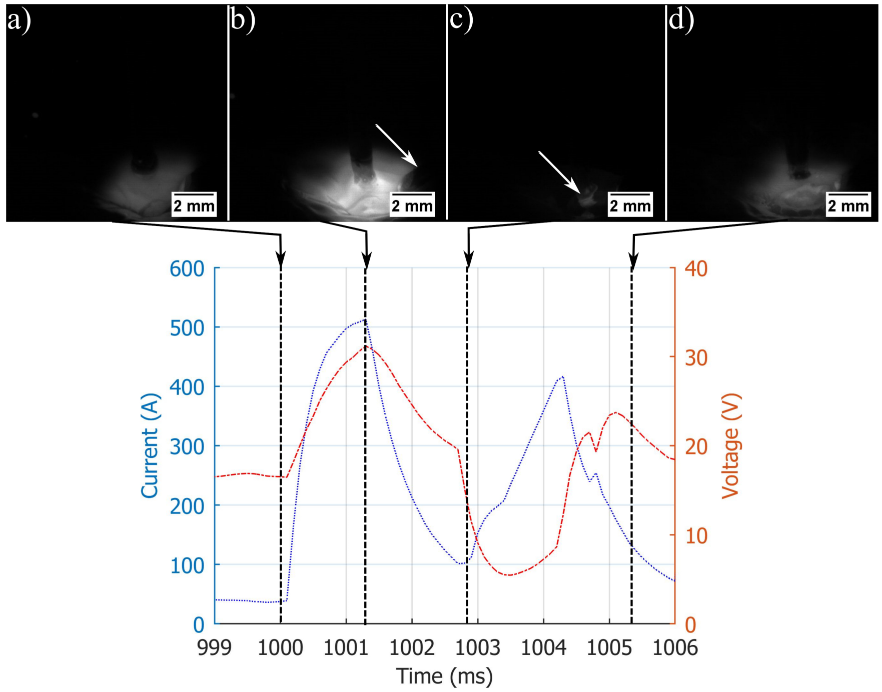

Figure 5.14: Metal transfer over one period for P-GMAW-300ipm-1.0-16ipm-20%.

Figure 5.15 shows the metal transfer for 60% in cold wire feed rate. The cold wire is fed directly into the welding pool and, despite the short arc length, the arc is deflected towards the cold wire. Consequently, the droplet is detaches towards the cold wire, leading to short-circuit during the detachment.

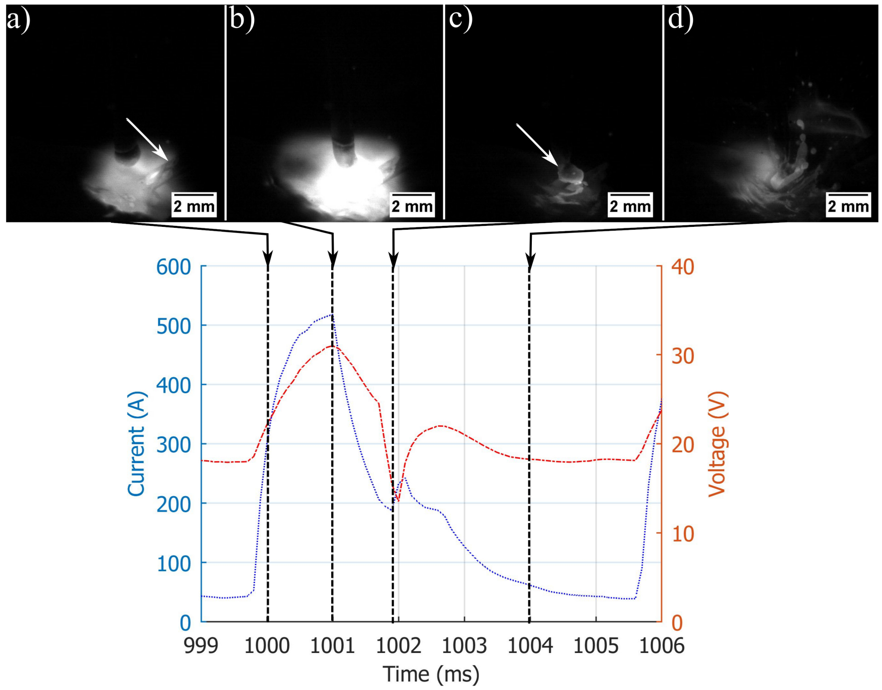

Figure 5.15: Metal transfer over one period for P-GMAW-300ipm-1.0-16ipm-60%.

Figure 5.16 shows the mechanism of droplet detachment when using 100% cold wire feed rate. Again the arc is deflected towards the cold wire, but detaches before touching the weld pool thereby, avoiding the short-circuit. Consequently, the metal transfer occurs in a stable way, but spatter still occurs as discussed in Section 6.3.3.

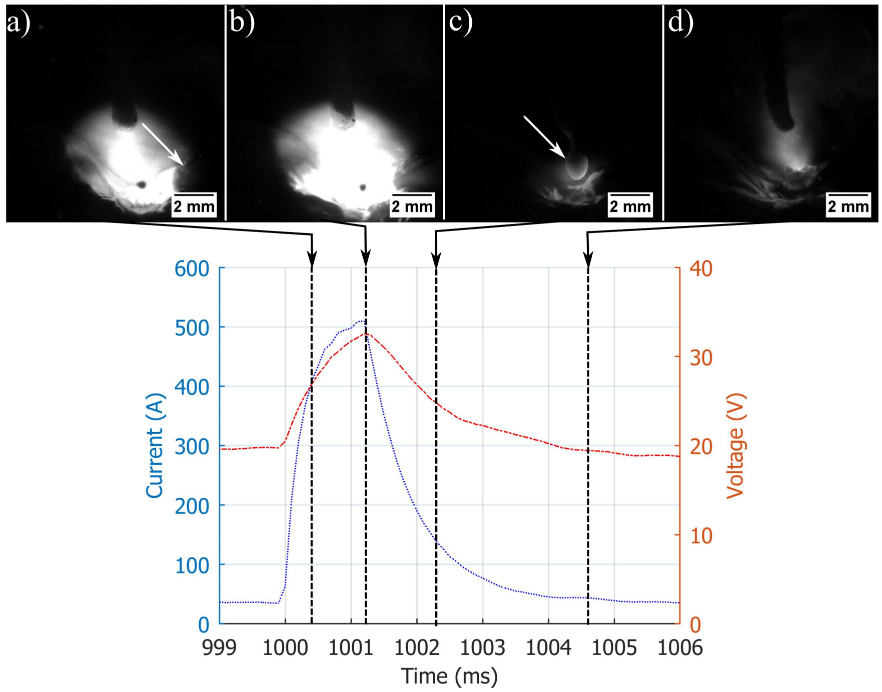

Figure 5.16: Metal transfer over one period for P-GMAW-300ipm-1.0-16ipm-100%.

The metal transfer mechanism also influences the size of the detached droplet. As explained earlier droplet diameter was estimated from the volumetric mass volume, considering the ODPP condition. Figure 5.17 shows that there is no change in the droplet size independent of current ratio and cold wire feed rate, in spite of the increased observed effective current for low current ratio conditions. This seems to support the hypothesis that the increase in current does not lead to a significant increase in pinching force.

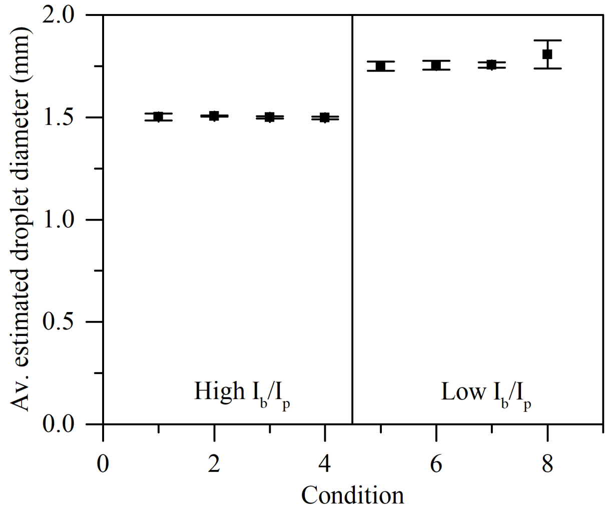

Figure 5.17: Estimate droplet diameter for high and low current ratios with different cold wire feed rates. The conditions can be seen at Table 5.2.

5.4.3 Bead Aspect, Cross-Section And geometry

This section will deal with the quality and geometry of the obtained weld beads, and their suitability for industrial applications. Figure 5.18 shows that all the beads have uniform geometries, without superficial flaws such as porosity or humping.

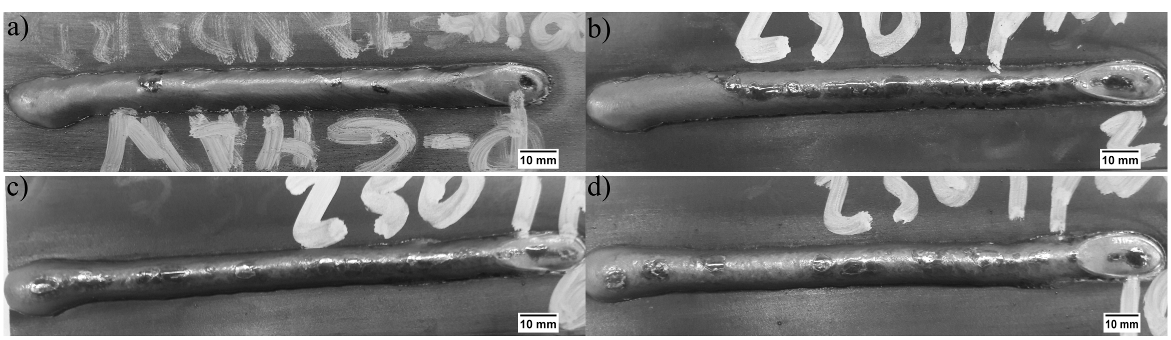

Figure 5.18: - Bead aspects of the high current ratio $\left(\frac{I_b}{I_p}\right)$ conditions: a) P-GMAW-250ipm-1.5-16ipm; b) CW-P-GMAW- 250-1.5-16ipm-20%; c) CW-P-GMAW- 250-1.5-16ipm-60%; and d) CW-P-GMAW-250 ipm-1.5-16ipm-100%.

The high current ratio beads do not exhibit spatter, since this condition provides sufficient power to melt the additional wire. The spatterless condition is also facilitated by the absence of short-circuits, and this is enhanced by an increase in arc length to allow the detachment of droplets without contact with the melt pool.

In contrast, the welds in Figure 5.19 show spatter. In this case it comes from the short-circuiting as the droplet hangs from the electrode due to the short arc length. The amount of spatter increases with cold wire feed rate until it reaches its maximum at a 100% feed rate. Nevertheless, the beads do not present superficial porosities, or humping despite the amount of metal deposited.

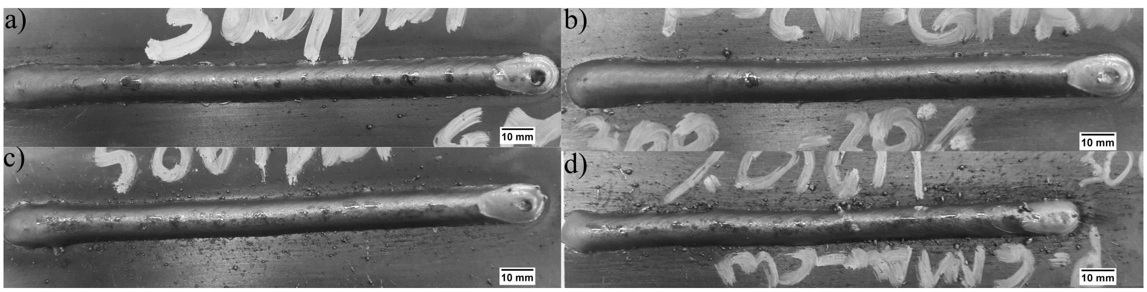

Figure 5.19: Bead aspects of the low current ratio $\left(\frac{I_b}{I_p}\right)$ conditions: a) P-GMAW-250ipm-1.5-16ipm; b) CW-P-GMAW-250-1.5-16ipm-20%; c) CW-P-GMAW-250ipm-1.5-16ipm-60%; and d) CW-P-GMAW-250 ipm-1.5-16ipm-100%.

Figure 5.20 shows the cross-sections of the beads shown in Figure 5.18. There is no porosity, inclusions or undercuts. The penetration profile is drastically reduced with a cold wire feed rate of 100%.

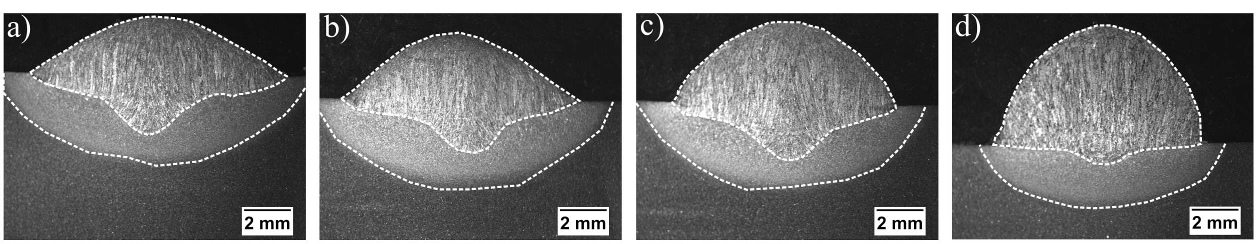

Figure 5.20: Cross-sections for high current ratio: a) P-GMAW-250ipm-1.5-16ipm; b) CW-P-GMAW-250-1.5-16ipm-20%; c) CW-P-GMAW-250 ipm-1.5-16ipm-60%; and d) CW-P-GMAW-250 ipm-1.5-16ipm-100%.

Figure 5.21 shows the cross-sections of the beads in Figure 5.19. The effect of the finger-profile is attenuated since the droplet momentum is reduced due to the small arc length as there is no change in the droplet size, as discussed earlier. However, Figure 5.21c contains a small discontinuity indicated by an arrow. This is likely a stray inclusion originating from the wire which contains a high content of Si (1.15% wt) to deoxidize the molten pool. This inclusion in unlikely to originate from the substrate surface, since the surfaces were cleaned with a wire brush and abrasive disc before welding. Apart from that observation there is no porosity or undercut observed in welds in Figure 5.21. Another factor contributing to the difference in bead profile is the lower amount of available power when low current ratios are applied, corresponding to a decreased influence of arc pressure on the centre of the welding pool.

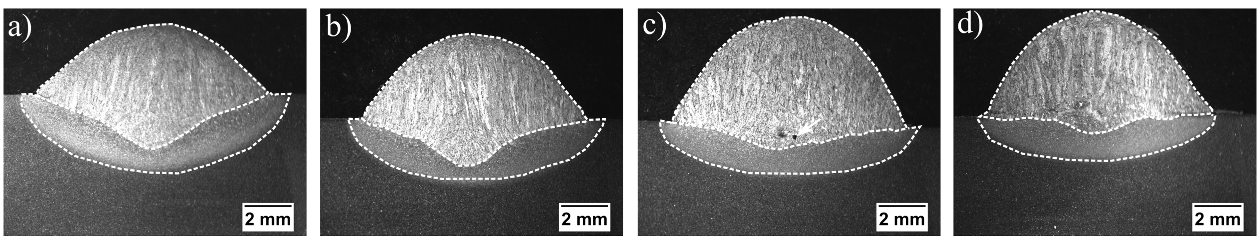

Figure 5.21: Cross-sections for conditions 1 to 4 which are high current ratio: a) P-GMAW-250ipm-1.5-16ipm; b) CW-P-GMAW-250-1.5-16ipm-20%; c) CW-P-GMAW-250 ipm-1.5-16ipm-60%; and d) CW-P-GMAW-250ipm-1.5-16ipm-100%.

Figure 5.22 presents the average penetration width, and bead height, for high and low current ratios. Bead width decreases (Figure 5.22a) for high current ratios, meanwhile, for low current ratio the width remains practically constant. This variation in bead width likely is related to the amount of latent thermal energy available in the pool.

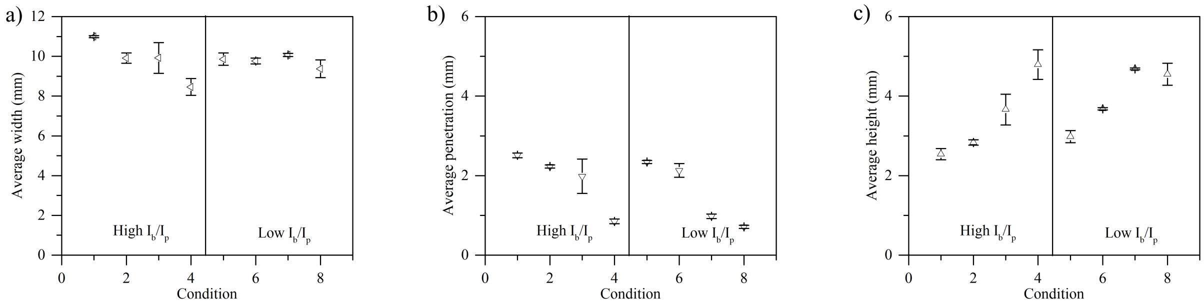

Figure 5.22: Geometric features of the weld beads with different conditions of cold wire feed rate, which can be seen at Table 5.2: a) Bead width; b) Depth of penetration; and c) Bead height. Results are the average of three cross-sections.

Figure 5.22b shows that penetration varies inversely with cold wire feed rate for both current ratio conditions. For high current ratio it is still possible to feed more wire in order to further decrease penetration, meanwhile, at low current ratios penetration depth plateaus. Coupled with the decreasing in penetration, the bead height increases (Figure 5.22c) for both current ratios as a result of the additional cold wire. The data seems to indicate that high current ratios accommodate more cold wire feed, which is not the case for low current ratios.

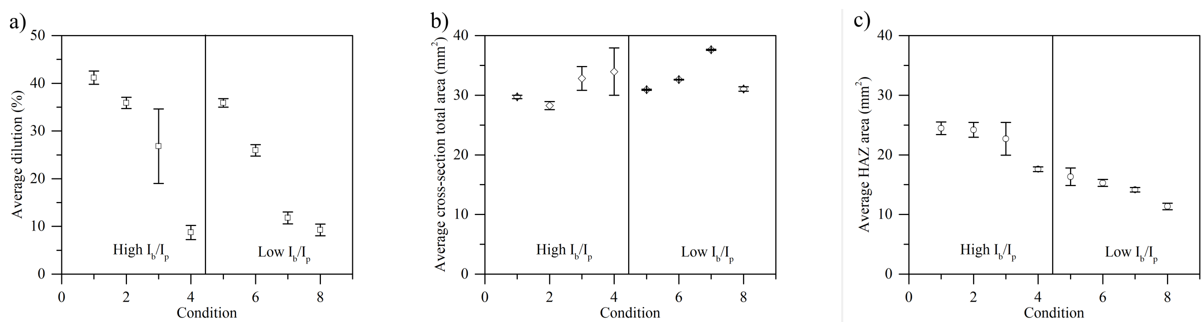

Figure 5.23: Geometric features of the weld beads with different conditions of cold wire feed rate, which can be seen at Table 5.2: a) Dilution; b) Total cross-section area; and c) HAZ area. Results are the average of three cross-sections.

Figure 5.23 summarizes the measured data from the cross-sections that are related to the heat content of the molten pool or the heat that diffused across the base metal. Figure 5.23a shows the variation of dilution with cold wire feed rate, again indicating that a limit seems to have been attained for low current ratio, which is not the case for high current ratio. Figure 5.23c outlines the heat affected zone (HAZ) area of the beads. It can be observed that with the introduction of cold wire for both current ratios, this zone decreases, indicating that the amount of heat diffused through the HAZ decreases with higher cold wire fractions. On the other hand, this seems to point to the fact that the bead top is most sensitive to the thermal distribution caused by the cold wire feed. More heat is being lost through the top of the bead than through the bottom of the bead to the base metal, as indicated by the increase in bead height.

5.4.4 Hardness and Microstructures

Figure 5.24 presents hardness maps corresponding to high current ratio conditions. The hardness of the HAZ progressively decreases with an increase in cold wire feed rate. Figure 5.24a shows that the hardness of the HAZ is higher than the base and weld metal in the region shown in yellow. Meanwhile, in Figure 5.24d shows less hardness indicating that the hardening of the HAZ was suppressed. This seems to be linked to a lower cooling rate caused by increase of cold wire feed rate. A refinement of the prior austenite grain structure in the HAZ will also suppress hardening by avoiding formation of martensite in favour of softer ferrite and bainite.

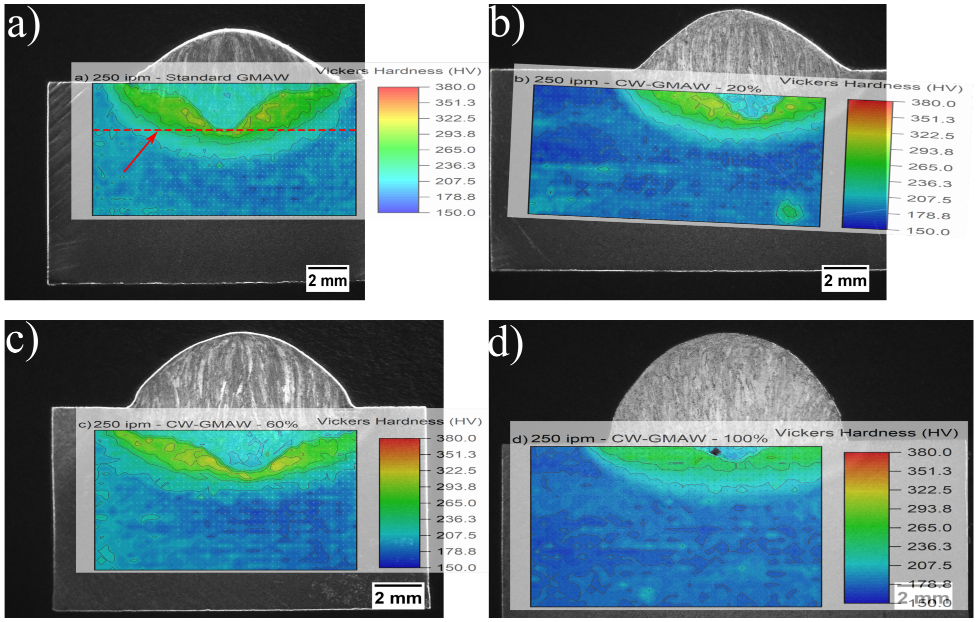

Figure 5.24: Figure 24 - Vickers hardness maps: a) P-GMAW-250ipm-1.5-16ipm; b) CW-P-GMAW-250-1.5-16ipm-20%; c) CW-P-GMAW-250 ipm-1.5-16ipm-60%; and d) CW-P-GMAW-250 ipm-1.5-16ipm-100%.

Figure 5.25 shows the hardness maps for the low current conditions. These generally exhibit the same trend, indicating a hardness reduction in the HAZ with an increasing in cold wire feed rate. However, the hardness obtained in this low current ratio is higher than that obtained in the high current ratio condition. For the highest cold wire feed rate (Figure 5.25d) the average hardness in the HAZ is 302 HV, and Figure 5.25c indicates an average hardness of 279 HV.

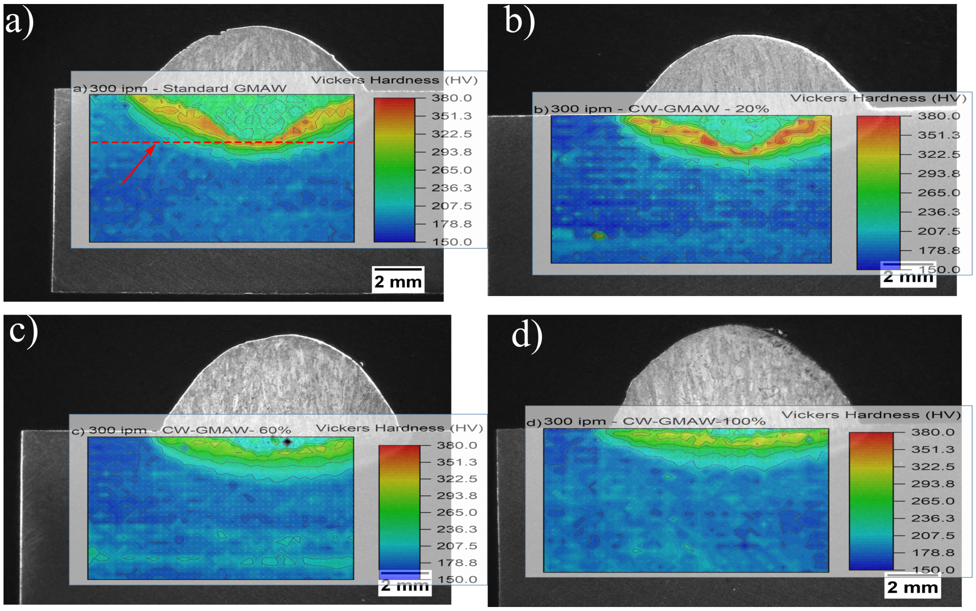

Figure 5.25: Vickers hardness maps. a) P-GMAW-300ipm-1.0-16ipm; b) CW-P-GMAW-300ipm-1.0-16ipm-20%; c) CW-P-GMAW-300ipm-1.0-16ipm-60%; and d) CW-P-GMAW-300ipm-1.0-16ipm-100%.

Figure 5.26 presents the hardness values along the closest line to the fusion zone as noted by the red dashed line in Figure 5.25. The low current ratio induces higher hardness compared to low current ratio regime. Figure 5.26a clearly shows that the increase of cold wire feed rate supresses hardening of the HAZ. However, Figure 5.26b shows that the softening of the HAZ is restricted to 60% and 100% cold wire feed rates. With a 20% feed rate there is hardening of the HAZ, which is comparable to standard P-GMAW with low a current ratio.

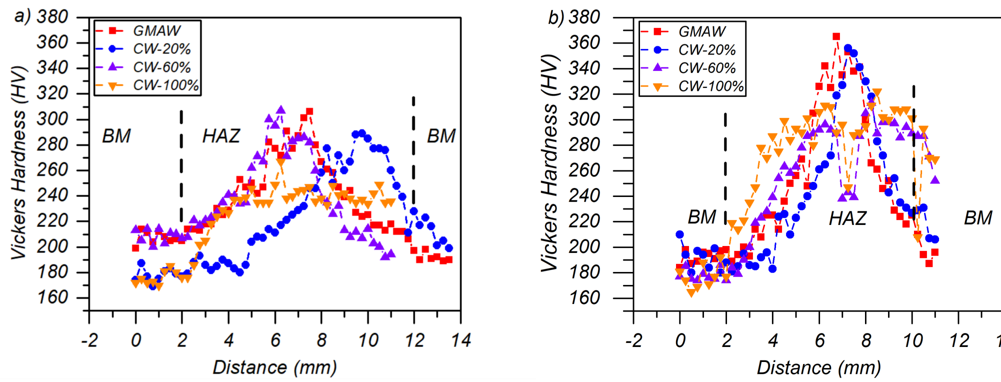

Figure 5.26: Vickers hardness of the closest line, starting at the left corner of the hardness maps, to the fusion zone: a) 250 ipm-1.5-16 ipm; and b) 300 ipm-1.0-16 ipm.

Figure 5.27 shows the microstructures in the center of the weld bead for the high current ratio condition.

The microstructures consist of grain boundary (PF (G)), intragranular ferrite (PF (I)), acicular ferrite (AF), and secondary ferrite with aligned second phase (FS (A))[87]. The width of PF(G) decreases and the AF fraction increases with an increase in cold wire feed rate.

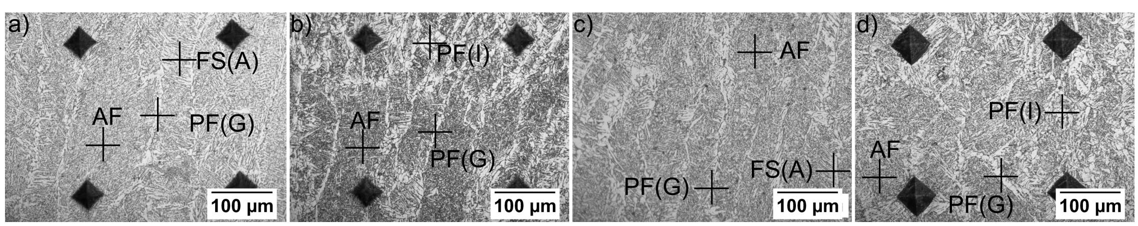

Figure 5.27: Microstructures in the center of the weld metal: a) P-GMAW-250ipm-1.5-16ipm; b) CW-P-GMAW-250-1.5-16ipm-20%; c) CW-P-GMAW-250ipm-1.5-16ipm-60%; and d) CW-P-GMAW- 250 ipm-1.5-16ipm-100%.

Figure 5.28 presents the fusion line morphology of the high current ratio condition. As the cold wire fraction increases the grains in the HAZ are refined. Figure 5.29 shows the microstructure of the center of the weld bead. This microstructure consists of the same microstructure discussed earlier, although the increase in acicular ferrite with increased cold wire feed rate is more pronounced as shown in Figure 5.29d.

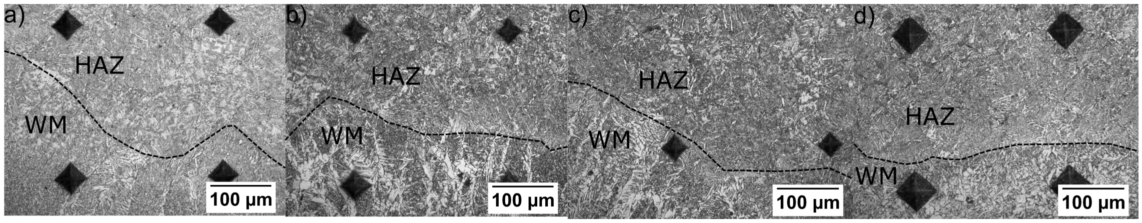

Figure 5.28: Microstructures at the fusion zone: a) P-GMAW-250ipm-1.5-16ipm; b) CW-P-GMAW-250-1.5-16ipm-20%; c) CW-P-GMAW-250ipm-1.5-16ipm-60%; and d) CW-P-GMAW-250 ipm-1.5-16ipm-100%.

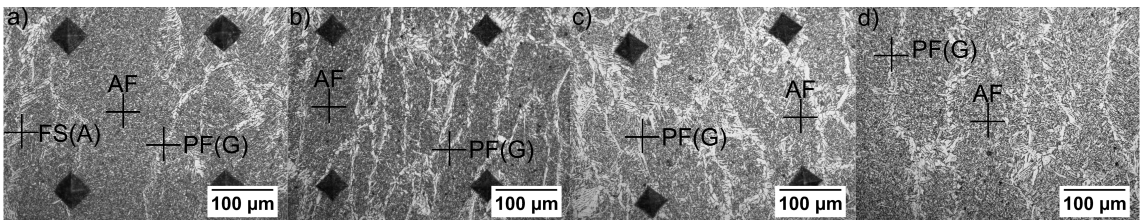

Figure 5.29: Microstructures in the center of the weld metal: a) P-GMAW-300ipm-1.0-16ipm; b) CW-P-GMAW-300ipm-1.0-16ipm-20%; c) CW-P-GMAW-300ipm-1.0-16ipm-60%; and d) CW-P-GMAW-300ipm-1.0-16ipm-100%.

Figure 5.30 shows the microstructures on the fusion zone for the low current ratio condition, again showing the same trend with increasing the cold wire feed rate. However, in contrast to the high current ratio shown in Figure 5.28, increasing in cold wire feed does not consistently soften the HAZ, but depends on other parameters, as can be seen by the difference in indent sizes. The hardness maps suggest that a 60% cold wire feed rate, shown in Figure 5.25d), leads to hardening of the HAZ compared to Figure 5.25c. In terms of microstructures the HAZ seems to consist of bainitic structures since their hardness reaches values of 340 HV for Figure 5.25a and Figure 5.25b, which reflect the microstructures in Figure 5.30a and Figure 5.30b respectively.

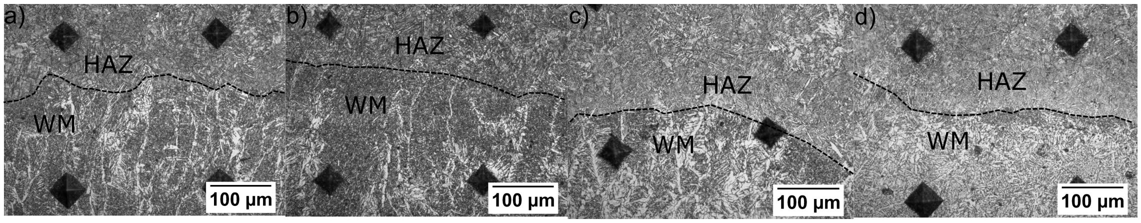

Figure 5.30: Microstructures at the fusion zone: a) P-GMAW-300ipm-1.0-16ipm; b) CW-P-GMAW-300ipm-1.0-16ipm-20%; c) CW-P-GMAW-300ipm-1.0-16ipm-60%; and d) CW-P-GMAW-300ipm-1.0-16ipm-100%.

5.5 Discussion

The mechanism through which the welding power source responds to the increase in melting rate caused by cold wire feed is very important to weld quality and efficiency. This mechanism will be henceforth be called *wire melting accommodation*. The high current ratio condition implies that high heat input is imposed. For example, for this condition the peak and background currents are approximately 460 A and 56 A, resulting in a heat input of approximately 7.60 kW. In contrast, the peak and background current for low current ratios were approximately 510 and 43 A, respectively, resulting in a heat input of approximately 5 kW. The mechanism of wire melting in each condition is different.

Since there is sufficient heat to melt the wire at high current ratios, one expects the values of peak and base current cannot be changed once pre-set, considering the internal regulation does not cause the peak time to increase. In contrast, for the low current ratio the heat input seems insufficient to accommodate the melting the extra wire, and so the internal regulation mechanism causes the peak time to increase, increasing the melting capacity of the arc. This accommodation of higher cold wire fractions causes the average current to increase, increasing the heat input to the substrate, at low current ratios.

Based on the work of Essers and Walter, the total cross-section area of the beads is an indication of the total heat content of the weld pool [88]. As expected, the high current ratio conditions present indicate a higher heat content. In contrast to what was expected from the low current ratio condition, the welded area initially increases and then decreases possibly indicating a reduction of the heat content of the weld pool when 100% of cold wire is fed with a low current ratio (low heat input).

For lower energy weld pool cold wire functions as a heat sink causing the reduction of the bead width. At higher energies the cold wire is not able to absorb higher energy fractions of the welding pool. A physical understanding of this can be obtained through an energy balance:

$$\dot{Q} = \dot{m}\left(c_p \Delta T + L\right) \tag{5.7}$$

where $\dot{Q}$ is the absorbed power in (kW), $\dot{m}$ is the cold wire feed rate in (kg/s), c_p is the specific heat (kJ/kgK), ΔT is the difference of temperature between the cold wire and the melt pool, and L is is latent heat of the weld pool (kJ/kgK). Thus, an increase in the in power entails a higher ΔT since the temperature of the melt pool is likely to increase. On the other hand, for low energy parameters (low heat input) the cold wire absorbs less energy, and so melting only has a small effect on bead width.

This *wire melting accommodation mechanism* also controls the effective current for low current ratio. The arc efficiency of P-GMAW can be written as [78]:

$$\eta_{aw} = \frac{Q_{aw}}{\left[U_{avg} I_{eff} - \psi I_{eff}\right]} \tag{5.8}$$

where Q_{aw} is the heat transmitted to the welding pool by the electric arc, ψ is the melting potential of the anode material,U_{avg} is the voltage, and I_{eff} is the effective current. Scaling Q_{aw} by the HAZ area reveals that, as the effective current increases, the efficiency of the arc decreases for low current ratios with cold wire feed ratio increase. This condition would be suitable to weld heat sensitive materials.

The microhardness and microstructures results imply changes in cooling rate caused by the cold wire feed rate. The trend of increasing AF phase fraction with the cold wire feed rate indicates a lower cooling rate that the cooling rate for a high fraction of cold wire, while high current ratios, are associated with higher heat input. However the trend differs for low current ratios which result in low heat input, so the cooling rate tends to be faster. In the last situation, the increase of cold wire causes a high cooling rate, leading to a higher hardness observed in the HAZ, along with a narrower HAZ region. Certainly these results in hardness and microstructures imply important differences in heat input, which will be the subject of further study by water calorimetry.

The results gathered in this study, for high current ratio, certainly can be compared to those reported by Mohammadijoo et al. [49] who showed that

for cold wire tandem GMAW the use of cold wire reduced the HAZ area, the HAZ microhardness, and the prior austenite grain size. However, a comparison to other process might be difficult since the CW-P-GMAW is still under study and information regarding its the gross heat input, is still lacking as well as its suitability for welding using different joint geometries and positions.

5.6 Summary

Bead-on-plated welds were deposited onto mild steel in order to study the feasibility of cold wire pulse gas metal arc welding (CW-P-GMAW) and the influence of feeding cold wire with low and high current ratios. The following conclusions can be drawn:

1. The use of cold wire feed is feasible for both low and high current ratio conditions and uniform weld beads were obtained;

2. For low current ratios the duty cycle is altered so that peak time is increased in order to melt more material. This increase in duty cycle leads to higher mean and effective currents;

3. This change in mean current entails differences in transmitted heat across the welding pool for high and low current ratios. This leads to a smaller HAZ area and dilution when using pulsed current compared to conventional GMAW;

4. The increase in cold wire feeding seems to favour the nucleation of acicular ferrite.

Chapter 6

Globular to Spray Transition in Cold Wire Gas Metal Arc Welding [1]

6.1 Overview

The electrical current required for a transition from globular-to-spray droplet transfer during gas metal arc welding (GMAW) is determined by the specified wire feed speed, in the case of constant voltage power supplies. Generally, in narrow gap welding (NGW), spray transfer is avoided, because this transfer mode can severely erode the groove sidewalls. This work compares the globular-to-spray transition mechanism in cold wire gas metal arc welding (CW-GMAW) versus standard GMAW. Synchronized high speed imaging with current and voltage sampling were used to characterize the arc dynamics for different cold wire mass feed rates. Subsequently, the droplet frequency and diameter were estimated, and the parameters for a globular-to-spray transition were assessed. The results suggest that the transition to spray occurs in CW-GMAW at a lower current than in the standard GMAW process. The reason for this difference appears linked to an enhanced magnetic pinch force, which is mainly responsible for metal transfer in higher welding current conditions.

[1]This chapter is based on the following paper: Ribeiro, R. A., Assunção, P. D. C.; Dos Santos, E. B. F.; Braga, E.M.'; and A. P. Gerlich. Submitted for publication in The welding Journal Research Supplement (2020).

6.2 Background

Understanding the phenomena controlling metal transfer in gas metal arc welding (GMAW) is fundamental to identifying the correct specifications and processes parameters used in a welding procedure. The use of incorrect parameters may impair the quality and reliability of welds in service.

While studying metal transfer, a key parameter is the critical arc current at which globular transfer transitions to spray transfer. This is presently poorly understood due to the complexity of the underlying physics. For instance, Lowke [89] proposed an equation to calculate the transition current, but this model is only applicable to welding using 100% argon shielding gas, while a wide range of welding applications uses mixed Ar-CO_2 gases or pure $_2$ shielding gas.

Moreover, the model only takes into account the steel wire diameter, the surface tension of the molten metal, and the magnetic permeability of free space. Lowke [90]subsequently extended the equation to aluminum and copper electrodes. Methong et al. [91] reported that during the transition in a binary shielding gas (argon and carbon dioxide) the metal vapour concentrates towards the edges of the arc, with increasing welding current.

Ribeiro et al. [92] reported that in cold wire gas metal arc welding (CW-GMAW) the increased cold wire feed rate leads to a significant increase in current compared to the standard GMAW when in spray transfer mode. Moreover, Ribeiro et al. [93] reported that CW-GMAW operating in spray transfer can be used to weld narrow gap welds (NGW) with no sidewall erosion, since the sidewalls are not eroded during welding as the arc is pinned preferentially to the cold wire.

The CW-GMAW process involves an increase in current when the cold wire feed rate increases,however, unlike GMAW when this occurs the area of the heat affected zone (HAZ) decreases. It is worthwhile to study the influence of this phenomenon on the globular to spray transition in order to clarify how metal transfer mechanisms differ from conventional GMAW before it can be used in practical applications. This work seeks to identify the conditions under which CW-GMAW transitions to spray transfer in comparison to GMAW using similar welding parameters.

6.3 Experimental Methodology

Bead-on-plate welds were deposited on AISI 1020 plain carbon steel with thickness of 6.35 mm (1/4 in), using a Lincoln Electric Power Wave R500 power source operating in constant voltage (CV). ER70S-6 was used as electrode wire and cold wire, with nominal diameters of 1.2 mm (0.045 in.) and 0.9 mm (0.035 in.) respectively. Table 6.1 presents the nominal chemical composition of the welding wire and the base metal. The shielding gas mixture used for all welds was Ar-15%CO_2 was used at the flow of 40 ft^3/h (19 l/h).

Table 6.1: Nominal composition of the welding wire and base metal.

Material	**Nominal chemical composition (% wt.)**						
	C	**Si**	**Mn**	**P**	**S**	**Cr**	**Fe**
AISI 1020	0.18	-	0.30	-	Max. 0.005	-	Bal.
ER70S-6	0.15	1.15	1.85	0.025	0.035	0.05	Bal.

The equipment and torch layout for welding is presented in Figure 6.1, where the cold wire feed position can be seen relative to the electrode wire and the device used to feed the auxiliary wire. During welding, the current and voltage were recorded at a frequency of 10 kHz for two seconds in order to assess the electric properties of the arc *in situ*. Moreover, synchronized high speed imaging was used to monitor the dynamic behaviour of the arc at 5000 fps for two seconds with a shutter speed of 25 microseconds, while a 900 nm $\pm$ 10 nm filter was used to visualize the arc. To determine of the welding parameters used in this study, preliminary welds were performed to identify parameters that caused the natural metal transfer to be fully-globular and fully-spray. Thereby, the transition current range from globular to spray was identified for standard gas metal arc welding (GMAW).

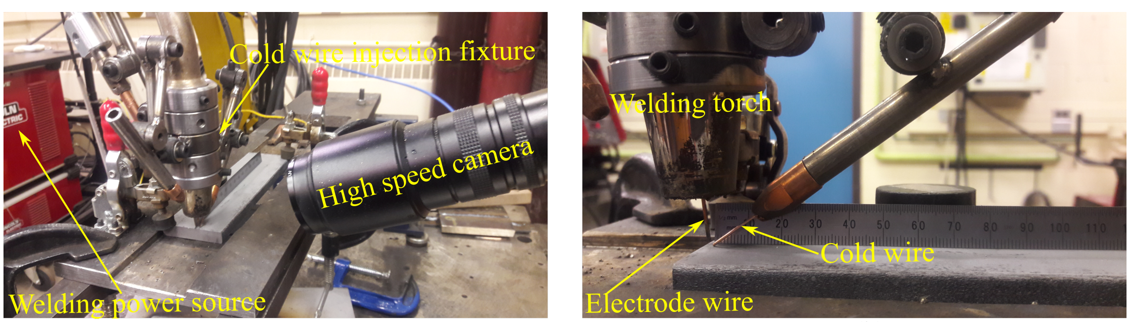

(a) (b)

Figure 6.1: General set-up for welding experiments.

Subsequently, a cold wire feed was introduced to determine if the globular-to-spray transition occurred at a different current in CW-GMAW. Table 6.2 presents the welding parameters used to determine the range of globular-to-spray transition which occur in standard GMAW, along with their response in current and voltage. It was found that the range for the transition current for GMAW is 265 A to 293 A which are shown in Table 6.2 under the mixed transfer mode (Globular + Spray).

Table 6.2: Welding parameters used to determine the globular to spray transition along with the average transition voltage and current.

Welding process	**WFS (in/min) [m/min]**	**Voltage (V)**	**Travel speed (in/min) [cm/min]**	**CTWD (mm)**	**Transfer mode observed**	**Avg. voltage (V)**	**Avg. current (A)**
GMAW	250 [6.3]	25	25 [63.5]	17	Globular	24.5	239.6
GMAW	270 [6.7]	26			Globular	25.8	242.1
GMAW	290 [7.4]	27			Globular	26.8	243.8
GMAW	310 [7.9]	28			Globular + Spray	27.8	264.9
GMAW	330 [8.4]	29			Globular + Spray	29.2	292.8
GMAW	350 [8.9]	30			Spray	29.8	

After determining the globular-to-spray transition parameters, the same parameters were used to carry out CW-GMAW, at cold wire feed rates of 20%, 80%, and 140%. These feed rates refer to mass feed rate in units of (kg/s) as a fraction of the welding electrode wire mass rate. For all the cold wire assisted welds the CTWD was kept the same (17 mm).

The images obtained using a 900 nm band-pass filter were processed in order to measure the droplet detachment frequency (Hz) manually. However, prior to the manual measurement of droplets, the fast Fourier transform (FFT) of the voltage signal was performed to estimate the droplet frequency. Due to of 2% - 12% margin of error between the manually counted and FFT estimated droplet frequency, the reported droplet frequency in this work refers to the manually counted value. Moreover, the FFT determined value of frequency cannot be statistically treated to provide the mean and variation range, since it is only one value of frequency. The droplet diameter was estimated from the detachment frequency. The droplet frequency was counted in five intervals of 0.36 seconds each, summing in total 1.8 seconds of the total 2 seconds sampled during welds. The values presented are thus the average of 5 measurements which consider approximately the whole sampled time, and the error bars represent a 95% confidence interval.

Based on droplet diameter measurements, the transition from globular to spray could be identified based on whether the droplet is smaller than 1.2 mm (the nominal electrode wire diameter). Table 6.3 presents the welding parameters for cold wire welds and the current and voltage response measured during welding. The droplet diameter was calculated from the measured values of drop detachment frequency [86]:

$$d_d = \left(\frac{WFS \cdot {d_e}^2}{40 \cdot fd} \right)^{\frac{1}{3}} \tag{6.1}$$

where d_d is the droplet diameter, WFS is the wire feed speed in units of, d_e is the diameter of the wire electrode, and f_d is droplet frequency.

Table 6.3: Welding parameters used for CW-GMA welds to investigate the globular to spray transition, along with the response in voltage and current.

Welding Process	WFS (in/min) [m/min]	CW pct. (%)	Voltage (V)	Travel speed (in/min) [cm/min]	CTWD (mm)	Average voltage (V)	Average current (A)
CW-GMAW	310 [7.8]	20	28	25 [63.5]	17	28.1	270.3
		80				28.1	274.4
		140				28.2	275.4
	330 [8.4]	20	29			29.1	279.5
		80				29.1	283.0
		140				29.1	299.1

The instantaneous arc resistance (R_i) is estimated using the values of the instantaneous voltage (U_i) and instantaneous current (I_i) according to:

$$R_i = \frac{U_i}{I_i} \tag{6.2}$$

The values of R_i are averaged over the sampled period of two seconds and will be presented in Section 6.4.4.

6.4 Results

6.4.1 Metal Transfer Dynamics

Figure 6.2 shows the oscillograms for the standard GMAW conditions used to identify the transition zone between globular and spray modes. High speed images are shown only at the transition, which occurred between 310 in/min and 350 in/min of wire feed speed, and the fully-spray condition, at 350 in/min of wire feed speed.

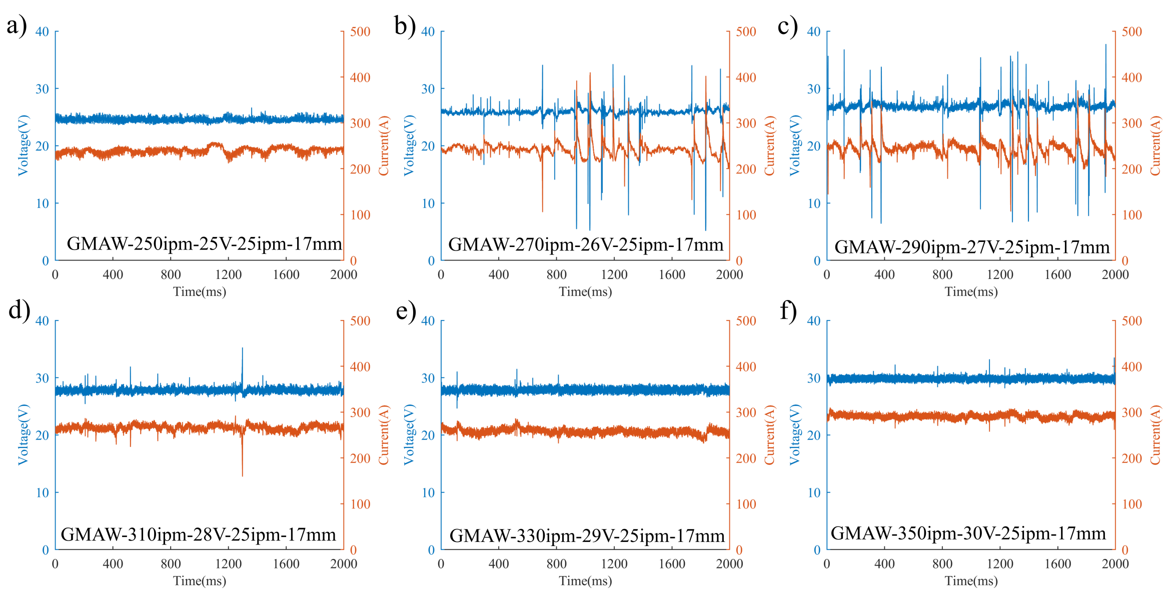

Figure 6.2: Oscillograms for standard GMAW conditions. Plot for an entire sampling period 2 seconds at 10 kHz: a)GMAW-250 in/min; b)GMAW-270 in/min; c) GMAW-290 in/min; d) GMAW-310 in/min; e) GMAW-33o in/min; f) GMAW-350 in/min.

Figure 6.3 shows representative high speed images of the two conditions in which globular-to-spray transition occurs, namely Figure 6.3(a) and Figure 6.3(b); and the fully-spray condition in Figure 6.3(c). As noted, the criterion adopted to distinguish between those was based on whether the droplet diameter is longer than the electrode diameter, corresponding to globular transfer. A droplet diameter lower than the electrode diameter, indicates a spray transfer mode. However, during transition the droplet size fluctuate lower or higher than the electrode diameter.

The conditions shown in Figure 6.2b and Figure 6.2c correspond to the transition from globular transfer mode to short-circuit, which Scotti et al. [94] described as interchangeable metal transfer (ITM). This can be ascribed to: a) a variation in specific resistivity of the arc column, and b) a higher post short-circuit current. These two features in ITM come from higher increase in wire feed speed compared to a small increase in voltage, as one can be noted from the welding parameters in this study. As soon as the energy in the arc is sufficient to sustain a spray transfer, the interchangeable transfer ceases.

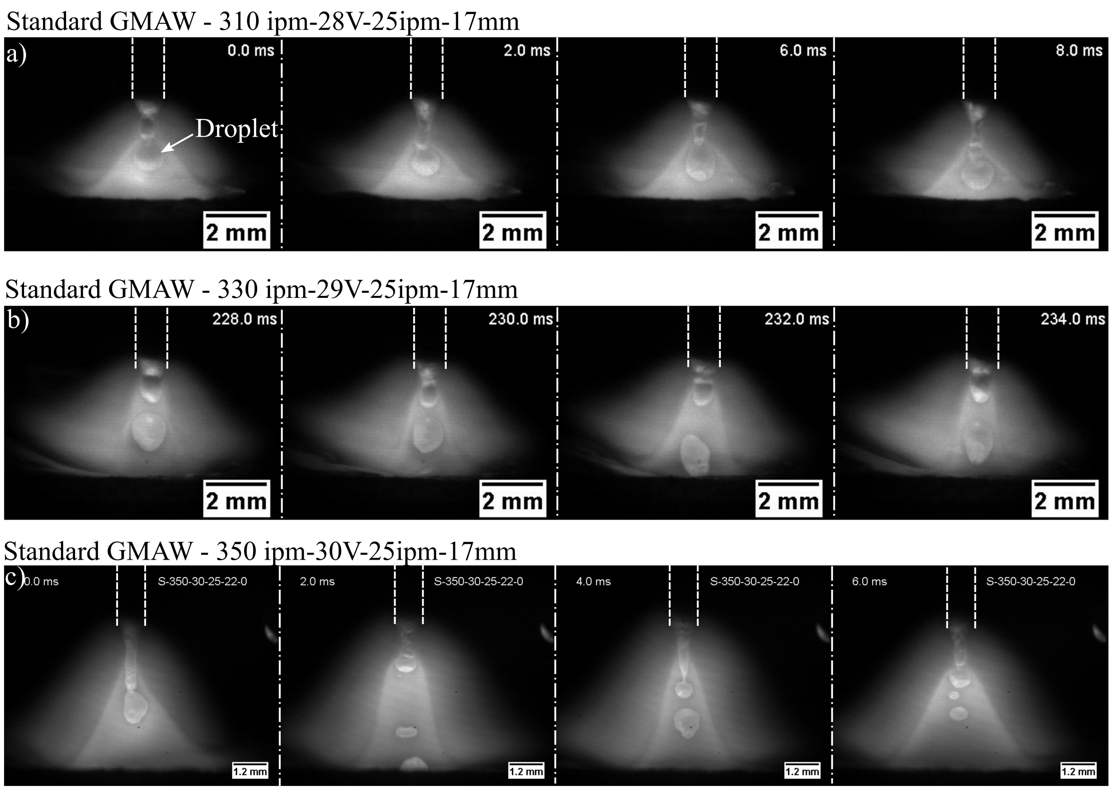

Figure 6.3: High speed images of transition from globular to spray (a) and (b), and the fully spray condition (c).

The spray transfer current in standard GMAW is on average 294.7 A, as reported in Table 6.2. Figure 6.4 shows the high speed images of the weld in the transition region with cold wire feed. The droplet size is close to the wire diameter when 20% cold wire feed rate is used (Figure 6.4a). When 80% cold wire feed rate is used (Figure 6.4b) there is an instantaneous decrease in droplet diameter, showing that the transition from globular to spray begins at this cold wire feed rate. Further increasing the cold wire feed rate leads to a full axial spray transfer mode with droplets smaller than the wire diameter. In fact, the current applied for the spray regime condition is, on average 275.4 A, which is smaller than the current for fully spray transfer for standard GMAW using the same wire feed speed and voltage.

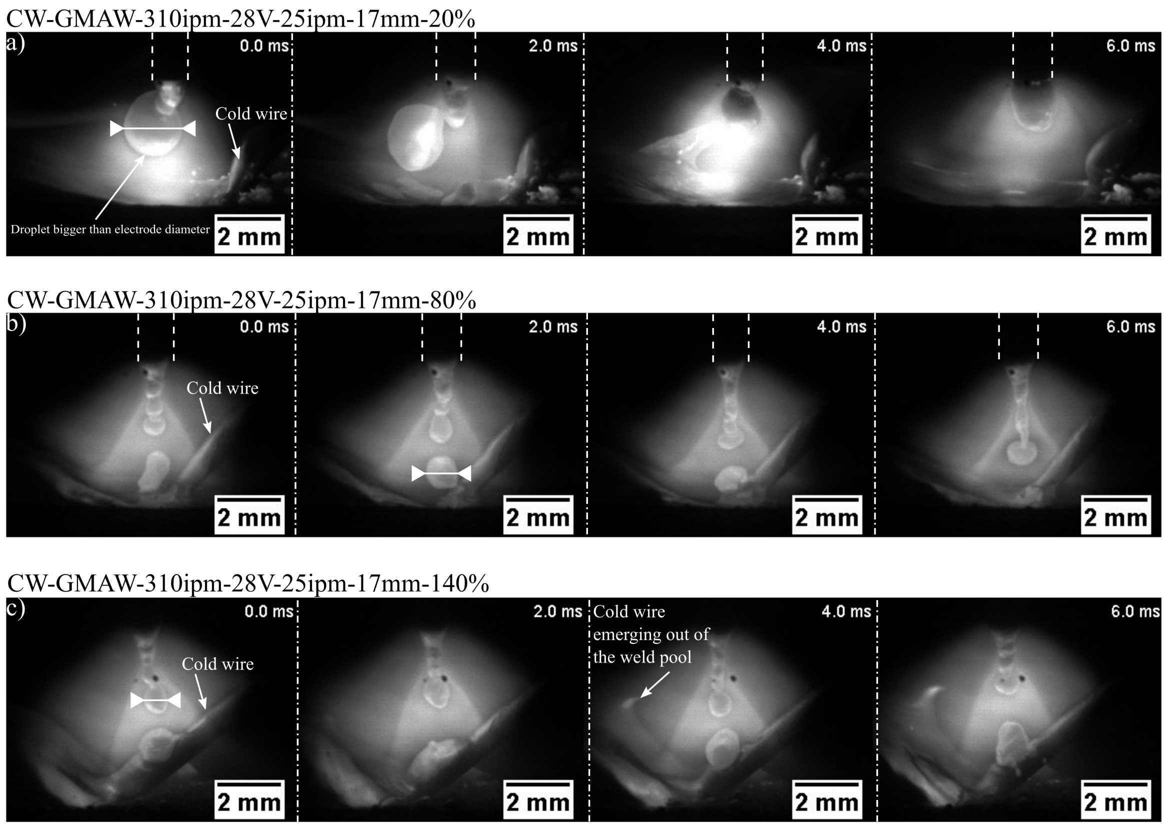

Figure 6.4: High speed images of CW-GMAW-310ipm-28V-25ipm-17mm. a) 20%, b) 80%, and c) 140%.

It is also interesting to note that when the cold wire is introduced at a feed rate of 20%, there is an instability of voltage and current signals, which is reflected in current oscillation in Figure 6.5a. When the cold wire feed is increased to 80%, causes a stabilization of the current and voltage signals as shown in Figure 6.5b.

However, cold wire feed rate at 140% an instability in the voltage and current signals is caused by the injection of more cold wire than can be accommodated by the arc. This causes part of the cold wire to emerge out of the pool and disturb the arc, cf. Figure 6.4c and Figure 6.5c. In Figure 6.5c, this disturbance is a short-circuit caused by the cold wire tip, since when this happens the voltage decreases to levels below 10 Volts.

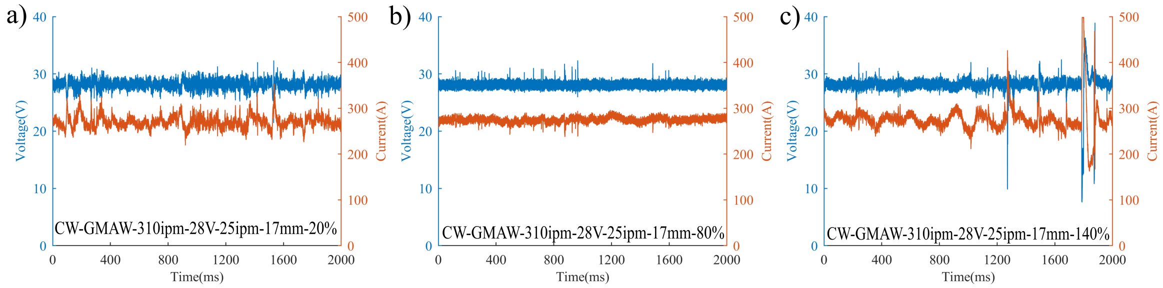

Figure 6.5: Oscillograms for CW-GMAW with WFS equal to 310 in/min with progressive values of cold wire feed rate: a) 20%; b) 80%; and c) 140%.

Figure 6.6 shows the high speed images for the CW-GMAW welds using of rate of 330 in/min. Figure 6.6a shows that when 20% cold wire feed is introduced the droplet diameter is about the size of the wire diameter, causes behaviour similar to that shown in Figure 6.5. When 80% cold wire feed rate is introduced in the arc, the droplet diameter starts to decrease to levels lower than the electrode diameter. Again, for this particular feed rate, there is an stabilization of the arc dynamics which reflects the decrease in variance of the measured signals of voltage and current. The arc is partially pinned to the cold wire, as expected when using 80% cold wire feed rate [92].

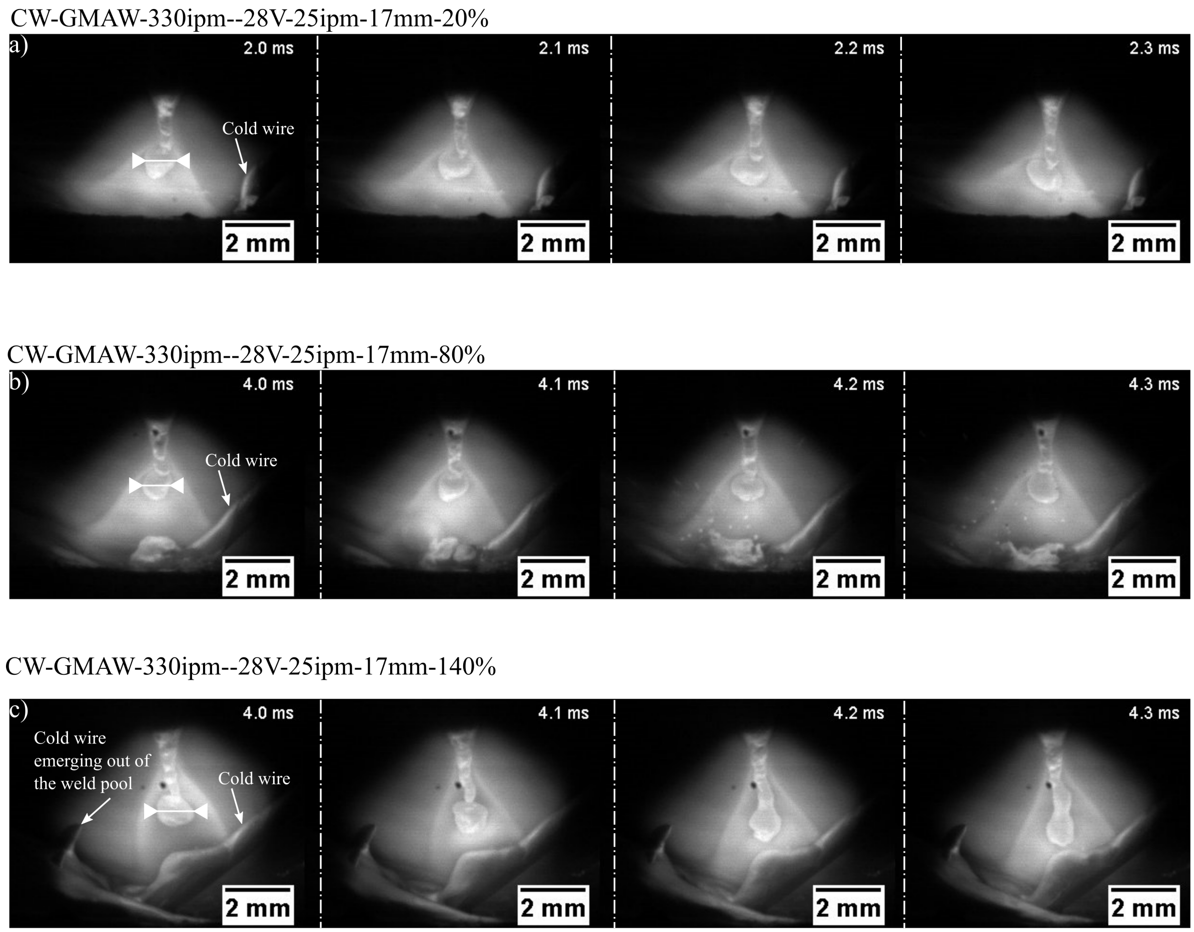

Figure 6.6: High speed images of CW-GMAW-330ipm-28V-25ipm-17mm: a) 20%; b) 80%; and c) 140%.

Further increase in the cold wire as observed in Figure 6.5c, leads to instabilities due to insufficient energy level in the arc to sustain the extra wire feed. At the cold wire fraction of (140%), part of the cold wire again emerges out of the pool. This cold wire emerging out of the pool can short-circuit the arc (refer to Figure 6.7c), causing the instantaneous values of voltage to drop to levels below 10 Volts. It can be seen that the arc is completely attached to the cold wire.

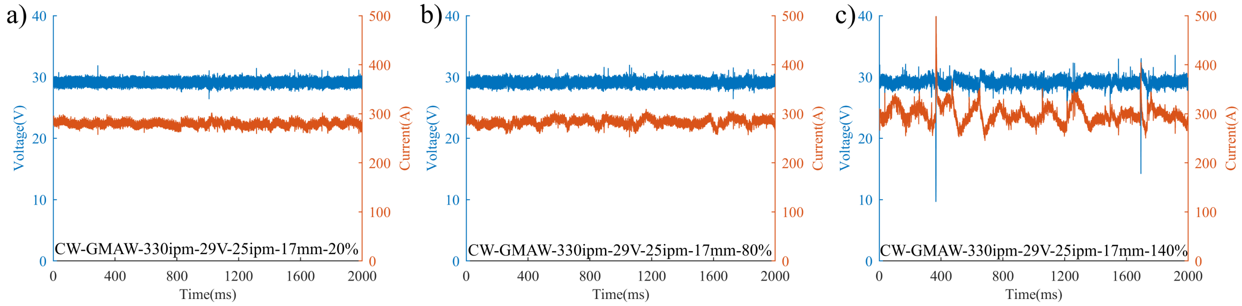

Figure 6.7: Oscillograms for CW-GMAW with WFS equal to 330 in/min with progressive values of cold wire feed rate: a) 20%; b) 80%; and c) 140%.

Figure 6.8 shows the oscillograms for 350 in/min, which is a fully axial spray transfer mode. A cold wire feed rate of 80% can be accommodated by the energy supplied by the arc so no instability can be detected. In fact, it appears that the arc stabilizes since the spread of voltage and current are reduced.

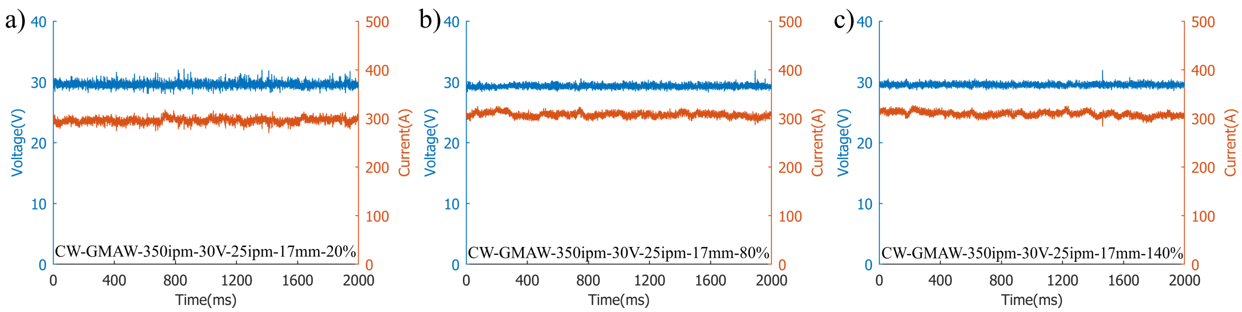

Figure 6.8: Oscillograms for CW-GMAW with WFS equal to 350 in/min with progressive values of cold wire feed rate. a) 20%; b) 80%; and c) 140%.

It is also observed that increasing the cold wire feed rate to 140% does not cause instabilities (Figure 6.8c). The transition current for spray in standard GMAW using 350 in/min is 294.7 A, cf. Table 6.2.

6.4.2 Cyclogrammes

Cyclogrammes show the voltage plotted against the current in order to elucidate the operational modes/points. during welding operation. They can be used to determinate process stability as well transfer mechanism as based on the shape of the cloud of points [72]. The experimental conditions employing 270 in/min and 290 in/min, Figure 6.9b and Figure 6.9c, respectively, present interchangeable metal transfer between spray and short-circuit which is consistent with the process results. Once this range from 270-290 in/min is exceeded the metal transfer across the arc moves develops into spray, improving stabilization as indicated by the reduction of the area in the cyclogrammes for standard GMAW.

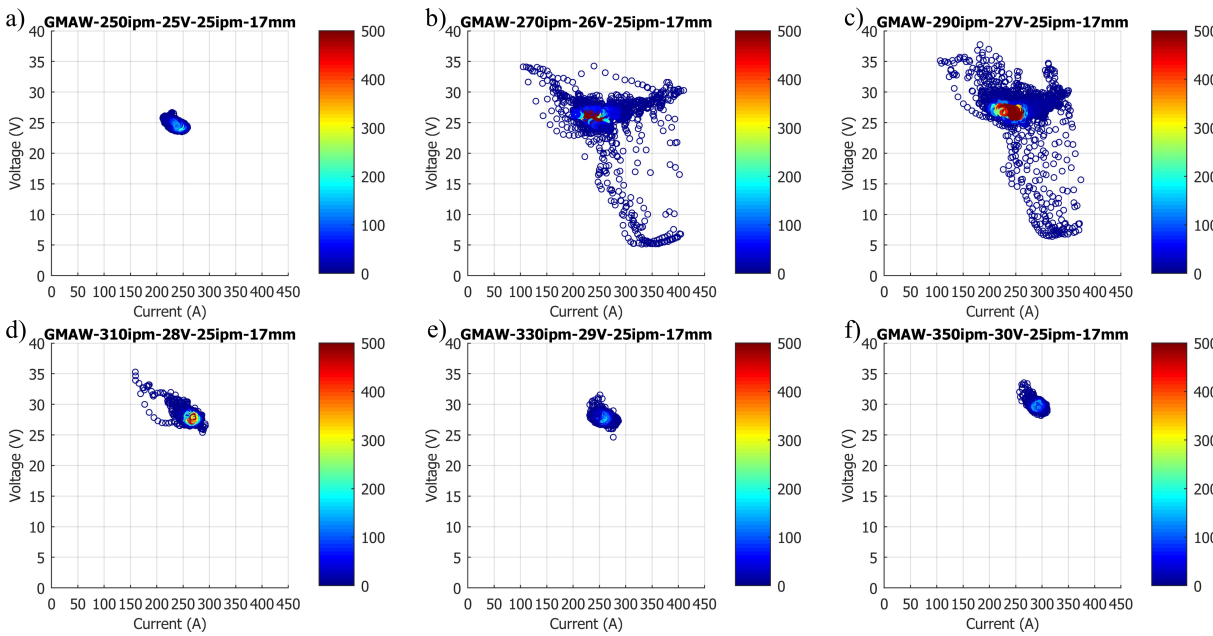

Figure 6.9: Cyclogrammes for GMAW conditions. Color bar indicates density of data points.

Figure 6.10 shows that a cold wire feed rate of 80% stabilizes the metal transfer as indicated by the reduction of the cyclogramme area in comparison to standard GMAW (Figure 6.10a). However, further increasing of the cold wire fraction leads to short-circuits, as seen in Figure 6.10c where some points fall below 10 Volts.

During unstable conditions the cluster of the points increases, as a response of the power source feedback to stabilize the welding operation, however certain points fall close to 10 Volts, experiencing short-circuit, as seen in Figure 6.10c. This attempt to stabilize voltage/current response is caused by feedback in the welding source to maintain operation at a constant voltage (CV). This mechanism serves to keep the arc close to the set-point voltage and current through inductance control which accounts for the current variation in time after a short-circuit in order to re-ignite the arc. In fact, this cluster of points could become a supplementary indication of stability of a welding process parameter in addition to the *sole area* of the cyclogramme which represents the total area formed by points in a cyclogramme irrespective of the cluster occurrence [71].

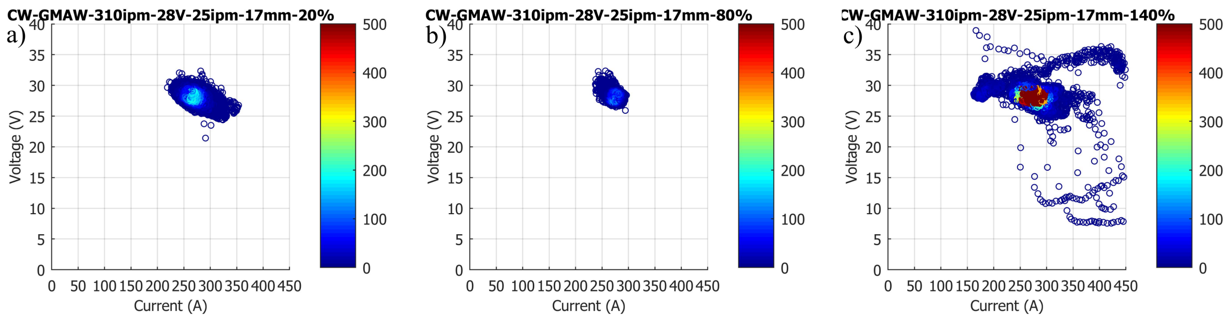

Figure 6.10: Cyclogrammes for CW-GMAW conditions using $WFS = 310in/min$. Color bar indicates density of data points.

Figure 6.11 shows cyclogrammes for the 330 in/min condition. A 20% cold wire feed rate stabilizes of the welding based on the reduced area of the cyclogramme, Figure 6.11a, compared to Figure 6.9e. Inversely the cold wire feed rate of 80% (Figure 6.11b)causes a small increase that can considered within the stability limits. However, at a 140% cold wire feed rate the welding, the stability is compromised by the short-circuit events caused the cold wire contact with droplets still hanging on the electrode wire.

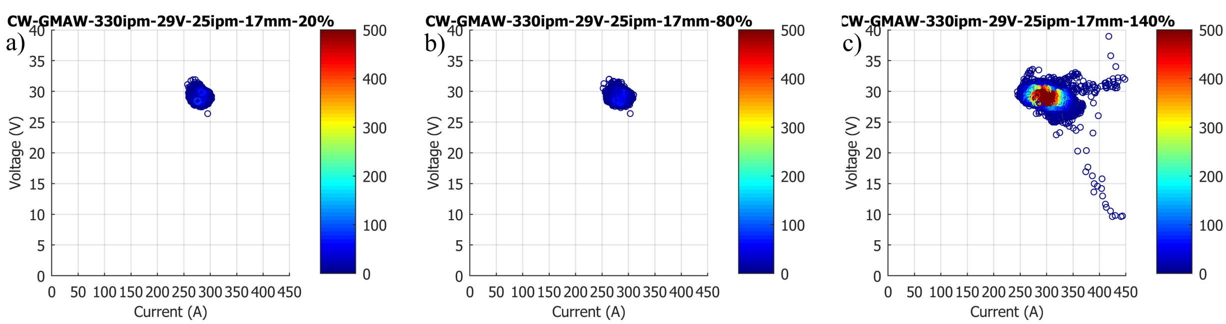

Figure 6.11: Cyclogrammes for CW-GMAW conditions using WFS of 330 in/min. Color bar indicates density of data points.

At a cold wire feed rate of 140% the cluster of points increases as a result of the power source feedback system which attempts to stabilize the arc after short-circuits. Figure 6.12

shows the cyclogrammes for the 350 in/min condition, which corresponds to fully developed spray mode. When 20% cold wire feed rate is used there is a reduction of the cyclogramme area, as can be seen comparing Figure 6.12a to Figure 6.9e. The reduction of area is most pronounced when higher cold wire fractions are used, for instance, 80% and 140%.

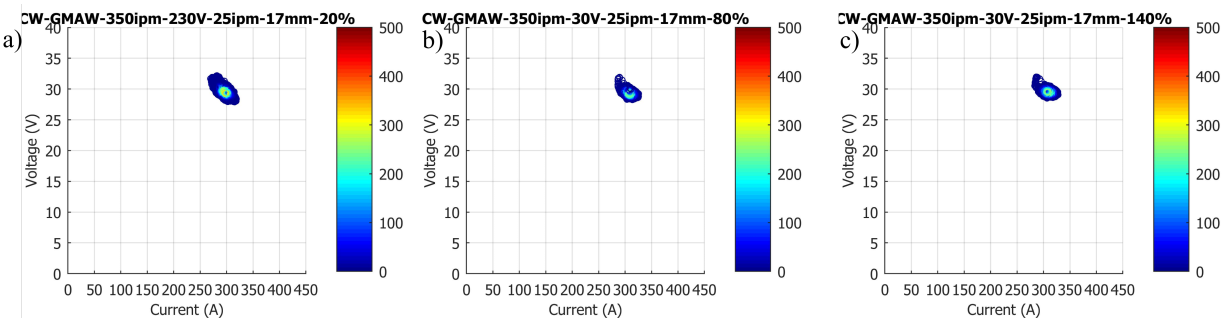

Figure 6.12: Cyclogrammes for CW-GMAW conditions using WFS of 330 in/min. Color bar indicates density of data points.

In contrast to the previous situations, the increase of the density of data points in Figure 6.12 is not related to instabilities in the electric arc or short-circuits caused by the cold wire emerging out of the weld pool. Rather, this is due to a higher stabilization of the welding process with the progressive stabilization of the arc due to arc pinning to the cold wire when the cold wire feed rates increase provided there is enough energy in the melt pool to melt this extra wire.

6.4.3 Droplet Frequency And Diameter

The frequency of the droplets and their estimated diameter are presented in Figure 6.13. Figure 6.13a and Figure 6.13b show the droplet frequency for 310 in/min condition. Introducing the cold wire increases the droplet frequency. Though specifically for Figure 6.13a, the droplet frequency appears unaltered in comparison to the standard GMAW, given the limits of variation represented by the confidence level at 95%. The current for fully-developed spray at 350 in/min is 295 A.

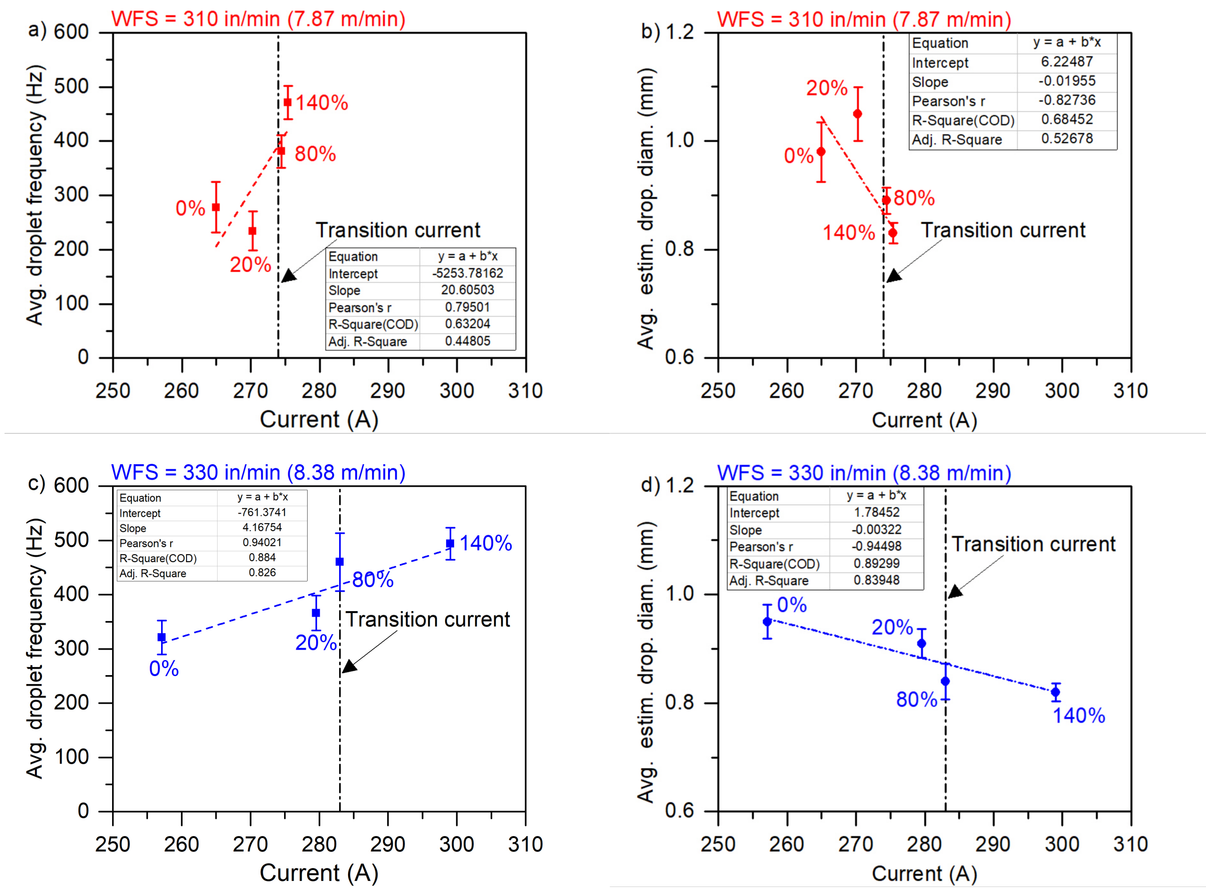

Figure 6.13: Average droplet frequency and estimated average droplet diameter. Error bars represent 95% confidence intervals. The 0% condition indicates the standard GMAW.

The increase in detachment frequency, corresponds to a decrease in droplet diameter which is caused by the increase in the tapering Lorentz force, which varies directly with the current[20]. Figure 6.13b shows that the trend in droplet detachment frequency (Figure 6.13a) is maintained with the droplet starting to undergo the spray condition at an 80% cold wire feed rate. This phenomenon is due to the increase in current to melt the extra wire introduced in the arc. At a cold wire feed rate of 80% the transition to spray occurs in much lower current than fully spray condition as reported in Section 6.4.1.

Figure 6.13c and Figure 6.13d show the droplet frequency and the droplet diameter respectively for 330 in/min. Similarly to the case described in the previous paragraph the transition for spray starts again at 80% cold wire feed rate, in which the error bars indicate that the droplet frequency is higher than the droplet frequency of reference. Using a WFS value of 330 in/min, the transition to spray is more gradual than when using a WFS of 310 in/min. Similarly,the transition to spray starts at a cold wire feed rate of 80% when compared to the reference level, cf. Figure 6.13c and Figure 6.13d. The reason for the difference in the slope behaviour of these two cases remains unclear, and is worthy of future study.

6.4.4 Average Resistance Of The Arc Plasma

Figure 6.14 presents the arc resistance for the welds using 310 in/min, 330 in/min, and 350 in/min wire feed speed. The arc resistance was estimated using Equation 6.2 as described in the methodology. Valensi et al.[95] reported that,in the transition from globular to spray the conductivity of the plasma column increases due the metal vapour generation rate increase. The conductivity varies inversely with the resistance of the arc column. Then, an increase in conductivity will represent a decrease in the plasma column resistance.

The resistance of the plasma column in a fully developed spray condition (350 in/min) is equal to 0.1028Ω (Figure 6.14c). Comparing the resistance for the conditions of 310 in/min and 330 in/min to this standard value one can expect the resistance limit to allow a fully spray transfer for the conditions mapped out in this work. According to Figure 6.14a the resistance for 80% is 0.1025 Ω which is lower than the reported value for spray using 350 in/min. Also, according to Figure 6.14b the resistance for an 80% feed rate is 0.1030 Ω, which is close to the value reported in Figure 6.14a. This indicates the results of arc resistance are consistent with the droplet frequency measurements. For the CW-GMAW conditions in which the WFS is 310 in/min and 330 in/min, the transition to spray suddenly occurs at an 80% cold wire feed rate, with arc current values of 274.42 A and 283.01 respectively, as indicated in Table 6.3. These currents are inferior to the average current of 294.65 A, reported in Table 6.2, for a fully spray regime transfer in standard GMAW.

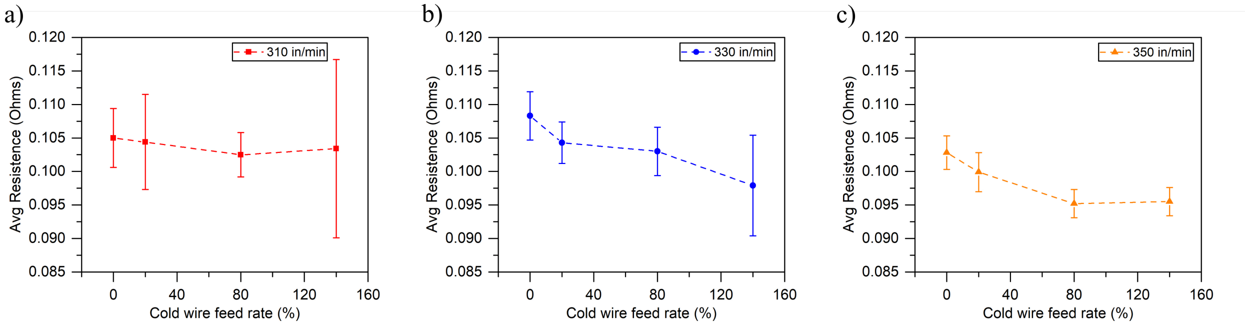

Figure 6.14: Arc resistance values based on instantaneous values of current and voltage, for three distinct conditions: a) 310 in/min; b) 330 in/min; and c) 350 in/min. Error bars show at 95% level confidence interval.

The size of the variation around the average arc resistance at 140% in Figure 6.14a and Figure 6.14b is due to the short-circuit (disturbances) caused by the excessive amount of cold wire in the arc. The arc resistance plots indicate that increasing the cold wire fraction leads to the pining of the electric arc to the cold wire for high cold wire fractions ($\geq$ 100%), provided that there is enough energy to accommodate this high cold wire fraction. When there is enough energy to melt the cold wire (using 350 in/min as electrode wire rate) the resistance variation is lower than in the standard GMAW for 80% and 140% cold wire feed rates. as can be see in (Figure 6.14c). The decrease of the resistance indicates an improvement in arc conductivity, which accounts for stability and an increase in current, leading to higher values of detachment force from the self-induced magnetic field.

6.5 Discussion

6.5.1 Metal Transfer And Globular-to-spray Transfer Mechanism In CW-GMAW

There are two theories that could explain the phenomena of metal transfer in welding: the static balance force theory (SBFT) by Waszink and Graat [96], and the pinch instability theory (PIT) proposed by Allum [97, 98]. The SBFT acutely predicts the droplet diameter in globular transfer mode, while the PIT performs better in spray transfer. However, neither can predict the globular-to-spray transfer current. Recently Zhao and Chung [99] reported that the phase field method can approximate the globular-to-spray transition current, along with the droplet sizes in the transition regime.

During metal transfer droplets are subjected to three forces: a) electromagnetic force (F_{em}); gravitational force (F_g); and surface tension force (F_s). In this analysis the viscous drag force of the plasma and the arc pressure are disregarded since they account for only 10% of (F_s) according to Waszink and Graat [96]. In globular transfer droplet detachment is governed by (F_g) since the droplet diameter is large, while in spray, detachment is governed by the electromagnetic force (F_{em}).

The mechanism of hastening the onset of the globular-to-spray transfer in CW-GMAW is related to the current increase caused by higher total wire feed – (both electrode and cold wire feed rate) – applied in CW-GMAW. This mechanism is similar to the one proposed by Kim and Eagar [20]. The total power delivered to the anode $\left(\dot{Q}_{total}\right)$ can be written as:

$$\dot{Q}_{total} = \left(\frac{3}{2}kT/e + V_a + \phi\right) I + \left(\frac{\bar{\rho L}}{A} I^2\right) \tag{6.3}$$

where k is is the Boltzmann constant, T is the electron temperature, e is the electron charge, V_a is the anode voltage drop, ϕ is the work function of the electrode material, $\bar{\rho}$ is the average resistivity of the electrode material, L is the electrode extension, A is the cross-sectional area of the electrode, I is the welding current. The first parenthesis is the power imparted by the electron condensation while the second parenthesis is the power due to Joule effect. The total wire feed in CW-GMAW causes the Joule power to increase, acting similar to an increase in electrode extension. Thus the electrode melting occurs at reduced arc currents in CW-GMAW compared to standard GMAW, leading to electrode tapering at lower currents compared to standard GMAW. From the SBFT theory the only holding force in the electrode droplet is the surface tension (F_s):

$$F_s = \pi d_e \gamma \tag{6.4}$$

where d_e is the electrode diameter, and γ is the surface tension coefficient of the molten electrode. Thus as tapering of the electrode proceeds, d_e decreases and, consequently F_s decreases as well which cause smaller droplets to be formed, accounting for the sooner globular-to-spray transition in CW-GMAW.

6.5.2 Arc stability And Arc Resistance

The methodology proposed to assess arc stability using the cyclogrammes in Section 6.4.2 uses: a) the area of the cyclogramme; and b) the cluster of points in the cyclogramme.

These two features are complementary, in the sense that when the welding operation is stable the area of the cyclogramme decreases along with the cluster of points, cf. Figure 6.9a, Figure 6.9e, and Figure 6.9f for standard GMAW. When the cold wire feed rate reaches 80% the stability in CW-GMAW is comparable to the standard GMAW, cf. Figure 6.11b and Figure 6.12b. The increase in density of points, observed for instance in Figure 6.10c and Figure 6.11c, are caused by the feedback mechanism in the attempt welding power source to maintain the instantaneous voltage/current near the values of current and voltage set before the welding operation.

The transition to spray transfer is accompanied by a reduction in resistance (increase of conductivity) of the arc column as shown in Figure 6.14. This mechanism is likely due to higher ionization caused by the increase in metal vapour (from electrode and cold wire derived). Lancaster [10] reported that in iron or steel arcs the ionization is due to small amounts of metal vapour originating from the electrode. The introduction of cold wire causes a reduction in CTWD resistance, which is the sum of electrode extension resistance and arc resistance [100]. This decrease in arc resistance likely facilitates the flow of charge inside the arc. This facilitation in current flow likely increases the current density, which might explain why the electromagnetic force becomes increasingly dominant with additional cold wire feeding [101].

6.6 Summary

Standard and cold wire GMAW welds at constant voltage were performed to identify the current at which the transfer mode transitions from globular to spray. The transition to spray was studied using high speed imaging and high frequency sampling electrical signals. The following conclusions can be reached:

1. The transition from globular to spray in cold wire GMAW occurs at lower currents when compared to standard GMAW for the same process parameters;

2. The transition from globular-to-spray occurs due to increase in current with the increase of cold wire feed rates which leads to an increase in tapering of the electrode by electron condensation which reduces the surface tension force (only droplet holding force);

3. The resistance of arc plasma column seems to decrease with the increase of cold wire feed rates, which accounts for an increase in current. This is probably due to higher metal vapour fraction generated by the cold wire.

Chapter 7

Uncertainty analysis of a water–flow calorimeter while welding in short-circuit and spray transfer regimes [1]

7.1 Overview

The thermal efficiency of arc welding influences the cooling rate, peak temperature, and microstructures of a weld, which affects the material properties of the welded joint. This work quantifies the uncertainty of thermal efficiency measurements on gas metal arc welds using low (2.5 kW) and high (9.5 kW) arc powers. In order to understand the effect of calorimeter parameters on the measured efficiency, a two factor, two level full factorial design was carried out for each arc power condition. In this study, the factors are flow rate (2 l/min and 5 l/min) and plate thickness (0.25 in [6.35 mm] and 0.375 in [9.53 mm]). The results show that the uncertainty in the thermal efficiency measurements increases when both higher flow rates and plate thickness are used. Moreover, the use of a thick plate causes the heat transfer regime to change, increasing the cooling rate and decreasing the observed thermal efficiency. Uncertainty is also influenced by the metal transfer mode during welding.

[1] This chapter is based on the following paper: Ribeiro, R. A.; Assunção, P. D. C; Dos Santos, E. B. F.; Daun, K.J.; and Gerlich, A. P. Welding in the World (2020). url: https://link.springer.com/article/10.1007/s40194-020-00931-1

7.2 Background

Recently Scotti highlighted the importance of improving the accuracy [2] of thermal efficiency estimates in gas metal arc welding (GMAW) [104]. Attempts to improve the robustness of GMAW thermal efficiency estimates have focused on both calorimeter design and experimental techniques. For instance, Liskevych and Scotti proposed the gross heat input (GHI) concept, in which the amount of heat generated by a welding process, measured using a liquid nitrogen calorimeter[29], asymptotically reaches a limit when the weld bead length becomes infinitesimal. They also analyzed the intrinsic errors in this calorimetry approach [6], including the time elapsed between welding and immersing the weld in liquid nitrogen. Pepe et al. [105] used this method to report the thermal efficiency of waveform control as being 85%.

Haelsig, Kusch, and Mayr proposed a new water calorimeter model, and used it to show that weld thermal efficiency can be increased by increasing the carbon dioxide content in the shielding gas[106], increasing the voltage[30]. Prior research by the same authors reported that process derivatives of GMAW such as tandem GMAW have distinct thermal efficiencies, which depends on wire feed speed (WFS)[107]. For instance, the thermal efficiency of standard GMAW is higher than its pulsed GMAW for a fixed wire feed speed of 3.5 m/min and subsequent research indicated that efficiency is also affected by the geometry of the weld joint [108].

Other studies account for the effect of calorimeter variables on thermal efficiency. For instance, Hurtig et al. [109] reported that in a water-cooled stationary anode calorimeter, variations in voltage and water flow propagate into a standard deviation of $\pm$ 9% in the reported efficiency.

These results show that the inferred welding process thermal efficiency is affected not only by process parameters, but also by the calorimeter design, and its operating parameters. However, a study of the calorimeter measurements based on an uncertainty analysis standard such as PTC 19.1-2018[103] is not currently available.

The goal of the present study is to assess the uncertainty in the calorimeter measurements, and the inferred/apparent thermal efficiency of standard constant voltage GMAW over a range of nominal arc powers, while varying the plate thickness and water flow rate on the calorimeter. The results show that increasing the plate thickness and water flow reduces

[2] The international vocabulary of metrology (VIM)[102] defines accuracy as the closeness between a measurand (the quantity to be measured) and its true value. On the other hand, uncertainty is a non-negative parameter which characterizes the dispersion attributed to a measurand [102]. In summary, the error limits within which the true value of the measurand lies [103].

the measured thermal efficiency, and the uncertainty is higher for low arc power compared to high arc power using a water-flow calorimeter.

7.3 Experimental Methodology

7.3.1 Calorimeter System

The calorimeter system consists of the calorimeter block, the torch electrical signal measurement system, thermocouples to measure the water temperature, and a rotameter to measure the water flow rate. Figure 7.1 shows the calorimeter block, consisting of a 200 $mm \times 127$ $mm \times 40$ $mm\,(8$ $in \times 5$ $in \times 1.5$ $in)$ AISI 1020 steel block with a water cooling channel. The channel geometry is designed to enhance water mixing in the inlet, middle, and outlet regions of the calorimeter in order to maximize heat transfer. The specimens were sealed against water leaks using a rubber gasket mounted on the edges of the calorimeter block in contact with the workpiece. Moreover the specimens were held using a fixture shown in Figure 7.1b. The calorimeter was mounted on a Teflon plate to insulate it from the fixture used to hold the plate during welding. The water hoses connected to the calorimeter were made of rubber to minimize heat losses, and had a thickness of 3.2 mm.

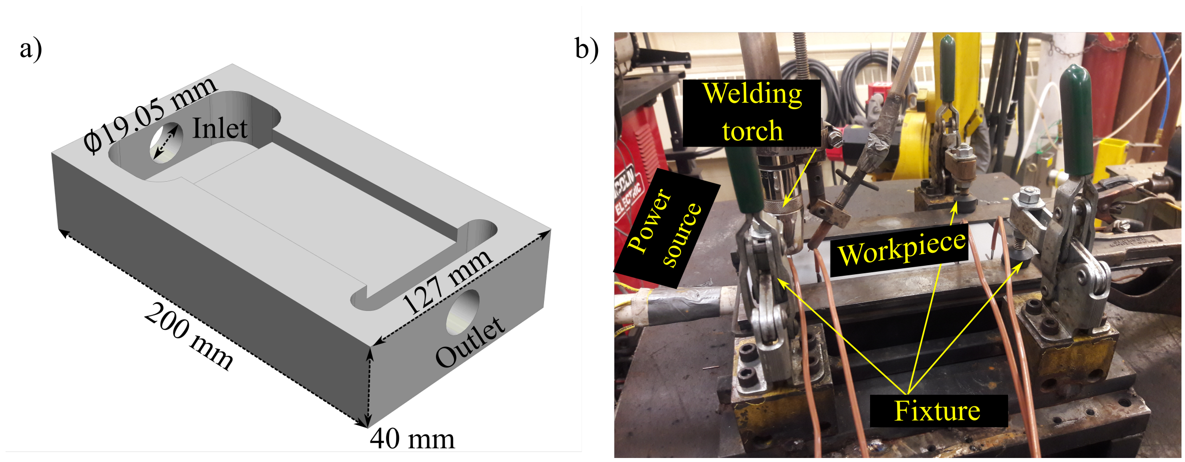

Figure 7.1: Calorimeter schematic and general experimental set-up.

The torch electrical measurements were performed using a LEM LT505-S current sensor, and a LEM LV100-100 voltage sensor, both acquired using an NI DAQ 6061 device. The current and voltage signals were acquired for a total of 2 seconds at a frequency of 10 kHz. Voltage was measured between the welding torch and the workpiece on the calorimeter, and current was measured using a Hall-effect sensor put around the ground cable. Water temperature was measured using eight 0.8 mm-diameter K-type thermocouples at a sample frequency of 5 Hz. Four thermocouples were put in the water inlet and four in the water outlet pipes to measure the water temperature. The water flow rate was measured using a turbine meter (Omega FTB 604B).

7.3.2 Welding Parameters

The calorimeter was evaluated using two welding parameters: a low arc power parameter operating in short-circuit transfer mode, and a high arc power to induce spray transfer mode. The welding surfaces consisted of AISI 1020 steel plates with different thicknesses: a thin plate of 6.35 mm (0.25 in), and a thicker plate of 9.53 mm (3/8 in). A carbon steel wire electrode (ER70S-6) with a diameter of 1.2 mm (0.045 in) was used for all welds, with Ar-15%CO_2 shielding gas at a flow of 15 l/min (32 cfh).

The welding power source was a Lincoln R500 with a Fanuc ArcMate 120i robotic manipulator. An ABIROB A 500 ECO (air cooled) welding torch was used for the welds and was kept at 90° to the workpiece. Table 7.1 provides the welding parameters used during calibration of the calorimeter as well the references for the previously reported thermal efficiency values from other studies. Preliminary experiments were performed to verify the arc stability obtained using the weld parameters for both short-circuit and spray transfer regimes, at travel speeds in the lower ranges of those typical of heavier section welding.

The travel speed chosen for the short-circuit mode was found to provide a stable arc while avoiding excessive formation of spatter. The arc power settings are typical values which would be commonly used in short-circuit and spray transfer modes. Moreover, the values presented in Table 7.1 are close to the lower end of the range of 75%-93% of thermal efficiency values for GMAW welding with CO_2 shielding gas reported by Grong [110] which indicates that the values of efficiency in Table 7.1 are close to the expected values of thermal efficiency for the experimental conditions studied in this work.

It is important to note that if a different calorimeter was used in the experiments, the values of thermal efficiency measured would be different from those reported in this work. Even for the same type of calorimeter, the results reported here are not exactly equal those reported in the literature. In fact, the values taken from the literature remain close the limit of variation of the thermal efficiency reported here.

It must be noted that the thermal efficiency values measured using a particular calorimeter do not represent the true efficiency of a welding process, but only the efficiency measured using this particular instrument. In order to determine a value of thermal efficiency that would be independent of the instrument and welding parameters used, another methodology must be used. For instance, the approach reported by Liskevych and Scotti [29].

Table 7.1: Welding parameters for calorimetry uncertainty experiments.

Cond.	**WFS (in/min) [m/min]**	**Voltage (V)**	**Travel speed (in/min) [cm/min]**	**CTWD (mm)**	**Power (kW)**	**Transfer mode regime**	**Thermal efficiency reported in the literature (%)**
Low arc power	118 [3]	19	12 [30]	17	2.5	Short-circuit	72 [111]
High arc power	394 [10]	30	27 [70]	17	2.5	Spray	70 [106]

7.3.3 Thermal Efficiency Calculations

In order to calculate the welding thermal efficiency, the experiment is assumed to have reached steady state, according to the methodology proposed by Sikstrom[112]. Thermal efficiency is given by define welding thermal efficiency as[113]:

$$\eta = \frac{c_p \bar{\dot{m}} \int_0^{t_{weld}} \left(\bar{\Delta T}\right) dt}{P t_{weld}} \tag{7.1}$$

where $c_p = 4.184 kJ/(kg \cdot K)$ is the specific heat of water at 290 K [114], $\bar{\dot{m}}$ is the average flow rate, the instantaneous flow rate is $\bar{\dot{m}} = \forall(t) \cdot \rho$, where $\dot{\forall}$ is the instantaneous volumetric flow indicated by the rotameter and ρ is the density of water at 290 K ($998 kg/m^3$) [114], $\Delta T = T_{out} - T_{in}$ is the difference between the water outlet (T_{out}) and the inlet temperatures (T_{in}), (t_{weld}) is the welding time. For the uncertainty analysis U (average voltage) and I (average current)were calculated independently in order to derive the sensitivities. However, for the thermal efficiency calculations using Equation 7.1, the average power (P) was calculated as [115]:

$$P = \langle Ui \cdot I_i \rangle \tag{7.2}$$

This analysis does not directly indicate how the heat losses (spatter, heat radiated away from the electric arc, weld pool evaporation, and heat lost from the weld bead) may impact the thermal efficiency, but is accommodated for the uncertainty analysis. However, based on the literature it is expected that the heat losses account for 11.5% to 20% of the thermal efficiency values. Liskevich et al. [6] reported that heat losses can significantly affect the thermal efficiency through variation in plate thickness and weld bead length. For instance, for short-circuit conditions (GMAW, 150 A, 20 V, 34 cm/min, Ar-25%CO_2, at the flow of 14 l/min using a 1.2 mm AWS ER70S-6 wire) the losses can be up to 11.5% [6].

Moreover, Radaj [116] indicated losses of around 20% for GMAW operating in an open arc (non-submerged) condition with a metal electrode, at currents and voltages lower or equal to 250 A and 25 V respectively. Of these losses, 5% is due to spatter. Additionally, increasing the bead height will increase losses through radiation and convection at the bead top. In the case of GMAW, losses through convection, weld pool evaporation, and spatter are considered to be lower than the losses through radiation[117].

7.3.4 Uncertainty Analysis

In the context of uncertainty analysis, Equation 7.1 is called the 'reduction equation' since it reduces the observed data into a derived parameter, in this case, the welding thermal efficiency. Hence it can be re-written as:

$$\eta = \frac{c_p \bar{\dot{m}} \bar{\Delta T}}{UI} \tag{7.3}$$

where $\left(\bar{\Delta T}\right)$ is by definition the average temperature difference over the interval $[0, t_{weld}]$. The sensitivities are calculated as:

$$\frac{\partial \eta}{\partial \dot{m}} = \frac{c_p \bar{\Delta T}}{UI} \tag{7.4}$$

$$\frac{\partial \eta}{\partial c_p} = \frac{\bar{\dot{m}} \bar{\Delta T}}{UI} \tag{7.5}$$

$$\frac{\partial \eta}{\partial \bar{\Delta T}} = \frac{\bar{\dot{m}} c_p}{UI} \tag{7.6}$$

$$\frac{\partial \eta}{\partial U} = -\frac{\bar{\dot{m}} c_p \bar{\Delta T}}{U^2 I} \tag{7.7}$$

and

$$\frac{\partial \eta}{\partial I} = -\frac{\bar{\dot{m}} c_p \bar{\Delta T}}{U I^2} \tag{7.8}$$

Equation 7.4 to Equation 7.8 can be used to derive the combined uncertainty (u_η):

$${u_\eta}^2 = \sum_{i=1}^{J} {\theta_{i,B}}^2 {s_{i,B}}^2 + \sum_{i=1}^{J} {\theta_{i,S}}^2 {s_{i,S}}^2 \tag{7.9}$$

where $\theta_{i,B}$ and $\theta_{i,S}$ are the systematic and random sensitivities of uncertainties of the J variables respectively, while $s_{i,B}$ and $s_{i,S}$ are the elemental systematic and random uncertainties for each J variable, respectively. These elemental uncertainties are variations in the measurements of water temperature, mass flow, voltage, and current. Finally, with the combined uncertainty, the expanded uncertainty (U_η) can be obtained, which can be calculated to a 95% confidence level:

$$U_\eta = 2 \cdot u_\eta \tag{7.10}$$

7.3.5 General Experiment Description

In order to reduce the random errors each experimental run was replicated five times for a total of 40 experiments: 20 experiments at the low arc power condition and 20 experiments at the high arc power condition. The test matrix is summarized in Table 7.2.

Table 7.2: General experimental matrix for low arc high arc power conditions.

Experimental run #	**Nominal flow rate (l/min) [kg/s]**	**Plate thickness (in) [mm]**	**Number of replicates**
1	2 [0.03]	0.25 [6.35]	5
2	5 [0.08]	0.25	5
3	2	0.375 [9.53]	5
4	5	0.375	5

During the welding process, the electrical signals, the temperatures in the inlet and outlet of the calorimeter, and the mass flow were recorded simultaneously. The four thermocouple readings at the inlet and outlet were averaged, so that the average inlet and outlet temperatures were used in the calculations. All the welds had a length of 120 mm. Finally, the thermal efficiency was calculated using Equation 7.1.

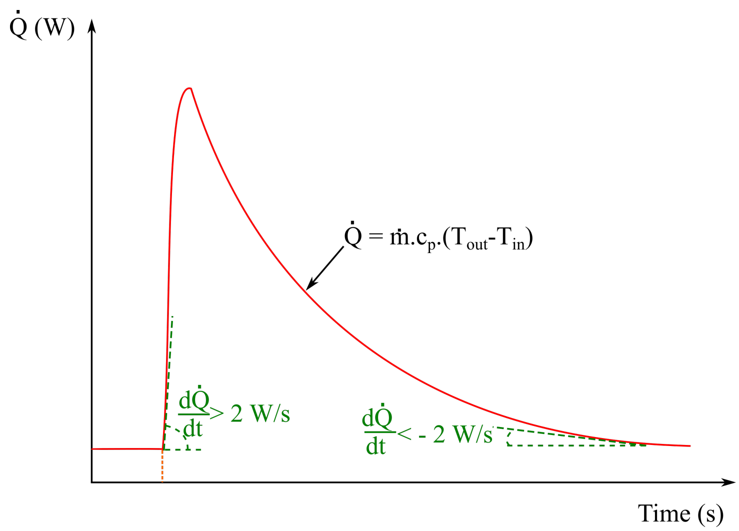

Figure 7.2: Schematic of the variation of power with time, used to calculate the residual power criterion for thermal efficiency calculation.

The power rate criterion was used to calculate thermal efficiency. This criterion assumes a minimum power rate to start and stop the integration process when calculating thermal efficiency, as shown in Figure 7.2. When the instantaneous power rate is higher than 2 W/s, the integration starts and proceeds until the instantaneous power rate is less than -2 W/s. This criterion is used to determine the start and finish for the integrals during thermal efficiency calculation. A justification for this treatment will be given in Section 7.5.

7.4 Results

7.4.1 Oscillograms – Characterizing The Transfer Modes

Figure 7.3 shows the oscillograms for the low arc and high arc power conditions. For the low arc power condition the transfer mode is short-circuit. Based on the oscillograms shown in Figure 3a the short-circuit voltage is approximately 5 V. A fast Fourier transform (FFT) analysis indicates that the droplet detachment frequency is around of 25 Hz (Figure 7.4a). In the case of the high power arc condition, the FFT analysis of the spray transfer mode signal indicates that the droplet detachment frequency is around of 386 Hz, as seen in Figure 7.4b.

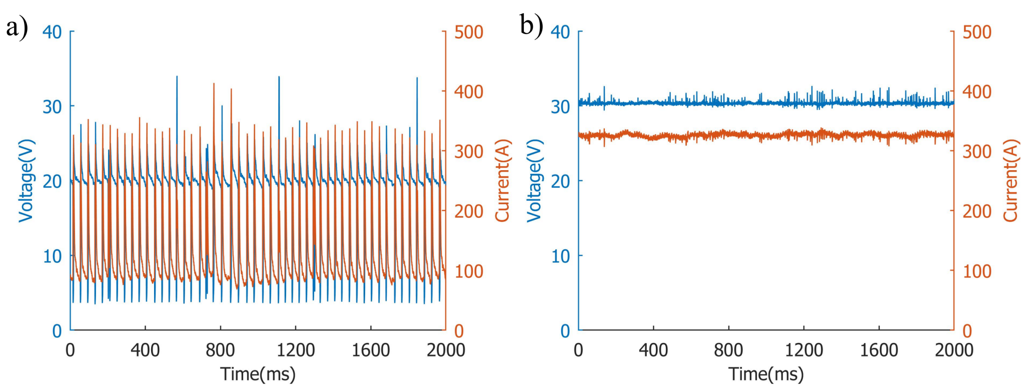

Figure 7.3: Oscillograms for: a) low arc power ; and b) high arc power.

TThe short-circuit signals give an instantaneous average power, calculated using Equation 7.2, 2.66 kW, which is slightly higher than the expected power of 2.5 kW taken from the literature. In comparison, the instantaneous average power for the spray transfer mode at high power mode is 9.88 kW.

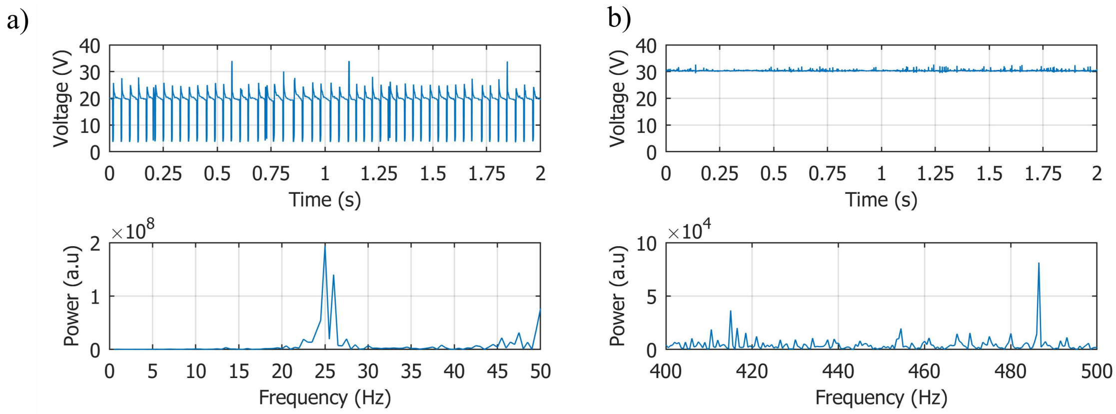

Figure 7.4: FFT for: a) low arc power ; and and b) high arc power.

7.4.2 Average Instantaneous Arc Energy

The average arc energy corresponds to the energy required to deposit a particular length of weld bead on the welding surface. The power source generates approximately the same amount of power for each run in short-circuit mode which is low arc energy, as shown in Figure 7.5a. However, in spray mode using high arc energy, the energy generated exhibits more variation when compared to the short-circuit regime, as seen in Figure 7.5b.

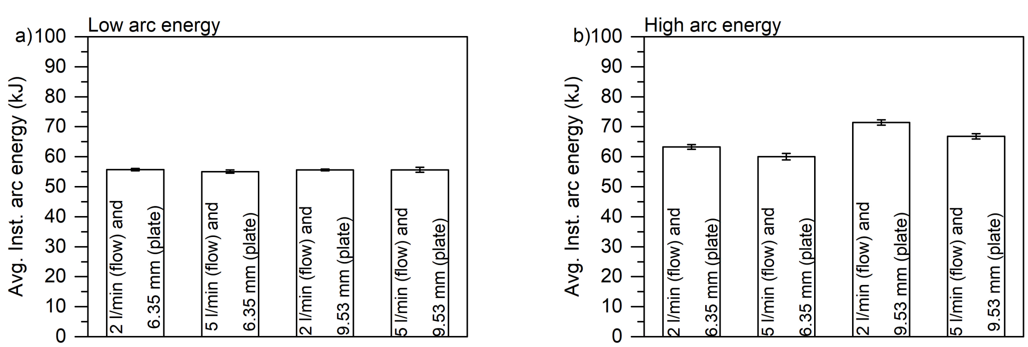

Figure 7.5: Instantaneous average arc energy, the energy that was delivered by the arc electric for weld bead of 120 mm. Each is an average of five tests, error bars represent confidence intervals at 95%.

Table 7.3 shows the values of average instantaneous voltage, current, power, and nominal heat input for the low and high arc power conditions. It can be seen that the values of average heat input remain within the variation of ± 1%. The values of average power in spray regime vary within a range of ± 3%, indicating that the calorimeter parameters do not significantly influence the stability of the electric arc during welding.

Table 7.3: Instantaneous average values of voltage, current, power, and nominal arc energy, and the experimental conditions are summarized in Table 7.2.

Low arc power - short-circuit				
Run #	**Average voltage (V)**	**Average current (A)**	**Average power (kJ/s)**	**Average heat input (kJ/mm)**
1	19.22	129.36	2.36	0.47
2	19.26	128.33	2.31	0.46
3	19.25	128.86	2.35	0.47
4	19.25	129.81	2.35	0.47
High arc power - spray				
Run #	**Average voltage (V)**	**Average current (A)**	**Average power (kJ/s)**	**Average heat input (kJ/mm)**
1	30.35	328.62	9.97	0.85
2	30.28	322.05	9.75	0.84
3	30.23	325.67	9.84	0.84
4	30.30	326.98	9.91	0.85

7.4.3 Bead Aspects

Figure 7.6 and Figure 7.7 show the bead aspects for the low arc power and high arc power operating conditions, respectively. Figure 7.6 shows no significant increase in spatter produced during welding in short-circuit mode, nor are there differences on the welding pool shape aspect. This indicates that the stability during welding was not considerably affected by the calorimeter parameters for the low arc power conditions.

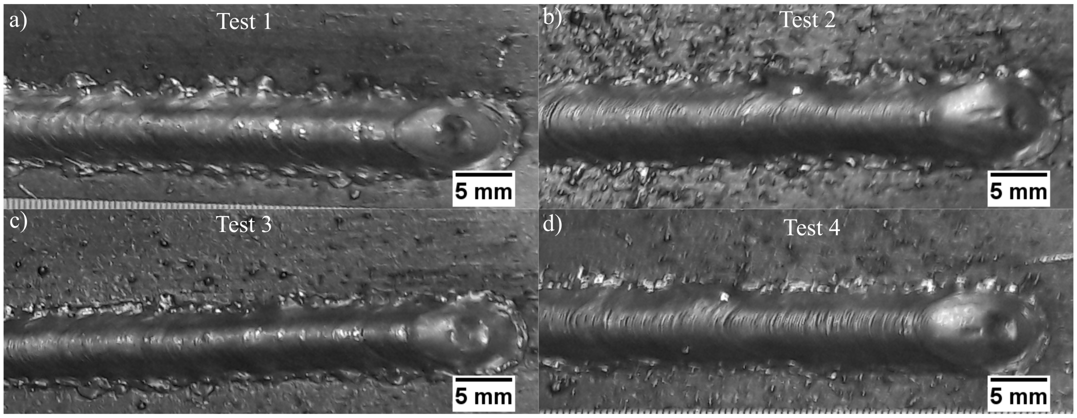

Figure 7.6: Representative weld bead surfaces for low arc power: a) test 1; b) test 2; c) test 3; and d) test 4. Test conditions are summarized in Table 7.2.

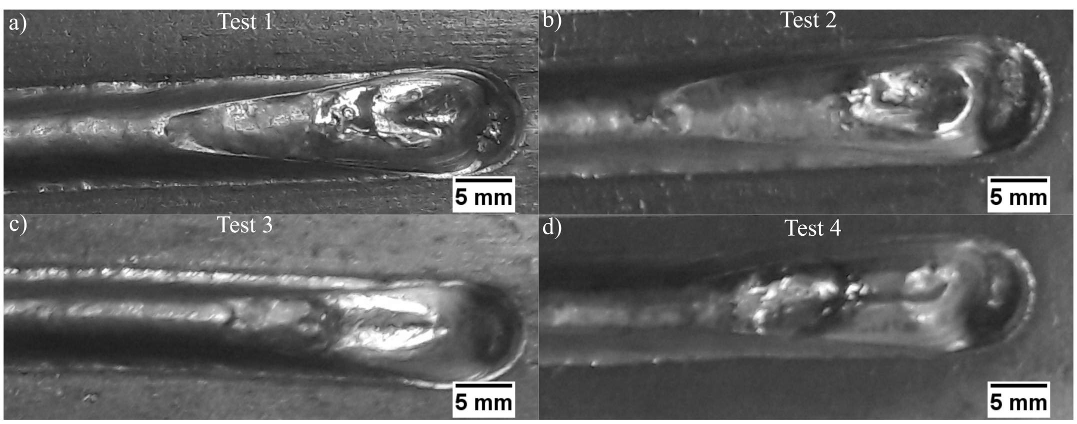

Figure 7.7: Representative weld bead surfaces for high arc power: a) test 1; b) test 2; c) test 3; and d) test 4. Test conditions are summarized in Table 7.2.

Figure 7.7 shows that there is no spatter adjacent to the weld beads welding in spray transfer regime. This indicates that the different calorimeter parameters do not affect the welding stability. Moreover, the shape of the weld pool is also not affected by the calorimeter.

7.4.4 Thermal Efficiency: Maximum And Minimum Values

Figure 7.8a shows the cyclogramme for low arc power, which reveals two distinct regions. The green rectangle delimits the transfer region in which the arc is extinguished and bridging transfers occurs; in this scenario the only heat transferred to the weld is via the droplet. The red rectangle delimits the open arc region in which there is no droplet transfer, and the heat comes from the arc itself. Averaging the instantaneous arc power from these two regions causes the average power to decrease compared to the cyclogramme in Figure 7.8b. This systematic power variation during short-circuit transfer increases the variance in data.

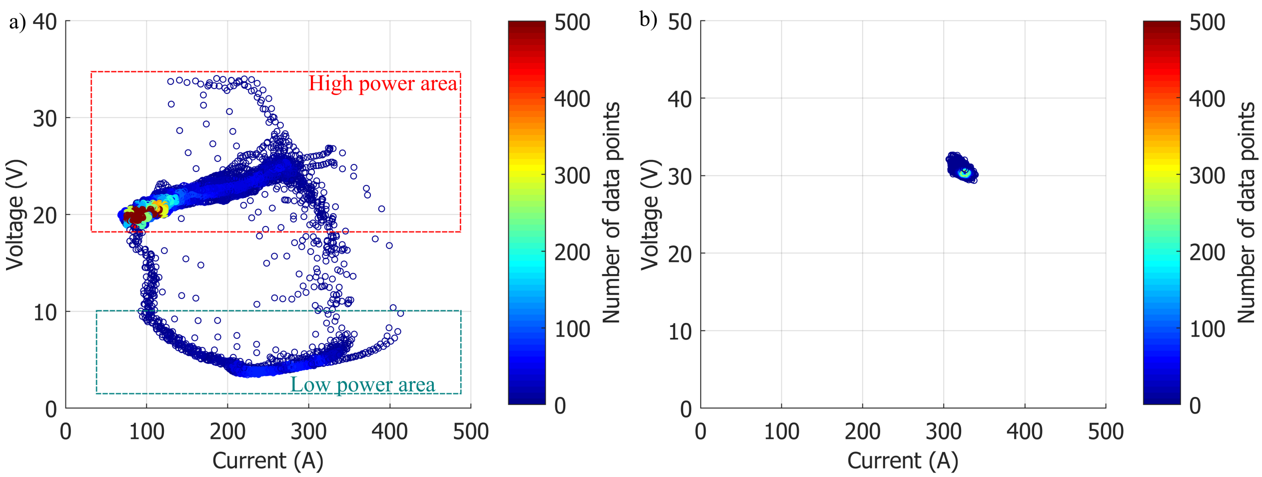

Figure 7.8: Typical cyclogrammes for: a) low arc power; and and b) high power.

Figure 7.9 shows the thermal efficiency calculated using the power rate criterion with error bars indicating minimum and maximum values. Figure 7.9a shows that the scatter in short-circuit regime is higher than in spray transfer, and that increasing the flow and plate thickness the scatter is much larger for the short-circuit mode (comparing Runs # 1 and # 2 to # 3 and # 4) . The large variance in the data collected in short-circuit regime welding is likely due to the natural oscillation of the arc between two regions as shown in Figure 7.8a.

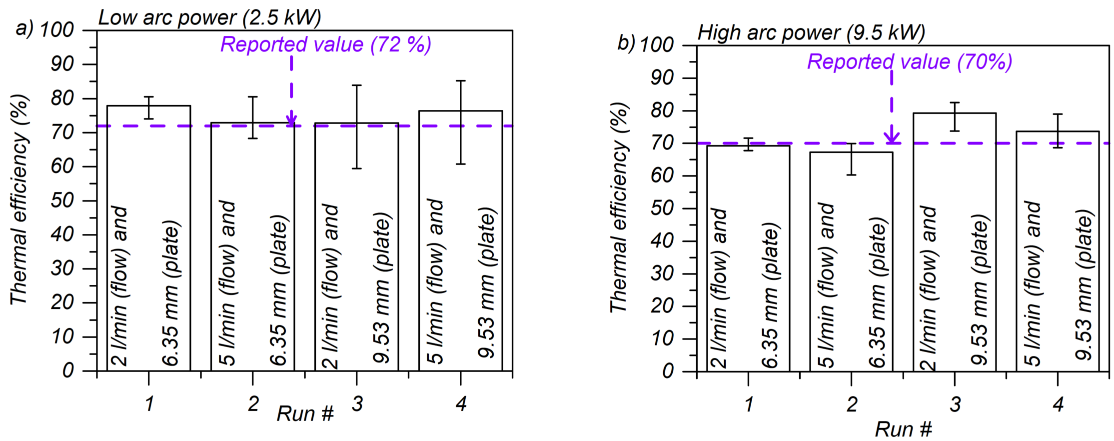

Figure 7.9: Average thermal efficiency: a) low arc power; and b) high arc power. Error bars represent minimum and maximum.

Figure 7.9a reveals that plate thickness has a greater effect on efficiency than flow rate, when using low arc powers (Considering that the variation in Run #2 is higher than Run #1). Comparing run #2 (5 l/min and 6.35 mm plate) and run #4 (5 l/min and 9.53 mm plate) the increased variance appears to be related to an increase in plate thickness, and this leads to heat loss to the environment through the sides of the workpiece. This may affect the cooling rate at the back of the plate and increase its variability. On the other hand, for thin plates, more heat is transferred directly to the calorimeter, accounting for the decreased variance compared to the thick plate conditions during low power arc welding.

Figure 7.9b shows that comparing runs #1 (2 l/min and 6.35 mm plate) and #2 (5 l/min and 6.35 mm plate) there is an slight increase in variance in run #2, which is likely caused by an increase in flow rate. The increase in variance due to flow rate still occurs when using high arc power, as shown in Figure 7.9b (When Comparing Run #1 to Run #2), but it is less pronounced than when high arc power is used, as shown in Figure 7.9a. The use of high arc power combined with high plate thickness promotes heat loss through the side of the workpiece, so that a higher fraction of heat still is transferred to the calorimeter, in comparison to the low arc power conditions, which accounts for the low variance observed in the results. Moreover, the effect of plate thickness on high arc power welding conditions, specifically for run #2 and run #4, seems to be negligible since the variance in the results is approximately constant, *cf.* Figure 7.9b.

7.4.5 Thermal Efficiency: Uncertainty Analysis

Figure 7.10 presents the expanded uncertainty to a 95% confidence level for the data calculated using the 2 W/s power rate criterion. Figure 7.10a shows that the uncertainty increases substantially when the flow and plate thickness increase (Comparing Runs #1 and #3 to Runs #3 and #4). It may be possible to avoid these measurement conditions, or improve the uncertainty of the measurements by using better sensors.

Comparing run#3 (2 l/min and 9.53 mm plate) and #4 (5 l/min and 9.53 mm plate), in Figure 7.10a, which have the same plate thickness but different flow rates, it can be observed that the effect of increasing the flow is small in the context of the two uncertainties. In Figure 7.10b, one notes that the uncertainties are lower compared to those showed in Figure 7.10a, demonstrating that the system is more robust to measurements involving high arc power (in spray transfer mode).

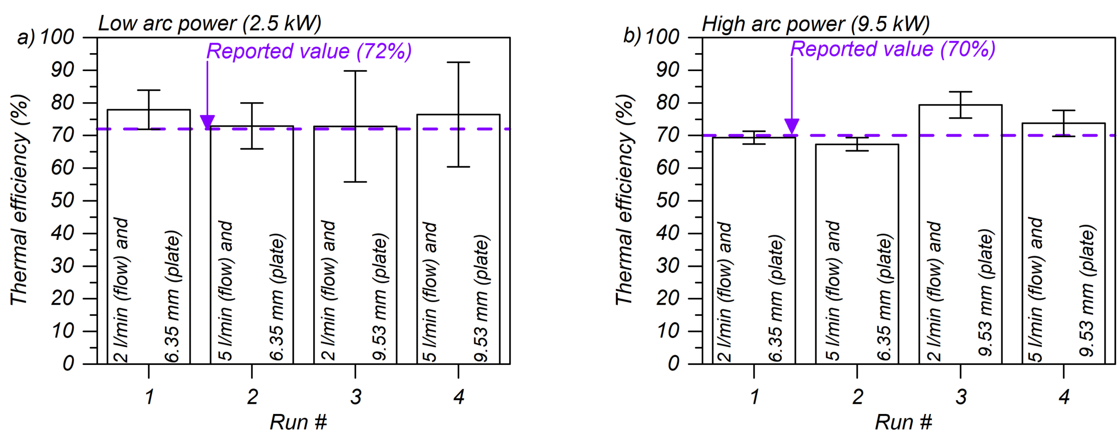

Figure 7.10: Average expanded absolute uncertainty: a) low arc power; and b) high arc power. Error bars represent 95% confidence intervals.

The estimate of thermal efficiency for spray transfer, based on run #1 (2 l/min and 6.35 mm plate), had an average uncertainty of 2% (*cf.* Figure 7.10b) while, for short-circuit transfer, in run #1, the uncertainty is 6%, as shown in Figure 7.10a. It seems from that the decreased uncertainty in high arc power weld conditions is due to the absence of oscillation between power regimes as discussed in Figure 7.8, and to the higher fraction of power transferred to the calorimeters despite the increased heat losses due to thick plates. It seems that the most accurate data is obtained using low flow rate and a thinner plate, again, probably due to the fact that, a thinner plate accommodates a higher amount of heat transferred to the calorimeter.

7.5 Discussion

7.5.1 Electrical Data And Thermal Efficiency

Given the similarities between the experimental set-ups reported in the literature and the one reported in this work, it is logical to suppose that the values of thermal efficiency and its uncertainties should also be similar to those reported here. In this light, for the short-circuit data, it was observed that the highest efficiency value reported was 85% (run #4, 2nd replicate), while the lowest was 59% (run #3, 4th replicate) as shown in Figure 7.9a. The highest value occurred for stable short-circuit transfer, while the lowest value occurred during unstable transfer. The unstable nature of short-circuit transfer is associated with metal spatter, which accounts for the drop in efficiency. According to Haelsig and Mayr [30] the energy lost by the arc (short-circuit), including spatter, is around 6%, which is consistent with the value of 5% value reported by Radaj [116]. In the case of spray transfer, the efficiency varied between 60% (run #2, 4th replicate) and 83% (run #3, 3rd replicate) shown Figure 7.9b.

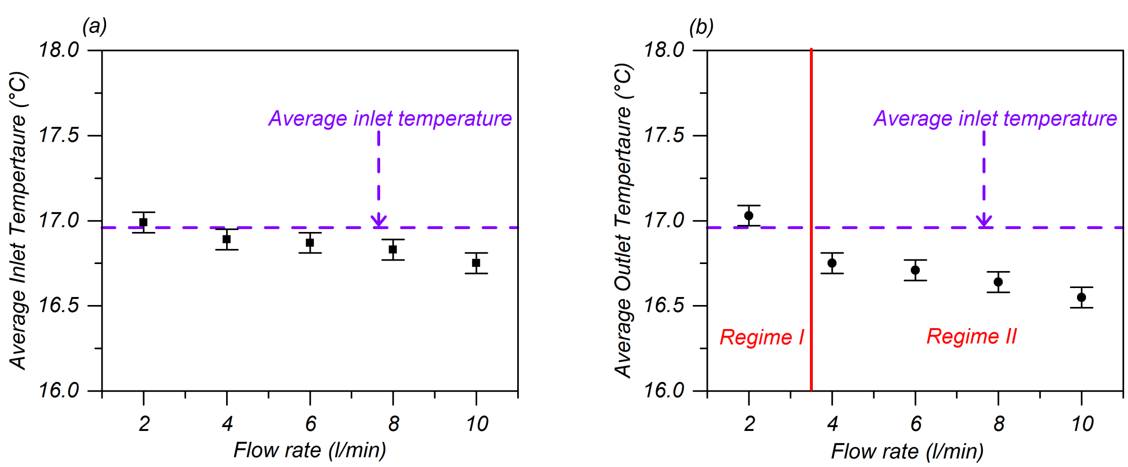

Figure 7.11: Effect of the flow on the measured temperature in absence of welding: a) inlet temperature; and b) outlet temperature. Each point is the average of three measurements.

As expected, the increase in flow rate will decrease the outlet temperatures (*cf.* Figure 7.11), however it is expected that this alone will not affect the thermal efficiency since the total enthalpy variation will be constant. In Figure 7.11b two regions can be distinguished: a) regime I for flow rates lower than 4 l/min, and b) regime II for flow rates higher or equal to 4 l/min. In region II, a substantial departure from the average inlet temperature (purple dashed line) can be noted with increased flow rate, indicating that in this region the effect of increased mass flow affects the measured outlet temperature, however, as discussed, this shall not affect the measured efficiencies.

7.5.2 Uncertainty In Measurements And Power Rate Criterion

Although the different combinations of plate thickness and water flow rate lead to different thermal efficiency average values, these values are statistically indistinguishable. For instance, in Figure 7.10a the reported efficiency for run #1 is 77% with an uncertainty of 6%, while, for Figure 7.10b the efficiency for run #1 is 71% with an uncertainty of 16%. In addition, the power rate criterion can be further refined if equipment with higher precision is employed.

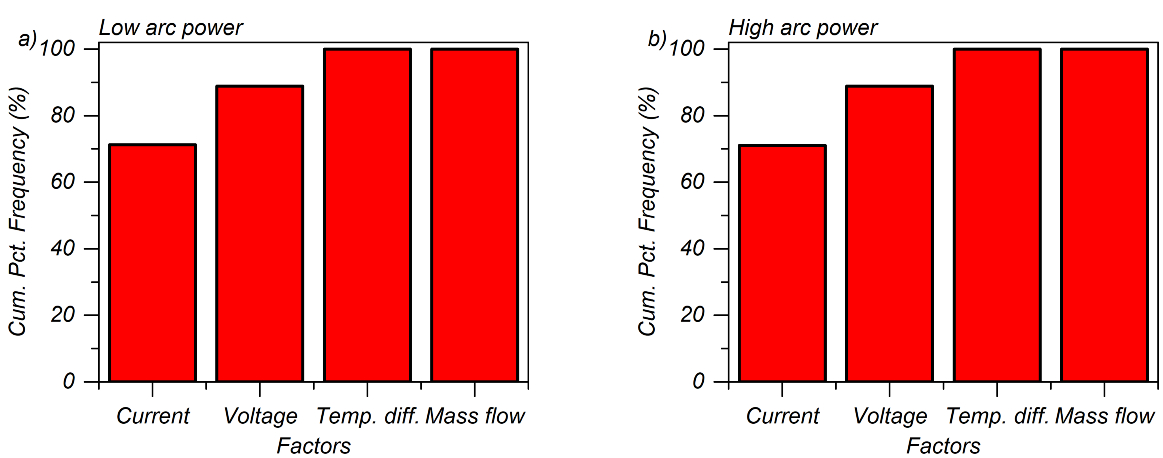

Figure 7.12: Cumulative percentual frequency of uncertainty for the different factors: a) low arc power; and b) high arc power.

Figure 7.12 shows the cumulative percentual uncertainty contribution of current, voltage, water temperature change, and mass flow on the uncertainty calculated based on Equation 7.9. The results shows that higher uncertainty is caused by the measurement of current.

The voltage, temperature measurements, and mass flow measurements do not contribute significantly to the overall compounded uncertainty. To improve the values of uncertainty the current Hall-effect sensor should be improved, as some of the high frequency small oscillations produced by the welding power supply may not be quantified while operating in constant voltage.

Figure 7.13 shows the representative variation related to different power rate criteria used to calculate thermal efficiency for both low and the high arc powers. This value defines the temporal interval over which the thermal efficiency is calculated. This method provides an efficient truncation to avoid potential errors caused by instabilities in the start and end tails of the integrated curve.

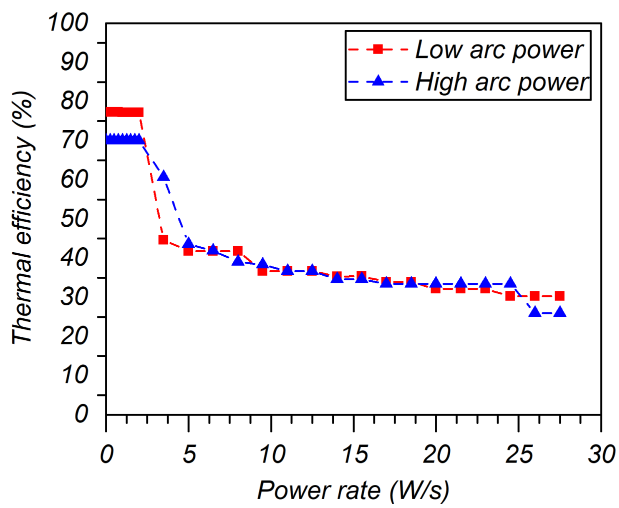

Figure 7.13: Representative variation of thermal efficiency as a function of residual power for low arc and high arc power conditions.

Moreover, the highest measured value of efficiency differs for low and high arc power conditions. The reason is likely the different heat transfer rates inherent to the calorimeter. In the spray regime (using high arc power) the highest efficiency calculated is approximately 70% while for the short-circuit regime (using low arc power) the efficiency is approximately 77%, *cf.* Figure 7.13. It is hypothesized that in the low arc power condition, more energy is absorbed by the calorimeter due to the reduced energy losses through radiation, which is consistent with Pepe *et al.* [105] which reported that radiation losses are approximately 10% in GMAW. A detailed account of the individual heat losses for the welds is beyond the scope of the present work, and it would require the use of different calorimeter types.

7.6 Summary

Gas metal arc welds, in short-circuit and spray regimes, were performed on AISI 1020 steel plates with different thicknesses, in order to study the effect of the calorimeter set-up on the measured value of thermal efficiency so that the effect of the process parameters on the overall uncertainty in efficiency values were known. From the results the following scientific findings can be drawn:

1. The calorimeter set-up affects the apparent value of thermal efficiency measured by the calorimeter. The use of low flow rates and thin plates promotes lower values of uncertainty in the measurement;

2. The low arc power condition has higher uncertainty than higher power condition. This is due to the power variation during short-circuit transfer, which is avoided when using high arc power to induce spray transfer;

3. A calorimeter sensitivity value of 2 W/s has provided a repeatable way to calculate thermal efficiency while avoiding the instabilities in the start and end tail of the integrated curve to calculate it.

Chapter 8

CW-GMAW: Welding Thermal Efficiency [1]

8.1 Overview

Cold wire gas metal arc welding (CW-GMAW) has been increasingly used in heavy-gauge manufacturing where high deposition rates are required. In such applications, the thermal efficiency of the CW-GMAW is crucial, yet it is not reported in the literature. Water calorimetry experiments were conducted to assess the thermal efficiency of CW-GMAW for two cold wire feed fractions and three common transfer modes: short-circuit, globular, and spray, and compared to standard GMAW. After producing the welds, three cross-sections were cut and analyzed in terms of penetration and dilution. Vickers hardness maps were used to account for the cooling rate across the weld cross-sections in high arc power samples. Results have shown that feeding a cold wire into the arc can re-introduce part of the lost heat, back to the weld pool in the short-circuit regime; or act to increase the heat content in the weld pool when in spray transfer regime.

8.2 Background

The thermal efficiency or the true heat input during welding has recently been the subject of detailed studies aiming for a more thorough understanding of this parameter, and

[1] This chapter is based on the following paper: Ribeiro, R. A.; Assunção, P. D. C; Braga, E. M.; Daun, K. J.;, and Gerlich, A. P. Submitted for publication in Welding in the World (2020).

to develop better procedures to accurately measure it [104, 29]. Thermal efficiency directly controls the cooling rate, which determines the microstructure and corresponding mechanical properties[116].

Thermal efficiency was traditionally thought to depend only on the type of welding process. However, reported thermal efficiencies for the same process will often conflict, depending on the values of travel speed, and power source energy employed [118]. A critical analysis of the influence of the calorimeter performance was published in which the effects of water flow, material type, and current were analyzed for a water-cooled stationary anode calorimeter [32] used for gas tungsten arc welding (GTAW). It was concluded that in spite of a $\pm$ 9% variation, the calorimeter was still capable of an accurate estimation of the energy transferred to the workpiece.

Haelsig et al. identified the key process features that influence thermal efficiency and proposed a model for gas metal arc welding (GMAW) operating in short-circuit, spray, and pulsed transfer modes, while employing a modified water-flow calorimeter [119]. They concluded that the arc length influences the amount of energy transferred to the workpiece, which is logical based on the increased radiative and convective losses increasing in arc length.

In the case of cold wire gas metal arc welding (CW-GMAW), energy transfer during welding must be quantified before it can be employed in industrial settings such as structural, naval, or pipeline welding [57, 93]. Accordingly, this study aims to measure the thermal efficiency of CW-GMAW for short-circuit, globular, and spray metal transfer modes which are most commonly used, while using cold wire feed rates of 60% and 100% for short-circuit, while 60% and 120% were applied for both globular and spray regimes.

In the present work, the influence of the calorimeter operating conditions on the measured value of thermal efficiency is evaluated here in detail. Two flow rates (2 l/min and 5 l/min), and two plate thicknesses (0.25 in [6.35 mm] and 0.375 in [9.53 mm]). The results show that efficiency depends on the calorimeter set-up and on the cold wire feed rate. Limits for cold wire feed rate were identified to which the efficiency increases or decreases in reference to standard GMAW using the same parameters.

8.3 Experimental Methodology

A water calorimeter was designed using numerical modeling to maximize heat transfer, and was fabricated from steel in order to evaluate welding efficiency. Figure 8.1 shows a drawing of the calorimeter fixture and a photograph of the set-up during the test. The welds were performed in the three natural transfer modes: short-circuit, globular, and spray, in order to asses the CW-GMAW process over all the range of possible welding droplet transfer modes.

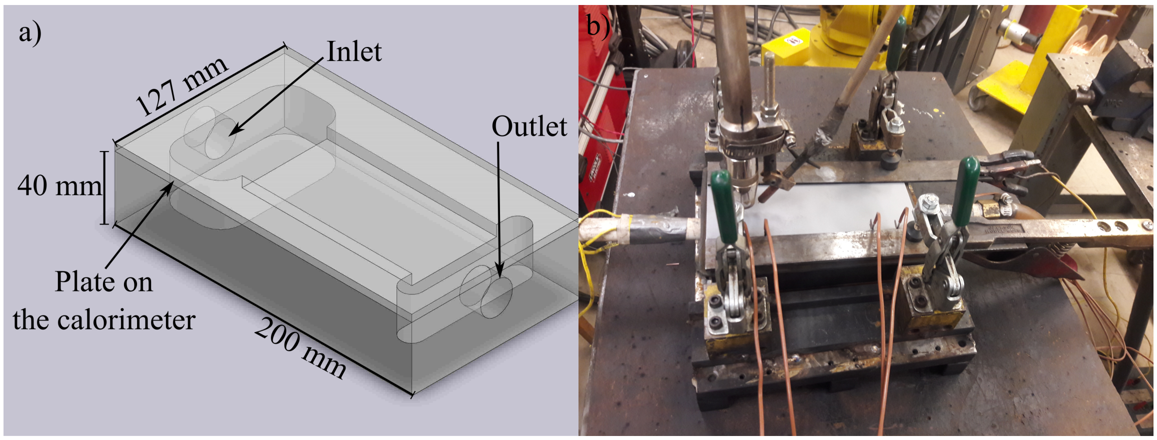

Figure 8.1: Calorimeter set-up: a) drawing of the calorimeter; and b) photo of the calorimeter on its fixture.

Bead-on-plate welds with a length of 120 mm were performed on AISI 1020 plain carbon steel. The plate dimensions were 200 mm [8 in] x 127 mm [5 in] x 40 mm [1.6 in]. ER70S-6 was used for the main electrode and cold wire, the wire diameters were 1.2 mm and 0.9 mm for the electrode and cold wire, respectively. The welding parameters used in this study are summarized in Table 8.1. The shielding gas for all tests was Ar-15% CO_2 at the flow rate of 40 ft^3/h or 19 l/min. Three replicates were performed for each condition. During all welds the cold wire leaded the arc and the welding torch was kept perpendicular to the substrate.

Table 8.1: Welding parameters.

Process	WFS (in/min) [m/min]	Voltage (V)	Travel speed (in/min) [cm/min]	CTWD (mm)	C.W. feed rate (%)
Short-circuit transfer regime					
GMAW	250 [63.5]	20	25 [63.5]	17	-
CW-GMAW	250	20	25	17	60
CW-GMAW	250	20	25	17	100
Globular transfer regime					
GMAW	280 [7.11]	28	25	17	-
CW-GMAW	280	28	25	17	60
CW-GMAW	280	28	25	17	120
Spray transfer regime					
GMAW	350 [8.89]	30	25	17	-
CW-GMAW	350	30	25	17	60
CW-GMAW	350	30	25	17	120

The calorimeter was operated using two water flow rates of 2 l/min and 5 l/min. Two plate thicknesses were used during the test, 9.5 mm [0.375 in] and 6.3 mm [0.25 in]. The test matrix is summarized in Table 8.2, which was repeated for each transfer mode to assess the influence of the calorimeter set-up on the efficiency value. The three values of efficiency were used to calculate the uncertainty at 95% confidence interval.

Table 8.2: Experimental matrix

Test number	Plate thickness (in) [mm]	Water flow (l/min)	Number of replicates
1	0.25 [6.35]	2	3
2	0.25	5	3
3	0.375 [9.53]	2	3
4	0.375	5	3

The calorimetry experiments are performed in steady state, as proposed by Sikstron[112]. The thermal efficiency was calculated using:

$$\eta = \frac{c_p \bar{\dot{m}} \int_0^{t_{weld}} \bar{\Delta T} dt}{P t_{weld}} \tag{8.1}$$

where c_p is the specific heat of water at 290 K (4.184 $kJ/\left(kg \cdot K\right)$) according [114], $\bar{\dot{m}}$ is the average mass flow rate, the instantaneous mass flow rate $\dot{m} = \forall(t) \cdot \rho$, where $\forall(t)$ instantaneous volumetric flow rate, measured by the rotameter, and ρ is the density of the water at 290 K (998 kg/m^3); $\bar{\Delta T}$ is the average difference between outlet and inlet temperatures of water in the calorimeter, and t_{weld} is the welding time. For the purpose of uncertainty analysis, the average voltage U and the average current I were used to derive the sensitivities. For thermal efficiency calculations using 8.1, the average power P was:

$$P = \langle U_i \cdot I_i \rangle \tag{8.2}$$

The heat losses (spatter, heat radiated out of the electric arc, and heat lost from the weld bead) effects on thermal efficiency are not directly accounted in this work as discussed prior in Chapter 7.

Uncertainty analysis was performed on the calorimetry results, based on the methodology prescribed in the standard, PTC ASME 19.1 2018 – Test Uncertainty [103]; further details can be found Chapter 7. After the calorimetry tests, three cross-sections were cut to represent each test condition. These cross-sections were subjected to standard metallographic procedures to analyze their macrostructures. Hardness maps of welds produced in the spray transfer regime cross-sections were measured using a load of 500 gf and the dwell time of 10 s. The cross-sections were etched using a 5% Nital solution in order to investigate the microstructure effect on the Vickers hardness observed. These microstructures were classified using the International Institute of Welding (IIW) guidelines for ferritic steel weld metals [87].

8.4 Results

8.4.1 Oscillograms

The oscillograms in Figure 8.2 show that introducing the cold wire does not affect the stability of the welding arc, considering that the cold wire welds exhibit similar voltage and current waveforms compared to GMAW over a sample period of 200 microseconds. However, when welding on a calorimeter, the depth of the welding pool is reduced by the accelerated cooling imposed by the water flow on the back of the welding plate, which will affect the weld bead as will be discussed in Section 8.4.3.

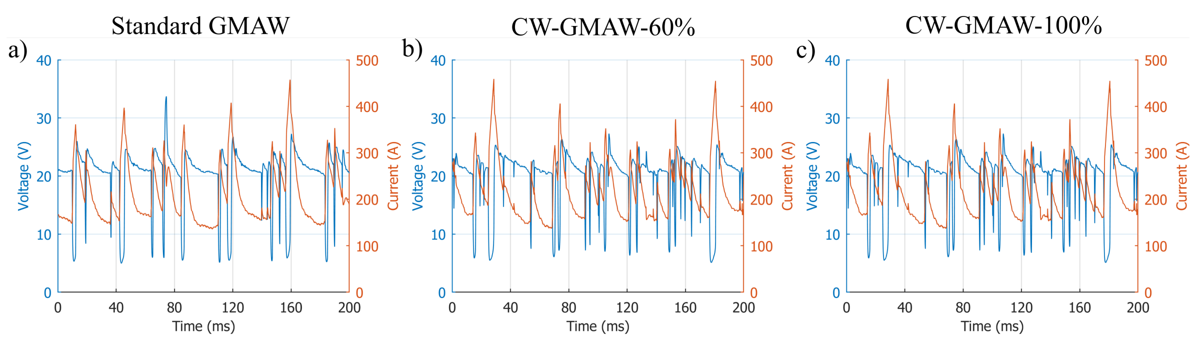

Figure 8.2: Representative oscillograms for the short-circuit transfer mode: a) standard GMAW; b) CW-GMAW-60%; and c) CW-GMAW-100%.

For instance, the voltage coefficient of variation (COV) is defined as the standard deviation of the voltage sample divided by its instantaneous average. This statistic is commonly used to assess arc stability in constant voltage (CV) mode. The COV for the GMAW condition is 0.24 while the COV for CW-60% and CW-100% operating in short-circuit is 0.22. Although the electrical dynamics of the arc does not appear to be affected directly by the calorimeter based on the COV values, nonetheless, an increase in the cold wire feed fraction might increase the short-circuit events, thus increasing the spatter level.

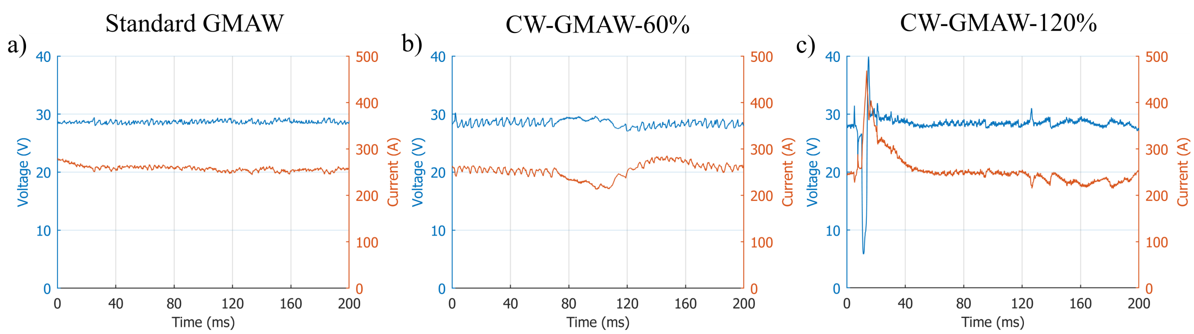

Figure 8.3: Representative oscillograms for the globular transfer mode: a) standard GMAW; b) CW-GMAW-60%; and c) CW-GMAW-120%.

Figure 8.3 shows the representative oscillograms of the welds produced with a globular transfer mode. In this case the cooling effect of the calorimeter significantly affect the arc dynamics. For instance, in Figure 8.3a although the WFS was 280 in/min [7.1 m/min] and the voltage was 28 V, short-circuit events are still discernible (where voltage $<$ 10 V), which would not be expected for these values of WFS and voltage without the calorimeter. These effects still persist in the CW-60% and CW-100% welds, but, the number of such events decrease substantially. In all three welding conditions which operated in globular transfer regime the average voltage is around 28 V due to stabilization factor of the welding power source.

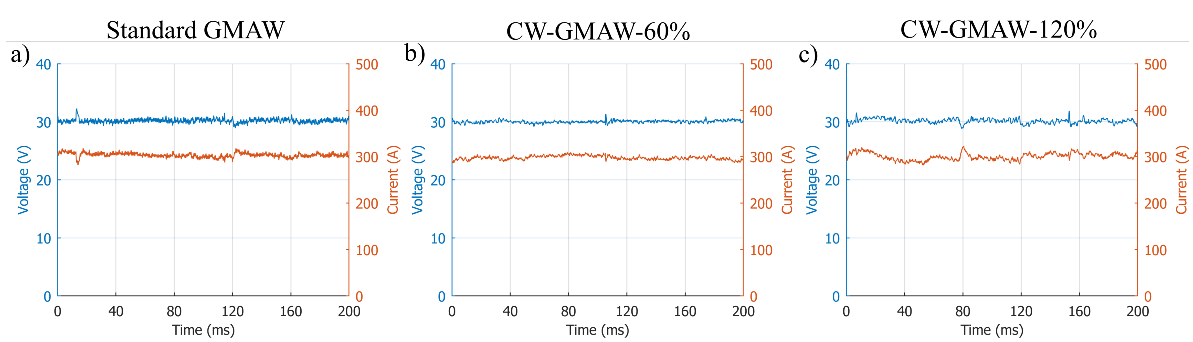

Figure 8.4: Representative oscillograms for the spray transfer mode: a) standard GMAW; b) CW-GMAW-60%; and c) CW-GMAW-120%.

Figure 8.4 shows the oscillograms for the spray condition, which indicate that the dynamic features of the arc are minimally affected by the cooling provided by the calorimeter since no short-circuit event can be discerned. A minor increase in fluctuation of the voltage and current can be noted when 120% cold wire (COV = 0.0194) is used compared to the more stable 60% cold wire feed rate(COV = 0.0081) and conventional GMAW (COV = 0.0125). The average voltage for all welds was maintained at approximately 30 V which indicates that the arc column was stable during the welds.

8.4.2 Cyclogrammes

Figure 8.5 shows the cyclogrammes for all the welds operating in short-circuit transfer mode. The reduction scatter events in Figure 8.5b and Figure 8.5c compared to Figure 8.5a suggests higher stability in CW-60% and CW-100%, only considering the arc dynamics. Furthermore, the data presented in Figure 8.5b and Figure 8.5c show a reduction in the area of the cyclogrammes (inside the dashed ellipse) compared to Figure 8.5a; this is associated with increase of cold wire feed rate, as reported in Chapter 3 of this thesis.

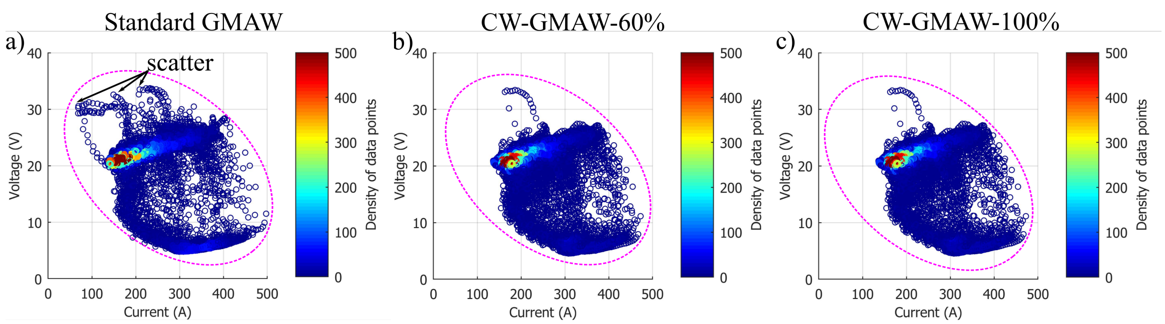

Figure 8.5: Cyclogrammes for the short-circuit transfer mode indicating enhanced stability with increase in cold wire feed rate: a) standard GMAW; b) CW-GMAW-60%; and c) CW-GMAW-100%.

Figure 8.6 shows the cyclogrammes for the globular regime. The data indicate that, although the severity of short-circuit events (where voltage < 10 V) decreases for CW-60% (Figure 8.6b), it increases again for CW-120% (Figure 8.6c) indicating that the CW feed rate became excessive for the energy balance inside the weld pool. The number of short-circuits in Figure 8.6a, is higher than for CW-60% as shown in Figure 8.6b, in Figure 8.6c, the number of short-circuits increase again. This indicates that the internal regulation system of the welding power source accommodated better the fraction of 60% cold wire feed in spite of the effect of the calorimeter on the weld pool heat balance. This is corroborated by the reduced area of points in Figure 8.6b, in comparison to Figure 8.6a and Figure 8.6c.

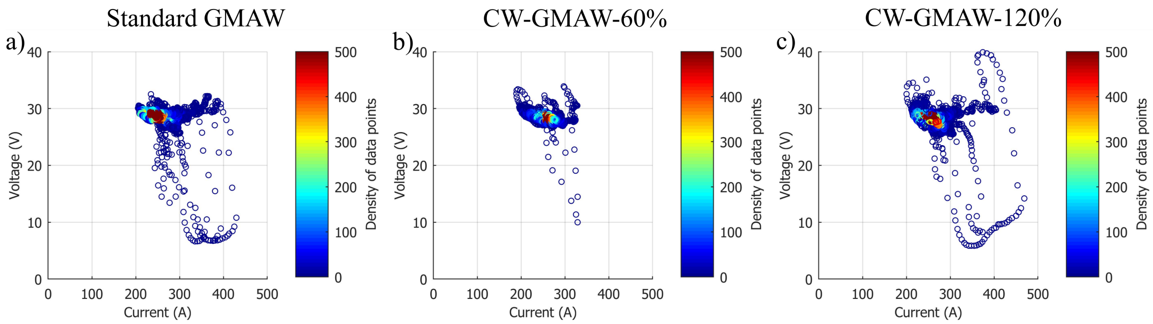

Figure 8.6: Cyclogrammes for the globular transfer mode: a) standard GMAW; b) CW-GMAW-60%; and c) CW-GMAW-100%.

Figure 8.7 shows the cyclogrammes for the spray transfer regime, indicating that the CW-60% welding parameter is more stable than standard GMAW and CW-120%. In prior work involving welding onto an isolate plate [15] the CW-120% was more stable than CW-60%. However, when welding with the calorimeter the trend is reversed. Welding with CW-60% using the calorimeter, this imposes a higher cooling rate at the back of the plate which decreases the energy available in the weld pool to accommodate the additional cold wire. Thus, when the feed rate is increased to 120%, there is lower energy to melt the additional wire, thus affecting the stability of the welding pool.

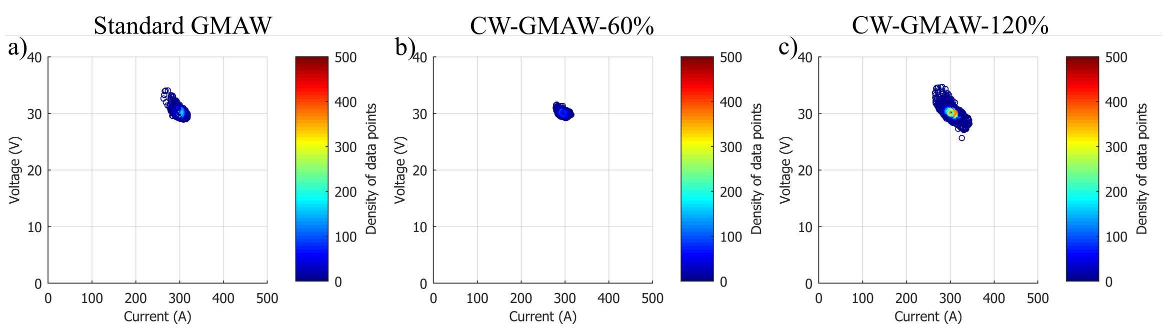

Figure 8.7: Cyclogrammes for the spray transfer mode: a) standard GMAW; b) CW-GMAW-60%; and c) CW-GMAW-120%.

For all welding conditions it can be seen that the response in voltage was kept close to 30 V which corresponds to the voltage set point. Figure 8.7c shows the the density of data points in the center of the cloud is higher, indicating the internal regulation system in the welding power supply able to maintain the instantaneous voltage response closer to this set point.

8.4.3 Bead Profile And Cross Sections

Bead Aspect

Figure 8.8 shows the representative bead profiles for the welds performed in the short-circuit regime. With the increase in cold wire feed rates, increased spatter leads to the deterioration of arc stability during welding.

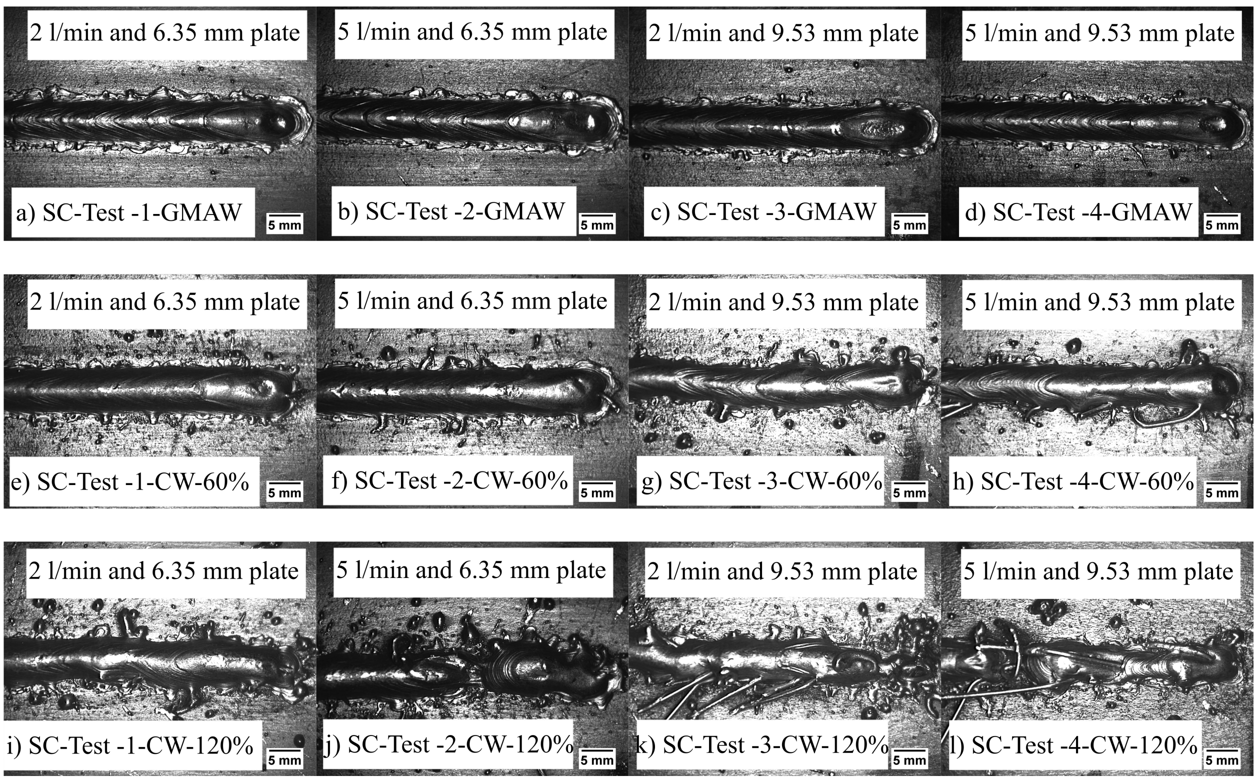

Figure 8.8: Bead aspects for the short-circuit transfer mode.

It is important to note that the deterioration of arc stability with increasing cold wire feed rate only seems to occur for welds on the calorimeter. When the welds cool in air the beads appear more uniform and continuous using CW-60% or CW-100%. The increase in spatter level increases the amount of energy waste during welding. Haelsig and Mayr recently [30] determined the energy balance in GMAW operating with short-arc through calorimetric techniques, it was determined that the energy lost through arc and substrate including spatter was around 6%. The additional cooling rate when 5 l/min of water is used can be verified through the reduction of the width in Figure 8.8a in comparison to Figure 8.8d.

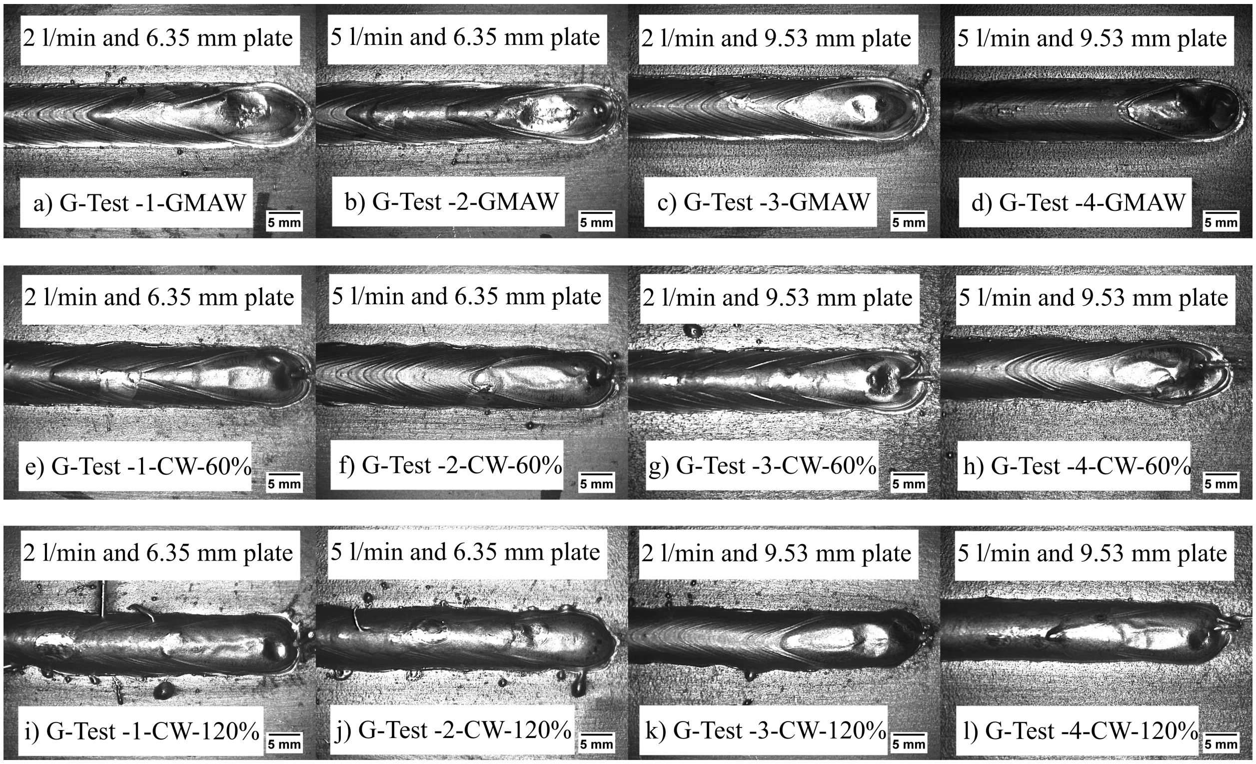

Figure 8.9: Bead aspects for the globular transfer mode.

Figure 8.9 shows the bead aspects for the globular regime. In contrast to the short-circuit mode in Figure 8.8 the amount of spatter is reduced for CW-60% and CW-120% conditions, indicating that the welding pool has more energy compared to the short-circuit mode. However, for CW-120%, the cold wire may be partially melted as shown in Figure 8.9i, depending on the instantaneous cooling rate provided by the calorimeter. The combination of a thick plate, high water flow rate, and a high cold wire feed rate may cause the cold wire to be only partially melted by the welding pool. This combination seems to favour the heat loss of the weld pool, which limits the accommodation of high cold wire feed rates.

Figure 8.10 presents the bead profiles for welds produced using spray transfer, where it can be observed that there is negligible spatter for standard GMAW and CW-GMAW-60% conditions, indicating that spatter occurs only when there is insufficient energy in the weld pool to accommodate the cold wire.

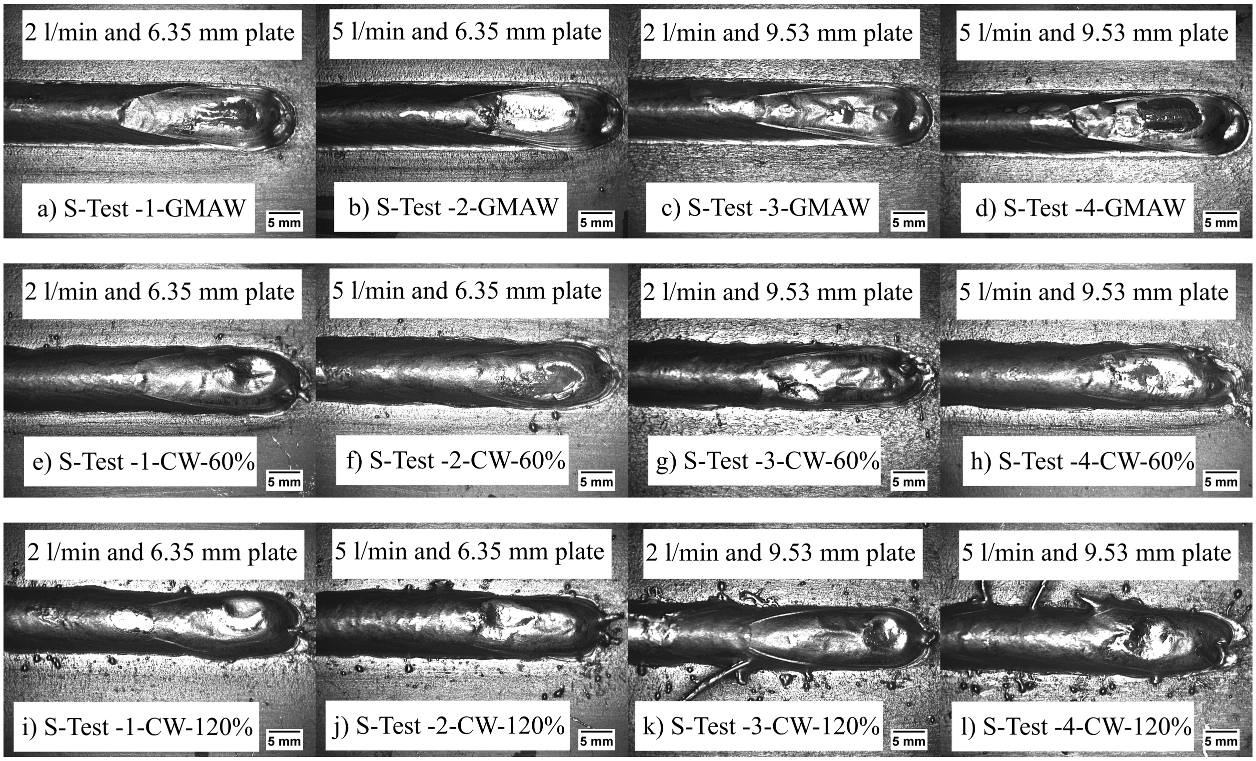

Figure 8.10: Bead aspects for the spray transfer mode.

Again when the combination of high flow rate, thick plate, and high cold wire feed rate is used, the cold wire may be only partially melted by the weld pool. This set of factors promotes heat transfer from the weld pool, to the calorimeter, impairing the ability of the weld pool to melt the cold wire and causing spatter through intermittent contact between the cold wire, the weld pool, and the semi-detached droplet. This leads to multiple short-circuits, a phenomenon described by Assunção [120] for negative polarity CW-GMAW, but this study shows that it also applies to positive polarity CW-GMAW.

Cross-sections

Figure 8.11 shows the representative cross-sections of welds fabricated in short-circuit mode. The cold wire feed causes weld discontinuities such as undercut (Figure 8.11h), inclusions (Figure 8.11j), porosity (Figure 8.11g), and lack of fusion (Figure 8.11l). All these defects come from the non-accommodation of the cold wire by the weld pool due to insufficient thermal energy.

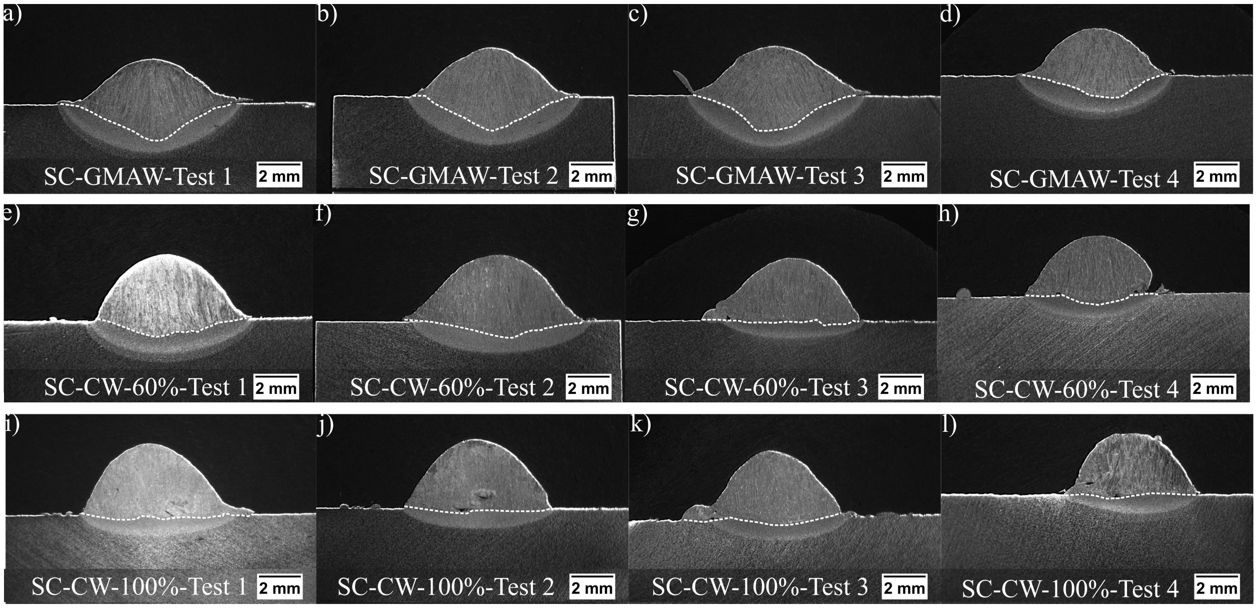

Figure 8.11: Macrographs for short-circuit transfer: Test 1 (2 l/min and 6.35 mm plate); Test 2 (5 l/min and 6.35 mm plate); Test 3 (2 l/min and 9.53 mm plate); and Test 4 (5 l/min and 9. 53 mm plate).

Introducing cold wire, as expected, reduces the penetration and dilution of the welds for all conditions, while for CW-100% the dilution is drastically reduced along with the heat affected zone (HAZ) area. Figure 8.12 shows the cross-section for the globular transfer regime; in contrast to Figure 8.11 (short-circuit mode), there are no internal defects found through the cross-sections examined, in spite of the partial melting of the cold wire. As expected, dilution and penetration in the welds were reduced with increasing cold wire feed rate.

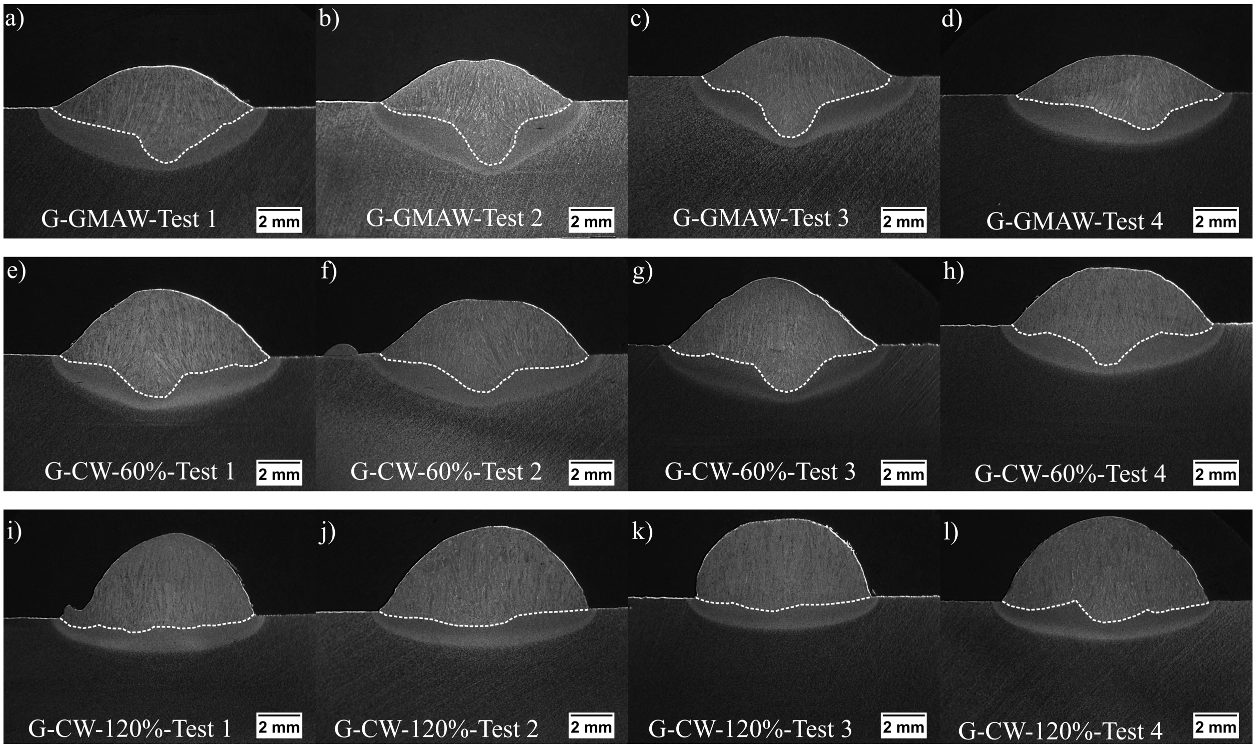

Figure 8.12: Macrographs for globular transfer: Test 1 (2 l/min and 6.35 mm plate); Test 2 (5 l/min and 6.35 mm plate); Test 3 (2 l/min and 9.53 mm plate); and Test 4 (5 l/min and 9. 53 mm plate).

Figure 8.13 shows the weld cross-sections obtained in spray transfer mode. No welding defects were found in the examined cross-sections for each condition. In Figure 8.13a and Figure 8.13b the HAZ extends through thickness of the plate. This condition can be characterized as a 2D according to Rykalin [121], while the other cross-section shows a condition called a *massive body* [2], which is a 3D condition. Additionally, the cooling rate for a semi-infinite body (3D regime) is lower than that for the 2D regime.

[2]This condition means that the temperature field does not reach to the full plate thickness.

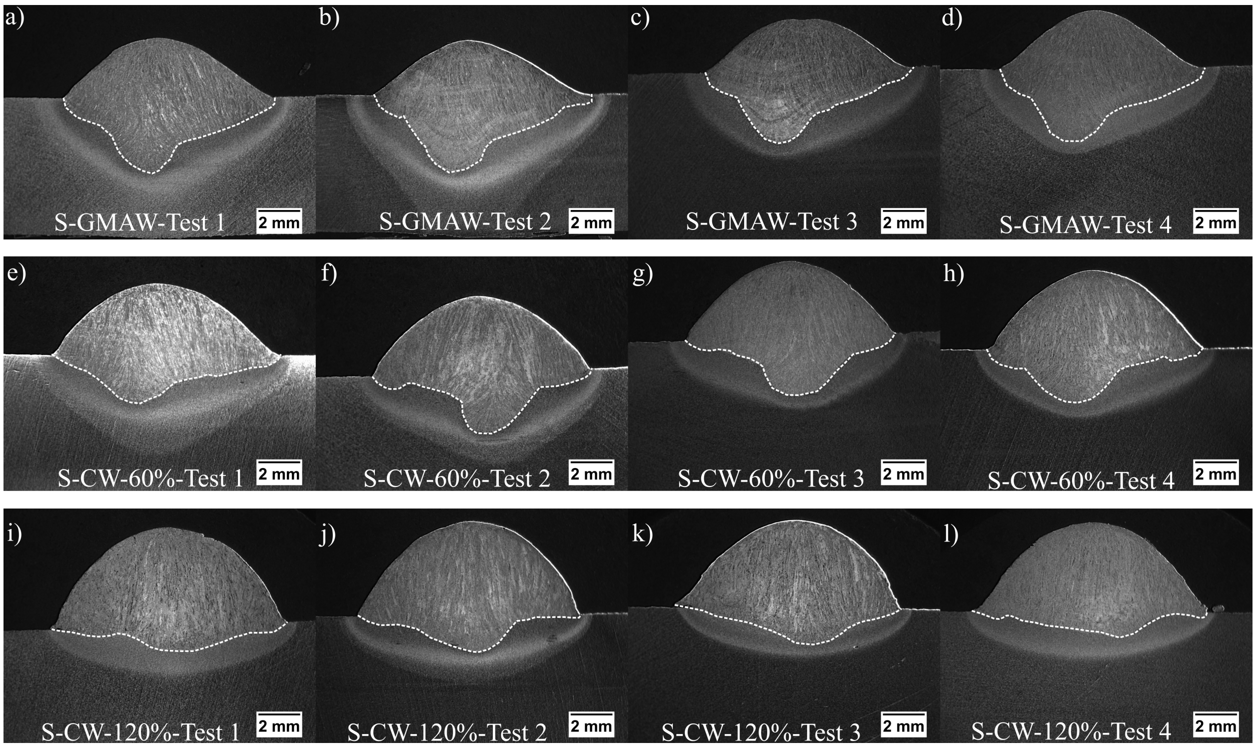

Figure 8.13: Macrographs for spray transfer: Test 1 (2 l/min and 6.35 mm plate); Test 2 (5 l/min and 6.35 mm plate); Test 3 (2 l/min and 9.53 mm plate); and Test 4 (5 l/min and 9. 53 mm plate).

The cooling rate does not depend on the plate thickness under 3D heat transfer conditions while for 2D conditions the cooling rate varies inversely with the square of thickness. Also the increase in height of the bead is more pronounced in spray compared to the globular regime, and this may also affect the cooling dynamics of the bead. Moreover, the increase in filler metal area in the bead has an impact on melting efficiency [36].

8.4.4 Thermal Efficiency And Uncertainty Values

Maximum/Minimum Values Of Thermal Efficiency

Figure 8.14 shows the thermal efficiency values for the short-circuit transfer regime where the error bars represent maximum and minimum values. The error bars for the short-circuit condition can reach values close to a 90% (Figure 8.14a), likely due to the welding pool cooling by the calorimeter. This will affect the morphology of the weld, and consequently, the measurements were not consistent, leading to increased scatter. Depending on plate thickness and flow rate, the CW-60% (Figure 8.14c) condition presents the highest average thermal efficiency.

Comparing Figure 8.14a (CW-60%) and Figure 8.14c (CW-60%), the first CW-60% condition has a lower average efficiency compared to the standard GMAW, while the second CW-60% condition presents higher efficiency than the standard GMAW. This is likely caused by the increase in the flow rate, which increases the cooling of the plate, favouring heat transfer to the calorimeter.

Figure 8.14b shows that the CW-60% condition has slightly higher efficiency than the standard GMAW. For all experiments in short-circuit the CW-100% condition exhibits lower efficiency than standard GMAW, and given the increase in bead height the heat is probably transferred preferably through bead top.

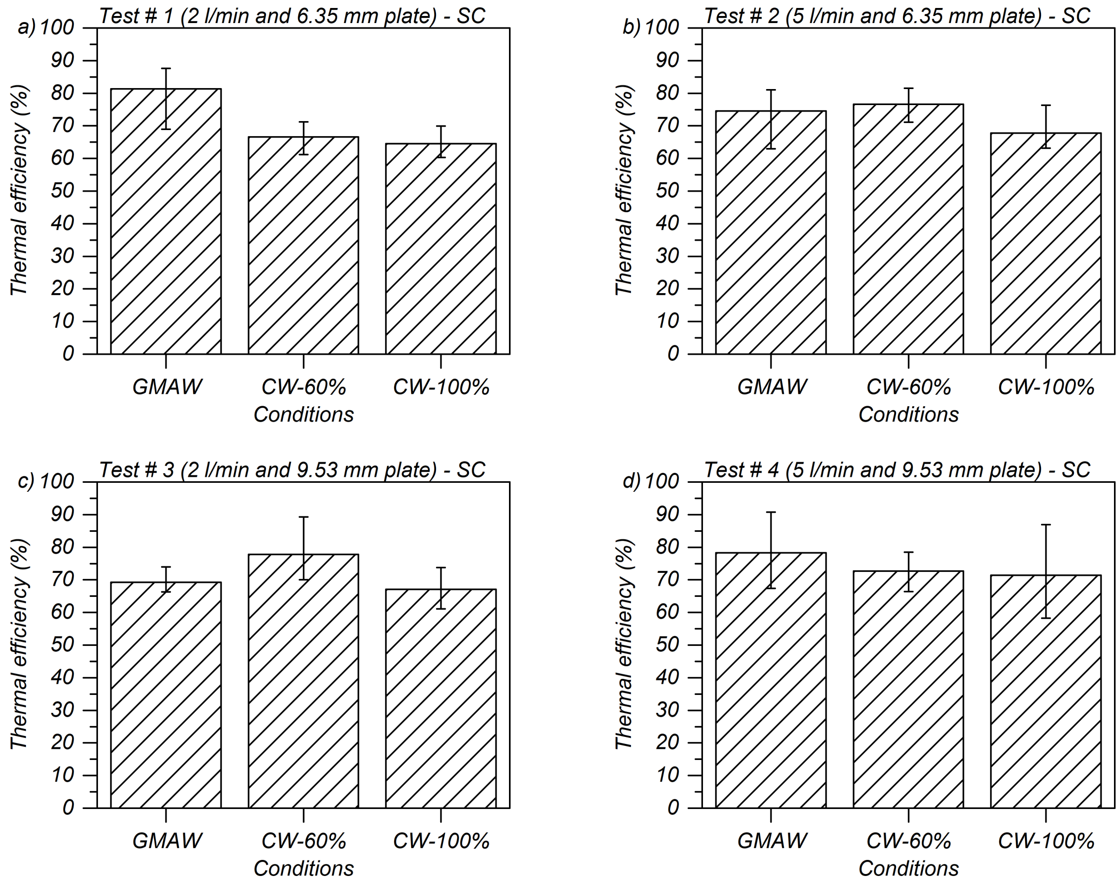

Figure 8.14: Average thermal efficiency for short-circuit conditions. Error bars represent maximum and minimum intervals: a) test 1; b) test 2; c) test 3; and d) test 4.

Figure 8.15 presents the thermal efficiency results for the globular regime, where the error bars also represent maximum and minimum intervals. Here it can be observed that CW-60% presents approximately equal thermal efficiency, on average, to the standard GMAW for all calorimetry conditions except in Figure 8.15a. The CW-120% condition in Figure 8.15c presents a lower efficiency, compared to standard GMAW and CW-60%.

This is likely because in CW-60% the cold wire recuperates part of the energy lost in the weld pool. The associated cooling conditions that favour the transfer of energy to the calorimeter increase the value measured by the instrument, as can be observed in Figure 8.15a to Figure 8.15c.However, as noted in Figure 8.15d CW-60% presents slightly lower efficiency than CW-120%. In this situation it is likely that more of the energy re-introduced by the cold wire is transferred to the calorimeter by the increased cooling effect promoted by the water flow (5 l/min) at the back of the plate. This explains the slightly higher measured efficiency in CW-120%, in Figure 8.15d, compared to CW-60% and standard GMAW.

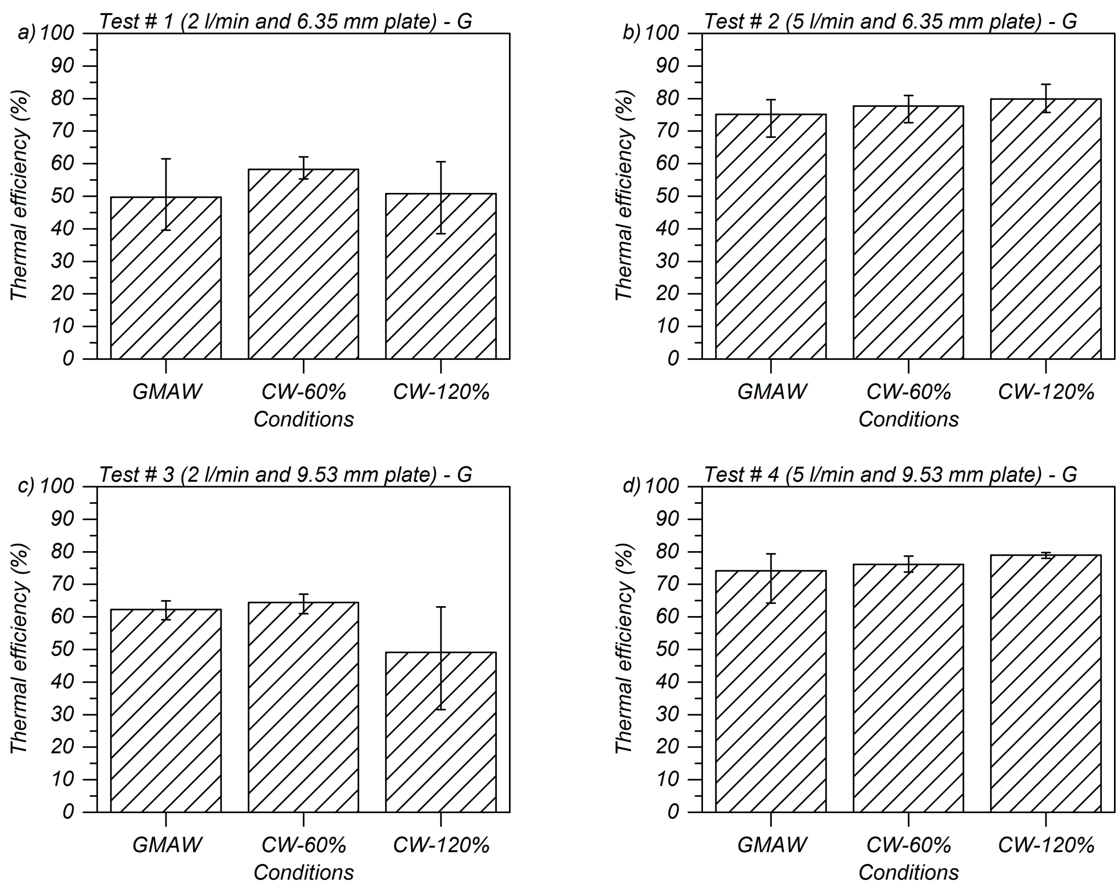

Figure 8.15: Average thermal efficiency for globular conditions. Error bars represent maximum and minimum intervals: a) test 1; b) test 2; c) test 3; and d) test 4.

Figure 8.16 presents the thermal efficiency measurements for the spray transfer regime. These results corroborate the trend that CW-60% presents higher thermal efficiency, on average, than the standard GMAW or CW-120% parameters for the majority of calorimetry conditions, shown in Figure 8.16a-c. In this set of experiments the spread of maximum and minimum values are reduced compared to short-circuit and globular modes, which is likely due to the higher energy of the weld pool that can sustain itself despite the higher cooling imposed by the calorimeter.

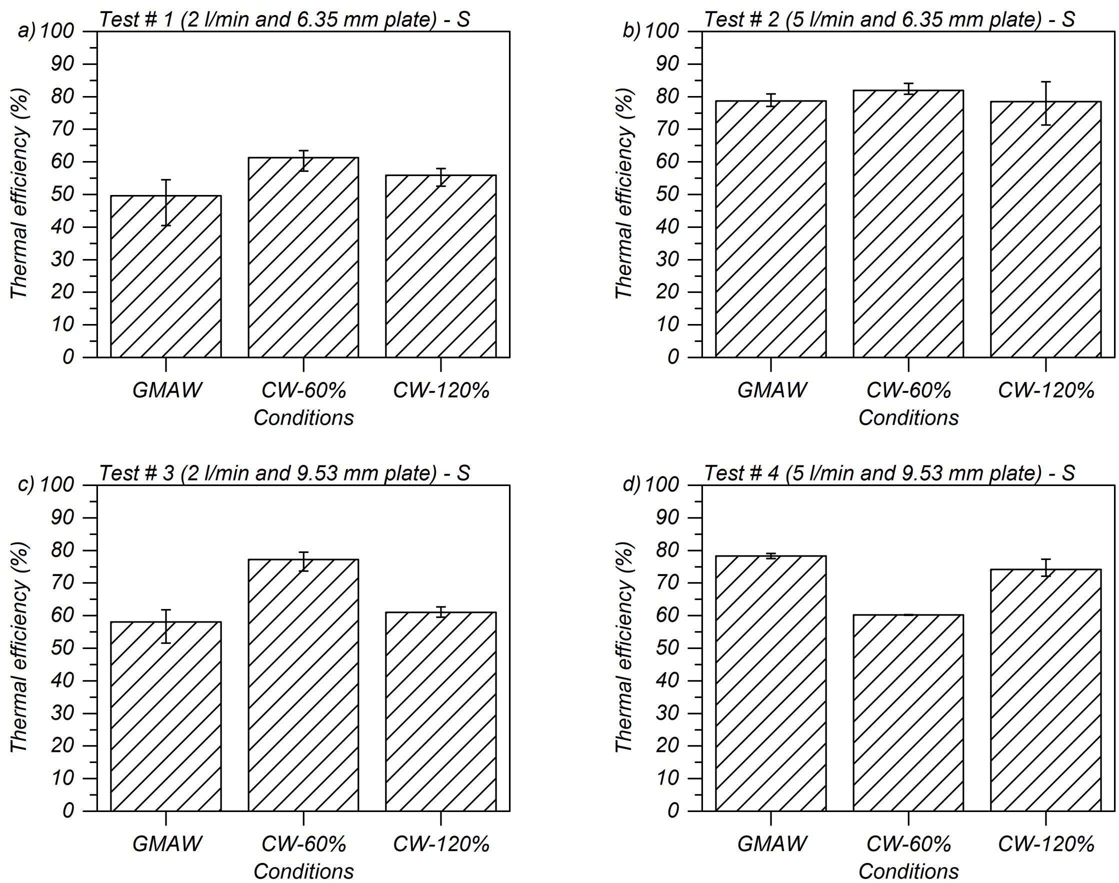

Figure 8.16: Average thermal efficiency for spray transfer conditions. Error bars represent maximum and minimum intervals: a) test 1; b) test 2; c) test 3; and d) test 4.

In Figure 8.16d CW-120% presents higher efficiency when high cooling water flow rate and thick plates are employed. It is likely the 5 l/min flow rate promotes increased heat transfer into the calorimeter given a higher thermal energy of the welding in spray transfer regime. In this situation the cold wire essentially re-introduces part of the heat that otherwise would be lost to the weld pool.

Uncertainty Of The Thermal Efficiency Measurements

Figure 8.17 presents the uncertainty associated with each measurement including the systematic and random uncertainties. The highest uncertainty values occur when a 5 l/min flow rate is used (Figure 8.17b and Figure 8.17d). This is consistent with results in prior work examining short-circuit transfer mode [122]. However, when CW-100% is used, the uncertainty limits decrease (Figure 8.17d), it seems that with the association of CW feed rate, thick plate, the certainty in measurements remains unaffected.

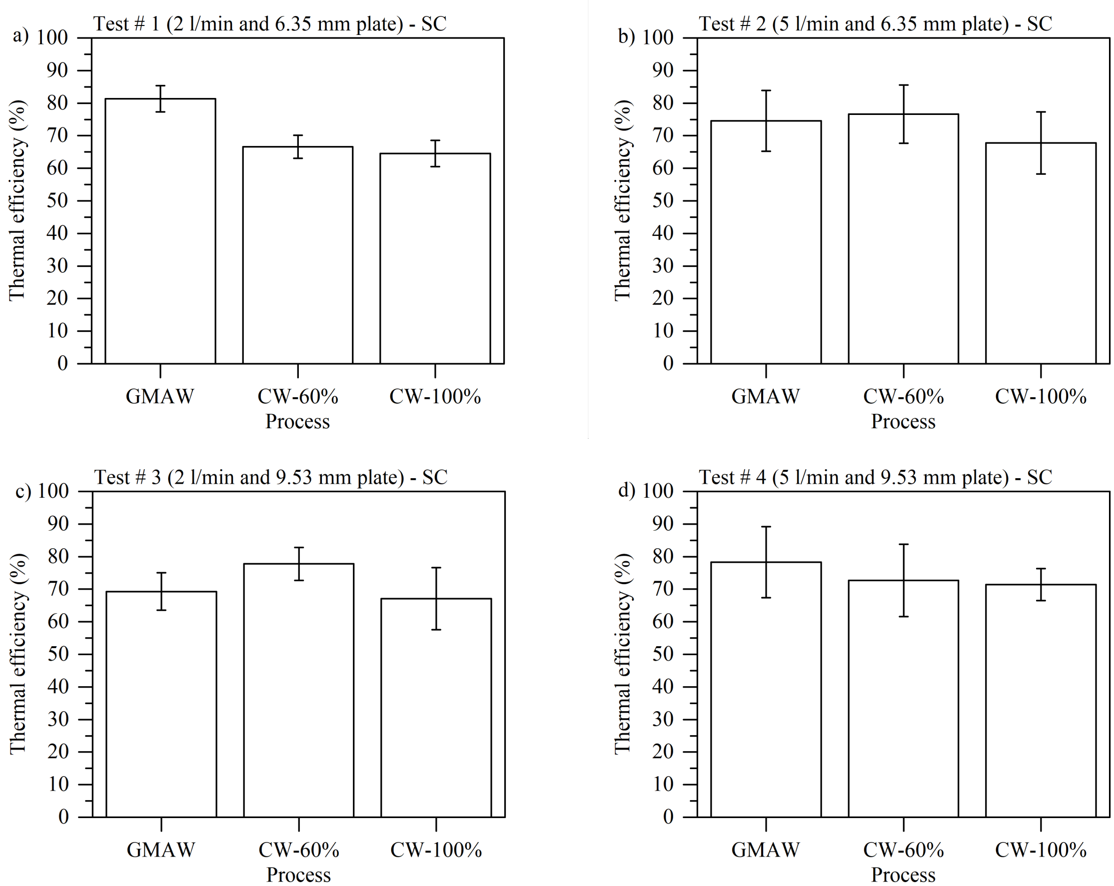

Figure 8.17: Average thermal efficiency for short-circuit transfer mode. Error bars represent uncertainty at 95% confidence intervals: a) test 1; b) test 2; c) test 3; and d) test 4.

Figure 8.18 shows the uncertainty for globular regime. The same trend is apparent as observed in Figure 8.17, though the uncertainty is higher for high flow rate. The uncertainties in globular mode are smaller than those in short-circuit mode. This is also consistent with the results shown in Chapter 7 in which the oscillation between high current and low current in short-circuit increase the variance in the measurements.

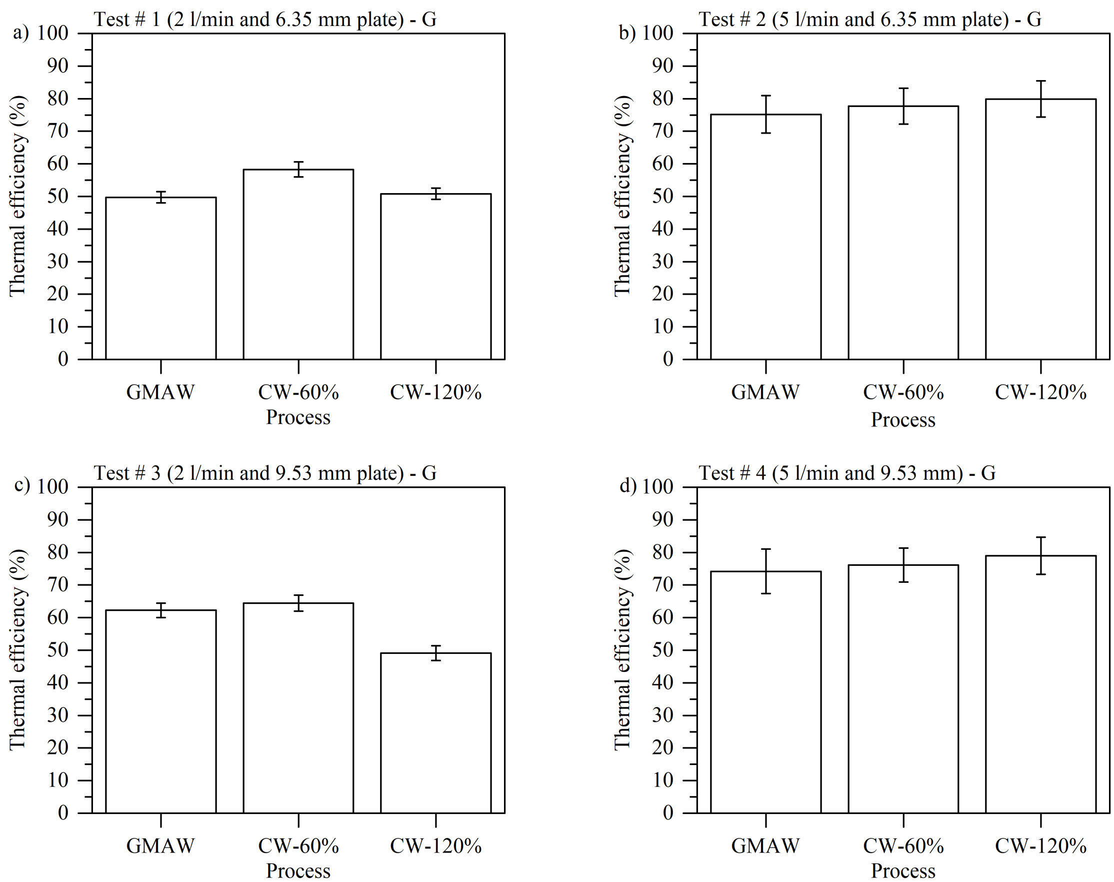

Figure 8.18: Average thermal efficiency for globular transfer mode. Error bars represent uncertainty at 95% confidence intervals: a) test 1; b) test 2; c) test 3; and d) test 4.

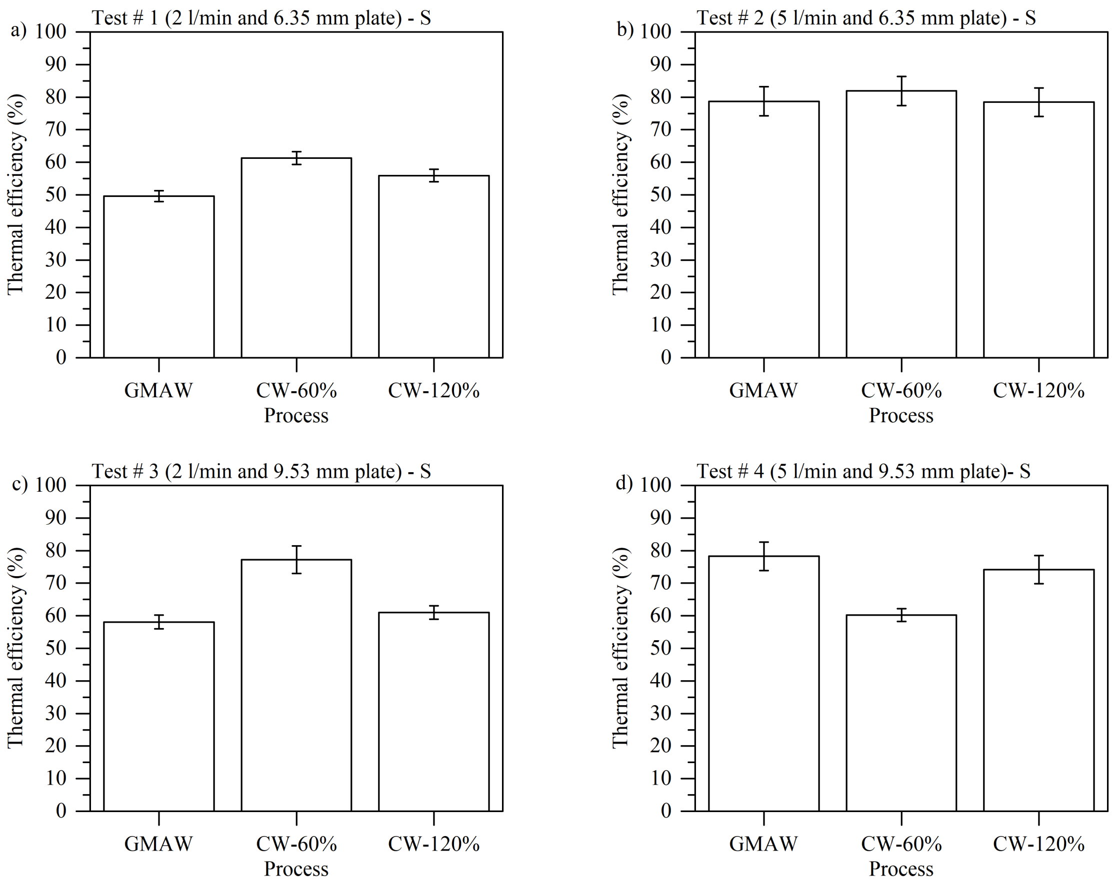

Figure 8.19: Average thermal efficiency for spray transfer mode. Error bars represent uncertainty at 95% confidence intervals: a) test 1; b) test 2; c) test 3; and d) test 4.

Figure 8.19 presents the uncertainties for spray transfer mode. There is little difference between the uncertainty values for globular and spray modes, shown in Figure 8.18 and Figure 8.19 respectively. The lowest value of uncertainty is observed when using 2 l/min cooling water and the 6.35 mm thick plate (Figure 8.19), which is the case for all transfer modes. The highest observed uncertainty is observed for highest cooling flow, 5 l/min which is also consistent for all other transfer modes.

8.4.5 Penetration And Dilution

Figure 8.20 presents the penetration for all transfer modes and calorimeter arrangements of flow and plate thicknesses. It can be seen that the penetration drops when the cold wire feed fraction increases, for all transfer modes. This is because increasing the cold wire feed rate increases bead height, consequently reducing penetration. Comparing Figure 8.20a, Figure 8.20d, and Figure 8.20g shows that for the short-circuit mode, CW-GMAW exhibits higher variance in the date compared to the globular regime (Figure 8.20b, Figure 8.20e, and Figure 8.20h). As the bead deposition was not consistent, (cf. Figure 8.8, for CW-60% and CW-100%) this leads to higher variation in the penetration throughout the bead.

Weld penetration seems to be affected more by the cold wire feed fraction than the calorimeter flow rate and plate thickness. For example comparing Figure 8.20e which globular regime CW-60%, the penetration does not change with different calorimeter settings; while the average penetration is much lower in Figure 8.20h for the globular regime using CW-120%. It can be seen that effect of doubling the cold wire feed rate more directly affects the penetration.

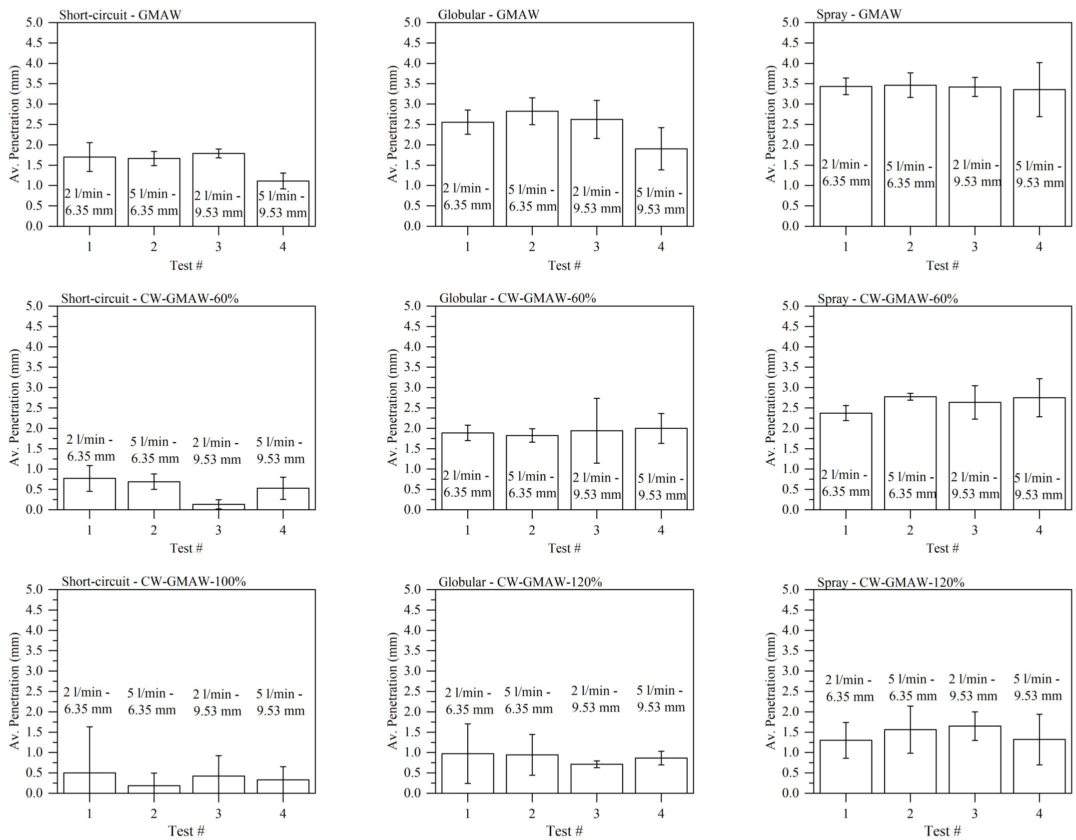

Figure 8.20: Penetration values for all transfer modes. The values of water flow rate (l/min) and plate thickness (mm) refer to different calorimeter set-ups. Error bars represent 95% confidence intervals.

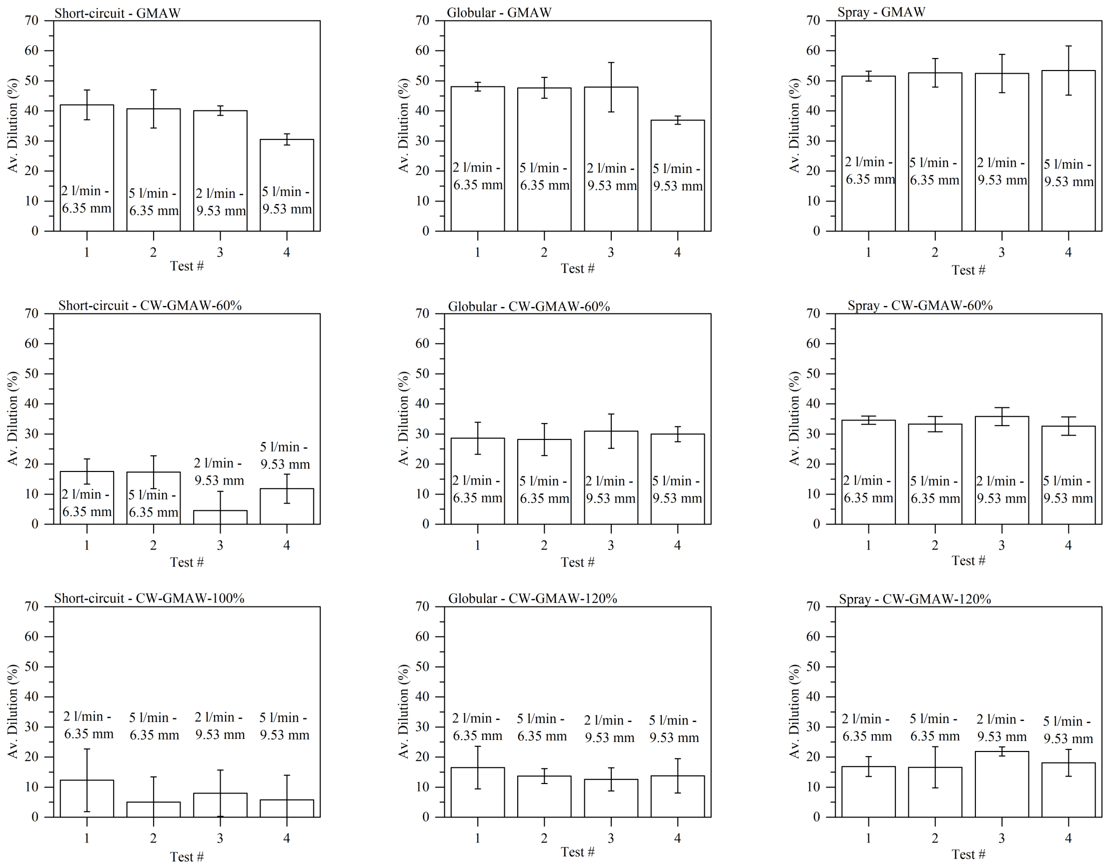

Figure 8.21: Dilution values for all transfer modes. The values of water flow rate (l/min) and plate thickness (mm) refer to different calorimeter set-ups. Error bars represent 95% confidence intervals.

Figure 8.21 shows the dilution for all transfer modes and cold wire feed fractions. In general, the dilution follows the same trend of penetration, since lower penetration determines lower dilution, for standard GMAW and CW-GMAW. As in the case of weld penetration, dilution seems more influenced by the cold wire fraction than by the calorimeter set-up. The uncertainty intervals for CW-60% are smaller (Figure 8.21f) compared to standard GMAW, (Figure 8.21c) both operating in spray mode.

8.4.6 Vickers Hardness Of The Welds Produced Using Spray Transfer

Figure 8.22 shows hardness maps of the spray welds, which were measured in order to provide a qualitative estimate of the cooling rate on the bead top surface and bottom (at the fusion line). The hardness maps were obtained on welds produced in spray mode considering the technological/practical interest associated with this transfer mode. Figure 8.22a to Figure 8.22d shows that the calorimeter set-up clearly influences the hardness across the beads. In test 1 (Figure 8.22a) with a flow rate of 2 l/min and a plate thickness of 6.35 mm the hardness across the bead is approximately 280 HV; in test 4 (5 l/min and 9.35 mm plate) the hardness across the bead is around 400 HV. This higher hardness indicates faster cooling rate in Test 4 compared to Test 1.

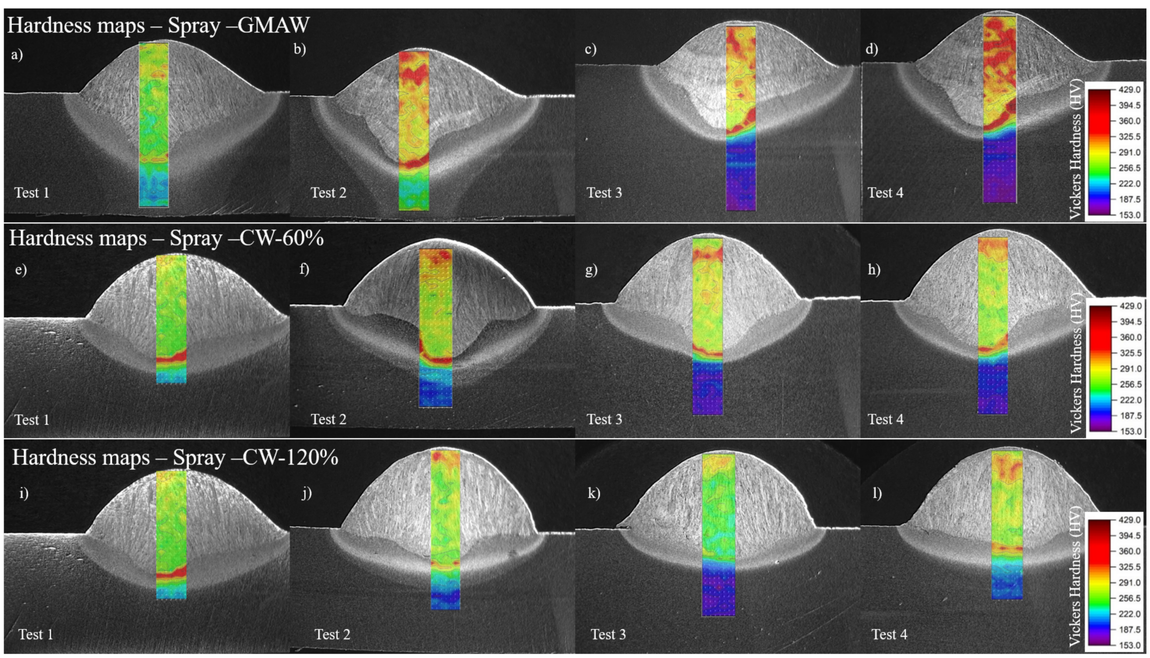

Figure 8.22: Hardness maps spray transfer cross-sections: test 1 (2 l/min and 6.35 mm plate); test 2 (5 l/min and 6.35 mm plate); test 3 (2 l/min and 9.53 mm plate); and test 4 (5 l/min and 9. 53 mm plate).

It can be seen in Figure 8.22i that faster cooling likely occurs in the fusion zone based on the higher hardness compared to Figure 8.22k. On the contrary, in Figure 8.22k the hardness is higher on bead top, suggesting that the cooling reaches higher values on the top. In Figure 8.22l, however, the hardness across the bead is about the same. The only difference between Figure 8.22k and Figure 8.22l is the flow that was increased to 5 l/min. It seems that the cold wire feed rates greater than 60% promote a higher cooling rate through the top if there is insufficient cooling to transfer the arc heat to the bottom of the welds.

8.4.7 Microstructures

Figure 8.23 shows the microstructures found at the top of the weld bead and at the fusion line for test 3 (6.35 mm plate thickness and 5 l/min flow rate) with reference to the Vickers hardness maps shown in Figure 8.22c, Figure 8.22g, and Figure 8.22k. These microstructures will help clarify the relatively high values of hardness found near the fusion line and bead top.

It can be seen in Figures 8.23a-b that in the top of the thickness of the primary ferrite (PF(G)) at the grain boundaries is reduced, which explains the higher hardness value, along with the presence of secondary ferrite with aligned phase (FS(A)). In the fusion line, it can be seen the presence of martensite (M) which accounts for the higher hardness in the HAZ. Moreover, near the fusion line, in the weld metal, the presence of acicular ferrite (AF) promotes higher hardness values.

Figure 8.23c shows that CW-60% at the top of the weld bead there is, qualitatively, higher fraction of AF compared to Figure 8.23a. The microstructures of the HAZ are also martensitic; and very thin PF(G)in the weld metal near the fusion line, cf. Figure 8.23d. Comparing Figure 8.23e to Figure 8.23a, it is possible that there is an increase in PF(G) which accounts for the decrease in hardness. Moreover, comparing Figure 8.23f to Figure 8.23b, it can be perceived that in the last, the HAZ is basically formed by PF(G) and intra-granular polygonal ferrite PF(I).

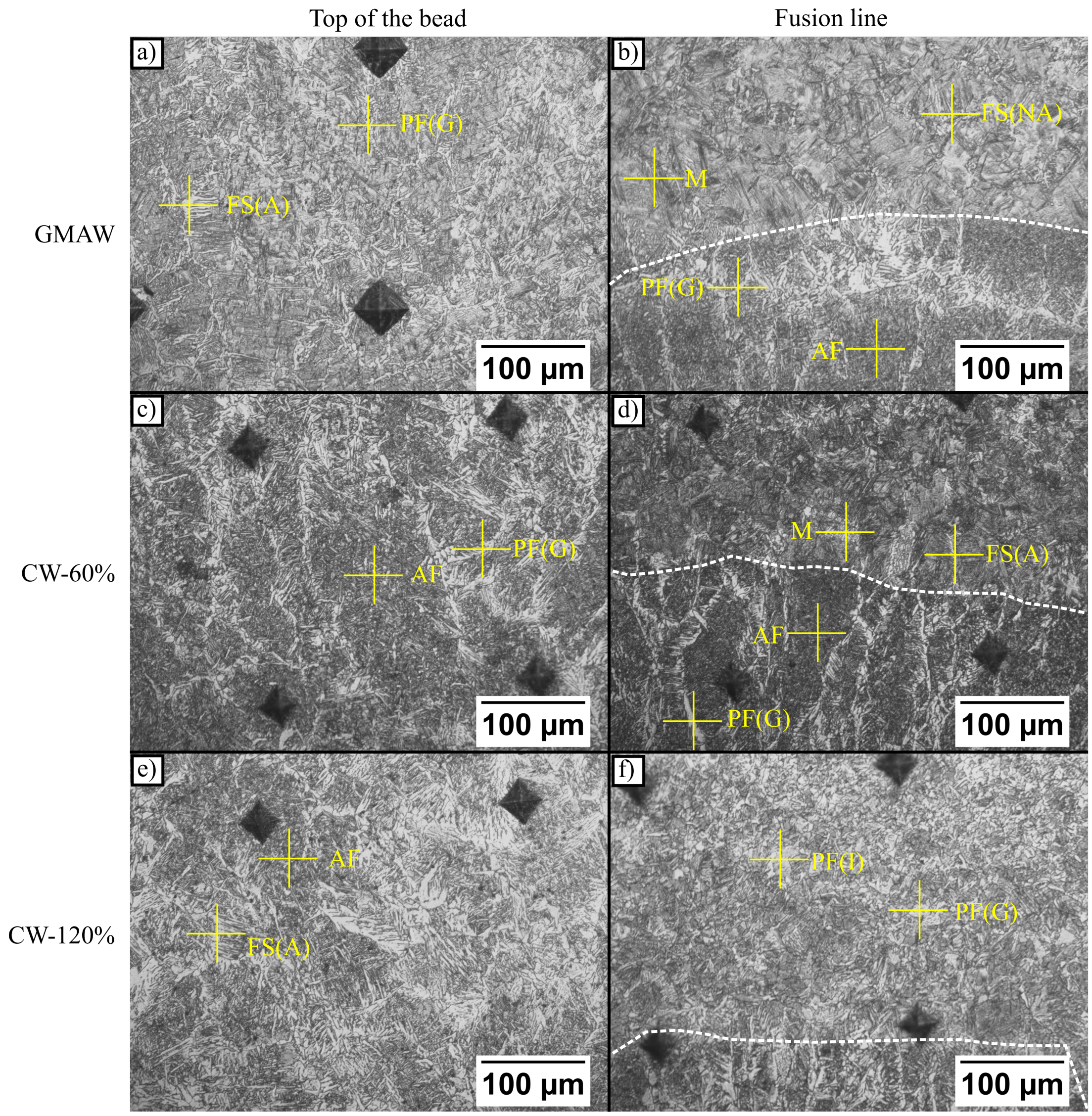

Figure 8.23: Microstructures at the top the bead and at the fusion line for the cross-sections shown in Figure 8.22 (Test 3): a) and b) GMAW; c) and d) CW-60%; and e) and f) CW-120%.

8.5 Discussion

The increase in short-circuit frequency through the cold wire can be demonstrated if one performs fast Fourier transform (FFT) of the oscillograms of short-circuit welds for different CW feed fractions, shown in Figure 8.2. The detachment frequency for standard GMAW is 31 Hz, while the frequency for the same condition welded outside a calorimeter is 28 Hz. The active cooling by the calorimeter reduces the energy available in the welding, consequently decreasing the open arc time. The cold wire feed exacerbates this effect as indicated by the increased short-circuit frequency of 36 Hz.

Figure 8.3a shows that during standard GMAW the voltage dropped to level corresponding to a short-circuit. It seems that the depletion of heat compromises the electron emission promoting short-circuits, i.e., the arc transitions temporarily to a lower energy transfer mode. Figure 8.4 shows that in spray mode the cooling effect of the calorimeter is balanced by the higher level of energy in spray transfer mode. There is no perceivable effect on the electrical signals, perhaps indicating that spray is better mass transfer regime to be studied using a water-flow calorimeter.

The cyclogrammes of the welding conditions (Figure 8.5 - Figure 8.7) for different transfer modes corroborate the notion that the calorimeter parameters and cold wire feed rate affect the electrical dynamics of the welds, and consequently the average power transferred to the substrate during the welding operation. Moreover, these factors affect the stability of the welding process. For instance, Figure 8.7b shows better stability than Figure 8.7c, which has the same conditions as Figure 8.7b but with an increase in cold wire feed rate.

The bead profiles show that short-circuit welds in standard GMAW are mildly affected by the calorimeter cooling, cf. Figure 8.8a-d. However, the calorimeter deeply affects CW-60% and CW-100%, shown in Figure 8.8e-l since under these conditions the welds are disrupted by the cold wire that cannot be melted by the heat available in the welding pool.

In globular transfer, the disrupting effect of the cold wire is less pronounced, as shown by Figure 8.12. Moreover, the incipient (short-circuit period less than 2 ms) short-circuits in the oscillograms did not occur in standard GMAW and CW-60% (Figure 8.3a and Figure 8.3b) but only in CW-120%, (Figure 8.3a), in all the sampled periods. For spray transfer, Figure 8.10 shows that the perturbing effect of the cold wire is negligible, though one can discern that some cold wire was not completed melted by the weld pool, for instance in Figure 8.10l.

The cross-sections in the short-circuit transfer regime (Figure 8.11) show defects as a result of the high cold wire feed rates for low energy. As the energy increases, in globular and spray transfer regimes, the defects are no longer visible in the examined cross-sections

(Figure 8.12 and Figure 8.13). The thermal efficiency values are presented first in the maximum/ minimum intervals around the average, and secondly in terms of uncertainty at 95% confidence intervals. The cooling rate imposed by the calorimeter affects the values of thermal efficiency, and this is less notable when using spray transfer, given the spread in the confidence intervals (Figure 8.16).

Based on the results of thermal efficiency the cold wire re-introduced part of the energy that would be transferred to the environment back to weld pool, notably when the cold wire feed ratio is 60%. This energy likely comes from the arc plasma and the weld pool. Increasing the cold wire feed rate to 120% the height of the weld bead increases favouring the preferential cooling through the top, likely by convection.

Higher values of efficiency can be expected for higher penetrations, provided that melting rate of the electrode is constant. In fact, Murray and Scotti [123], showed this by using a non-dimensional factor called the R_y number (Rykalin number), which was postulated earlier by Fuerschbach [124]. They modelled the penetration in terms of mass and heat contributions of the electrode for standard GMAW:

$$d = k \cdot A^a \cdot B^b \tag{8.3}$$

where d is the penetration, k is a positive constant, A is the non-dimensional mass transfer which is a function of the electrode melting rate, the viscosity of the welding pool, and the radius of the droplets; and B is the R_y number or non-dimensional heat transfer number, which is:

$$B = \frac{UIS}{\Delta H \alpha^2} \tag{8.4}$$

where $U$is the voltage, I is the current, S is travel speed, ΔH is volumetric enthalpy of base metal, and α is diffusivity of the base metal. Moreover, higher dilution entail higher efficiencies according to Kou [7].

However, for CW-GMAW this relation is not direct. For example, the dilution of CW-60% operating in globular mode does not change much for the different calorimeter conditions (Figure 8.21e), and the same happens in terms of penetration for the same condition. Nonetheless, the value of efficiency changes dramatically depending on the calorimeter conditions, varying from 65% to 75%, as show in Figure 8.18. The same trend occurs in spray transfer, for instance, observing the hardness maps one can see that the bead can loose heat from the top and bottom, and that increasing the cold wire feed rate to 120% in spray mode (Figure 8.22k) leads to the cooling preferentially through the top of the bead, thereby decreasing the efficiency (Figure 8.16c) in comparison to Figure 8.16b. Increasing the cooling rate through the increase in flow rate leads to an increase in thermal efficiency, as shown in Figure 8.16d.

The presence of martensite at the HAZ in GMAW while welding in a calorimeter is likely determined by the cooling rates experienced at the back of the plate. Likewise, at the top of the bead the cooling rate seems to be also high since the PF(G) is very thin, cf. Figures 8.23a-b. With the progressive increase in cold wire feed rate the cooling rate likely decreases, accounting for lower hardness in Figures 8.23k, while being higher at the top than near the fusion line.

Examining the microstructures near the fusion line, in Figures 8.23f, it can be seen that the microstructures are basically ferrite with no martensite present. This feature accounts for the reduction in hardness observed in Figure 8.22k. Moreover, it seems that with the increase in height promoted by the cold wire feed, the cooling at the top of the bead becomes the higher than the cooling at the fusion line, provided that the cooling at the back of the plate is reduced.

8.6 Summary

Bead-on-plate welds deposited in AISI 1020 plates were used to estimate the thermal efficiency of CW-GMAW process for two different cold wire feed rates, and compared to the efficiency of GMAW for the same cooling conditions (plate thickness and water flow on the back of the plate). These results point to the following conclusions:

1. The efficiency in CW-GMAW depends on the transfer mode, cold wire feed rate, and on the cooling conditions imposed by the measuring instrument (calorimeter) during welding;

2. When the cold wire feed rates are greater than 60% the efficiency is lower than in standard GMAW for short-circuit. For globular transfer mode, when the cold wire feed rate are lower than 60% the efficiency will be higher than standard GMAW. For spray transfer, when the cold wire feed rates are less than or equal to 60% the efficiency will be higher than standard GMAW, except when both high flow rate and high plate thickness are used; for cold wire feed rates greater than 60% the thermal efficiency will be approximately equal to the standard GMAW;

3. Qualitatively, as indicated by the through thickness hardness maps, for higher values of cold wire feed rate (greater than or equal to 60%), and low flow rate (lower than 5 l/min) the cooling rate on the top of the bead is higher than at the fusion line;

Chapter 9

Tensile Test Response of Standard Gas Metal Arc Welding Versus Cold Wire Welding Joints [1]

9.1 Overview

Increased welding productivity in the pipeline industry is fundamentally important to increasing the competitiveness of the Canadian energy industry. In order to cope with this paradigm, high productivity welding processes such as submerged arc welding (SAW) and flux-cored arc welding (FCAW) are commonly used in selected applications. However, the high nominal heat input associated with these processes can be detrimental to mechanical performance. This chapter compares the mechanical properties of joints fabricated using the standard gas metal arc welding (GMAW) versus cold wire gas metal arc welding (CW-GMAW). A set of V-groove, 45 degree joints were fabricated on ASTM A131 Gr. A steel plates, while ER 100S-G and ER90S-D2 wires were used as the electrode and cold wire, respectively. The standard GMAW joint was completely filled with 12 passes, while the CW-GMAW was filled with 8. After welding, the joints were cut and the macro and microstructures were examined through standard metallographic procedures. A combination of mechanical testing including hardness and transverse tensile test using digital image correlation (DIC) were used to evaluate the joints. The mechanical properties also suggest better performance using CW-GMAW versus the standard GMAW process.

[1]This chapter is based on the following paper: Ribeiro, R. A.; Assunção, P. D. C; Midawi, A. R. H; Braga, E. M.; and Gerlich, A. P. Weld - CWBA Journal, p. 22-28, Summer (2020).

9.2 Background

Welding science and technology is fundamental for large scale infrastructure manufacturing, given that it is main joining technique in heavy gauge joining worldwide. Two of the most important features of welding processes are productivity, the quantity of metal deposited in kg/h, and versatility indicated by the possibility of welding in different positions.

Recently McPherson [125] noted some common welding issues in large structures and summarized the basic welding processes used in such activities. Flux cored arc welding (FCAW), metal cored arc welding (MCAW), and shielded metal arc welding (SMAW) seems to be used in heavy gauge welding. However, a limiting factor for the procedures presented in his work is travel speed which is limited to 35 cm/min [14 in/min] which hinders the overall time to complete a joint.

A different class of process called hybrid-laser-arc is used in heavy-gauge welding. Roland et al. [126] reviewed the use of hybrid laser techniques in structural welding in Europe. The advantages of this technology are an increase in travel speed during welding as well as better control of the welding parameters, leading to lower level of distortion and residual stresses. The main drawbacks of these technologies are the high apparent costs and the specialized training to operate new equipments.

A possible alternative to existing high deposition welding processes, is cold wire assisted welding, such cold wire gas metal arc welding (CW-GMAW) which features higher deposition and potentially low distortion compared to standard techniques such as gas metal arc welding (GMAW). Recently, Costa et al. [55] compared the residual stresses in GMAW to CW-GMAW, concluding that CW-GMAW produced welds having lower residual stresses. Moreover, Marques et al [56] studied the fatigue behaviour of CW-GMAW and GMAW joints, concluding that distortion and fatigue resistance were improved in CW-GMAW.

This chapter reports an introductory work on the application of CW-GMAW to weld V-groove joints using a low alloy steel. This is an attempt to demonstrate the higher productivity and the acceptability of the mechanical properties (hardness and uniaxial tensile test) of the joints manufactured using CW-GMAW by the standards, and compare them to standard GMAW weld joints. Ultimately this effort seeks to demonstrate that these new welding processes could be for structural welding with higher productivity and mechanical reliability.

9.3 Experimental Methodology

9.3.1 Groove Geometry And Welding Parameters

Two welds were replicated for standard GMAW and CW-GMAW were manufactured in ASTM A 131 Gr A [127] as base metal, the electrode wire was ER 100S-G, and for CW-GMAW, the cold wire was ER 100S-G [128] as well. Table 9.1 gives the base metal and welding wires compositions.

Table 9.1: Nominal chemical composition in (.wt %) for the base metal and welding wires.

Material	C	Mn	Si	P	S	Ni	Cr	Mo	Cu	Fe
ASTM A131 Gr. A	0.21	0.53	0.5	0.035	0.035	0.02	0.02	0.02	0.02	Bal.
ER 100S-G	0.08	1.7	0.6	-	-	1.5	0.2	0.5	-	Bal.

The geometry of the welding joint is shown in Figure 9.1. Although not used in pipelines, it is important to note that use of metallic backing is common in other welding procedures, in this work a metallic back plate was used to prevent the electric arc burning-through the weld joint. The wire feed speed (WFS) in the electrode was 394 in/min [10 m/min], the voltage was 34 V, the CTWD was 19 mm for all welds, and travel speed was 25 in/min [63.5 cm/min]. These parameters were used for all welding passes and for both standard GMAW and CW-GMAW.

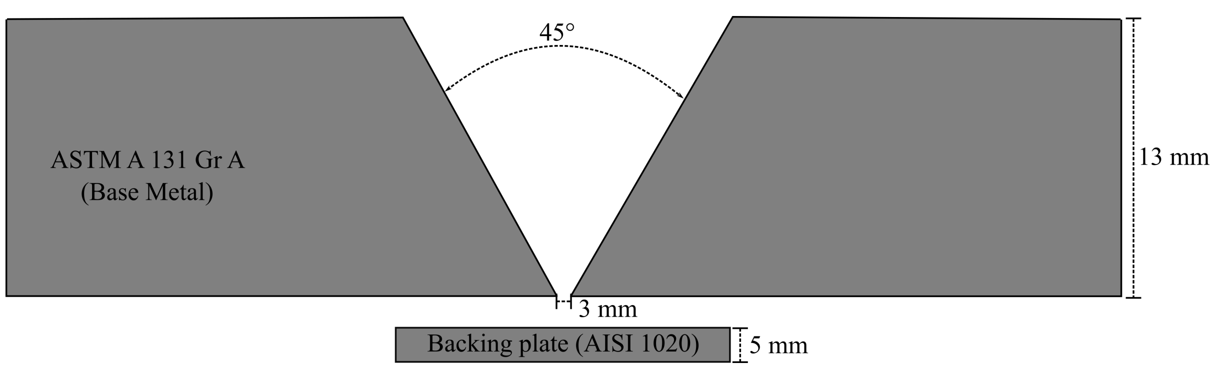

Figure 9.1: Groove schematics used to manufacture the weld joints.

The diameter of the electrode wire was 1.2 mm, and of the cold wire was 0.9 mm. The cold wire rate is given as a percentage of the mass rate of the electrode wire. In CW-GMAW the mass deposition rate was 50%

The cold wire feed speed was 498 in/min [12.65 m/min] . The shielding gas was Ar-25% CO_2 at a flow of 40 ft^3/h [19 l/min]. The welding power source used was a Lincoln R500 operating in constant voltage with a Fanuc ArcMate 120i robotic arm. Figure 9.2 shows the welding set-up for CW-GMAW. For the standard GMAW the same set-up was used but without the cold wire injector.

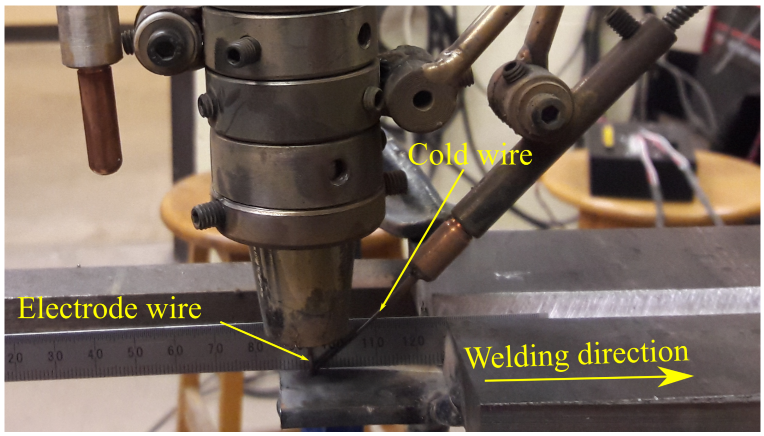

Figure 9.2: Detail showing the welding set-up for the CW-GMAW.

9.3.2 Metallographic Characterization and Tensile Test

After completing the welds, one joint was cross-sectioned into three specimens for metallographic examination and hardness maping. The specimens were subjected to standard metallographic procedures to analyse the macrostructure. The hardness was performed using a 500 gf indentation load and 10 s of dwell time. Tensile tests with digital image correlation (DIC) were performed with a cross-head speed of 1 mm/min. The joints were machined transversally to the joint longitudinal axis, according to ASTM E8-2010 [129].

The geometry of the tensile specimen is shown in Figure 9.3 the thickness of the tensile coupons was 2 mm. In order to measure the actual stress on the tensile coupon, a uniform gauge specimen was machined through the weld. The weld metal zone is situated at the middle of the tensile specimen, and test is used here as a comparative basis for the strength of the weld metal zone and the HAZ. Two tensile specimens were used, since this work is just to show that welds are acceptable in regards to metal construction standards.

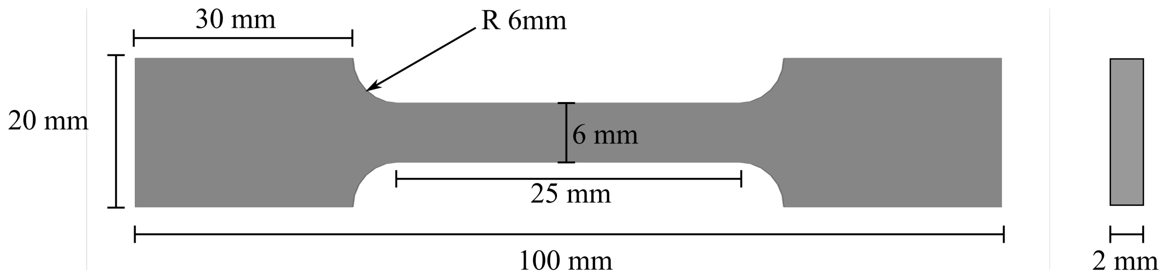

Figure 9.3: Schematic tensile coupon in which the weld metal is situated at the middle of the specimen.

9.4 Results

9.4.1 Oscillograms

Figure 9.4 shows the oscillograms for welds manufactured using GMAW and CW-GMAW. It can be observed that all the welds were performed in spray transfer mode, and using the same welding parameters for all the passes. The oscillograms for standard GMAW (Figure 9.4a, Figure 9.4c, and Figure 9.4e) indicate that the electric arc behaves similarly for root, fill, and cap passes showing the absence of short-circuits and consequently spatter.

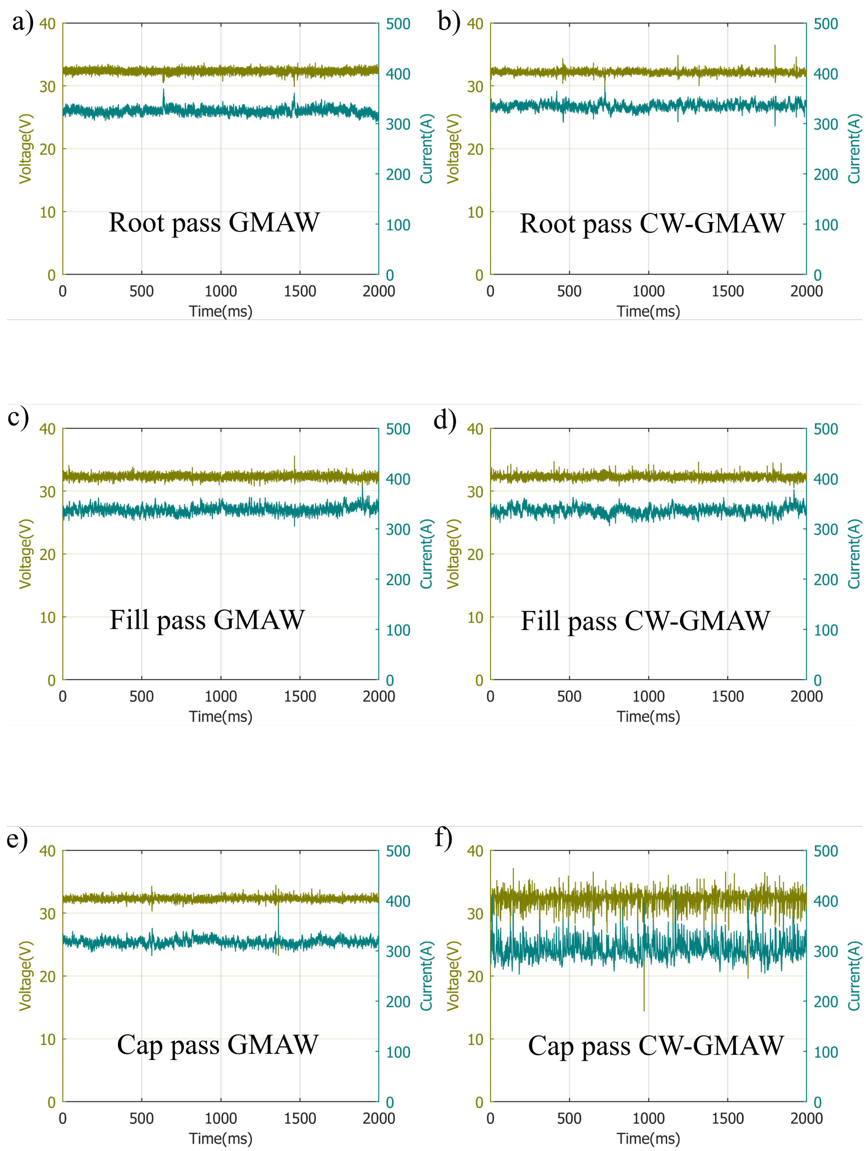

Figure 9.4: Oscillograms for standard GMAW and CW-GMAW showing representative oscillograms: for root pass; fill pass; and cap passes.

However, the oscillograms for CW-GMAW (Figure 9.4b, Figure 9.4d, and Figure 9.4f) show that the welding parameter has the same stability level as GMAW only for root and fill passes. The cap pass in CW-GMAW presents instability, likely due to the high cold wire fraction, which promotes increased droplet detachment as indicated by the spikes in voltage. This increase in droplet detachment frequency is likely caused by the 50% cold wire feed rate, which was also observed in Chapter 3, and causes the current to increase while welding in constant voltage due to the source internal current regulation through wire feed speed.

9.4.2 High Speed Images

High speed images for standard GMAW are shown in Figure 9.5. The sidewalls are completely covered by the weld pool indicating good wettability, and the diameter of the droplets is smaller than that of the electrode, confirming that the metal transfer was spray. When the droplets impinge the weld pool, there is a disruption that might cause spatter or short-circuit of the arc, while in the case a longer droplet attached the electrode wire touches the weld pool.

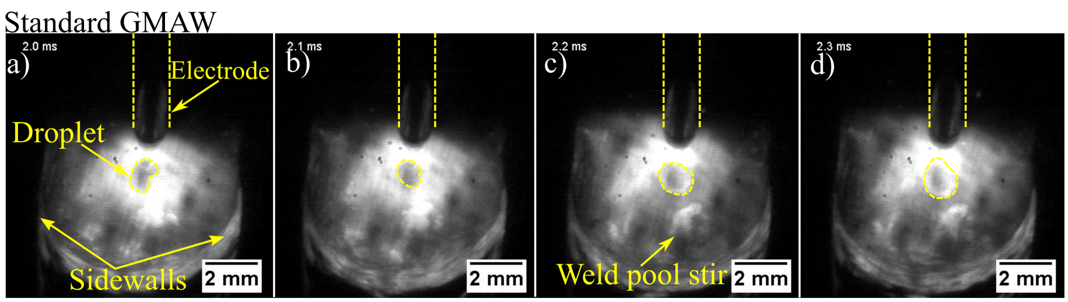

Figure 9.5: Metal transfer for standard GMAW.

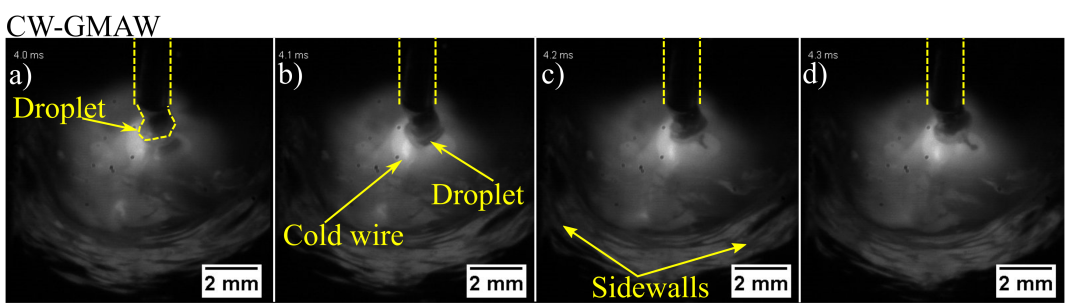

Figure 9.6: Metal transfer for standard CW-GMAW.

Figure 9.6 shows a image from high speed videography for CW-GMAW used in the V-groove joints. The wetting of the sidewall by the weld pool is effective, and the cold wire feed are seen at the edge of the weld pool, in Figure 9.6b. This is consistent with prior work [92] which found that, for cold wire feed rates of this order (50%), the arc does not climb the cold wire. Again the droplet diameter confirms that a spray transfer regime was achieved.

9.4.3 Macrographs And Hardness

Figure 9.7 shows the Vickers hardness maps performed on the welding cross-sections. It can be observed that using a cold wire feed can increase the hardness of the weld metal, suggesting that different cooling rates occur in the weld pool and weld joint when employing cold wire assisted welding. One can observe in Figure 9.7a the average hardness on the cap pass is 254 HV, and is approximately 200 HV in the boundaries between the passes. However, in CW-GMAW (Figure 9.7b) the hardness in the cap pass reaches 360 HV with the same hardness for the boundaries between the passes. Further ultrasonic tests indicated that the GMAW joint presented lack of fusion, while the CW-GMAW joint was exempt of defects.

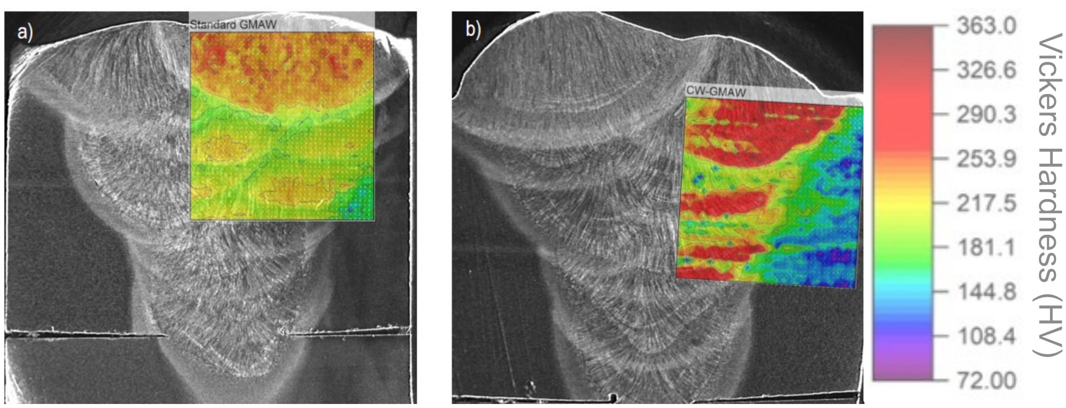

Figure 9.7: Hardness maps of the welds: a) Standard GMAW; and b) CW-GMAW.

This improvement in weld metal hardness in CW-GMAW is likely due to the presence of harder microstructures such as acicular ferrite, for example. This indicates that the increase in cold feed can lead to the nucleation of harder microstructures, therefore causing an improvement on the ultimate tensile response.

9.4.4 Tensile Tests

Engineering Stress-Strain Curves

Figure 9.8 shows the uniaxial tensile tests for standard GMAW and CW-GMAW joints displayed as engineering stress and strain. One can observe that GMAW-2 (Figure 9.8a) failed before reaching the ultimate stress, which is likely due to presence of an internal defect (such as porosity) in the weld metal that caused the sudden failure.

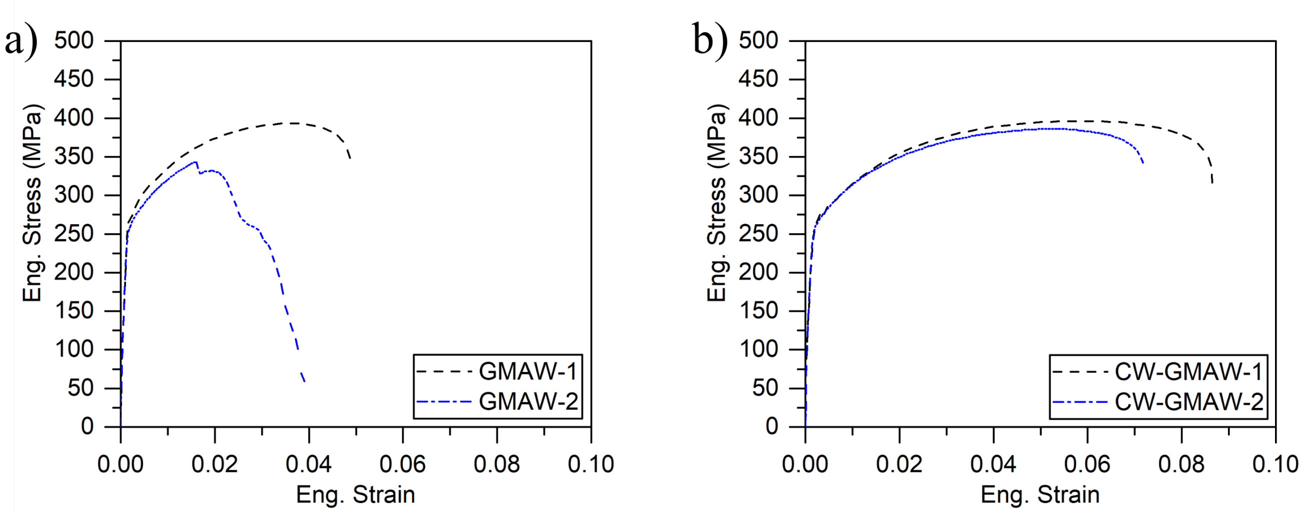

Figure 9.8: Engineering stress-strain curves for the welded joints: a) Standard GMAW; and b) CW-GMAW.

However, the CW-GMAW specimen exhibited a ductile behaviour without premature failure of the tensile specimen, which qualifies it to meet the common standard requirements for metal construction, such as ASTM A370 [130] for example.

DIC Strain Maps

Figure 9.9 shows the strain accumulation across a tensile sample demonstrating that the failures happened at the base metal. This was due to the over-matching [2] of the welded

[2]When the yielding stress of the weld metal is higher than the yielding stress of the base metal, this is called over-matching. On the the other hand, when both yielding stresses are equal, this is even-matching. When the weld metal yielding stress is lower than the base metal yielding stress, this is under-matching.

metal, which is requirement for heay-gauge welding, obtained through the selected welding wires. This is a common practice in welding as recommended by Koçak [131]. This overmatching prevents the yielding of the weld metal, in order to avoid strain concentrations in the welds.

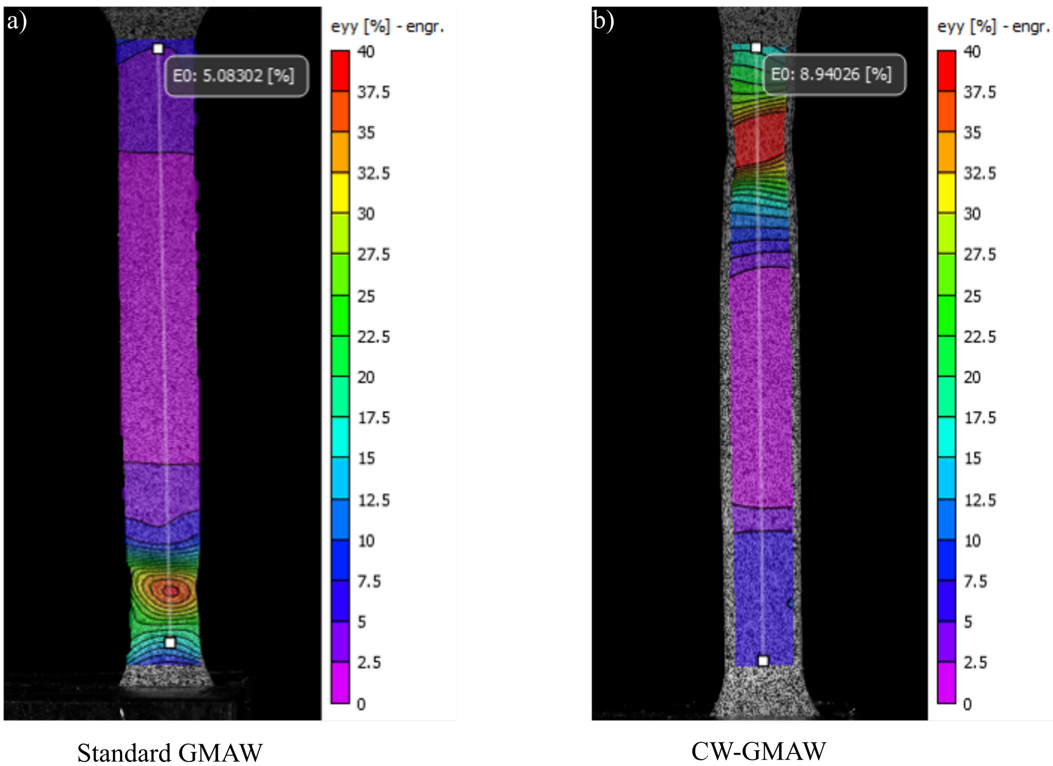

Figure 9.9: DIC iso-strain maps showing the local engineering strain distribution in the y-direction across the tensile specimen: a) Standard GMAW (GMAW-1); and b) CW-GMAW (CW-GMAW-1).

In Figure 9.9 the DIC maps show that both specimens failed outside the weld metal. Since the DIC maps show GMAW-1 and CW-GMAW-1 specimens. However, it must be emphasized that GMAW-2 failed within the weld metal zone, due to a defect present in such zone; and that no defect was found in the weld metal of CW-GMAW specimens.

9.5 Discussion

9.5.1 Welding Process and Characterization

The electrical signals indicate that the electric arc can better accommodate a higher fraction of cold wire when during the fill and cap passes as shown Figures 9.4b and 9.4d, whereas one can see that the cap pass of CW-GMAW is less stable than in standard GMAW, cf. Figure 9.4e and Figure 9.4f. This seems to indicate the cold wire fraction must be reduced for the cap pass, probably due to higher height of the welding pool in CW-GMAW versus standard GMAW.

The macrographs did indicate lack of fusion in standard GMAW specimen, indicating that the travel speed used in this work was excessive for the amount of metal deposited. However, the CW-GMAW specimens did not present any defect, indicating that the relation of travel speed and metal deposition rate was adequate, probably due to higher mass deposited while using CW-GMAW process.

The hardness seems to indicate that the introduction of one cold wire in CW-GMAW promotes the nucleation of higher hardness microstructures. This would be only possible if the cooling rate of the weld pool were increased by the cold wire addition. It seems that this hardness measurements support this for CW-GMAW joints but more studies are needed to clarify the issue.

9.5.2 Comparison to Other Welding Process Used In Heavy Gauge Welding

Submerged arc welding (SAW)is commonly used in heavy-gauge welding applications requiring high deposition rates. This process is restricted to 1G welding position and also imposes a high distortion due to the high energy transferred during welding. While, the results presented here are for CW-GMAW, and, constitute a first attempt to apply cold wire assisted processes to large infrastructure applications, CW-GMAW might represent an alternative to the SAW process since it presents high versatility and possibly transfers less energy during welding. Future work will assess its productivity in comparison to SAW for a wide range of parameters.

9.6 Summary

45 degrees V-groove welds were successfully manufactured using GMAW and CW-GMAW processes to verify the effect of cold wire feed on the mechanical properties and overall productivity with potential application to infra-structural applications. The following conclusions can be drawn from the results:

1. The productivity of CW-GMAW process is higher, enabling a 27% improvement in welding time, since the grooves are filled in 8 passes in CW-GMAW versus the required 11 by standard GMAW;
2. The thermal signature of CW-GMAW differs from standard GMAW, likely due to a different heat diffusion mechanism, as can be deduced from the hardness maps;
3. The CW-GMAW can offer superior mechanical performance over the GMAW joint, for the same welding parameters, due to an increase in hardness with the introduction of cold wire.

Chapter 10

Conclusions And Recommendations

10.1 Comprehensive Conclusion

The cold wire gas metal arc welding (CW-GMAW) was first developed for shipbuilding in 2010 [64]. While this technique has attracted increasing attention this is the first study to attempt a comprehensive understanding of the process from metal transfer, to thermal efficiency, culminating in mechanical properties of the welds. The data gathered during this study highlights the distict nature of CW-GMAW compared to standard GMAW process, with different interplay of process parameters and different energy transfer mechanisms.

10.1.1 Process Maps

The reported results on metal transfer showed an increase in the average instantaneous current, which increases the Lorentz force during the metal transfer, when high fractions of cold wire are used in spray. Consequently, in spray transfer the cold wire feed will refine the droplets as result of the increase of current, but also increase the electrode melting rate which is function of the current, for a given combination of voltage and current.

Moreover, the pinning of the arc promoted by the cold wire stabilizes the metal transfer and has a desirable effect, particularly for pipeline welding. It was also found that the increase in height promoted by the cold wire feeding causes heat losses through the bead top at rates likely similar to the heat transfer through bead bottom to the work-piece.

The data gathered in this thesis may be presented in process maps which will help future users in particular applications or future research. For instance, a common process map would have dilution and penetration as a function of the cold wire feed rate. Figure 10.1 shows such process maps, in which the penetration information is important for welding a joint, and the dilution will be used for welding overlays. Moreover, such process maps offer a qualitative information about the cross-section morphology of the welds.

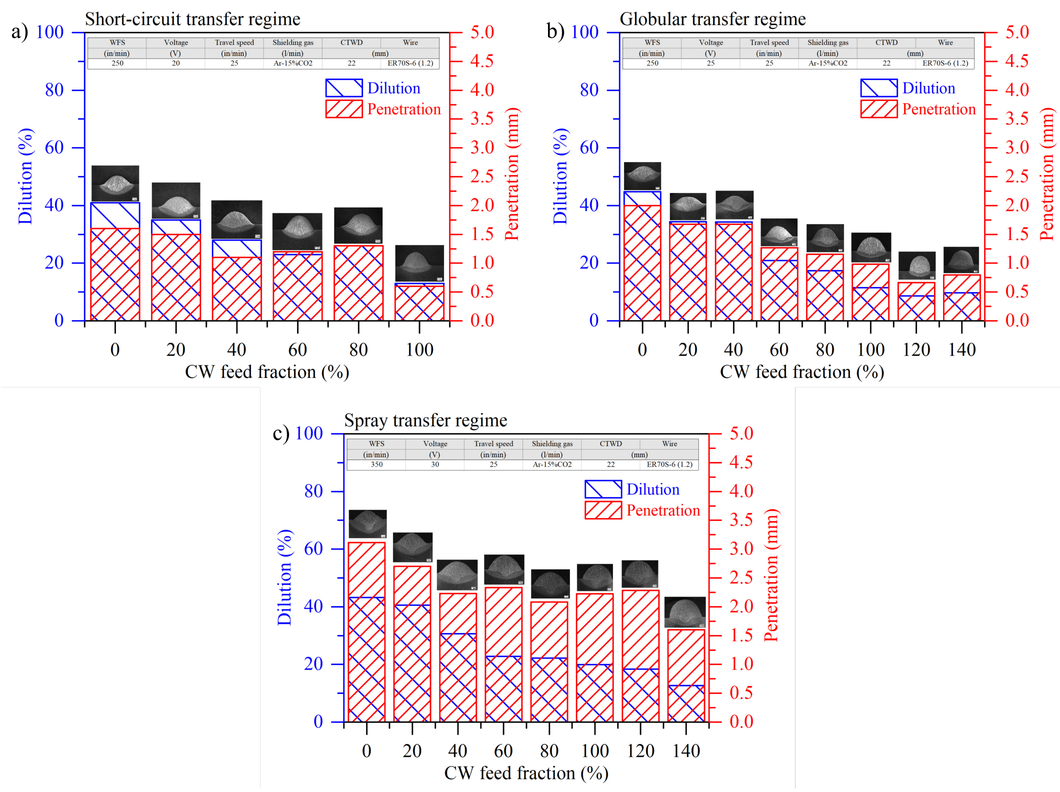

Figure 10.1: Process maps for GMAW: a) Low arc power; b) Intermediate arc power; and c) High arc power.

It is important to mention that such process maps were constructed for the welding parameters discussed in Chapter 3 which cannot be extrapolated for other parameters.

10.1.2 Cathode Spots Migration in CW-GMAW

Another subject that was discussed in this thesis but not properly explained is the displacement of the arc to the cold wire with the increase in cold wire for all natural transfer regimes. Figure 10.2 shows a high speed image of standard pulsed gas metal arc welding (P-GMAW) with 100% Argon as shielding gas. This experiment was perform after the experiments directly linked to the thesis as an effort to understand the mechanisms of the arc pinning to the cold wire [132].

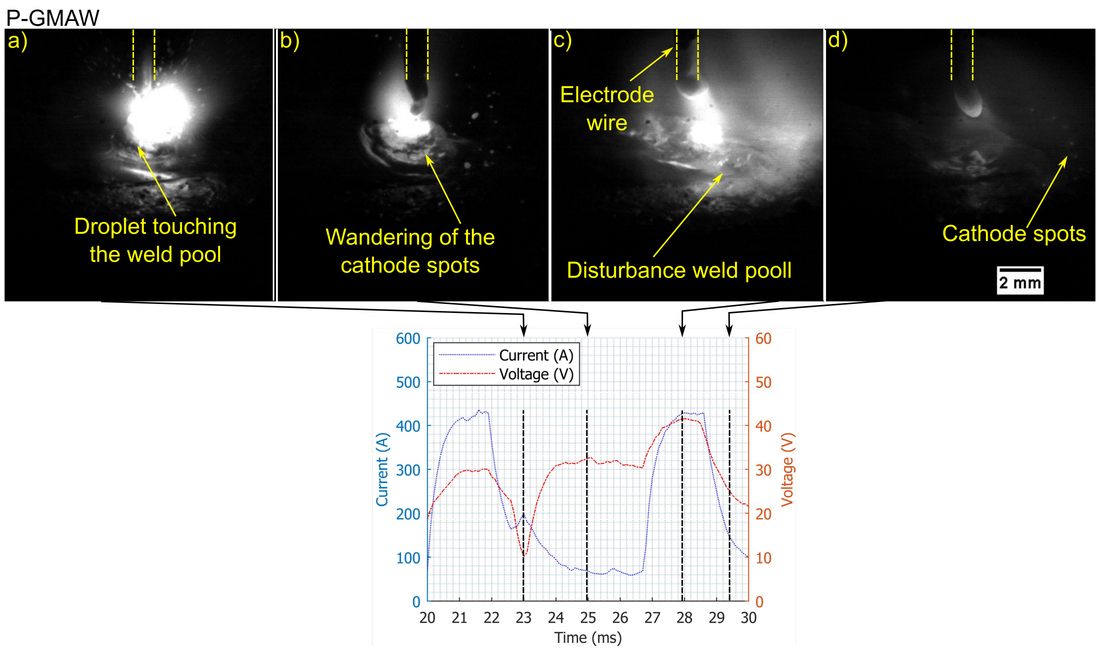

Figure 10.2: High speed image for standard P-GMAW welded with 100% Ar shielding gas showing the cathode spots near the weld pool.

It can be noticed in Figure 10.2 that the cathode spots are near the weld pool. These spots are emitting sites formed during welding which the electric arc running. The mechanisms that explain the formation of the cathode spots were reviewed by Lowke [133] and are beyond the scope of the present section.

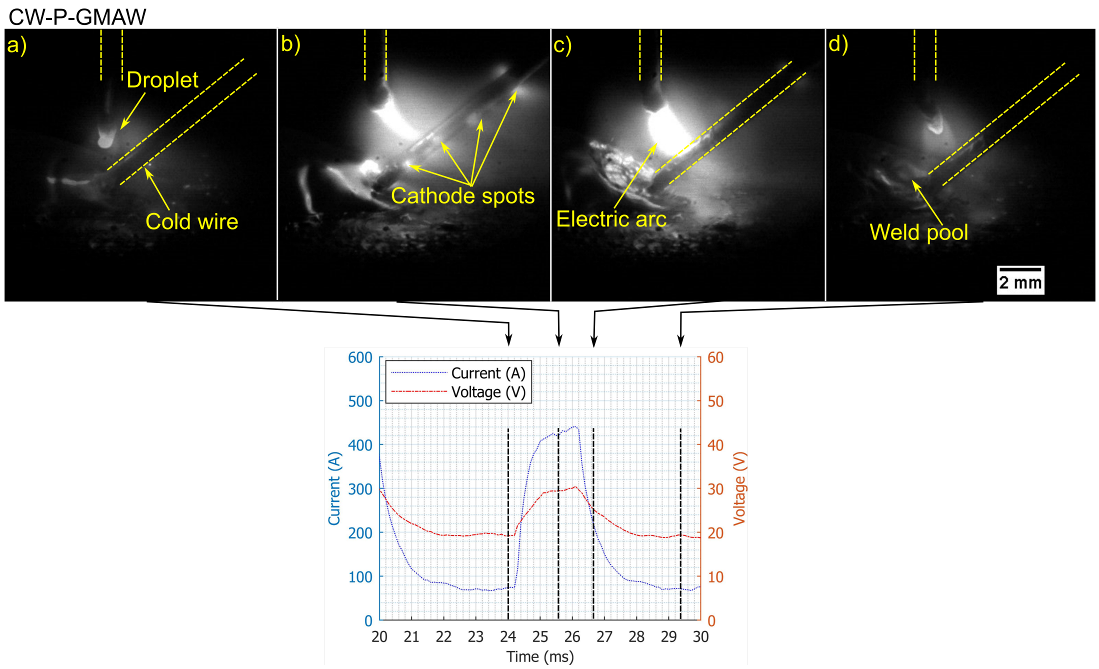

Figure 10.3: High speed image for standard CW-P-GMAW welded with 100% Ar shielding gas showing the cathode spots near the weld pool.

Figure 10.3 shows the cathode spots on the cold wire. Differently, from Figure 10.2, the welding appears to be more stable, since there is not wandering of the cathode spot on the surface of the weld pool. Basically, the arc appears to attach to the cold wire because the cathode spots are displaced to there. The mechanism which attempts to explain their displacement to the cold wire is currently under discussion elsewhere [132] and out of the scope of the present discussion.

10.1.3 Melting Efficiency

As result of this increase in height for high cold wire feed rates, the efficiency of the process decreases for the same metal transfer regime, indicating that the melting efficiency of the CW-GMAW is likely higher than standard GMAW. This can be shown using the definition of melting efficiency:

$$\eta_m = \frac{\left(A_{base} V t_{weld}\right) H_{base} + \left(A_{filler} V t_{weld}\right) H_{filler}}{\eta_a U I t_{weld}} \tag{10.1}$$

where η_m is the melting efficiency, A_{base} is the area of the weld metal due to the base metal, A_{filler} is the area of weld metal due to the filler metal, t_{weld} is the welding time, H_{base} is the volumetric melting enthalpy of the base metal, H_{filler} is the volumetric melting enthalpy of the filler metal, U is the instantaneous average voltage, I is the average instantaneous current, and η_a is the process thermal efficiency.

Equation 10.1 indicates that, since the thermal efficiency of CW-GMAW is lower than standard GMAW, for some cases, for example in short-circuit. Moreover, since no welds were performed for thermal efficiency measurements in actual narrow gaps, it is expected that the values measured will differ from the efficiency in narrow groove welds. However, the welds in thick plates can be taken as an approximation to real narrow groove welds, considering the geometry and aspect ratio of the gap versus plates.

The numerator of Equation 10.1 for CW-GMAW is higher than in standard GMAW, then the result in melting efficiency will be also higher for CW-GMAW. Therefore more heat is used to melt and the deposit the beads during welding, and less is transferred to the work-piece, resulting in lower dilution and penetration. In addition, the productivity of CW-GMAW is higher, offering superior deposition per pass and improved tensile response.

In summary, this study has shown that CW-GMAW is a viable alternative for standard CW-GMAW for narrow gap welding(NGW) in the flat position or any other welding application where low energy transfer to substrate, low dilution, low penetration, might be essential requirements.

10.1.4 Cold Wire Composition

ER70S-6 was selected as cold wire for the welding process due to its widespread use and availability. However, it must be emphasised that the melting efficiency depends on the wire material, which will determine the volumetric melting enthalpy. Moreover, even the thermal efficiency will change since the different materials possess different thermal conductivities which will affect the heat losses on the substrate during welding.

In addition, a change on welding material will likely determine a change in the quantity of cold wire that can be accommodated by the weld pool, due to a different heat capacity. Thus, the user has to bear in mind that the results reported here for thermal and melting efficiencies apply only steel welds, in flat position, for the boundary conditions.

10.1.5 Optimization Of Experimental Conditions For Future Work

The uncertainty analysis can help with the planning of future experiments. For instance, if the uncertainty in thermal efficiency (η):

$$\left(\frac{U_\eta}{\eta}\right)^2 = \left(\frac{U_{\bar{\dot{m}}}}{\bar{\dot{m}}}\right)^2 + \left(\frac{U_{\bar{\Delta T}}}{\bar{\Delta T}}\right)^2 + \left(\frac{U_U}{U}\right)^2 + \left(\frac{U_I}{I}\right)^2 \tag{10.2}$$

where $\bar{\dot{m}}$ is the average water mass flow, $\bar{\Delta T}$ is average difference temperature between outlet and inlet, U and I are the average voltage and current respectively. From Equation 10.2 it can be seen that the overall thermal efficiency uncertainty does not depend particularly on any variable. However, Figure 7.12 shows that the highest uncertainty is due to current measurement which implies that higher attention should be paid on how this variable is measured.

In order to optimize the measurement uncertainty of thermal efficiency so that the overall uncertainty be approximately 1%, each variable should be measured with at least 0.5%. Consequently, future experiments can be designed to reduce the uncertainty on thermal efficiency using the values found of uncertainty measurement in each variable.

10.2 Suggestions For Future Work

This work has raised some possible suggestions for future work.

1. Due to the high rate of deposition, defects occur in the root pass during NGW, highlighting the need to further study parameters and process configurations. Moreover, it remains to be established whether CW-GMAW is feasible for other welding positions than the flat position, and its effect on other metals such as stainless steel and aluminium.

2. A study on the influence of gas composition on the static and dynamic characteristics of the welding power source while welding V-groove welds. This response should be correlated to changes in dilution, penetration, and hardness. These promote changes in microstructures, which should be characterized according to ASTM E562-19 (*Standard Test Method for Determining Volume Fraction by Systematic Manual Point Count*). Calorimetry tests will be used to measure the energy delivered to the substrate and correlated to the percentage volume fraction of microstructures observed;

3. A thorough study on the use of CW-GMAW for narrow gap welding, specifically for root passes should be performed. Specifically, different types of backing should be tested, for instance metallic, ceramic, and no backing at all. Also, different current pulsation waveforms should be used in order to determine which one provides the best stability.

4. The methodology of the gross-heat input proposed by Liskevych and Scotti [29] should be extended to weld joints of different geometries to verify the effect of the joint geometry on the gross heat input. Moreover, as the gross heat input was proposed using a liquid nitrogen calorimeter, the metrological equivalence of water-flow and liquid nitrogen calorimeters should be established;

5. The effect of hot-wire polarity variation on the thermal efficiency and mechanical properties should be examined and compared to the effect of cold wire on thermal efficiency and mechanical properties of joints for ferrous and non-ferrous materials;

6. Lastly, other welding positions such as vertical upward, vertical downward, and overhead should examined using CW-GMAW. A study showing the feasibility of these positions for CW-GMAW in conjunction with different welding joint geometries would show the process capabilities and qualify this this technique for field applications.

10.3 List Of Contributions

The following list consists of papers or submitted as part of thesis research.

10.4 Manuscripts Published/Submitted As First Author

1. **Ribeiro, R.A.**, Assunção, P.D., Dos Santos, E.B., Ademir Filho, A.C., Braga, E.M. and Gerlich, A.P., 2019. Application of cold wire gas metal arc welding for narrow gap welding (NGW) of high strength low alloy steel. Materials, 12(3), p.335.

2. **Ribeiro, R.A.**, Dos Santos, E.B.F., Assunção, P.D.C., Braga, E.M. and Gerlich, A.P., 2019. Cold wire gas metal arc welding: droplet transfer and geometry. WELDING JOURNAL, 98(5), pp.135S-149S.

3. **Ribeiro, R.A.**, Assunção, P.D.C., Dos Santos, E.B.F., Braga, E.M. and Gerlich, A.P., 2020. An overview on the cold wire pulsed gas metal arc welding. Welding in the World, 64(1), pp.123-140.

4. **Ribeiro, R. A.**, Assunção, P.D.C.; Dos Santos, E.B.F.; Braga, E.M.; and A.P. Gerlich. Globular to spray transfer in cold wire gas metal arc welding. Welding Journal Research Supplement, 2020. *Submitted for publication.*

5. **Ribeiro, R A.**; P.D.C. Assunção; E.B.F. Dos Santos; K.J. Daun; and A. P. Gerlich. Uncertainty analysis of water–flow calorimeter while welding in short-circuit and spray transfer regimes. Welding in the World, 2020.

6. **Ribeiro, R A.**; Assunção, P.D.C.; Dos Santos, E.B.F; Daun, K.J.; and Gerlich, A.P. Welding thermal efficiency of cold wire gas metal arc welding. Welding in the World, 2020. *Under revision for submission for publication.*

7. **Ribeiro, R A.**; P.D.C. Assunção; Midawi, A.R.H; Braga, E.M; and Gerlich, A.P. Tensile test response of standard gas metal arc welding versus cold wire, and double cold wire gas metal arc joints. Weld - CWBA Journal, p.22-28, Summer, 2020.

8. **Ribeiro, R A.** and Gerlich, A. P. The arc stability mechanism and metal transfer during cold wire pulsed gas metal arc welding. Manuscript under revision. To be submitted to the Journal of Manufacturing Process, 2020.

10.5 Manuscripts Published/Submitted As Second Author

1. Assunção, P.D.A.C.; **Ribeiro, R.A.**; Dos Santos, E.B.; Gerlich, A.P.; and de Magalhães Braga, E., 2017. Feasibility of narrow gap welding using the cold-wire gas metal arc welding (CW-GMAW) process. Welding in the World, 61(4), pp.659-666. https://link.springer.com/article/10.1007/s40194-017-0466-5.

2. Assunção, P.D.C.; **Ribeiro, R.A.**; Dos Santos, E.B.F.; Braga, E.M.; and Gerlich, A.P., 2019. Comparing CW-GMAW in direct current electrode positive (DCEP) and direct current electrode negative (DCEN). The International Journal of Advanced Manufacturing Technology, 104(5-8), pp.2899-2910. https://link.springer.com/article/10.1007/s00170-019-04175-2.

3. Assunção, P.D.C.; **Ribeiro, R.A.**, Moreira, P.M.G.P.; Braga, E.M.; and Gerlich, A.P., 2019. A preliminary study on the double cold wire gas metal arc welding process. The International Journal of Advanced Manufacturing Technology 106 (11), pp. 5393–5405 (2020). https://link.springer.com/article/10.1007/s00170-020-05005-6.

4. Ribeiro, P.P.G; **Ribeiro, R.A.**; Assunção, P.D.C.; Braga, E.M; Gerlich, A.P. Metal transfer mechanisms in hot-wire gas metal arc welding (HW-GMAW). Welding Journal Research Supplement. *Accepted for publication on March 19th, 2020.*

References

[1] National Energy Board of Canada. Canada's Energy Future 2016. Technical report, National Energy Board, 2016.

[2] Environment Canada and Climate Chnage. NOVA Gas Transmission Ltd. – 2017 NGTL System Expansion Project: Review of related upstream greenhouse gas emissions estimates. Technical report, Canada, Environment and Climate Chnage, 2016.

[3] Paulo J Modenesi. Introdução à Física do Arco Elétrico E sua Aplicação na Soldagem dos Metais, 2102.

[4] W. J. Greene. An analysis of transfer in gas-shielded welding arcs. *Transactions of the American Institute of Electrical Engineers, Part II: Applications and Industry*, 79(3):194–203, 1960.

[5] J N DuPont and A R Marder. Thermal Efficiency of Arc Welding Processes. *Welding Journal*, 74(December):406s–416s, 1995.

[6] Olga Liskevych, Luisa Quintino, Louriel Oliveira Vilarinho, and Américo Scotti. Intrinsic errors on cryogenic calorimetry applied to arc welding. *Welding in the World*, 57(3):349–357, 2013.

[7] Sindo Kou. *Welding Metallurgy*. John Wiley & Sons, Inc., Hoboken, NJ, USA, second edition, oct 2002.

[8] P. W. Fuerschbach and G. A. Knorovsky. A Study of Melting Efficiency in Plasma Arc and Gas Tungsten Arc Welding. *Welding Journal*, 70(11):287297, 1991.

[9] J. C. Ion, K. E. Easterling, and M. F. Ashby. A second report on diagrams of microestrucuture and hardnes for Heat-Affected Zones in welds. *Acta Metallurgica*, 32(11):1949–1962, 1984.

[10] J.F. Lancaster. *The Physics of Welding*. Pergamon Press, Oxford, UK, 2nd edition, 1986.

[11] P.W. Fuerschbach. Energy Transfer Efficiencies (ETE) for Fusion Welding Processes, 2004.

[12] America Welding Society (AWS). A vision for welding industry. Technical report, AWS, 2015.

[13] Guy Quenneville. Latest CP derailment spilled 5 times as much oil as Husky pipeline leak in 2016, 2020.

[14] The Canadian Press. TransCanada plans $ 160M natural gas pipeline expansion to meet rising demand in Ontario, jul 2017.

[15] D. Yapp and S. A. Blackman. Recent developments in high productivity pipeline welding. *Journal of the Brazilian Society of Mechanical Sciences and Engineering*, 26(1):89–97, 2004.

[16] R. Miranda, A. Costa, L. Quintino, D. Yapp, and D. Iordachescu. Characterization of fiber laser welds in X100 pipeline steel. *Materials and Design*, 30(7):2701–2707, 2009.

[17] Y I Komizo. Overview of Recent Welding Technology Relating to Pipeline Construction. *Transactions of JWRI*, 37(1):1–5, 2008.

[18] Wojciech Suder, Supriyo Ganguly, Stewart Williams, and Bagus Yudodibroto. Root stability in hybrid laser welding. *Journal of Laser Applications*, 29(2):022410, 2017.

[19] Paulo Villani Marques and Paulo José Modenesi. Algumas equações úteis em soldagem (Some handy equations for welding). *Soldagem & Inspeção*, 19(1):91–101, mar 2014.

[20] Y-S. Kim and T. W. Eagar. Analysis of Metal Transfer in Gas Metal Arc Welding. *Welding Journal*, 72(6):269s–278s, 1993.

[21] D R Needham, J C, Cooksey, C J, and Milner. Metal transfer in inert-gas-shielded-arc welding. *British Welding Journal*, 7(2):101–114, 1969.

[22] J. C. Amson. Lorentz force in the molten tip of an arc electrode. *British Journal of Applied Physics*, 16(8):1169–1179, aug 1965.

[23] L. A. Jones, T. W. Eagar, and J. H. Lang. Magnetic forces acting on molten drops in gas metal arc welding. *Journal of Physics D: Applied Physics*, 31(1):93–106, 1998.

[24] John Norrish. A review of metal transfer classification in arc welding, 2003.

[25] Danut Iordachescu and Luisa Quintino. Steps toward a new classification of metal transfer in gas metal arc welding. *Journal of Materials Processing Technology*, 202(1-3):391–397, 2008.

[26] Américo Scotti, Vladimir Ponomarev, and William Lucas. A scientific application oriented classification for metal transfer modes in GMA welding. *Journal of Materials Processing Technology*, 212(6):1406–1413, 2012.

[27] Américo Scotti, Ruham Pablo Reis, and Olga Liskevych. Modelo descritivo do fluxo de calor em soldagem a arco visando o conceito de calor imposto efetivo. *Soldagem & Inspeção*, 17(2):166–172, jun 2012.

[28] Daniel Rosenthal. Mathematical theory of heat distribution during welding and cutting. *Wekding Journal*, 20(5):220s–234, 1941.

[29] Olga Liskevych and Américo Scotti. Determination of the gross heat input in arc welding. *Journal of Materials Processing Technology*, 225:139–150, 2015.

[30] A. Haelsig and P. Mayr. Energy balance study of gas-shielded arc welding processes. *Welding in the World*, 57(5):727–734, 2013.

[31] A. Haelsig, M. Kusch, and P. Mayer. New findings on the efficiency of gas shielded arc welding. *Welding in the World*, 56(11-12):98–104, 2012.

[32] K. Hurtig, I. Choquet, A. Scotti, and L. E. Svensson. A critical analysis of weld heat input measurement through a water-cooled stationary anode calorimeter. *Science and Technology of Welding and Joining*, 21(5):339–350, 2016.

[33] A. Wells. Heat flow in welding. *Welding Journal*, 31(5):263s–267s, 1952.

[34] Akira Okada. Application of Melting Efficiency in Welding and its Problems. *Journal of the Japan Welding Society*, 46(2):53–61, 1977.

[35] Cynthia L. Jenney and Annette O'Brien, editors. *Welding Handbook: Welding Science and Technology*, volume 1. American Welding Society (AWS), 2001.

[36] J. N. DuPont and A R Marder. Dilution in single pass arc welds. *Metallurgical and Materials Transactions B*, 27(3):481–489, jun 1996.

[37] William Hackenhaar, Arnaldo R. Gonzalez, Ivan G. Machado, and José A. E. Mazzaferro. Welding parameters effect in GMAW fusion efficiency evaluation. *The International Journal of Advanced Manufacturing Technology*, 94(1-4):497–507, jan 2018.

[38] J. Norrish. *Advanced Welding Processes*, volume 1. Woodhead Publishing Limited, Cambridge, 2006.

[39] T. Nakamura and K. Hiraoka. Ultranarrow GMAW process with newly developed wire melting control system. *Science and Technology of Welding and Joining*, 6(6):355–362, dec 2001.

[40] Liming Liu, Disheng Fang, and Gang Song. Experimental Investigation of Wire Arrangements for Narrow-Gap Triple-Wire Gas Indirect Arc Welding. *Materials and Manufacturing Processes*, 6914(August 2016):1–7, 2015.

[41] R. Phaonaim, M. Yamamoto, K. Shinozaki, M. Yamamoto, and K. Kadoi. Development of a heat source model for narrow-gap hot-wire laser welding. *Yosetsu Gakkai Ronbunshu/Quarterly Journal of the Japan Welding Society*, 31(4):3–6, 2013.

[42] VY. Malin. Monograph on Narrow-Gap Welding technology. Technical report, Welding Research Council (WRC), New York, 1987.

[43] Hiroshi Arita, Tomokazu Morimoto, Shigeo Nagaoka, and Toshihiko Nakano. Development of Advanced 3-Electrode MAG High-Speed Horizontal Fillet Welding Process. *Welding in the World*, 53(5):35–43, 2009.

[44] M. Häßler, S. Rose, and U. Füssel. The influence of arc interactions and a central filler wire on shielding gas flow in tandem GMAW. *Welding in the World*, 60(4):713–718, jul 2016.

[45] Y.M. Li, K.H., Chen, J.S. and Zhang. Double-Electrode GMAW Process and Control A novel welding process adds a GTAW torch to a conventional. *Wekding Journal*, 86(8):231s–237s, 2007.

[46] Kh Li and Ym Zhang. Consumable double-electrode GMAW-Part 1: The process. *Welding Journal*, pages 11–17, 2008.

[47] K.H. Li and Y.M. Zhang. Consumable Double-Electrode GMAW Part II : Monitoring , Modeling , and Control. *Wekding Journal*, 87(February):44s–50s, 2008.

[48] T. Xiang, H. Li, C. Q. Huang, H. L. Wei, J. X. Li, and Y. Gao. The metal transfer behavior and the effect of arcing mode on metal transfer process in twin-arc integrated cold wire hybrid welding. *International Journal of Advanced Manufacturing Technology*, pages 1–8, 2016.

[49] Mohsen Mohammadijoo, Stephen Kenny, Laurie Collins, Hani Henein, and Douglas G. Ivey. Influence of cold-wire tandem submerged arc welding parameters on weld geometry and microhardness of microalloyed pipeline steels. *The International Journal of Advanced Manufacturing Technology*, 88(5-8):2249–2263, feb 2017.

[50] Mohsen Mohammadijoo, Laurie Collins, Hani Henein, and Douglas G. Ivey. Evaluation of cold wire addition effect on heat input and productivity of tandem submerged arc welding for low-carbon microalloyed steels. *The International Journal of Advanced Manufacturing Technology*, 92(1-4):817–829, sep 2017.

[51] Karsten Günther, Jean Pierre Bergmann, and Dirk Suchodoll. Hot wire-assisted gas metal arc welding of hypereutectic FeCrC hardfacing alloys: Microstructure and wear properties. *Surface and Coatings Technology*, 334(September 2017):420–428, 2018.

[52] Karsten Günther. *Fertigungstechnik – aus den Grundlagen für die Anwendung Schriften aus der Ilmenauer Fertigungstechnik Band 1*. Phd thesis, Technische Universität Ilmenau, 2018.

[53] G. Gunter, K.; Bergman, J.P.; Zhang, C; Rosenberger, M.; and Notni. Hot Wire-Assisted Gas Metal Arc Welding of Ni-Based Hardfacing. *Welding journal*, 97(April):99s–107s, 2018.

[54] R. A. Ribeiro, E. B. F. dos Santos, P. D. C. Assunção, R. R. Maciel, and E. M. Braga. Predicting Weld Bead Geometry in the Novel CW-GMAW Process. *Welding Journal*, 94(September):301s–311s, 2015.

[55] E. S. Costa, P. D. C. Assunção, Emanuel B. F. Dos Santos, L. G. Feio, M. S. Q. Bittencourt, and E. M. Braga. Residual stresses in cold-wire gas metal arc welding. *Science and Technology of Welding and Joining*, 22(8):706–713, 2017.

[56] L. F. N. Marques, E. B. F. dos Santos, A. P. Gerlich, and E. M. Braga. Fatigue life assessment of weld joints manufactured by GMAW and CW-GMAW processes. *Science and Technology of Welding and Joining*, 22(2):87–96, feb 2017.

[57] P. D. C. Assunção, R. A. Ribeiro, E. B. F. dos Santos, Adrian P. Gerlich, and E. M Braga. Feasibility of narrow gap welding using the cold-wire gas metal arc welding (CW-GMAW) process. *Welding in the World*, 61(4):659–666, jun 2017.

[58] ASTM E384-17 - Standard Test Method for Microindentation Hardness of Materials, 2008.

[59] R. French Miller, Charles, Mark H. Crawford. Welding-Related Expenditures and Productivity Measurement in U.S. Manufacturing, Construction, and Mining Industries, 2002.

[60] M. Suban and J. Tušek. Dependence of melting rate in MIG/MAG welding on the type of shielding gas used. *Journal of Materials Processing Technology*, 119(1-3):185–192, dec 2001.

[61] Mohsen Mohammadijoo, Stephen Kenny, Laurie Collins, Hani Henein, and Douglas G. Ivey. Characterization of HAZ of API X70 Microalloyed Steel Welded by Cold-Wire Tandem Submerged Arc Welding. *Metallurgical and Materials Transactions A*, 48(5):2247–2259, 2017.

[62] Mohsen Mohammadijoo, Stephen Kenny, Laurie Collins, Hani Henein, and Douglas G Ivey. Effect of Cold-Wire Addition in the TSAW Process on Microstructure and Mechanical Properties of the HAZ of X70 Microalloyed Pipeline Steel. In *Volume 3: Operations, Monitoring and Maintenance; Materials and Joining*, page V003T05A051, Calgary, Alberta, Canada, sep 2016. ASME.

[63] S. J. Chen. Stability of the Cross-Arc Process — A Preliminary Study. *Welding Journal*, 94(5):158–168, 2015.

[64] F. G. da Silva. *Estudo da viabilidade do processo de soldagem FCAW com adição de arame frio aplicado a indústria naval [Feasibility study on cold wire FCAW process applied to naval construction]*. Master thesis (in portuguese), Federal University of Pará, 2010.

[65] AWS. *Specification for Carbon Steel Electrodes and Rods for Gas Shielded Arc Welding*. American Welding Society (AWS), Miami, FL, 2005.

[66] André Alves de Resende, Flávio Keocheguerians, and Louriel Oliveira Vilarinho. The influence of CO2 and O2 content on globular spray transition current when using argon-based blends in GMAW of ER70S-6 wire. *Welding International*, 24(8):593–601, 2010.

[67] A. Reis, R. P.; Souza, D.; Scotti. MODELS to describe PLASMA JET, ARC TRAJECTORY and arc blow formation in arc welding. *Welding in the World*, 55(3-4):24–32, 2011.

[68] X. Y. Cai, S. B. Lin, C. L. Fan, C. L. Yang, W. Zhang, and Y. W. Wang. Molten pool behaviour and weld forming mechanism of tandem narrow gap vertical GMAW. *Science and Technology of Welding and Joining*, 21(2):124–130, 2016.

[69] E.B. Michie, Ken; Blackman, Stephen; Ogunbiyi. Twin-wire GMAW:process characteristics and applications. *Welding Journal*, 78(5):31–34, 1999.

[70] Gang Zhang, Yu Shi, Ming Zhu, and Ding Fan. Arc characteristics and metal transfer behavior in narrow gap gas metal arc welding process. *Journal of Materials Processing Technology*, 245:15–23, 2017.

[71] Marjan Suban and Janez Tušek. Methods for the determination of arc stability. *Journal of Materials Processing Technology*, 143-144(1):430–437, 2003.

[72] Vinicius Lemes Jorge, Raul Gohrs, and Américo Scotti. Active power measurement in arc welding and its role in heat transfer to the plate. *Welding in the World*, 61(4):847–856, 2017.

[73] R. A. Ribeiro, E. B.F. Dos Santos, P. D.C. Assunção, E. M. Braga, and A. P. Gerlich. Cold wire gas metal arc welding: Droplet transfer and geometry. *Welding Journal*, 98(5):135S–149S, 2019.

[74] Bagnus Y. B. Yudodibroto, Marcel J. M. Hermans, Gert Ouden, and Ian M. Richardson. Observations on Droplet and Arc Behaviour during Pulsed GMAW. *Welding in the World*, 53(7-8):R171–R180, 2013.

[75] Emanuel B.F. Dos Santos, Rob Pistor, and Adrian P. Gerlich. Pulse profile and metal transfer in pulsed gas metal arc welding: droplet formation, detachment and velocity. *Science and Technology of Welding and Joining*, 22(7):627–641, 2017.

[76] Emanuel B.F. Dos Santos, Rob Pistor, and Adrian P. Gerlich. High frequency pulsed gas metal arc welding (GMAW-P): The metal beam process. *Manufacturing Letters*, 11:1–4, 2017.

[77] Kamal Pal and Surjya K. Pal. Effect of pulse parameters on weld quality in pulsed gas metal arc welding: A review. *Journal of Materials Engineering and Performance*, 20(6):918–931, 2011.

[78] Prakriti Kumar Ghosh. *Pulse Current Gas Metal Arc Welding*. Materials Forming, Machining and Tribology. Springer Singapore, Singapore, 2017.

[79] H. Tong, T. Ueyama, S. Harada, and M. Ushio. Quality and productivity improvement in aluminium alloy thin sheet welding using alternating current pulsed metal inert gas welding system. *Science and Technology of Welding and Joining*, 6(4):203–208, 2001.

[80] Aravinda Pai, Irappa Sogalad, S. Basavarajappa, and Prabhat Kumar. Results of tensile, hardness and bend tests of modified 9Cr 1Mo steel welds: Comparison between cold wire and hot wire gas tungsten arc welding (GTAW) processes. *International Journal of Pressure Vessels and Piping*, 169(September 2018):125–141, jan 2019.

[81] T. S. Cabral, E. M. Braga, E. A. M. Mendonça, and A. Scott. Influence of procedures and transfer modes in MAG welding in the reduction of deformations on marine structure panels. *Welding International*, 29(12):928–936, 2015.

[82] AISI 1020 Steel hot rolled, 2018.

[83] M. R. Bosworth. Effective heat input in pulsed current gas metal arc welding with solid wire electrodes. *Welding journal*, 70(5):111s–117s, 1991.

[84] Lincoln Electric. True Energy ™ Instantaneous Energy Values for the Weld, 2009.

[85] Roger Carter. *Analysis of pulsed gas metal arc welding (P-GMAW) heat input on UNS-S32101 lean duplex stainless steel*. Master thesis, Arizona State University, 2012.

[86] E.J. Soderstrom and P.F. Mendez. Metal Transfer during GMAW with Thin Electrodes and Ar-CO 2. *Welding Research*, 87(May):124–133, 2008.

[87] R.E. Dolby. Guidelines for the classification of ferritic steel weld metal microstructural constituents using the light microscope. *Welding in the World*, 24(7/8):144–148, 1986.

[88] R Essers, W.G. and Walter. Heat transfer and penetration mechanisms with GMA and plasma-GMA welding. *Welding Journal*, 60(2):37–42, 1981.

[89] J J Lowke. Physical basis for the transition from globular to spray modes in gas metal arc welding. *Journal of Physics D: Applied Physics*, 42:135204, 2009.

[90] J J Lowke. Globular and spray transfer in MIG welding. *Welding in the World*, 55(3-4):19–23, 2011.

[91] T. Methong, M. Shigeta, M. Tanaka, R. Ikeda, M. Matsushita, and B. Poopat. Visualization of gas metal arc welding on globular to spray transition current. *Science and Technology of Welding and Joining*, 23(1):87–94, 2018.

[92] R. A. Ribeiro, E. B.F. Dos Santos, P. D.C. Assunção, E. M. Braga, and A. P. Gerlich. Cold Wire Gas Metal Arc Welding: Droplet Transfer and Geometry. *Welding Journal*, 98(5):135S–149S, may 2019.

[93] Rafael A. Ribeiro, Paulo D.C. Assunção, Emanuel B.F. Dos Santos, Ademir A.C. Filho, Eduardo M. Braga, and Adrian P. Gerlich. Application of cold wire gas metal arc welding for narrow gap welding (NGW) of high strength low alloy steel. *Materials*, 12(3), 2019.

[94] Américo Scotti, Vladimir Ponomarev, and William Lucas. Interchangeable metal transfer phenomenon in GMA welding: Features, mechanisms, classification. *Journal of Materials Processing Technology*, 214(11):2488–2496, 2014.

[95] F. Valensi, S. Pellerin, Q. Castillon, A. Boutaghane, K. Dzierzega, S. Zielinska, N. Pellerin, and F. Briand. Study of the spray to globular transition in gas metal arc welding: A spectroscopic investigation. *Journal of Physics D: Applied Physics*, 46(22), 2013.

[96] J H Waszink, J H and Graat. Experimental Investigation of the Forces Acting on a Drop of Weld Metal. *Welding Journal (Miami, Fla)*, 62(4):108s–116s, 1983.

[97] C J Allum. Metal transfer in arc welding as a varicose instability. I. Varicose instabilities in a current-carrying liquid cylinder with surface charge. *Journal of Physics D: Applied Physics*, 18(7):1431–1446, jul 1985.

[98] C J Allum. Metal transfer in arc welding as a varicose instability. II. Development of model for arc welding. *Journal of Physics D: Applied Physics*, 18(7):1447–1468, jul 1985.

[99] Yangyang Zhao and Hyun Chung. Numerical simulation of the transition of metal transfer from globular to spray mode in gas metal arc welding using phase field method. *Journal of Materials Processing Technology*, 251(April 2017):251–261, 2018.

[100] H. Smartt and C. Einerson. A model for heat and mass input control in GMAW. *Welding journal*, 72(5):217s–229s, 1993.

[101] S. K. Choi, C. D. Yoo, and Y. S. Kim. Dynamic simulation of metal transfer in GMAW, part 1: Globular and spray transfer modes. *Welding Journal (Miami, Fla)*, 77(6):38–s, 1998.

[102] International vocabulary of metrology - Basic and general concepts and associated terms (VIM), 2012.

[103] ASME. ASME PTC 19.1-2018 - Test Uncertainty, 2018.

[104] Américo Scotti. Cares to Deal with Heat Input in Arc Welding: Applications and Modeling. *Advances in Welding Technologies for Process Development*, pages 101–138, 2019.

[105] N Pépe, S Egerland, P A Colegrove, D Yapp, A Leonhartsberger, and A Scotti. Measuring the process efficiency of controlled gas metal arc welding processes. *Science and Technology of Welding and Joining*, 16(5):412–417, 2011.

[106] A. Haelsig, M. Kusch, and P. Mayr. Calorimetric analyses of the comprehensive heat flow for gas metal arc welding. *Welding in the World*, 59(2):191–199, mar 2015.

[107] A. Haelsig, P. Mayr, and M. Kusch. Determination of energy flows for welding processes. *Welding in the World*, 60(2):259–266, 2016.

[108] A Hälsig, S. Pehle, M. Kusch, and P. Mayr. Reducing potential errors in the calculation of cooling rates for typical arc welding processes. *Welding in the World*, 61(4):745–754, jun 2017.

[109] Kjell Hurtig, Isabelle Choquet, Américo Scotti, and L.-E. Svensson. A critical analysis of weld heat input measurement through a water-cooled stationary anode calorimeter. *Science and Technology of Welding and Joining*, 21(5):339–350, jul 2016.

[110] Oystein Grong. *Metallurgical Modelling of Welding.* The Institute of Materials, London, UK, 2nd editio edition, 1997.

[111] Hernán Dario Hernández Arevalo and Louriel Oliveira Vilarinho. Desenvolvimento e avaliação de calorímetros por nitrogênio líquido e fluxo contínuo para medição de aporte térmico. *Soldagem e Inspecao*, 17(3):236–250, 2012.

[112] Fredrik Sikström. Operator bias in the estimation of arc efficiency in gas tungsten arc welding. *Soldagem e Inspecao*, 20(1):128–133, 2015.

[113] Sindo Kou and Y. Le. Heat Flow During the Autogenous GTA Welding of Pipes. *Metallurgical transactions. A, Physical metallurgy and materials science*, 15 A(6):1165–1171, 1984.

[114] Frank P Incropera. *Fundamentals of heat and mass transfer.* John Wiley & Sons, Inc., 6th edition, 2007.

[115] A. Joseph, D. Farson, D. Harwig, and R. Richardson. Influence of GMAW-P current waveforms on heat input and weld bead shape. *Science and Technology of Welding and Joining*, 10(3):311–318, 2005.

[116] Dieter Radaj. *Heat Effects of Welding.* Number 9. Springer Berlin Heidelberg, Berlin, Heidelberg, 1 edition, 1992.

[117] Stephan Egerland and Paul Colegrove. Using Solid State Calorimetry for Measuring Gas Metal Arc Welding Efficiency. In Wladislav Sudnik, editor, *Arc Welding*, number 1, chapter 12, pages 265–280. InTech, 1st ed. edition, dec 2011.

[118] Nils Stenbacka. On arc efficiency in Gas Tungsten Arc Welding. *Soldagem & Inspecao*, 18(4):380–390, 2013.

[119] André Hälsig. *Energetische Bilanzierung von Lichtbogenschweißverfahren (Energy balancing of gas shielded arc welding process).* Ph.d thesis, Technische Universitat Chemnitz, 2014.

[120] P D C Assunção, R A Ribeiro, E. B. F. Dos Santos, E M Braga, and A P Gerlich. Comparing CW-GMAW in direct current electrode positive (DCEP) and direct current electrode negative (DCEN). *The International Journal of Advanced Manufacturing Technology*, jul 2019.

[121] N.N. Rykalin. Calculation of heat processes in welding. In *42nd Annual Meeting of the American Welding Society*, page 64, 1960.

[122] R. A. Ribeiro, E. B. F. Dos Santos, P D C Assunção, K J Daun, and A P Gerlich. Uncertainty analysis of a water flow calorimeter while welding in short-circuit and spray transfer regimes. *Welding in the World*, jun 2020.

[123] P.E. Murray and A. Scotti. Depth of penetration in gas metal arc welding. *Science and Technology of Welding and Joining*, 4(2):112–117, 1999.

[124] P. W. Fuerschbach. A Dimensionless Parameter Model for Arc Welding Processes. In *International Conference on Trends in Welding Research*, Gatlinburg, TN, USA, 1994.

[125] N. A. McPherson. Welding issues for ship structures. *Journal of Marine Engineering and Technology*, 9(3):31–41, 2010.

[126] Frank Roland, Luciano Manzon, Pentti Kujala, Markus Brede, and Jan Weitzenböck. Advanced joining techniques in European shipbuilding. *Journal of Ship Production*, 20(3):200–210, 2004.

[127] ASTM. A131-A131M - 14 Standard Specification for Structural Steel for Ships, 2014.

[128] AWS. AWS A5.28 A5.28M:2005 - Specification for low-alloy steel electrodes and rods for gas shielded arc welding, 2005.

[129] ASTM E8. ASTM E8 standard test methods for tension testing of metallic materials. *Annual Book of ASTM Standards 4*, (C):1–27, 2010.

[130] ASTM. A370: Standard Test Methods and Definitions for Mechanical Testing of Steel Products. *ASTM International*, pages 1–50, 2014.

[131] Mustafa Koçak. Integrity of Welded Structures : Process - Property – Performance (3P) Relationship, 2010.

[132] R. A. Ribeiro and A.P. Gerlich. The arc stability mechanism and metal transfer during cold wire pulsed gas metal arc welding, 2020.

[133] J. J. Lowke. A unified theory of arcs and their electrodes, 1997.